The Characterisation of Liquid Sprays Injected from Circular and Non-Circular Nozzles into High Speed Subsonic Cross-Airstreams

Nicholas J. Regan

D.Phil Thesis 2011

Supervised by
C.A. Long, N. R. Atkins & P. R. N. Childs

Thermo-Fluid Mechanics Research Centre
Department of Engineering and Design
University of Sussex
Brighton
BN1 9QT

Declaration

I confirm that this is my own work and the use of all material from other sources has been properly and fully acknowledged.

Nicholas Regan

Abstract

This study was motivated by a need to better understand the sprays that can develop when oil leaks occur in gas turbine engines. Current gas turbine engines incorporate an extensive network of oil distribution pipes which deliver lubrication oil to bearings and seals at various locations across the engine. Parts of the oil pipe network are situated in hot, high pressure engine cavities where an oil leak, from a fractured pipe or leaking seal, could ignite and lead to an engine fire.

Oil leaks in gas turbine engines create liquid injection in cross-airstream situations, a subject which has been widely studied for combustion systems. However, previous studies are almost exclusively based on circular nozzle geometries. For a fractured oil pipe, the geometry through which the oil leaks approximates to a slot shape rather than a circular nozzle.

Sprays which develop in cross-airstreams are most sensitive to the parameters of Weber number ($We_{g\,eq}$) and momentum flux ratio (q). A wide range for these parameters are considered to be possible in engine oil leak scenarios because of the variety of crack dimensions possible and range of airflow conditions across the different sections of the engine; from zero to in excess of $We_{g\,eq} = 4000$ and $q = 300$ could be possible in extreme cases.

The aim of this study was to generate and then characterise sprays in representative conditions. The main focus was the characterisation of the droplets which formed in the sprays, with the key objective of providing validation data for CFD codes. Droplet characterisation was performed using a phase Doppler particle analysis system. High speed video as well as pulsed laser sheet digital imaging were also used in the study to provide insight into upstream features of the spray field.

A 0.5 x 5.38 mm slot shaped nozzle geometry was used in two orientations; perpendicular alignment ⇊ and parallel alignment ⇊. Water was injected into a cross-airstream over a twelve point test matrix with momentum flux ratios (q) values within the range of $4 \lesssim q \lesssim 32$ and Weber number ($We_{g\,eq}$) values within the range of $300 \lesssim We_{g\,eq} \lesssim 1600$.

The position of the spray was highly dependent on slot nozzle orientation. The spray was considerably further offset from the nozzle injection wall in parallel alignment ⇊, compared to the perpendicular alignment ⇊. However, the centre-line distribution of Arithmetic Mean Diameter (AMD) was similar for both orientations, albeit offset further from the injection wall for the parallel slot nozzle. The underlying structure of droplet size distribution was consistent with results for sprays from circular nozzles.

At low liquid injection pressures the sprays produced by the perpendicular aligned slot ⇊ exhibited impingement, producing large droplets in the near wall region. Where impingement was not present, the data showed that AMD was not significantly influenced by the orientation of the slot nozzle; with all tests generating results in the range of $16\ \mu m \lesssim AMD \lesssim 80\ \mu m$.

Acknowledgements

Firstly, I would like to thank Peter Childs for providing me this opportunity and his considerable support.

I would like to extend my thanks to Nick Atkins whose contributions to the work and my progress were crucially important.

I am also extremely grateful to Chris Long for his contributions, technical guidance and support throughout my time at the TFMRC.

I gratefully acknowledge the support of Rolls-Royce Plc. and extend my thanks to all the fluid systems team at Derby and in particular, Guy Snowsill and Tim Scanlon.

I am also very grateful to Ken Hart not only for his technical contributions but also for his encouragement and interest in my progress.

I am also considerably thankful for the efforts and contributions to the work from Paul Hutcheson and the team at the University of Surrey.

This list would be incomplete without mentioning the many wonderful characters that I have worked alongside at the TFMRC.

And, I would like to recognise the support my family and friends have provided me through this process.

I dedicate this thesis to my ever missed father

Contents

Glossary of Symbols and Acronyms

Acronyms

A	Area	$\dot{m}$	Mass-flow rate
a	Speed of sound	Oh	Ohnesorge number
AMD	Arithmetic mean diameter	P	Total pressure
AR	Aspect ratio	p	Static pressure
b	Slot span	PDPA	Phase Doppler particle analysis
b	Slot span	PIV	Pulsed Laser Anemometry
C	Coefficient	q	Momentum flux ratio
CFD	Computational fluid dynamics	R	Universal gas constant
d	Diameter/dimension	r	Radius
Fr	Froude number	Re	Reynolds number
fps	frames per second	SMD	Sauter Mean Diameter
g	Gravitational acceleration	t	Time
HSV	High speed video	T	Temperature
I	Turbulence intensity	U	Nozzle exit velocity
K	Cavitation parameter	V	Velocity in y axis
k	Turbulent kinetic energy	W	Crossflow velocity
Kn	Knudsen number	w	Slot width/smallest dimension
l	Nozzle through-length	We	Weber number
L	Nozzle length scale	x	Position in nozzle axis
LDA	Laser Doppler anemometry	y	Position lateral axis
M	Mach number	z	Position in crossflow axis

Subscripts

1	Upstream location	h	Hydraulic (diameter)
2	Downstream location	l	Liquid phase
11	Arithmetic mean diameter	mfp	maximum flux position
22	Sauter mean diameter	mean	mean average value
b	Breakup (length, parameter)	nc	non-cavitating nozzle flow
d	Discharge (coefficient)	noz	nozzle
drop	Droplet property	pen	Penetration
eq	Equivalent (diameter)	TS	Test section property
f	Frontal (dimension)	v	Vapour
flip	Hydraulic flipped nozzle flow	visc	Viscosity (coefficient)
g	Gas phase		

Greek Symbols

σ	Surface tension	ϕ	Injection angle
μ	Dynamic viscosity	ρ	Density
Θ	Slot orientation to crossflow	τ	Time (response)
Δ p	Pressure differential across crack	γ	Ratio of specific heat capacities
Δ t	Time-step	ω	Natural frequency
η	Kolmogorov length scale	Ω	Maximum growth-rate
		ν	Kinematic Viscosity

Nozzle Injector Symbols

$\overset{\Downarrow}{\odot}$	Round nozzle	$\overset{\Downarrow}{\ominus}$	Horizontal slot nozzle
$\overset{\Downarrow}{\oplus}$	Vertical slot nozzle		

Chapter 1

Introduction

This chapter introduces the requirement, scope and goals of this study which was sponsored by Rolls-Royce Plc. The work reported in this thesis describes an experimental study, carried out at the University of Sussex, which contributed to a wider project involving four Universities and Rolls-Royce Plc, Derby.

Gas turbine engines incorporate an extensive network of oil distribution pipes which deliver lubrication oil to bearings and seals at various locations across the engine. The wider project was motivated by a need for more in-depth understanding of the oil sprays that develop when the oil system integrity fails.

Parts of the oil pipe network are situated in hot, high pressure engine cavities where an oil leak, from a fractured pipe or leaking seal, could ignite and lead to an engine fire, as presented in Figure 1.1. The heat transfer and local temperatures during such an incident are potentially hazardous to engine reliability and integrity, with engine oil having an Energy Density of 33 MJ/kg and a stoichiometric flame temperature approaching 2400 K.

Although intuitively it would seem possible to design-out such occurrences by increasing the pipe wall thickness, such methodology is at odds with the general requirement to reduce engine weight and, in any case, absolute prevention is impossible. Tools that enable accurate predictions of the risks provide a platform from which the engine's oil system design can be optimised.

The project partners and their roles were as follows:

Karlsruher-Institut-fuer-Technologie (KIT) - Identifying engine vulnerability
University of Surrey - CFD test rig simulations
University of Hertfordshire - Oil systems consultancy
Rolls-Royce Plc, Derby - Project integration and CFD engine simulation
TFMRC, University of Sussex - Experimental characterisation of sprays

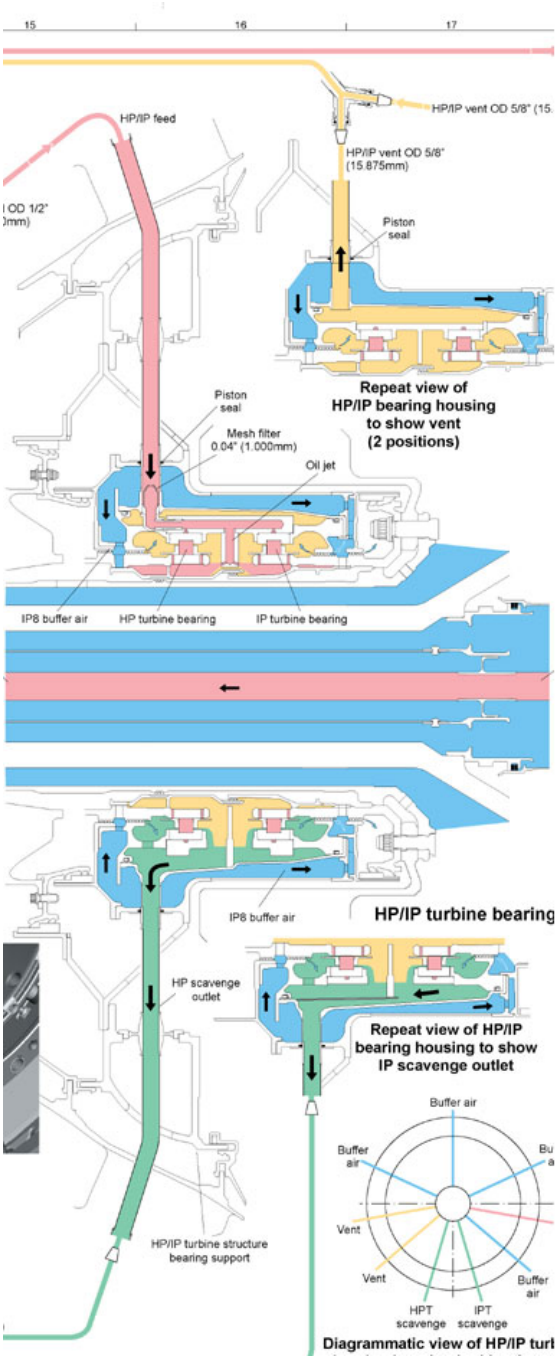

Figure 1.1: Example of oil pipework architecture (from Rolls−Royce Plc.)

Advances in materials and improvements in engine cooling air systems allow for higher working temperatures and cycle efficiency. However, increased cavity

temperatures heighten the risk of an oil fire, because of greater heat transfer to the leaking oil. Hence, as well as providing tools to evaluate the level of risk for oil fires in current engine designs, the findings from this work are expected to play a role in supporting future engine developments.

For an oil fire to occur the criteria for combustion must be met - the oil to air ratio must be within flammability limits typically 1:3 to 1:30 for engine oil/air by mass and the mixture must be heated to the minimum ignition temperature ≈ 580 K at typical engine cavity pressures (**Hart, Hutcheson and Regan (2009)**).

Assessing the risk through actual engine testing with contrived oil leaks presents a number of problems, not least, because the lack of a fire does not preclude the possibility of a fire. Then there is the number of the different conditions possible in different cavities at various stages through the engine. As such, it was necessary to assess the risk more generally and aim to understand the behaviour and characteristics of the oil sprays that can develop. The compilation of a computer simulation specified for the task was considered to have the greatest potential for providing a universal tool that could be utilised to assess the risk across different engine cavities - a procedure for this was outlined by **Young (2002)**. The procedure involves CFD codes to quantify the risk and would provide an important tool to inform the design process of new gas turbine engines, avoiding oil system routing that present a greater risk.

However, CFD solutions rely on a variety of empirical models, all of which require validation at representative non-dimensional conditions. Understanding the physical parameters to which oil fire risk is sensitive is crucial.

An engine's vulnerability to an oil fire was investigated in a substantial analytical and experimental work programme carried out by Willenborg at the University of Karlsruhe. Willenborg reported his findings in *Methodology for Assessing Oil Fire Risk*, **Willenborg (2004)**. This work highlighted that a major factor in oil fire risk is the length of time the oil spray remains within an engine cavity - *the residence time*. Willenborg confirmed larger droplets exhibited extended residence times and therefore droplet sizes were an important factor.

As the risk for an oil fire is related to the size of the droplets that form when lubrication oil leaks into the engine's air systems, it follows that the capability of Young's CFD based procedure relies on accurate knowledge of the droplet sizes possible.

In order to demonstrate the capability of CFD for this application, Paul Hutcheson at the University of Surrey, completed a Ph.D study which involved CFD

modeling of the two component flow situation and in particular performing predictions of the specific experiments carried out at the TFMRC. Hutcheson's (Ph.D) modelling study was conducted simultaneously with the experimental work being completed at the TFMRC at the University of Sussex, with close coordination between the two institutes. Consequentially, a detailed account of how the experimental data produced can be used for CFD validation and comparison is available in **Hutcheson (2011)**. This thesis focuses on the flow physics and the insights made possible by the experimental data that has been produced.

When oil leaks from the engine's oil system into an engine cavity, it encounters an airstream which breaks-up the oil continuum to form droplets. The mean sizes of the droplets formed depend most significantly on the balance between the dynamic forces of the airstream serving to break-up the oil continuum and the oil's surface tension forces serving to hold it together as a continuum. This is an important relationship in all spray studies and is defined by the Weber Number parameter:

$$\mathrm{We}_g = \frac{\rho_g \left(W_g - W_l\right)^2 L}{\sigma} \tag{1.1}$$

The scenario of liquid injection into cross-airstreams is a situation that arises in many combustion systems and, as a result, the relevant flow physics in the context of combustion has been widely explored and reported. However, inconsistencies between past studies and the current interest cannot be ignored and require new data in order to address the knowledge gap.

In particular, the current interest contrasts with previous works in the following respects: **spray nozzle geometry**, **rotating airstream** and **engine oil liquid properties** - outlined in the following text.

Nozzle Geometry

The failure of an oil pipe can occur through interference with an adjacent component or cyclical stressing. The geometry possible for a breached oil pipe is expected to be wide-ranging but evidence suggests approximation to a slot, as can be seen in Figure 1.2, rather than a round nozzle as features in the vast majority of previous work.

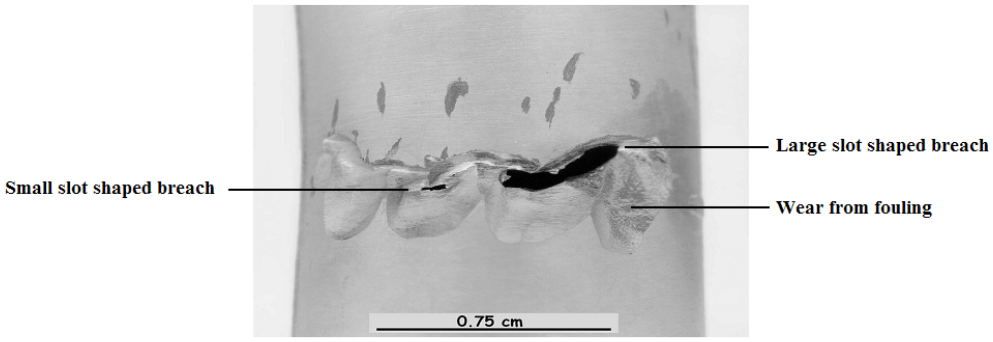

Figure 1.2: In-service pipe failure (from Rolls−Royce Plc.)

The lower end of the range can be assumed to be cracks measuring just a few microns in both directions. The upper end of the range is not obvious, however, at some point the engine's oil system would no longer be able to maintain its normal operating pressure, triggering a warning and pilot intervention with an engine shutdown.

For sprays emanating from **round nozzles**, the size of the droplets in the downstream spray field scale with nozzle diameter, this is because the average diameter of the droplets are related to the diameter of the liquid jet from which they came and, in turn, the diameter of the liquid jet is related to the nozzle from which it came; as illustrated by the falling column of liquid in Figure 1.3

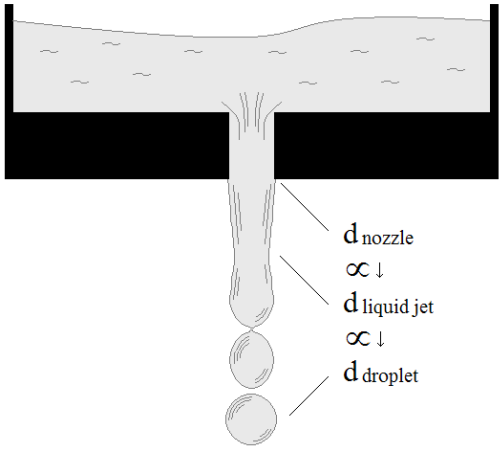

Figure 1.3: Nozzle diameter ∝ liquid jet diameter ∝ droplet diameter

The equivalent relationship for droplets from liquid sheets that emanate from slot shaped nozzles has had little study, especially into sub-sonic cross-airstreams.

Rotating Airstream

In the case of oil leaking into a gas turbine engine cavity, the merging airstream may engage at different orientations; axial, circumferential and radial airflows all exist within different engine cavities. In the vast majority of spray in cross-airstream studies, the airstream follows a linear flow path in an open circuit wind tunnel arrangement and the liquid is injected from a perpendicular nozzle.

Engine Oil Liquid Properties

Engine oil at 100 °C has the following liquid properties compared to water at 20 °C:

	Mobil Jet 254 (100 °C)	Water (20 °C)
Density	ρ = 888 kg/m^3	ρ = 998 kg/m^3
Surface Tension	σ = 0.0197 N/m	σ = 0.0728 N/m
Kinematic Viscosity	ν = 5.3 cSt	ν = 1 cSt
Dynamic Viscosity	μ = 0.0047 Pa.s	μ = 0.001 Pa.s

As stated above, droplet size scales most significantly with the non-dimensional parameter of Weber number which is a ratio of *the external dynamic forces* to the *internal liquid surface tension forces*, as in Equation 1.1 above. Consequentially, the influence of the liquid's surface tension on the resultant spray characteristics can be addressed using non-dimensional scaling.

Dynamic viscosity and liquid density can be accounted for through the non-dimensional parameter of Ohnesorge number (Oh) which is a ratio of *the dynamic viscosity* to the *square route of the liquid density and surface tension*:

$$\mathrm{Oh} = \frac{\mu_l}{\sqrt{\rho_l \, \sigma_l \, L}} \tag{1.2}$$

Hsiang and Faeth (1992) showed for Oh $\lesssim$ 0.4 break-up regime is unaffected by Ohnesorge number, as is the case for engine oil at 100 °C and where the characteristic length scale is L > 0.02 mm. Water also satisfies this criterion and can, to an extent, provide a substitute to using hot engine oil in tests.

Through consultation with Rolls-Royce Plc. and the other project partners, given the lack of previous experimental work with slot nozzle geometries it was agreed that it was preferable to focus the available resources on completing an extensive test matrix using water and delivering a wide range of test points for CFD validation, i.e. in preference to completing a small number of tests using volatile liquids.

This introduction has so far concentrated on how oil leaks can occur in gas turbine engines and the situations that can arise as a result. In doing so, it has highlighted some gaps between the open literature and the current interest - in particular the lack of previous work on sprays in cross-airstreams from slot nozzles. The following sub-section focuses more generally on the features of a spray in cross-airstream flow field.

1.1 Introduction to Sprays in Cross-Airstreams

As a liquid is injected into a cross-airstream (through a round nozzle) surface tension tends to maintain the liquid jet as a cylindrical uniform continuum. The cross-airstream acts to break it up. Atomisation of the bulk liquid comes about through two mechanisms which are described below and illustrated in Figure 1.4.

1. **Column Break-up**, as the liquid exits the nozzle and forms a jet, waves develop on the surface. The jet is accelerated in the direction of the cross-airstream and the waves grow downstream until, eventually, a wave trough will break through the jet.

2. **Surface Stripping** is due to the relative velocity at the liquid/gas interface. In this mechanism, the shear forces that develop at the liquid/gas interface strip liquid from the jet surface to form relatively small droplets.

Figure 1.4 identifies the main features of a spray in a cross-airstream. Of these features, it is the characteristics of the droplets that provide the most interest within this study since the risk of an oil fire is related to the droplet size. However, the droplet properties are very much a product of the flow behaviour that occurred before they formed and attention is also given in this study to the upstream spray features.

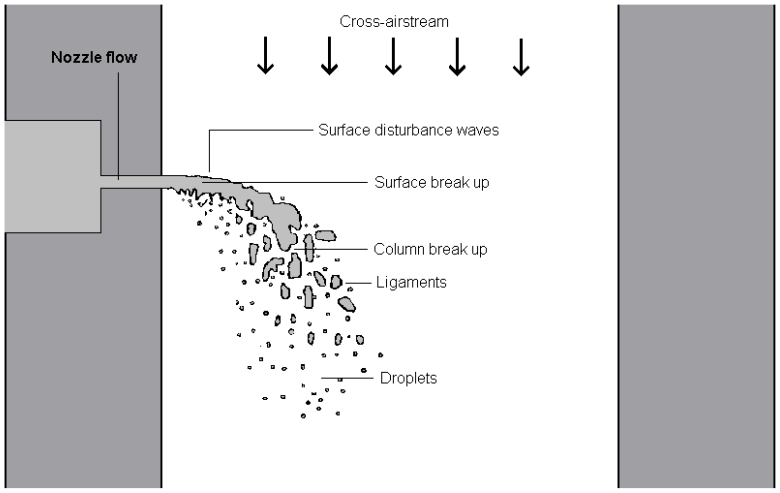

Figure 1.4: Spray regions

Below is a summary of the spray regions featured in Figure 1.4, starting with the liquid flow in the nozzle and working downstream.

Nozzle Flow
The liquid flow characteristics in the nozzle can influence the droplet sizes in the spray field. In addition to the usual laminar and turbulent flow types, the nozzle flow will exhibit one of the following regimes: non-cavitating; cavitating; or, hydraulic flip.

As with any nozzle the features that influence the flow characteristics are: the differential pressure across the nozzle entry/exit; the inlet edge (which can be sharp or have a radius); and, the passage-length to diameter ratio. The situation is more complicated where the nozzle is something other than round, as is the case for the current interest.

These different states of nozzle flow and their influence on the spray field are discussed in the literature review in the following chapter.

Liquid Jet/Sheet Behaviour
The behaviour of the liquid continuum, as it emerges from the nozzle exit and extends into the cross-airstream prior to its disintegration, has a determining influence on the position of the downstream droplets (relative to the point of injection). The free liquid body is a fundamental part of the spray field's shape and structure; its behaviour is influenced by the upstream nozzle flow characteristics and also by interference with the cross-airstream.

As liquid emanates from the nozzle into a cross-airstream an exchange of momentum ensues, as the initially perpendicular liquid jet is accelerated in the

direction of the airstream. The balance of the liquid-flow to gas-flow momentum is defined by the **momentum flux ratio (q)**.

$$q = \frac{\rho_l U_l^2}{\rho_g W_g^2} \tag{1.3}$$

At high q, where there is high liquid-flow to gas-flow momentum, the liquid body penetrates deeply into the gas stream and the momentum exchange occurs gradually; the liquid body's behaviour is characteristically steady in this condition.

In contrast, at low q, because the liquid body has low momentum it does not penetrate far into the gas stream - the liquid body turns about a short radius and the momentum exchange occurs in a small volume with the result of a more intense momentum exchange and less steady behaviour.

Droplet Analysis
Droplet size and locations are of paramount importance in identifying oil fire risk. For this study, perhaps the most important issue is the validation of CFD used to model different scenarios; the characterisation of the droplets represents the main focus for this study.

1.2 Coordinate System for the Current Study

It is helpful to keep in mind the coordinate system with respect to the spray field that has been adopted in the current work as illustrated in Figure 1.5.

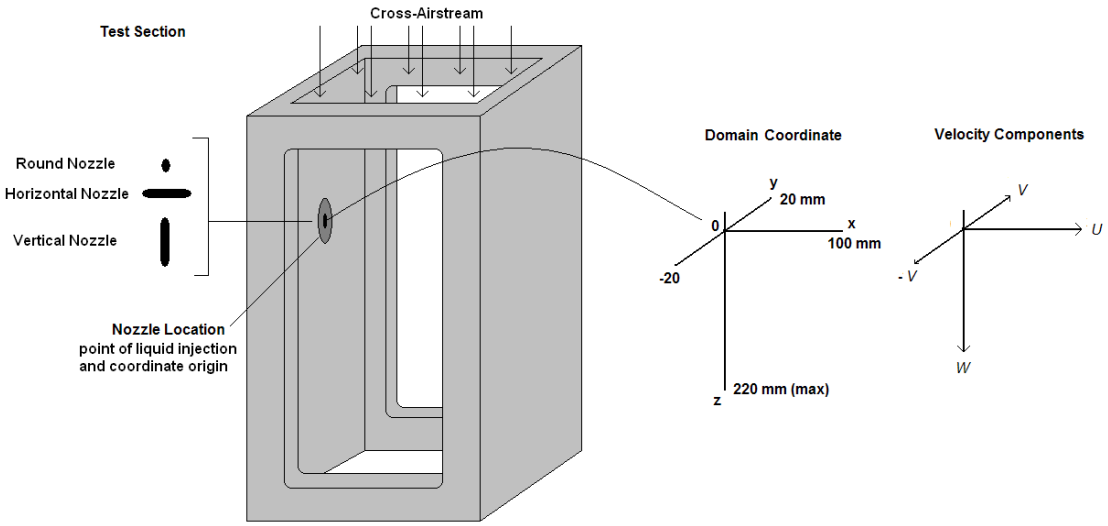

Figure 1.5: Test section coordinate system

The origin of the coordinate system is the centre of the nozzle exit and the test domain extends:

$$\begin{array}{rcrll} 0 & < x < & 100 & \text{mm} & \text{(direction of liquid injection)} \\ \text{-}20 & < y < & 20 & \text{mm} & \text{(transverse direction)} \\ 0 & < z < & 220 & \text{mm} & \text{(direction of the cross-airstream)} \end{array}$$

In this experimental study, tests were completed using two nozzle types, round and slot; and the slot nozzle was used in two orientations. For clarity symbols have been developed to designate and differentiate between the nozzles and orientations as follows:

Round nozzle: ⇓⊙
Horizontal slot nozzle: ⇓⊖
Vertical slot nozzle: ⇓⊖

1.3 Thesis Structure

Following this introduction chapter, Chapter 2 presents a review of the relevant previous work.

Chapter 3, a completely new test rig was designed and built for this study - this chapter highlights the key design choices and provides a description of the spray test facility. The test facility instrumentation and corresponding systems as well as uncertainty for the measured conditional parameters are described.

Chapter 4, provides descriptions of the experimental methods employed in spray characterisation as well as providing information for their particular setup for the TFMRC spray facility.

Chapter 5, concerns the air and water flow fields. This chapter provides a detailed analysis of the velocity distribution and turbulence levels of the cross-airstream and presents the discharge coefficients that were measured for the water injector nozzles.

Chapter 6, presents data from experiments using a round nozzle. The main aim of these experiments was to confirm the capability of the TFMRC spray rig and the newly acquired Phase Doppler Particle Analyser. This chapter provides a foundation for the main results chapter which follows it.

Chapter 7, presents the slot nozzle spray characterisation data - the main findings of this experimental study.

Chapter 8, presents some final conclusions and discusses further work that could extend the current achievements of the study.

Appendices A, B and C present data for all the test points covered, for the ⇓⊙, ⇓⊖ and ⇓⊙ nozzles respectively.

Chapter 2

Literature Review

This chapter begins with a broad introduction to the subject of liquid sprays, followed by a description of the physics involved with the break-up of a droplet, after which the focus extends to liquid sprays in a cross-airstream.[1]

2.1 Introduction

The main objective of this study was to investigate the type of sprays that are expected to form when oil leaks into hot, high-pressure engine cavities. Such events produce a liquid injection in a cross-airstream situation - a subject that has been studied extensively with the aim of improving combustion systems in heat engines. However, publications are almost exclusively based on liquid injection from round nozzles and the geometry of oil pipe failure approximates to a slot providing a major difference from the present interest.

According to **Lefebvre (1989)** the earliest examples of investigations into liquid break-up were from **Bidone (1829)** and **Savart (1833)**. Current understanding appears to stem from the contributions made by: Joseph Plateau 1801-1883, Hermann Helmholtz 1821 - 1894, Lord Kelvin 1824 - 1907 and Lord Rayleigh 1824 - 1907. Among other contributions, in 1873, the Belgium physicist Plateau showed that a falling column of water exhibited a finite length due to intrinsic instabilities. Lord Rayleigh extended the work of Plateau in his treatise named *On the Instability of Jets*, **Rayleigh (1878)** in which, he further defined the instabilities through a theoretical analysis and this formed the basis of understanding.

[1]Note on Coordinate System: The current study has the coordinate system x = the liquid injection or spray transverse direction, y = the spray spread direction and z = direction of the cross-airstream. All other studies are adjusted to fall in-line with the current study.

Moving on from Lord Rayleigh's treatise the study of sprays became more segregated in the twentieth century, as applications of sprays became more diverse. This literature review concentrates on *liquid sprays in subsonic cross-airstreams* with an emphasis on experimental characterisation. The first example of an experimental investigation of liquid sprays in subsonic cross-airstreams, rather than stationary air, appears to be **Chelko (1950)** working for NACA.

The advent of the gas LASER in the early sixties contributed greatly to the experimental characterisation capabilities through velocimetry and, a decade or so later, with particle sizing through the Phase Doppler Analysis technique. Pulsed laser sheet and coupled imaging techniques that allow for clear images of the jet are also widely used. In addition, high-speed video has developed considerably in recent years providing macroscopic insight into the *temporal* and *spatial* characteristics of the flow field.

The processes involved in bulk liquid atomisation are complex, however, it can be said that breakup originates from instabilities at the liquid/gas interface. There are a number of similarities between the break-up of an isolated liquid droplet and the break-up of larger less stable bodies of liquid. The break-up of an isolated droplet provides a good starting point in the explanation of bulk liquid atomisation.

2.2 Droplet Break-up Physics

A droplet is considered to be unstable if the internal force at its surface is less than the external dynamic force acting on it. The gas Weber number (We_g) defines the balance of internal and external pressure acting on a droplet.

$$We_g = \frac{\rho_g \, (W_g - W_l)^2 \, L}{\sigma} \tag{2.1}$$

Where L, the characteristic length scale, is the diameter in the case of an isolated droplet

A droplet will break-up with different characteristics depending on We_g magnitude.

At low We_g, **capillary forces** dominate the process, with the characteristic result defined as *bag break-up*.

At high We_g, **shear forces** dominate the process with the characteristic result defined as *shear break-up*.

Between these two distinguishable regimes, a process known as *multi-mode break-up* is observed, as illustrated in Figure 2.1.

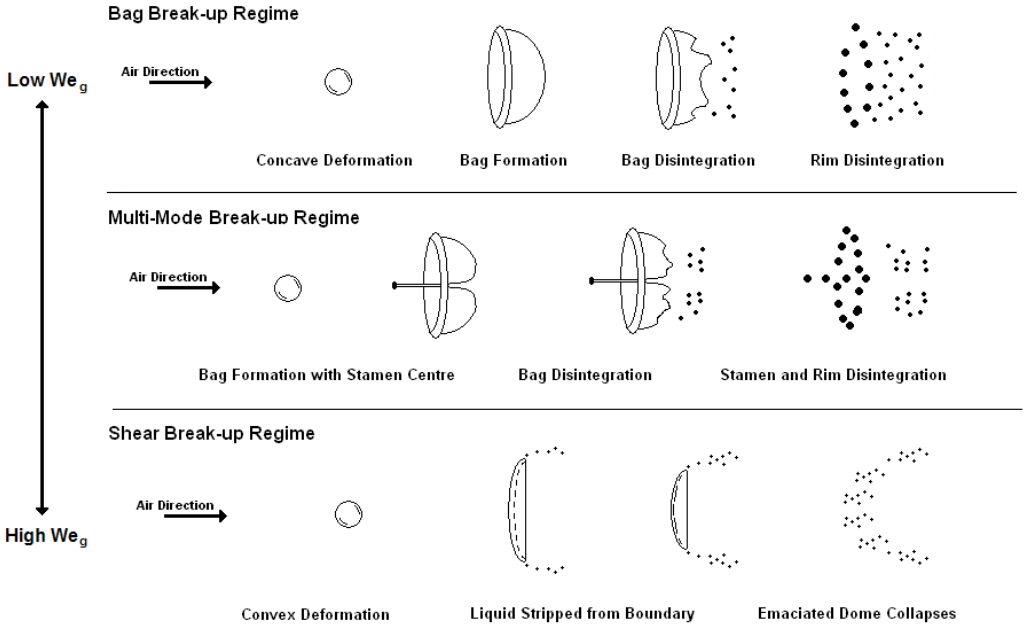

Figure 2.1: Droplet break-up regimes

In *bag break-up*, the droplet takes on a concave shape relative to the direction of the airstream. A thin sheet extends from a circular rim that disintegrates to form small droplets and the rim collapses to form relatively large droplets. Conversely, in the *shear break-up* regime, the initial droplet takes on a convex shape to the airstream. Liquid is stripped from the surface producing small droplets. At some point the emaciated dome can no longer be maintained and a complete collapse ensues. In the *multi-mode break-up* regime, the droplet forms a shape that appears to combine both the bag and shear break-up mechanisms, a toroidal bag is formed with a stamen like central region extending towards the direction of the airstream. In multi-mode break-up the droplet diameter has a distinct pair of peak values as result of the confluent mechanisms, for example Figure 2.2.

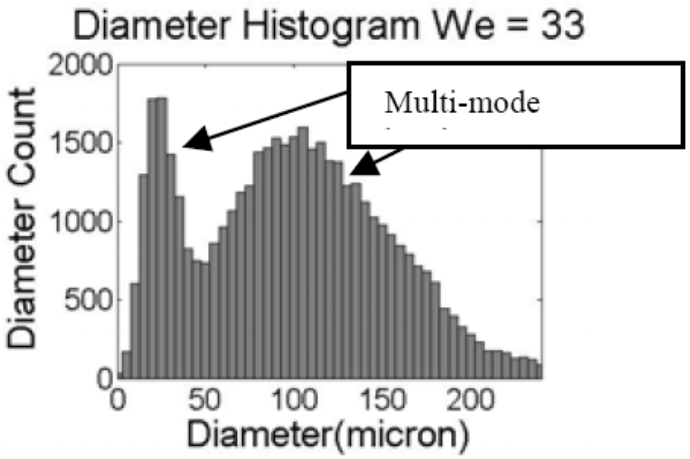

Figure 2.2: Multi-mode break-up at $We_g = 33$, **Lubarsky et al. (2007)**

In general, for liquids with low dynamic viscosity disintegration is independent of the liquid's viscosity. The point at which liquid viscosity becomes influential involves other factors as defined by the Ohnesorge number (Oh):

$$\text{Oh} = \frac{\mu_l}{\sqrt{\rho_l \, \sigma_l \, L}} \tag{2.2}$$

The Ohnesorge number provides a scale that accounts for liquid viscosity. **Hsing and Faeth (1992)** presented the table in Figure 2.3 showing where break-up is independent of Ohnesorge number (Oh):

- **Bag break-up** occurs $13 > We_g > 32$;
- **Multi-mode break-up** occurs $32 > We_g > 82$; and
- **Shear break-up** dominates from $We_g > 82$.

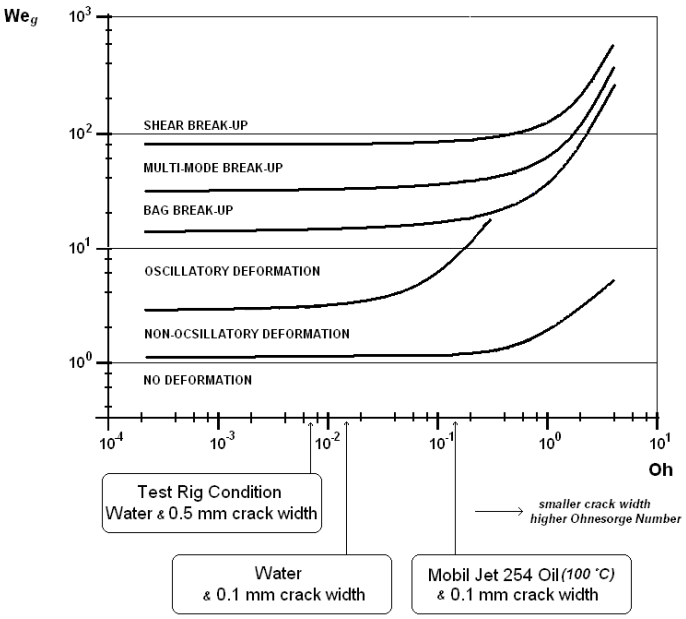

Figure 2.3: Droplet break-up regimes replotted from **Hsiang and Faeth (1992)** - flagged points based on water: ρ = 998 kg/m^3, σ = 0.0728 N/m, μ = 0.001 Pa.s; and, Mobil Jet 254 Oil (100°C): ρ = 888 kg/m^3, σ = 0.0197 N/m, μ = 0.0047 Pa.s

Liquids with low dynamic viscosity, such as water or hot engine oil, generally speaking have low Ohnesorge Numbers i.e. in the region where disintegration is independent of dynamic viscosity. However, the Ohnesorge number definition (presented above) includes a characteristic length scale - assuming this is proportional to the crack width for a pipe breach, the positions flagged in Figure 2.3 show that for oil leaks from small crack widths ($L < 0.1$ mm) in an engine, Ohnesorge number may become influential.

A fourth regime known as *catastrophic break-up* occurs at very high We$_g$ levels (outside the range in Figure 2.3), in which a convex dome is formed in a manner similar to the shear driven break-up mechanism. However, in catastrophic break-up, the dome structure exhibits waves on the surface with ligaments extending from the extremity, as illustrated in Figure 2.4.

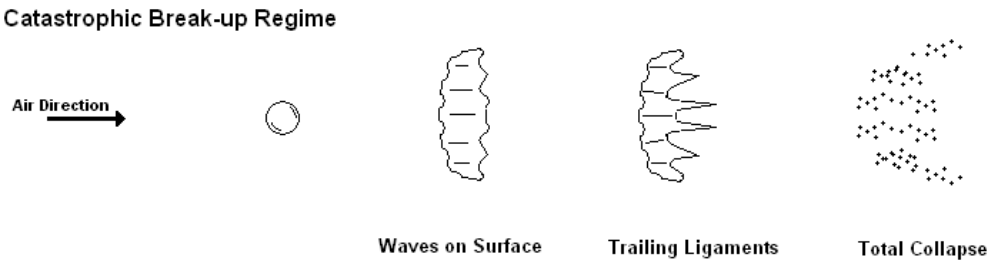

Figure 2.4: Catastrophic droplet break-up regime

The magnitude of We_g required to produce catastrophic break-up is unclear, as there is variation among authors. For example, **Borisov et al. (1981)** reported catastrophic break-up occured as low as $We_g > 210$, where as, **Chryssakis and Assanis (2005)** reported the onset as $We_g > 800$.

The four break-up regimes listed above are described in the *context of isolated droplets* that have a velocity differential with their surrounding gas, like a falling raindrop. However, in the *context of bulk liquid atomisation* the four regimes are collectively referred to as *secondary break-up mechanisms*; where the process of bulk liquid atomisation through a simple[2] nozzle is:

Bulk Liquid → Liquid Body → Ligaments and Droplets → Secondary Break-up

For *secondary break-up* to occur, i.e. subsequent to the initial formation of droplets from the liquid body, sufficient relative velocity between the droplet and the air is required. However, since the relative velocity between the liquid and air reduces within the liquid-body flow, in most practical applications there is a low incidence of secondary droplet break-up. Therefore, the disintegration of the *liquid body* plays an important role in the resulting mean droplet sizes in the downstream spray plume, the following section reviews this important step in the bulk liquid atomisation process.

2.3 Disintegration of Liquid Bodies

In the process of liquid atomisation, as liquid is ejected from a liquid reservoir through a simple nozzle, a body of liquid forms at the exit of the nozzle. For

[2]Complex nozzles or atomisers suppress any liquid body forming, with liquid atomisation predominantly occurring at the nozzle exit plane.

a round nozzle the liquid continuum is cylindrical. Where the geometry of the nozzle is a slot, the liquid body produced is sheet-like. In both cases, as the liquid exits the confines of the nozzle, surface tension forces hold the liquid together as a continuum.

Any imbalance between the cohesive surface tension forces and the external dynamic forces leads to disruption on the liquid surface. These surface disruptions lead to the formation of oscillations and perturbations, which can be considered to be the result of interfacial instabilities (**Lefebvre (1989)**). Such imbalances fall into two categories, intrinsic ***capillary*** instabilites and extrinsic ***non-capillary*** instabilities. Disintegration of the liquid body is dominated by the fastest growing instability. The transition from capillary to non-capillary led liquid column disintegration produces four distinguishable regimes, listed in Table 2.1:

Regime	Description	Dominant Mechanism	Criteria/Boundary
1	Rayleigh break-up	Surface tension forces	$We_g > 0.4$
2	First wind induced	Surface tension force; dynamic pressure of ambient air	$We_g > 1.2 + 3.4\ Oh^{0.9}$
3	Second wind induced	Dynamic pressure of ambient air opposed by surface tension force initially	$13 < We_g < 40.3$
4	Atomisation	Unknown	

Table 2.1: Description of jet break-up regimes **Lefebvre (1989)**

In the case of a liquid jet injected into stationary air, any relative velocity is due to the velocity of the liquid jet and the jet Reynolds Number provides an appropriate scale. Figure 2.5 is a plot of the variation of Ohnesorge Number with liquid jet Reynolds Number, on which the boundaries of the distinguishable jet break-up regimes are defined.

To give Figure 2.5 a point of reference, superimposed on the original plot is a line of constant Ohnesorge Number that represents a 1 mm water-jet at 20 °C and on this three points are identified that represent mean jet velocities of 1, 10 and 100 m/s. Hence, at 1 m/s jet break-up would occur in the capillary led Rayleigh Mechanism regime, where as, at 100 m/s atomisation would be observed.

As is the case for the disintegration of isolated droplets, the droplet sizes in the downstream spray are greatest when the disintegration of the liquid jet occurs in the Rayleigh Mechanism and droplet sizes are smallest when disintegration oc-

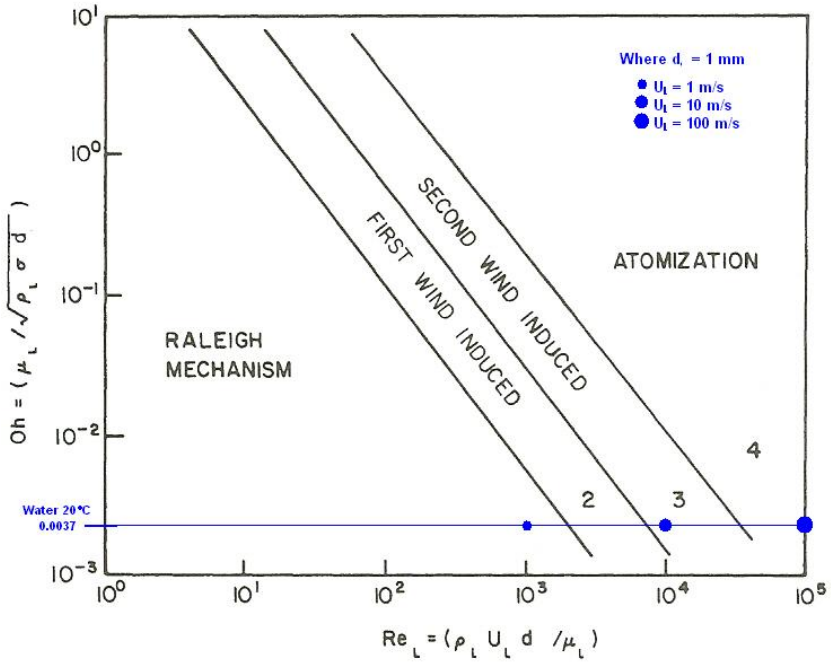

Figure 2.5: Droplet break-up regimes **Lefebvre (1989)**

curs in the Atomisation regime. Since the regime in which the liquid continuum disintegrates depends on the relative velocity between it and the surrounding gas, in the case of an oil leak in a gas turbine engine, it would be expected that in the majority of incidents the cross-airstream would dominate the disintegration process and therefore take place in the Atomisation regime.

The following subsections present an account of the sources of ***capillary*** and ***non-capillary*** instabilities that lead to Rayleigh Mechanism and Atomisation break-up regimes respectively.

2.3.1 Capillary Based Instabilities

Plateau-Rayleigh Instability

Perhaps the simplest arrangement is a falling column of water - column collapse is inevitable because surface tension will tend to reduce a liquid's surface area to a minimum (i.e. a sphere, as was illustrated in Figure 1.3). Plateau showed experimentally that a falling column of water broke up into droplets when its length extended to between 3.13 and 3.18 of the initial column diameter. Later, Rayleigh showed theoretically that for an inviscid column the break-up length was π times the initial column diameter, **Rayleigh (1878)**.

Rayleigh-Taylor Instability

Rayleigh-Taylor (RT) instability is observed when two fluids of different densities collide, typically liquid and gas. The dynamic pressure of the gas can be considered a spoiling force and surface tension of the liquid, a restoring force. Unlike a spring-mass system however, there is little chance of the restoring force returning the situation to a previous state. The spoiling force produces a convoluted three-dimensional deformation of the liquid surface. This then changes the relationship of the drag experienced between the liquid droplet and the gas flow, and therefore the original spoiling force is not restored. As a result, this is an unstable system.

Rayleigh-Taylor instability causes oscillations to form on a jet or sheet, such as those in Figure 2.6.

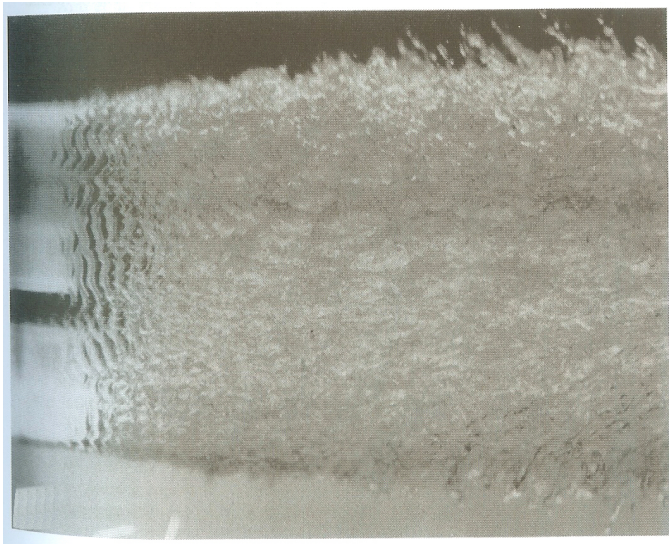

Figure 2.6: Liquid jet in stationary air,**Taylor and Hoyt (1983)**

An examination of Figure 2.6 shows the growth of capillary led waves on the surface of a liquid jet, injected into **stationary air**; note that the waves are very faint at the nozzle exit and become increasingly distinguishable. Capillary waves also grow from the nozzle exit when the liquid jet is in a **cross-airstream** - in such cases, as the jet turns in the direction of the cross-airstream, the wavelength is protracted on the upstream (windward) face and contracted on the downstream (leeward) face, as illustrated in Figure 2.7.

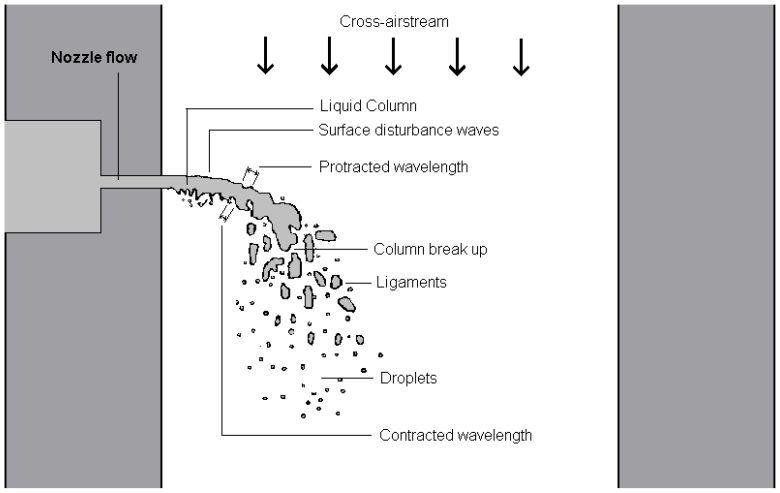

Figure 2.7: Liquid jet in cross-airstream

The waves grow in amplitude until, eventually, the wave-trough is sufficiently large as to break the continuum of the liquid column, forming a ligament from the corresponding (preceding) wave-crest - this process is called *column break-up*. Increasing the velocity of the cross-airstream, increases the spoiling force with the effect of shortening the wavelength and therefore reducing the size of the ligaments produced.

2.3.2 Non-Capillary Based Instabilities

Kelvin-Helmholtz Instability

Kelvin-Helmholtz instability (KH) can occur at the surface interface between two fluids of different density when there is a differential velocity between them. An example, from nature, is presented in Figure 2.8 on the upper surface of a dense cloud with a relative velocity between it and the lighter air above - the visible cloud highlights the characteristic rolls associated with this phenomena.

Figure 2.8: Example of Kelvin-Helmholtz instability from nature, with kind permission from Giselle Goloy

Turbulence within a flow-field is generally thought of with respect to a solid surface, where the strength of the turbulence decreases with distance from that surface within a boundary layer. Where the surface is another fluid (but with greater density to that of the turbulent stream), the heavier fluid surface exhibits a dynamic response. The characteristic KH rolls form as a result of the surface of the heavy-fluid responding dynamically to tangential forces created from turbulence in the less heavy fluid.

Figure 2.9 shows the results of a numerical model of a KH instability for a density ratio of 10:1 at three levels of differential velocity; as reported by **Price (2008)**.

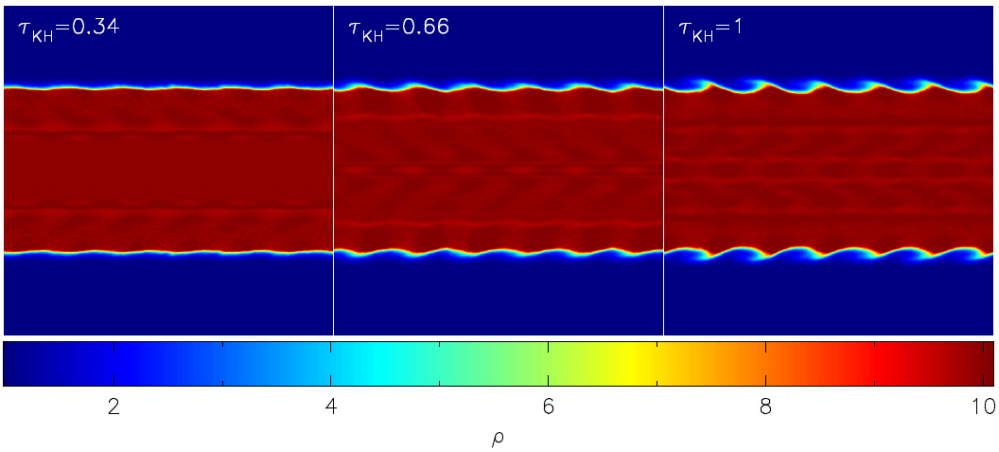

Figure 2.9: Propagation of Kelvin-Helmholtz waves in a heavy fluid (red) as a light fluid (blue) flows over it from right to left (presented at three differential velocities), **Price (2008)**

From left to right, Figure 2.9 shows how increasing the relative velocity between the fluids increases the size and definition of the perturbations.

For liquid jets in a high speed cross-airstream, the relatively spiky KH driven perturbations (compared to the smoother RT led waves), provide a favourable surface for the shear force at the interface to strip liquid from the surface. Because increasing differential velocity between the fluids results in greater size and definition of the perturbations this leads to an increase in liquid being stripped from the surface, i.e. surface break-up. As surface break-up produces small droplets, this contributes to a reduction in average droplet size in the downstream spray.

The previous sections in this chapter have defined the processes involved with the disintegration of an isolated droplet which led on to describing the atomisation of bulk liquid. Subsequently, the difference between capillary and non-capillary led disintegration was described and this was followed by descriptions of the destabilising mechanisms that occur in each. The following section describes a non-dimensional analysis carried out to identify the key dependent variables that influence the size of the droplets in a spray field.

2.4 Non-Dimensional Analysis

In order to describe the non-dimensional analysis it is first necessary to introduce the concept of mean droplet diameter. A spray contains a statistical distribution of droplet diameters and depending on a particular interest different methods

for describing the mean diameter of a droplet population are available. In this thesis two such definitions are used and these are described below:

Arithmetic Mean Diameter (AMD) or D_{10}
The Arithmetic Mean Diameter is a simple unweighted mean of the droplet population and is defined by the expression:

$$AMD = \frac{1}{N} \sum_{i=1}^{N_i} n_i D_i \tag{2.3}$$

where: D_i is the diameter of the size class i, N_i the number of size classes (bins), n_i the number of droplets in each size class and N the total number of droplets, see Figure 2.10

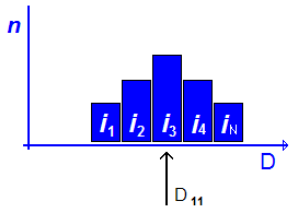

Figure 2.10: Example AMD compilation

Sauter Mean Diameter (SMD) or D_{32}
The Sauter Mean Diameter is a ratio of the total volume to the total surface area (hence the subscript notation of D_{32}). SMD is used when the total surface area of the spray, compared to the total volume is of interest - e.g. this is useful when evaporation rate is of interest and, as a result, is often used to compare combustion sprays.

$$SMD = \sum_{i=1}^{N_i} n_i D_i^3 / \sum_{i=1}^{N_i} n_i D_i^2 \tag{2.4}$$

Physical Variables
A non-dimensional analysis using the Buckingham-Pi theory was completed by **Hutcheson (2008)** to identify the key dependent variables that influence the SMD of a spray field. The spray global SMD was chosen to be the dependent variable and was proposed to depend on the following 18 physical variables:

ρ_g	Gas Density	kg/m^3
ρ_l	Liquid Density	kg/m^3
μ_g	Dynamic Gas viscosity	Pa.s
μ_l	Dynamic Liquid viscosity	Pa.s
σ	Liquid surface tension	kg/s^2
w	Nozzle width	m
b	Nozzle height	m
l	Nozzle passage length	m
d_{hg}	Wind tunnel geometry (hydraulic diameter)	m
W	cross-airstream velocity	m/s
U_l	Liquid injection velocity	m/s
a_g	Local speed of sound	m/s
$P_l - p_v$	Differential of liquid total pressure and its vapour pressure	kg/m.s^2
θ	Liquid injection velocity, relative to cross-airstream velocity	m/s
g	Gravitational acceleration	m/s^2
η_g	Kolmogorov turbulent length scale	m
I_g	Turbulence intensity in the wind tunnel	m/s
λ_g	Molecular mean free path of the gas	m

Table 2.2: physical variables

The non-dimensional parameters are listed below.

Weber Number (We$_g$)

The Weber number is widely used in two-phase flow analysis. It is the ratio of inertial (external) forces and surface tension (internal) forces. Deformation can be said to occur for We >1 where inertial forces overcome the liquid surface tension.

$$\mathrm{We}_g = \frac{\rho_g \, (W_g - W_l)^2 \, L}{\sigma} \tag{2.5}$$

Where: $(W_g - W_l)$ is the relative velocity between the two phases.
Note: throughout this study $W_l = 0$ because the liquid is injected perpendicular to the airstream.

Momentum Flux Ratio (q)

Momentum flux ratio is a measure of the balance of the discrete liquid phase momentum to that of the continuous gas phase. Hence in a cross-airstream arrangement, a high value of q implies a spray that will penetrate far into the cross-airstream.

$$q = \frac{\rho_l \, U_l^2}{\rho_g \, W_g^2} \tag{2.6}$$

Ohnesorge Number (Oh)
The Ohnesorge number is the ratio of viscous forces to the square root of inertial and surface tension forces, it is influential when liquid viscosity is sufficiently high to delay the break-up process.

$$\mathrm{Oh} = \frac{\mu_l}{\sqrt{\rho_l \, \sigma \, L}} \tag{2.7}$$

Gas Mach Number ($\mathbf{M}_g$)
The gas Mach number expresses the cross airstream as ratio of the speed of sound. In general, the conditions of subsonic and supersonic airstreams are considered as fundamentally different situations. At gas Mach numbers > 1, shock waves forming at the intersecting fluids introduce pressure boundaries that affect the break-up process.

$$\mathrm{M}_g = \frac{W_g}{a_g} \tag{2.8}$$

Liquid Injection Froude Number ($\mathbf{Fr}_L$)
The liquid injection Froude number is used where the effects of gravity are influential on the break-up process.

$$\mathrm{Fr}_L = \frac{U_l}{\sqrt{g \, L}} \tag{2.9}$$

Note: throughout this study the effects of gravity are assumed to be insignificant on the break-up process.

Nozzle Cavitation Parameter (K)
The nozzle cavitation parameter is used when the intensity of the nozzle cavitation needs to be accounted for in the break-up process.

$$K = \frac{(p_1 \, - \, p_v)}{(p_1 \, - \, p_2)} \tag{2.10}$$

Where: 1 = Upstream, 2 = Downstream and v = Vaporisation

Gas Knudsen Number ($\mathbf{Kn}_g$) The gas knudsen number is used in rarefied gas-streams where very low gas pressures affect the break-up process.

$$\mathrm{Kn}_g = \frac{\lambda_g}{L} \tag{2.11}$$

Where: λ_g is the molecular mean free path of the gas.

2.5 Review of Open Literature

The following is a review of the appropriate body of open literature. Firstly, a selection of previous studies is presented to provide an overview - followed by a detailed examination of the individual affects on the flow from changes in: nozzle flow regime; liquid viscosity; nozzle size; nozzle shape; rotation in the cross-airstream; angled injection; and, downstream static airstream pressure.

2.5.1 Sprays in Cross-Airstreams

Early attempts to characterise the sprays produced when liquid is injected into a high-speed airstream were conducted by **Chelko (1950)** and **Ingebo (1967)**. Ingebo, reported spray penetration and volume flux obtained with a probe arrangement. He produced correlations based on the nozzle diameter, liquid Reynolds number and gas Weber number. Spray penetration is currently considered to scale with the momentum flux ratio (q) (Equation 2.4). Among the first to produce such predictions in subsonic airstreams was **Hojnacki (1972)**, who correlated experimental data to give the result of transverse spray penetration as:

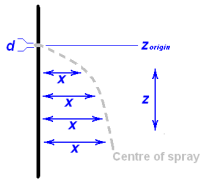

$$\frac{x}{d} = 2.1\,(\bar{q})^{0.5}\left(\frac{z}{d}\right)^{0.27} \tag{2.12}$$

Currently, the most appropriate exponent for (q) is not clear, as there is discrepancy between laboratories, for example:

Wotel et al. (1991), provided the result of transverse spray penetration as:

$$\frac{x}{d} = 1.19\,(\bar{q})^{0.45}\left(\frac{z}{d}\right)^{0.45} \tag{2.13}$$

Inamura et al. (1993), produced equations for jet penetration and jet widths as:

$$\frac{x}{d} = (1.18 + 0.24d)\,(\bar{q})^{0.36}\,ln\left[1 + (1.56 + 0.48d)\,\frac{z}{d}\right] \tag{2.14}$$

$$\frac{y}{d} = 1.4\,(\bar{q})^{0.18}\left(\frac{z}{d}\right)^{0.49} \tag{2.15}$$

The amount of *sideways* spread the spray exhibits is much less affected by q than the transverse penetration as can be seen from an inspection of Equations 2.14 and 2.15.

Chen et al. (1993) were the first to scrutinise the multi-zone nature of the liquid jet. Their main contribution was the observation that owing to the **three** stages of jet disintegration, accurate definition of the transverse penetration was only possible by means of a **three-stage** equation (see Equation 2.16).

$$\frac{x}{d} = 9.91\,(\bar{q})^{0.44}\left[1 - exp\left(\frac{-x/d}{13.1}\right)\right]\left[1 + 1.67exp\left(\frac{-x/d}{4.77}\right)\right]\left[1 + 1.06exp\left(\frac{-x/d}{0.86}\right)\right] \tag{2.16}$$

Equation 2.16 incorporates three exponential terms representing the three distinct stages of disintegration: liquid jet; ligament; and, droplet region, as was previously illustrated in Figure 2.7.

Inamura et al. (1997) reported an investigation into relatively simple cases but employing a relatively wide scope of spray characterisation techniques: instantaneous photography, high speed video (at 40 kfps), PDPA droplet characterisation and a manual mass flux measurement approach. Their experiments were conducted in a 60 *by* 60 mm wind tunnel and tests up to $q \leq 12$. To investigate the influence of nozzle size and liquid flow rate two nozzles were used, 1 mm and 2 mm in diameter.

The population as well as the average diameter of droplets varies with location within a spray field and hence there is a spray density distribution over a cross-section of a spray field. This feature is measured as the volume of liquid that passes through a cross-sectional area each second (typically $cm^3/cm^2/s$) and is known as mass flux. In Inamura's experiments the influence of q on peak mass flux was small showing that increasing q greatly promoted spray dispersion - i.e. higher liquid flow rate and greater dispersion more-or-less cancel out, so peak mass flux was relatively constant.

Mean droplet sizes based on SMD from the 1 mm nozzle were much smaller than those from the 2 mm nozzle as would be expected since drop size is proportional to nozzle diameter - as was illustrated in Figure 1.3. Also, the mean droplet axial velocities (i.e. in the direction of the cross-airstream) for the 2 mm nozzle are lower than those for the 1mm jet - this was considered to be because of the

increased liquid flow rate from the 2 mm nozzle causing a greater blockage to the cross-airstream producing a more significant wake region.

The droplet axial velocity increases rapidly downstream, thus the droplet velocity distribution develops a uniform profile with axial distance as the wake region diminishes.

[The wake region, which forms in the region 'under' the liquid jet, influences the distribution of droplets within the spray field and is an important feature. For a liquid sheet emanating from a slot nozzle, the blockage created by the sheet to the cross-airstream not only depends on its liquid flow-rate but also its orientation to the cross-airstream. As will be seen in the Results chapter this study performed tests using a slot nozzle in two orientations providing different wake regions using the same nozzle and conditional parameters - hence the effects of the wake region can be viewed in isolation of nozzle size, q and We_g.]

At low air velocity (high q), regular disturbance waves appear on the liquid surface. The disturbance surface waves on the windward edge look two dimensional from a side-on-viewpoint and their wavelength decreases with increases in airstream velocity. In the spray plume droplet diameter peaked in the far periphery.

At high air velocity (low q), the jet bends rapidly and the surface disturbance waves are greatly amplified. At even higher air velocity, regular motion of the surface wave is no longer distinguishable, instead numerous hollows were observed on the surface. Droplet diameter no longer peaked in the far periphery but in the spray core. This is attributed to the sharp radius of curvature the liquid jet experiences when the cross-airstream dynamic pressure is high. This behaviour was further explained in **Wu et al. (1998)**.

Wu et al. (1998), reported on liquid spray structures from a round nozzle in subsonic cross-airstream. In this study they focused on the details of the spray plume using PDPA as the main characterisation method. Their aim was to relate spray structures to break-up processes and develop correlations for the prediction of spray structures.

They used a round nozzle of 0.5 mm diameter and L/d = 4 with a tapered inlet edge. Water was used as the injectant giving the following test conditions:

$$\rho_l = 998 \text{ kg/m}^3$$
$$\mu_l = 0.000956 \text{ kg/m/s}$$

$$\sigma_l = 0.0705 \text{ N/m}$$
$$12.8 < U_l < 42.5 \text{ m/s}$$
$$1152 < \text{We}_l < 12800$$
$$6660 < \text{Re}_l < 22200$$
$$5.3 < q < 59.1$$
$$\text{Oh} = 0.0051$$

The test section duct dimensions were 125 spread *by* 75 transverse *by* 406 long (mm). Tests were conducted with the static pressure in the test section duct set to 0.2 bar (gauge). Turbulence intensity was less than 3% at centre of the tunnel and the boundary layer thickness was less than 4 mm. The continuous phase cross-airstream had the following properties and test conditions:

$$\rho_a = 1.633 \text{ kg/m}^3$$
$$T_a = \textit{ambient}$$
$$\text{M} = 0.2,\ 0.3 \ \& \ 0.4$$
$$(W_{mean} = 69,\ 103 \ \& \ 137\ m/s)$$
$$54 < \text{We}_g < 217$$
$$3120 < \text{Re}_g < 12800$$

Their PDPA system was setup in the 150° scattering angle, i.e. utilising first order refraction. The traverse-step-size was set to 2.54 mm at each plane. PDPA measurements were taken at three axial planes at 100, 150 and 250 mm downstream of the nozzle injector. Droplet properties were averaged over more than 1500 individual droplet measurements. Included in their main conclusions were the following observations.

At high q, the momentum exchange is progressive and a weak wake region is observed downstream. In-line with **Inamura et al. (1997)**, the largest droplets within the plume tended to the far periphery of the plume.

At low q, there is always an intense momentum exchange that sets up a significant wake region downstream, the largest droplets tend to accumulate in the central region of the spray plume. In addition it was observed that the liquid jet, as it formed at the nozzle exit, impinged on the exit orifice and caused an increase in *SMD*.

For each condition, flux averaged droplet size was shown to be consistent at the three downstream planes tested. It was concluded that the break-up process must be completed by 100 mm downstream - this also confirmed the absence of coalescence.

Droplet SMD decreased with increased cross-airstream velocity or increased liquid injectant velocity.

Liquid mass flux was shown to fall away sharply outside a small area in which it peaked, with 30% of the total liquid mass contained within 7% of the total area of the plume and 70% of the liquid mass within 25% of the total area. In combustion systems this means there is a small volume of intense heat and therefore being able to accurately predict the location of peak mass flux is important. A correlation was produced that related the position of peak mass flux with distance from the nozzle wall as a function of q and downstream (axial) distance.

Within the interest of this study the dispersion is important as an accumulation of droplets in a small volume could increase the possibility for an unwanted fire because a flammable oil to air ratio could be achieved.

The work described above was an extension of a previous investigation by the same laboratory in which they had focused on the details of the liquid jet behaviour and reported in **Wu et al. (1997)**. The experimental setup was similar to that described above, although in these experiments the influence of dynamic viscosity had also been addressed by testing with various liquids as described below:

Water: μ = 0.00865 Pa.s
Ethyl Alcohol: μ = 0.00957 Pa.s
30% Water/Alcohol: μ = 0.0184 Pa.s
40% Glycerol/Water: μ = 0.0366 Pa.s

Because these tests were aimed at the details of the liquid jet a shadow-graphic technique had been utilised, based on an open camera and a pulsed laser with 10 ns duration. The key conclusions from this study are as follows:

- When q was high, the liquid jet penetrated relatively far into the cross-airstream, in the x direction, and exhibited surface break-up before column disintegration.
- The jet trajectory and break-up length was shown to have only a weak dependence on the liquid's dynamic viscosity.
- The distance to the break-up point in the direction of the airstream (z) of the liquid jet was shown to approximate to a constant value that was unaffected by q.

- They reported the transition from column to surface break-up mechanisms when:

$$\frac{\bar{q}}{0.81\ We_g} > 1 \tag{2.17}$$

Because of the general importance of droplet sizes in sprays and the influence on this that the liquid jet break-up mechanism has, they produced a chart to highlight the division between the conditions which lead to surface or column break-up dominated jet disintegration - as presented in Figure 2.11.

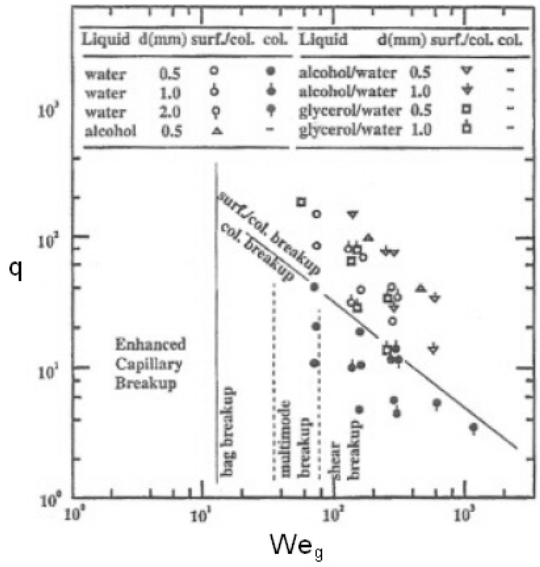

Figure 2.11: Liquid jet disintegration regime map, **Wu et al. (1997)**

The combination of the work by Wu et al. provides a relatively comprehensive account for sprays in cross-airstreams. As part of their studies they generated a number of correlations to predict the behaviour of the jet and the characteristics of the spray field - a selection of which are presented below.

Cross sectional area:

$$\frac{A}{A_{noz}} = 121\,(\bar{q})^{0.34}\left(\frac{z}{d}\right)^{0.52} \tag{2.18}$$

Spray penetration limit:

$$\frac{x_{limit}}{d} = 4.3\,(\bar{q})^{0.33}\left(\frac{z}{d}\right)^{0.33} \tag{2.19}$$

Maximum-flux-penetration:

$$\frac{x_{mfp}}{d} = 0.51\,(\bar{q})^{0.63}\left(\frac{z}{d}\right)^{0.41} \tag{2.20}$$

Spray spread width limit:

$$\frac{y_{limit}}{d} = 7.86\,(\bar{q})^{0.17}\left(\frac{z}{d}\right)^{0.33} \tag{2.21}$$

Liquid jet trajectory:

$$\frac{x}{d} = 1.37\,(\bar{q})\,\sqrt{\left(\frac{z}{d}\right)} \tag{2.22}$$

Transverse distance to column fracture point:

$$\frac{x_b}{d} = 3.07\,(\bar{q})^{0.53} \tag{2.23}$$

Axial distance to column fracture point:

$$\frac{z_b}{d} = 8.06 \tag{2.24}$$

2.5.2 Effect of Nozzle Flow Regime

It is well understood that nozzle flow (as illustrated in Figure 2.12) may cavitate, as a result of static pressure reduction and flow separation at the nozzle entry as the flow velocity increases.

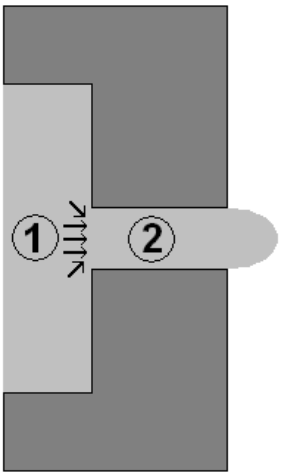

Figure 2.12: Nozzle flow arrangement

For a liquid ρ = constant

$$P_1 + \frac{1}{2}\rho U_1^2 = P_2 + \frac{1}{2}\rho U_2^2 \tag{2.25}$$

Since $U_2 >> U_1$; $P_2 < P_1$
If, $P_2 < P_{sat}$ at T_2, then local boiling occurs and so will cavitation.

The affect of cavitation on the liquid jet for spray in subsonic cross-airstream was the subject of a study by **Ahn et al. (2006)**. Their study used transparent nozzles together with flow visualisation techniques to determine the flow within the nozzle along with the corresponding liquid jet characteristics.

Their work defined the possibility of three nozzle flow regimes as illustrated in Figure 2.13:

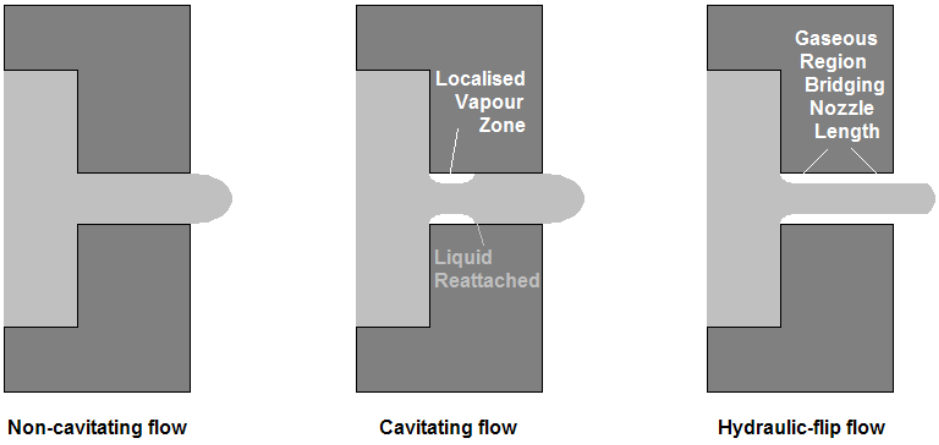

Figure 2.13: Nozzle flow regimes

A *Non-cavitating flow* was defined when there was no detectable flow separation in the nozzle passage.

Cavitating flow was defined by the existence of flow separation, developing at the nozzle inlet. Cavitation produced a localised vapour zone in the upstream section within the nozzle passage. At some point within the nozzle passage, the liquid flow recovers and reattaches to the nozzle wall.

Hydraulic-flip can be considered as an advanced level of a cavitating flow, where the liquid flow fails to reattach to the nozzle wall prior to the nozzle exit junction. In this condition downstream air backfills the nozzle wall surface, to form a tube shaped gaseous region stretching back the nozzle inlet.

The consequence of these distinct nozzle flow regimes on jet trajectory and break-up length are as follows.

Effect of Nozzle Flow Regime on Liquid Jet Trajectory
It was shown that with increasing cavitation (i.e. increasing upstream nozzle pressure), the nozzle discharge coefficient decreased gradually. At the onset of hydraulic-flip the discharge coefficient dropped suddenly and attains a near constant value.

The trajectories observed for both non-cavitating and cavitating nozzle flow agreed well with Equation 1.18 from **Wu et al. (1997)**. However, for a hydraulically-flipped nozzle it was shown that the equation was invalid due to the reduced effective diameter. Definitions to account for a smaller effective diameter, to incorporate as an alternative means with which to normalise the transverse dimension were produced, see Equation 2.26 and Equation 2.27.

$$A^* = A\frac{C_{d\,flip}}{C_{d\,nc}} \tag{2.26}$$

$$V^* = V_{flip}\frac{A_{nozzle}}{A^*} \tag{2.27}$$

Where $*$ = effective hydraulic flip

The definitions were shown to be a more appropriate scale for a nozzle flow in the hydraulic-flip regime.

Effect of Nozzle Flow Regime on Liquid Jet Break-up Lengths
As well as the formulation of correlations for jet trajectory the jet length was investigated. Jet length is determined by the break-up point of the jet and is defined with respect to the axial distance z_b as set out in Figure 2.14.

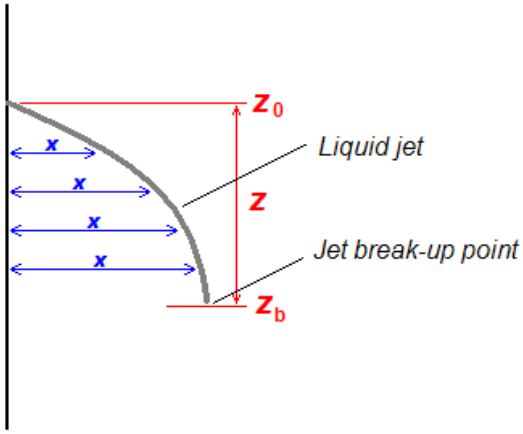

Figure 2.14: Break-up location

For non-cavitating nozzle flows $z_b/d = 8.02$, in good agreement with Equation 2.25 from **Wu et al. (1997)**. However, as cavitation and turbulence intensity in the nozzle flow increased, so the break-up length became shorter. For hydraulic-flip it was reported that $z_b/d < 8.02$. This was considered to be due to the liquid jet acceleration waves propagating upstream. Because the liquid is detached from the nozzle wall and therefore the break-up process starts at the nozzle entry rather than the nozzle exit, correlations also depend on nozzle length.

2.5.3 Effect of Liquid Viscosity

Birouk et al. (2003), extended the work of **Wu et al. (1997)**, by investigating the jet behaviour for a wider range of liquid viscosities in low speed cross-airstreams. Although the low speed cross-airstreams (W $\leq$ 22 m/s) of Birouk's work is somewhat lower than those in the present study, it provides interest due to being one of a very limited number of studies to use gas turbine engine lubrication oil as the liquid injectant.

Their study was aimed at controlling the liquid jet break-up process in order to maintain a liquid jet as a continuum until it impinges on a bearing assembly. Shaft-windage creates a cross-airstream environment in the bearing chamber. Consequentially the liquid oil jet could break-up before reaching the target of the bearing assembly, leading to insufficient lubrication of the bearings.

Their study set out to identify the effects of viscosity on liquid jet behaviour by varying independently the cross-airstream velocity, liquid jet velocity and most crucially the viscosity of the injected liquid (by varying its temperature). The round nozzle used incorporated a 1 mm diameter orifice leading to a maximum liquid jet velocity of 5.8 m/s. A stroboscope was used to visually freeze the flow field and a camera utilised to capture images of the jet structure.

The study identified the two familiar modes of liquid jet disintegration: *column and surface break-up*. Their findings showed that the transition between the two break-up regimes was influenced by the liquid's dynamic viscosity. The study defined that We_g affects the cross sectional deformation of the jet, whilst We_l affects longitudinal instabilities of the jet. Hence they established regime boundaries according to a coupled criteria involving We_g and We_l:

Column break-up:

$$1 < We_g < 7$$
$$141 < We_l < 315$$

Transition:

$$3 < We_g < 9$$
$$149 < We_l < 939$$

Surface break-up:

$$4 < We_g < 14$$
$$323 < We_l < 1119$$

Previously **Wu et al. (1997)**, had concluded that over the dynamic viscosity range $0.000865 :< \mu_l :< 0.00366$ Pa.s, jet trajectory only had a weak dependence

on dynamic viscosity. **Birouk et al. (2003)**, found that transverse jet penetration (x_b) is only independent of the liquid's viscosity up to 0.019 Pa.s and stream-wise jet penetration (z_b) only up to 0.029 Pa.s. The study produced new correlations for jet transverse and stream-wise penetration which included the effect of liquid viscosity given below:

$\mu_l < 0.019$ Pa.s: $$x_b/d = 3.13\, q^{0.53} \tag{2.28}$$

$\mu_l > 0.019$ Pa.s: $$x_b/d = 8.6\, q^{0.87}\, Oh^2 \tag{2.29}$$

$\mu_l < 0.029$ Pa.s: $$z_b/d = 0.00368\, q + 14.095 \tag{2.30}$$

$\mu_l > 0.029$ Pa.s: $$z_b/d = 542.64\, q^{0.87}\, Oh^{25} \tag{2.31}$$

Working with engine oil in experiments posses considerable environmental and safety issues, due to the toxic nature and flammability of gas turbine engine oil. The dynamic viscosity of Mobil Jet Oil 254 is 0.0047 Pa.s at 100 °C rising to 0.023 Pa.s at 40 °C (where kinematic viscosity ν = 5.3 cSt and 26.4 cSt respectively). The approximate working temperature of oil in a gas turbine engine is 100 °C. Therefore working temperature engine oil has dynamic viscosity below 0.019 Pa.s, the level below which liquid disintegration is independent of dynamic viscosity.

The dynamic viscosity of room temperature water is approximately 0.001 Pa.s, which is lower than 100 °C engine oil at 0.0047 Pa.s, but since both liquids exhibit μ_l < 0.019 Pa.s, water has been considered to be representative of oil for the current study. Working with water in the present study eliminated any environmental and health issues from release to the atmosphere. Coupled with the free (almost) availability of tap water this allowed for an extensive test matrix and detailed spray characterisation of long duration.

It should be considered that an oil leak at start up, when the oil is cold, the oil viscosity might well be influential on the break-up mechanisms, however, this study is only concerned with oil propagation where the oil is at typical working temperature - 100 °C.

2.5.4 Effect of Nozzle Shape

Along with various co-authors, Joseph A. Schetz has numerous well cited publications within the broader subject of liquid injection into an airstream. Whilst the majority of his work was in supersonic airstreams, some studies were con-

ducted in subsonic airstreams. The most relevant publication to the current study (**Schetz and Padhye (1977)**) investigated spray penetration and mean droplet sizes for sprays in subsonic cross-airstreams through slot nozzles and is therefore consistent with slot shaped oil-pipe failures.

The main motivation for their study was due to an observation that the injectant from a slot nozzle in a parallel orientation (to the cross-airstream) penetrates further than it does from a perpendicular slot or round nozzle (see Figure 2.15). Possible applications were listed as: side force attitude control, thrust vector control, transpiration cooling of re-entry vehicles, injection of fuel into ramjet combustors and subsonic velocities in the bow shock

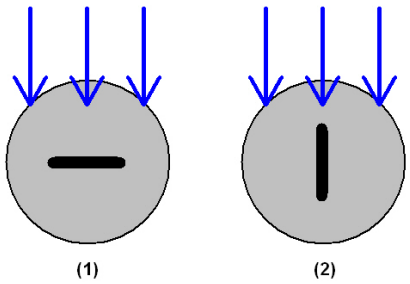

Figure 2.15: (1) Perpendicular (2) Parallel - aligned nozzles

[note: in the TFMRC test rig parallel alignment places the long dimension of the slot in a vertical orientation; and perpendicular alignment in a horizontal orientation]

The experiments were carried out in a 22.86 *by* 22.86 cm blow down wind tunnel with a uniform velocity distribution over the entire cross section. The cross-airstream mean velocity was set at 154 m/s with a static pressure of 1.055 bar g or 257 m/s with a static pressure of 0.669 bar g, both at ambient temperature. The nozzles incorporated a conical entry and circular corners to avoid cavitation and provide a uniform flow of the injectant. Water was supplied from a pressurised tank. Streak photographs with a long exposure of 2.5 ms were used to obtain time averaged pictures of the unsteady jet. Photomicrographs obtained with an exposure of 0.8 μs were used to examine wave patterns. Further photomicrographs using a short exposure of 15 nsec were obtained for droplet sizing. The distance traveled in 15 ns by a particle with a velocity of 154 m/s is 2.25 μm and 3.75 μm for 257 m/s, which is two orders of magnitude less than the reported diameter of the droplets.

Penetration distance was shown to follow $x_{parallel}$>x_{round}>$x_{perpendicular}$ and a cross stream penetration correlation was developed to take into account the shape and orientation of the nozzle:

$$\frac{x}{d_{ynoz}} = 13.5 \sqrt{\bar{q}}\, C_d \left(\frac{d_{eqv}}{d_{ynoz}}\right)^2 \left(\frac{d_{ynoz}}{d_{znoz}}\right)^{0.416} \tag{2.32}$$

Other key conclusions from their study are as follows:

- The structure of the liquid continuum was such that an increase in q, increases the axial distance to the gross fracture and a decrease in the wavelength of the surface disturbances.
- The axial distance to the gross fracture is largest for an parallel slot and least for a normal slot.
- Droplet diameters were reported to be of the order of 100 to 500 μm.
- An increase in free-stream Mach number decreased droplet size as would be expected.

To the current author's knowledge this remains the sole publication that provides useful correlations for spray penetration from non round nozzles in subsonic cross-airstreams. However, droplet sizing was limited as light scattering techniques were not employed. The current study extends their work by the utilisation of Phase Doppler Particle Analysis for droplet sizing.

2.5.5 Effect of Rotation in the Cross-airstream

Because it is known that the disintegration process of the liquid jet or sheet is primarily sensitive to the Weber Number, a rotating airflow is not expected to influence the break-up process - other than in the respect of how the rotation influences the relative velocity at air/liquid interface.

In the context of a gas turbine engine it is reasonable to expect that, if the oil emanating from a fractured supply pipe is exposed to an increased relative velocity due to some rotation or vortex formation, then the mean droplet size in the downstream spray will be less than that predicted by a simple straight cross-airstream arrangement. It should be noted that radial, axial as well as

circumferential airstreams are possible in engine cavities, if the relative velocity at the point of confluence is lower than expected, this could lead to larger droplets.

2.5.6 Effect of Angled Injection

As was stated previously, the orientation of a cracked oil pipe with respect to a cross-airstream cannot be known. Two orientations were included in the tests in the present study, the slot nozzle's major-dimension aligned and normal to the cross-airstream. A further consideration is the angle at which the liquid enters the cross-airstream. Because the liquid jet trajectory is different so is the spray penetration. **Fuller et al. (2000)** and later **Costa et al. (2006)** investigated the effect of liquid injection angle, as described by Figure 2.16.

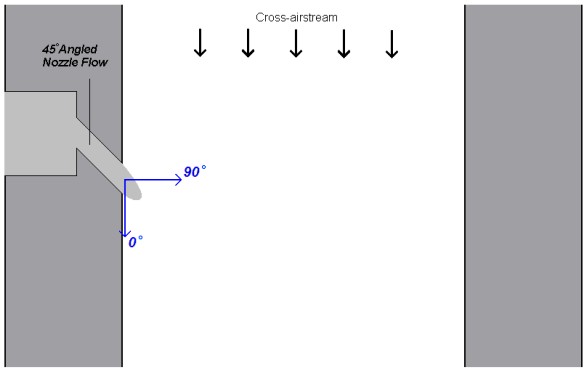

Figure 2.16: Angle of injection

Using shadowgraph photography to capture images of the jet behaviour, **Fuller et al. (2000)** defined an equation that distinguished between the dominance of non-aerodynamic and aerodynamic jet disintegration, i.e. column break-up and surface break-up. Their correlation extends Equation 2.17 from **Wu et al. (1997)** by introducing the angle of injection:

$$\tau_b = \frac{3}{2} \frac{U_l}{W_g - U_l cos\alpha} \sqrt{\frac{\rho_l}{\rho_g} We_l^{-1/3}} \tag{2.33}$$

When $\tau_b < 1$, aerodynamic forces dominate, and when $\tau_b > 1$, non-aerodynamic forces dominate. This equation shows that as the angle α reduces (i.e. the injection becomes more aligned with the cross-airstream) non-aerodynamic break-up becomes more likely.

Costa et al. (2006), tested injection through round nozzles angled at 15°, 30° and 45° from the plane of the nozzle wall. They concluded that jet penetration and atomisation quality was affected by nozzle angle. It was suggested that the jet break-up length was a maximum when the injection was aligned with the airstream (i.e. coaxial) and it was shown that the break-up length reduced moderately between the injection angles 15° and 30°, but sharply between 30° and 45°. This comparison was conducted at constant $q = 57.8$, but We_g varied because $We_g \propto \left(W_g - U_l\right)^2$ and for angled injection $U_l = U_{noz}\ cos\ \alpha$. Hence jet break-up length can not be correlated with q alone for angled injection; as it can where injection is perpendicular and $cos\ \alpha = 0$ (e.g. Equations 2.21 and 2.22).

2.5.7 Effect of Downstream Static Airstream Pressure

Since different engine cavities operate at different working pressures a further point of interest is the affect of downstream static pressure on the disintegration process. In the experimental setup of the current study the test section is maintained at 0.5 bar gauge, as this was required to seal the floating window arrangement. Since in combustion systems fuel is injected immediately downstream of the final compressor stage, i.e. at the maximum air pressure seen in the engine, liquid injection into elevated pressure air has received much attention. The reports of **Leong et al (2001)**, **Ragucci et al. (2000)**, **Becker and Hassa (2002)** and **Cavaliere et al. (2003)**, were all aimed at determining the role of downstream static pressure on the break-up process.

Becker and Hassa (2002) studied the break-up, penetration and atomisation of a plain jet at different static pressures ranging form 1.5 to 15 bar, using Mie Scattering, Shadowgraph and PDPA techniques. Jet A-1 kerosene was used as the liquid injectant hence viscosity was not influential $\mu < 0.019$ Pa.s. The work was aimed at investigating the role of downstream static pressure. Driven by the goal of reducing the specific fuel consumption of gas turbine engines, their interest was with regard to lean pre-mix pre-vaporised combustors, where liquid fuel is injected into a high pressure airstream. The test conditions were as follows:

$$d_{noz} = 0.45 \text{ mm } and\ L/d = 1.56$$
$$\text{test section dimensions} = 25 \text{ by } 40 \text{ mm}$$
$$W_g = 50 \text{ to } 100 \text{ m/s}$$
$$p_g = 1.5 \text{ to } 15 \text{ bar}$$
$$T_g = 290 \text{ K}$$
$$2 < q < 18$$

Transition from column to surface break-up was shown to be activated by increasing: q, W_g or ρ_g. Thus, confirming that the dominant break-up mechanism can be predicted from q and We_g, as set out in the regime map in Figure 2.11. This shows that the dominant break-up mechanism does depend on downstream static pressure. This result is expected of course because We_g is influenced by the static pressure i.e. $We_g \propto \rho_g \propto p_g$. Wu et al.'s prediction for transition from column to surface break-up dominated sprays (Equation 2.17) was reported to be a good fit for this data.

Other key conclusions from their study are as follows:

- Jet penetration and final break-up location were shown to be independent of the downstream static pressure and also of the dominant break-up mechanism.
- The cross section of the liquid jet was quite irregular at low jet velocity.
- At high velocity the cross section developed a well defined crescent shape.

They produced a correlation for jet penetration based on their complete data set. Further investigation uncovered the result that, the exponent of q within jet penetration correlations appears to depend on the range of q tested, as seen in Equation 2.34 and Equation 2.35

$$(1 < q < 40) \qquad \frac{x}{d} = 1.48\,(\bar{q})^{0.42}\, ln\left[1 + 3.56\,\frac{z}{d}\right] \tag{2.34}$$

$$(1 < q < 12) \qquad \frac{x}{d} = 1.57\,(\bar{q})^{0.36}\, ln\left[1 + 3.81\,\frac{z}{d}\right] \tag{2.35}$$

It was also recognised that if they correlated their data over a range of q similar to the results of previous authors, excellent agreement for the exponent was achieved. For example:

- **Chen et al. (1993)** found x/d scaled with $q^{0.44}$, where $3 < q < 45$, as seen in Equation 2.16; and,
- **Inamura et al. (1993)** found x/d scaled with $q^{0.36}$, where $q < 10$, as seen in 2.14.

This shows that the flow physics of *jet penetration* are not fully captured by the equations above and supports the need for Chen et al.'s more complex three part equation (Equation 2.16).

Albeit with some confusion for the appropriate exponent of q, **jet penetration** was shown to be independent of static pressure and was well predicted by **Wu et al. (1997)** correlation Equation 2.22.

In contrast, **spray penetration** was affected by the static pressure of the working section. **Wu et al. (1998)** correlations (Equation 2.19 and Equation 2.20) over-predicted the maximum flux penetration in Becker and Hassa's experiments.

The explanation for this was that elevated pressure led to increased surface break-up and produced a greater proportion of smaller droplets. Because smaller droplets break away from the liquid continuum with less initial transverse momentum and because the dense air at elevated pressure provides greater resistance to the initial flight-path of the droplets, the location of maximum flux is nearer to the nozzle wall. The cumulative effect is that spray penetration, is influenced greatly by airstream static pressure and therefore can not be accounted for by q alone. **Becker and Hassa (2002)** provided a simple model to predict liquid penetration which is based on the droplet relaxation time and is a function of droplet size, velocity, drag coefficient and airstream density.

In the present context of oil leaks in gas turbine engines - oil leaks in engine cavities operating at high pressures should present a lower risk for the generation of larger droplets. It should be noted that the dense air at high pressures provide a greater resistance to the dispersion of the spray and this could increase the concentration of oil in a given volume, especially in regions close to the leak source. However, since the air is dense the oil to air ratio by mass would be expected to be relatively low.

2.6 Chapter Synopsis

This chapter reported on an investigation of the open literature relevant to the current interest. The lack of open literature from tests using non-round nozzle geometries underpins the need for this study. The next chapter presents the test facility that was commissioned to carry out characterisation of sprays in cross-airstreams emanating from non-round nozzle geometries.

Chapter 3

Test Facility Design and Build

This chapter describes the component parts of the test apparatus designed and built for this study together with the important design features and choices. The chapter goes on to describe the instrumentation set up used to define the test conditions and the associated uncertainty of the measurements.

3.1 Introduction

A schematic of the main components of the test apparatus is presented in Figure 3.1 and the individual components are described in greater detail in following sub-sections.

Air flow was supplied to the test facility by an air compressor upstream of the test section. It passed through a Venturi tube mass flow measurement device, followed by an air filter and then an inlet control valve. The air was then ducted into an axisymmetric settling chamber before entering a bell mouth entry and a flow straightener. Finally the air entered the test section, which featured various injector parts. An exit control valve was used to set the pressure in the test section.

The various test nozzles were supplied from an electrically driven pump at up to 7 bar. The water passed through a filter and the delivery pressure was set by a regulator and the volumetric flow rate measured using a turbine flow meter. A photograph of the test equipment described above (during the installation phase) is shown in Figure 3.2.

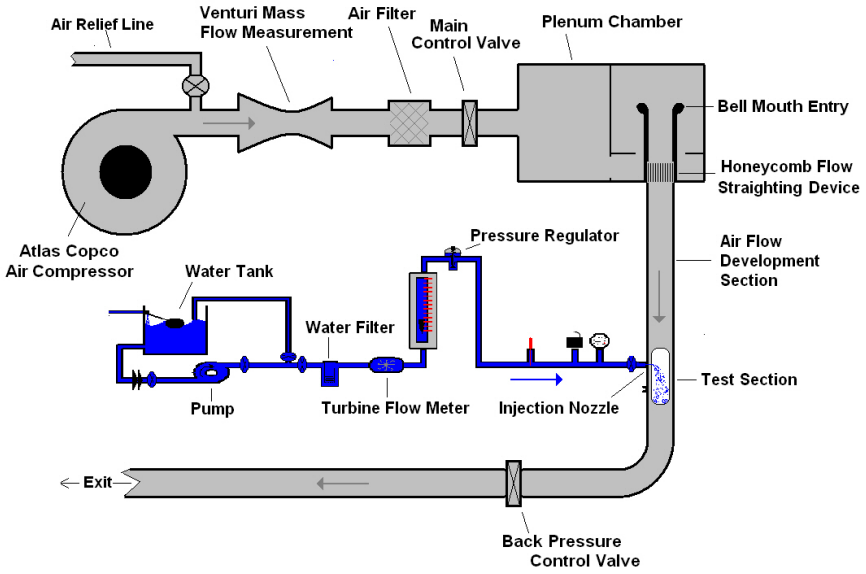

Figure 3.1: Schematic of the main components of the test facility

The main components described above are discussed in more detail in the following section.

3.2 Test Facility's Component Parts

This section discusses the individual component parts of the test facility and sets out the experimental methodology.

3.2.1 Air Compressor

The cross-flow air was supplied from an Atlas Copco ZT250 oil free screw compressor. The unit provided a mass flow rate up to 0.8 kg/s, at a maximum of 7 bar gauge pressure and at either 170°C or approximately ambient temperature after cooling.

The air supplied to the working section was controlled primarily by three manually operated control valves:

1. The compressor delivery bypass valve
2. The test rig inlet valve
3. The test rig exit valve

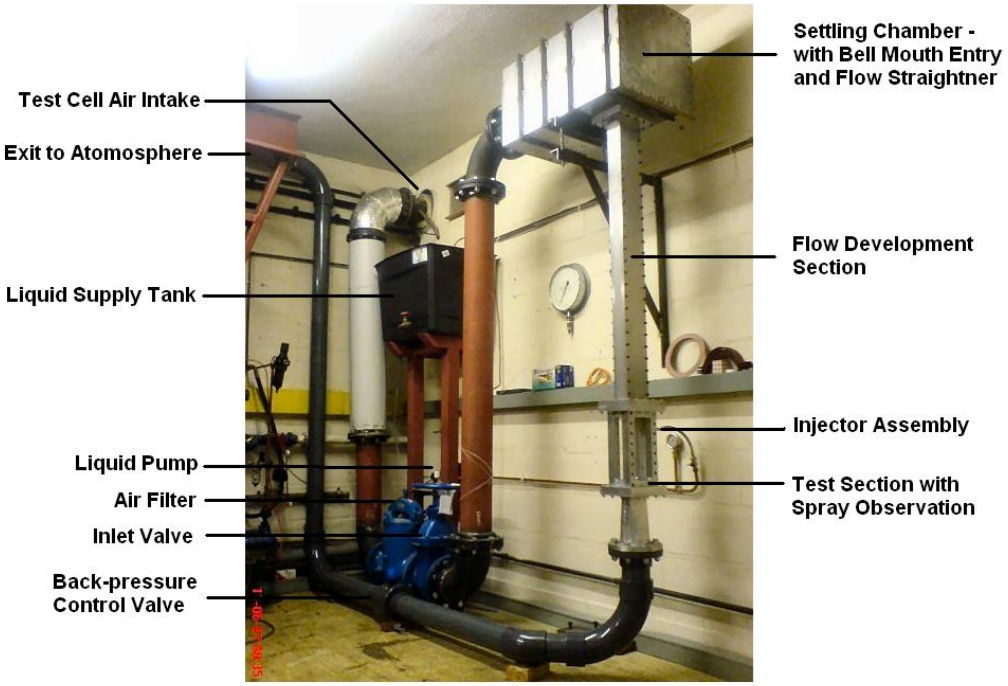

Figure 3.2: Photograph of the test facility

The compressor delivery bypass valve set the test section mass flow rate in the test apparatus by diverting more or less air flow direct to atmosphere. The test rig inlet valve was adjusted to maintain suitable back pressure (3 to 7 bar absolute) on the Atlas compressor outlet. The test rig exit valve was adjusted such that 0.5 bar gauge static pressure was maintained in the test section for all of the operating conditions, this was required to ensure the test section windows were sealed against the window frames.

In practice, the influence of each control valve is not entirely independent and they required fine tuning in combination to set the desired test condition. It proved possible to adjust the mean airstream velocity to within ± 2 m/s of the desired level.

3.2.2 Air Filtration

The nature of the PDPA system is such that incident light interfering with contaminants in the cross-airstream would disrupt the measurement process - scattering erroneous light in various directions. In view of this, the air was supplied to the working section through a 150 mm diameter in-line air filter that prevented the transport of any particles greater than 50 μm in size.

The PDPA system did not register any signal when there was no liquid spray present, indicating that the air filtration was sufficient. Furthermore, during the hot-wire cross-airstream turbulence analysis, there were no breakages of the fragile hot-wire probes indicating that the flow was free from debris.

3.2.3 Air Settling Plenum Chamber and Features

Before entry to the test section, the cross-airstream passes through a settling chamber which incorporated physical features designed to provide an even airstream into the test section, see Figure 3.3.

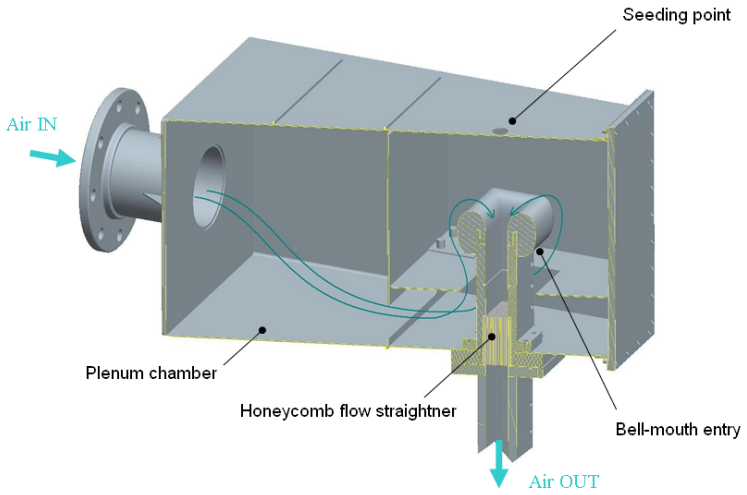

Figure 3.3: Flow conditioning within settling chamber

The internal dimensions of the settling chamber were 400 x 400 x 800 mm, with a 150 mm diameter inlet connection. After initial difficulties with the flow field in the working section, the chamber was modified to incorporate baffles that provided a more axisymmetric inlet to the development section. The plenum chamber also provided a convenient location to introduce seeding, which was required for detailed test section velocity field analysis.

3.2.4 Bell Mouth Entry and Honeycomb Straightening Device

The bell mouth entry was fixed to the outlet port of the plenum chamber, as seen in Figure 3.3. It provided a smooth acceleration into the entrance of the

flow development duct. The bell mouth entry was designed in accordance with the recommendations listed for a Long Radius Nozzle Entry within **ISO 5167-1 (2003)** and was constructed using a rapid prototyping technique. As the component is fully submerged it is not subject to any pressure differential and the comparatively weak component strength achieved by this technique was adequate, Figure 3.4a.

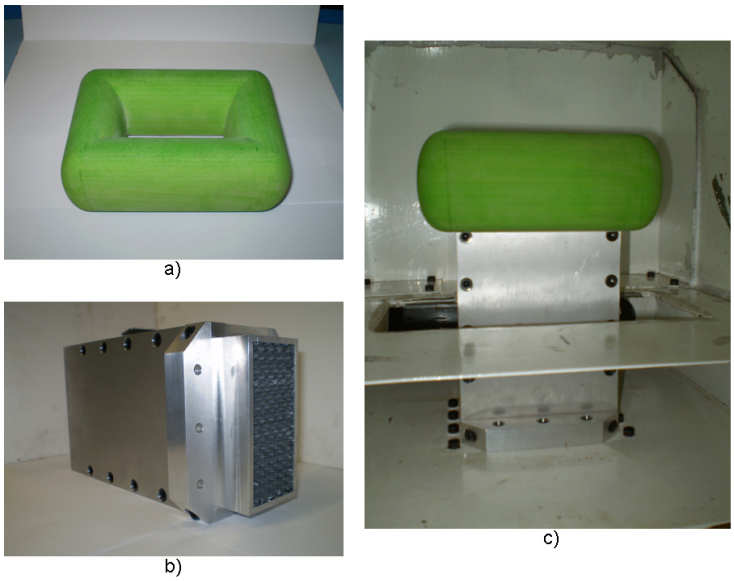

Figure 3.4: a) Bell mouth entry, b) Plenum duct and flow straightening device, c) Assembled

The bell mouth entry slotted into position on the plenum duct, Figure 3.4c and provided 150 mm of flow length prior to the honeycomb flow straightening device which had an aperture size of approximately 6 mm and a length of 90 mm, giving a length to diameter ratio of 15, Figure 3.4b.

3.2.5 Airstream Development Section

Classically, this type of study is carried out in archetypal wind tunnel arrangements, where the inlet to the working section is designed to provide a uniform velocity distribution (i.e. $W_{mean} = W_{local}$ everywhere). However, it is worth noting that in a gas turbine engine's secondary air system a variety of boundary layer behaviour would be expected on the various parts of the rotating (and stationary) disc surfaces, e.g. developing / developed layers in an annular passage between a drive shaft and the disc bores *and* thin shear layers where flow in one part of the system mixes with another flow.

In the current study a section of development duct has been included upstream

of the working section in an attempt to model more realistic boundary layers. The test cell height restricted the length of the section possible to 1200 mm and only a partially developed, rather than fully developed, flow was possible. However, the thickened boundary layer condition provides a more realistic test case for the CFD modelling.

The resultant cross-airstream velocity distribution produced and its measurement in the test section are described in detail in Section 9.

3.2.6 Spray Visualisation Section

The spray visualisation or test section is 300 mm long and incorporates B270 glass windows, of 12 mm thickness, on three sides for optical access. The glass windows slide into location through the top of the test section before it is bolted into its position. The windows sit against O-ring seals recessed into the window frame and as the pressure in the test section is raised the windows push against the seals. At 0.25 bar gauge, the windows sit firmly against the window frames and the quoted dimensions are achieved. Note that the experiments were conducted with the test section static pressure at 0.5 bar gauge.

For spray in cross-airstream experimental set-ups, there is a fundamental decision to make regarding the trade-off between maximising the cross-sectional area to allow for a wide range of momentum flux ratios that can be accommodated and, on the other hand, minimising the cross sectional-area to enable a wide range of Weber number to be tested (for a given compressor output).

As the momentum flux ratio increases, the axial penetration (throw) of the liquid injectant increases at a greater proportion to that of the lateral penetration (spread) (as defined by Equations 2.14 and 2.15). Hence, a rectangular cross-section is most suitable for limiting the spray from interfering with the test section walls whilst keeping the cross-sectional area as small as possible.

In order to provide a wider range of tests within this study, the test section was adapted by utilising an optional Acrylic insert that reduced the cross-section to enable higher cross-airstream velocities and therefore higher Weber Numbers.

The two test section configurations were:

1. A larger cross-section of 100 ± 0.05 mm transverse dimension and spanwise dimension 40 ± 0.1 mm.

2. A smaller cross-section with a reduced transverse dimension of 49.2 ± 0.05 mm and the same span-wise dimension of 40 ± 0.1 mm.

Figure 3.5 shows the test section dimensions.

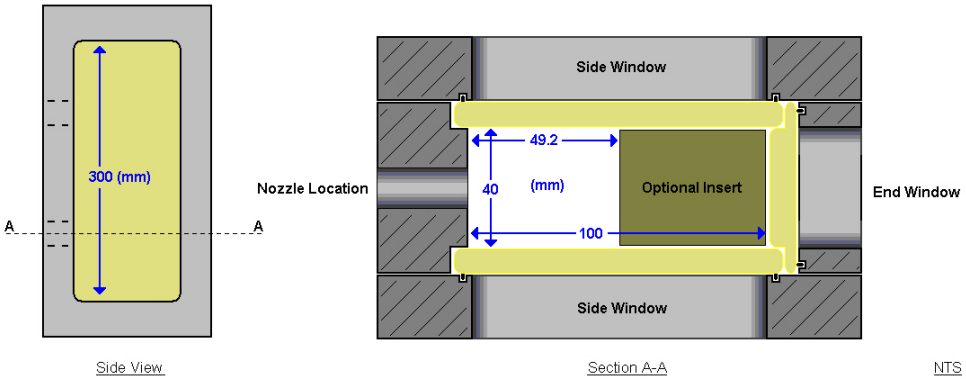

Figure 3.5: Cross sectional view of the test section

The larger cross-section configuration results in a maximum mean cross-airstream of 100 m/s. The reduced cross-sectional area increases the maximum mean cross-airstream velocity possible to 200 m/s. The reduced section utilised the same basic structure but, replaced the end window with the Acrylic insert attachment. The insert featured a profiled contraction, positioned far upstream. To confirm the local axial velocity distributions of both test section configurations, detailed Laser Doppler Anemometry and Hot-Wire Anemometry testing was conducted, the results of which are reported in Chapter 4.

3.2.7 Liquid Supply

The test liquid was supplied from a mains water supply and stored in an open tank. To ensure the pump inlet pressure was held at a constant value, the tank was replenished through an automatic float operated valve, see Figure 3.6.

The water was pumped from the open tank to the injector, en route were: a bypass line; a 20 μm water filter; a rotameter; a pressure regulator; a k-type thermocouple; a turbine flow meter; a pressure transducer and a pressure gauge.

In most sprays in cross airstream studies the liquid is supplied via a compressed gas and liquid reservoir arrangement. For this study large liquid volumes were required because the slot nozzle leads to relatively large volumetric flow rates, up to approximately 3 L/min.

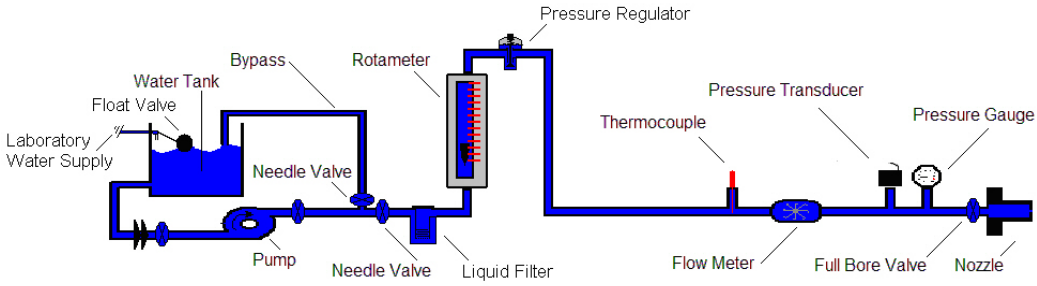

Figure 3.6: Discrete phase supply system

This approach leads to an arrangement that allows long test periods. It was possible to complete PDPA analysis at consecutive spray planes, without the need to shut down and restart. It proved possible to carry out tests in excess of 2 hours which allowed a high degree of definition to be obtained for an individual spray field.

During the design stage there had been some concern about the periodic consistency of liquid supplied from a pump, compared to that which could be achieved using an arrangement with compressed gas driving the liquid injection. However, these concerns were dismissed as the liquid jets and horizontally aligned sheets tend to be intrinsically unsteady, especially at low momentum flux ratio conditions. In contrast, for the vertically aligned slot case, frame-by-frame inspection of video obtained at 40 kfps, showed that this configuration led to remarkably steady flow fields. No unsteadiness was observed at frequencies less than 40 kHz and on this basis pump led unsteadiness was not considered to be a feature of the apparatus.

3.2.8 Pump

The liquid volumetric flow rate required depends on the nozzle geometry and pressure differential across it. Experiments were completed using two nozzle types:

1. Round nozzle with a 0.57 mm diameter (orifice area of 0.2552 mm^2).
2. Slot nozzle with an aspect of 0.5 x 5.38 mm (orifice area of 2.6364 mm^2)

The slot nozzle orifice is an order of magnitude larger than that of the round nozzle and the corresponding flow rates are therefore very different. The difference in flow rate could not be met by a single device. The solution was to install two alternative pumps in parallel. For the low flow rates (for the round nozzle)

a Totton AD4/90 multi-chamber diaphragm pump was used - providing up to 2 *l*/min at up to 8 bar.

For the high flow rates, required for the slot nozzle, a Lowara multi-stage centrifugal pump was used. This pump provided up to 15 *l*/min at pressure in excess of 8 bar.

3.2.9 Water Filter

To prevent the nozzle from becoming blocked during experiments, an in-line water filter was installed with a 20 μm polypropylene cartridge. With 20 μm filtration, the shortest length of the slot nozzle (500 μm) is 25 times larger than any particle passed.

3.2.10 Pressure Regulator

Experiments were carried out with the injector nozzle set at four liquid differential pressures: 0.5, 1.5, 3.5 and 6.5 bar, within the test section static air pressure was set to 0.5 bar. The liquid injection pressure was maintained by a Honeywell D06F pressure regulator.

3.2.11 Injection Nozzles

As previously stated, this report describes experiments completed using a round and a slot nozzle. Both nozzles were manufactured with a sharp inlet edge, the geometry of the nozzles used in the tests is illustrated in Figure 3.7.

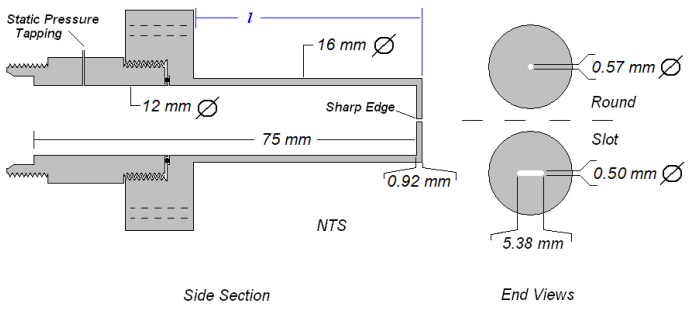

Figure 3.7: Injector nozzle nominal dimensions (all ± 0.01 mm)

The injectors were manufactured to have a nozzle length of 0.92 mm, this is because the nominal wall thickness of a typical oil pipe in Rolls-Royce engines

is also 0.92 mm. A digital microscope was used to capture detailed images of the nozzle orifices as can be seen in Figure 3.8.

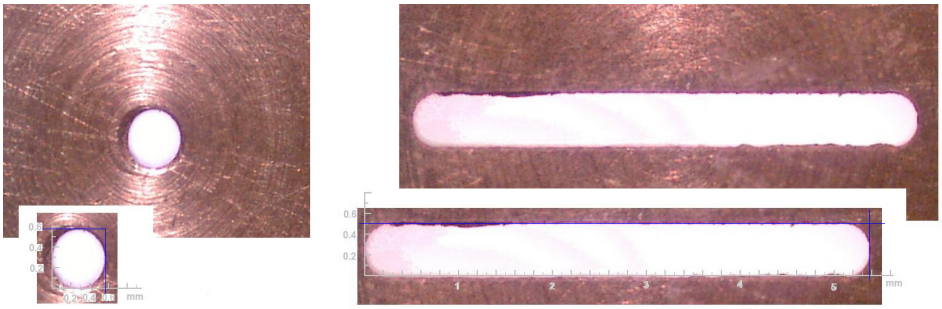

Figure 3.8: Digital microscope images of the nozzle orifices

From these images the round nozzle was classified as: d = 0.57 ± 0.01 mm. The slot nozzle was classified as: d_s = 0.50 ± 0.01 mm and d_l = 5.38 ± 0.01 mm. The slot nozzle orifice was achieved using a wire erosion technique. The use of laser drilling was explored with the potential for smaller orifices, but the surface finish was deemed to be unacceptable and irrecoverable within acceptable tolerances.

The nozzle assembly bolts to the test section wall against a recessed O-ring. The length l indicated in Figure 3.7, was carefully matched to the test section wall thickness to ensure the nozzle was flush with the test section internal wall to within a tolerance of 0.05 mm, which was less than the variations in wall surface finish.

This chapter has reported on the design and setup of an experimental test facility. Closely linked to the physical design of the test apparatus, is the instrumentation used to define test condition parameters. The following part of this chapter presents the instrumentation employed and how it was utilised to set up experiments, monitor experiments and compile permanent records of the test conditions.

3.3 Test Rig Instrumentation

The test rig was equipped with instrumentation to control, measure and record the relevant test conditions. The instrumentation measured pressure, temperature and liquid flow rate to determine bulk fluid flow. The instrumentation is distinct and operates independently from the more sophisticated optical measurements used to characterise local effects of the flow fields (which are described in the following chapter).

Figure 3.9 shows the arrangement of instrumentation that was used to monitor and log the relevant parameters during an experiment.

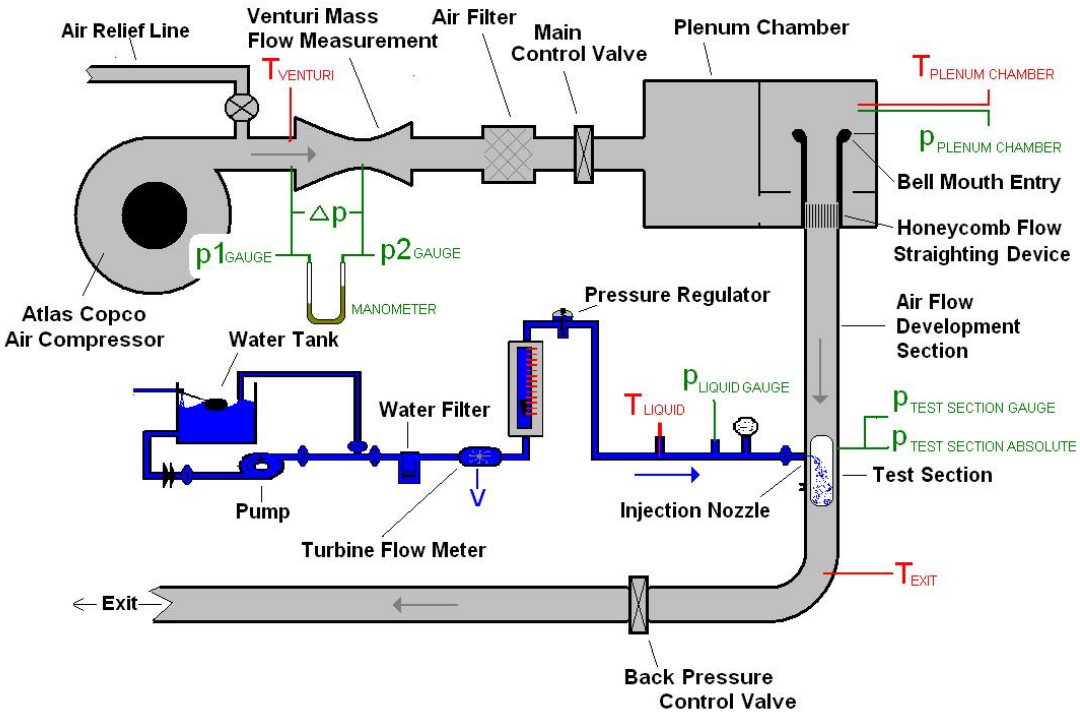

Figure 3.9: Instrumentation layout and location of parameter measurements

Figure 3.9 shows the location of five temperature measurements (red), seven pressure measurements (green) and a liquid volume flow measurement (blue). The devices are connected to various modules on a National Instruments (NI) data acquisition system.

3.4 Labview Routine

A Labview panel was written to assist the experiment process. The front panel of the Labview routine is presented in Figure 3.10.

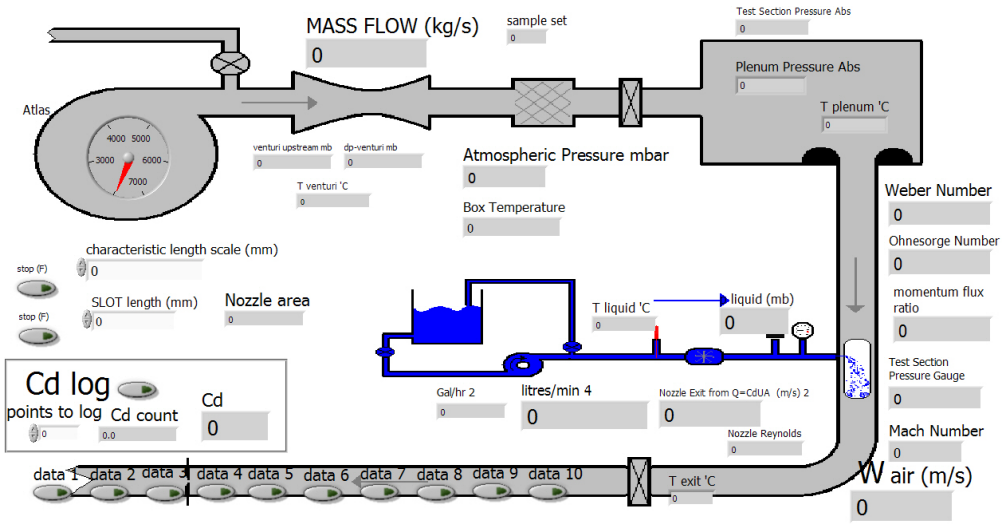

Figure 3.10: Front panel of Labview routine

The Labview routine only required information about the nozzle to be entered, all other parameters were automated. Weber number and momentum flux ratio were calculated in real time, which allowed control of the test rig using non-dimensional parameters.

3.4.1 Test Parameter Permanent Records

Labview stored the data logged over the duration of an experiment in simple text files. The experiments were typically in excess of 30 minutes duration and the test parameters were measured and logged each second, higher sampling rates were possible but unnecessary given the main task was to show that tests were constant - rather than trying to define changing test conditions. The text files created were transferred to a Microsoft Excel spreadsheet for post-processing. A template Excel 'book' design was developed in which each parameter logged was allocated a separate 'sheet'. A macro was developed that computed the mean of each parameter over the duration of the particular experiment. The results defined the conditions applicable to each experiment. For reference the mean test conditions calculated in the various sheets were superimposed

on a schematic diagram of the test rig in a separate separate sheet, similar in appearance to the front panel in Labview, as can be seen in Figure 3.11.

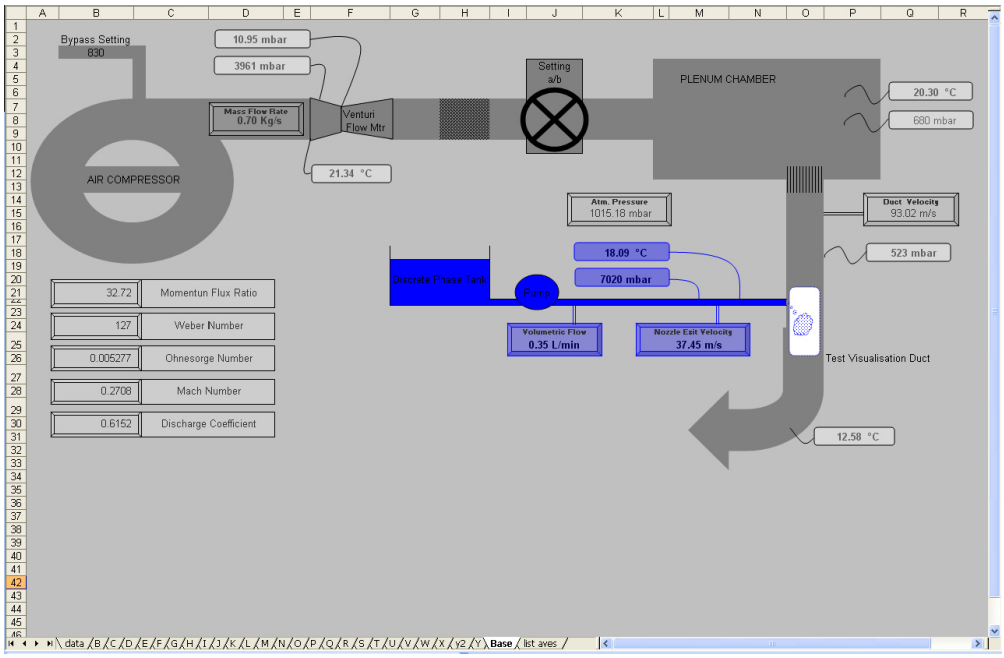

Figure 3.11: Base tab in the Excel template spreadsheet

As well as producing time averaged results for each experiment's conditions, on each individual sheet in the Excel book, each parameter was plotted against time and as a function of frequency. This visually indicated the stability of each parameter during an experiment, as can be seen in Figure 3.12 for Weber number over a 45 minute period.

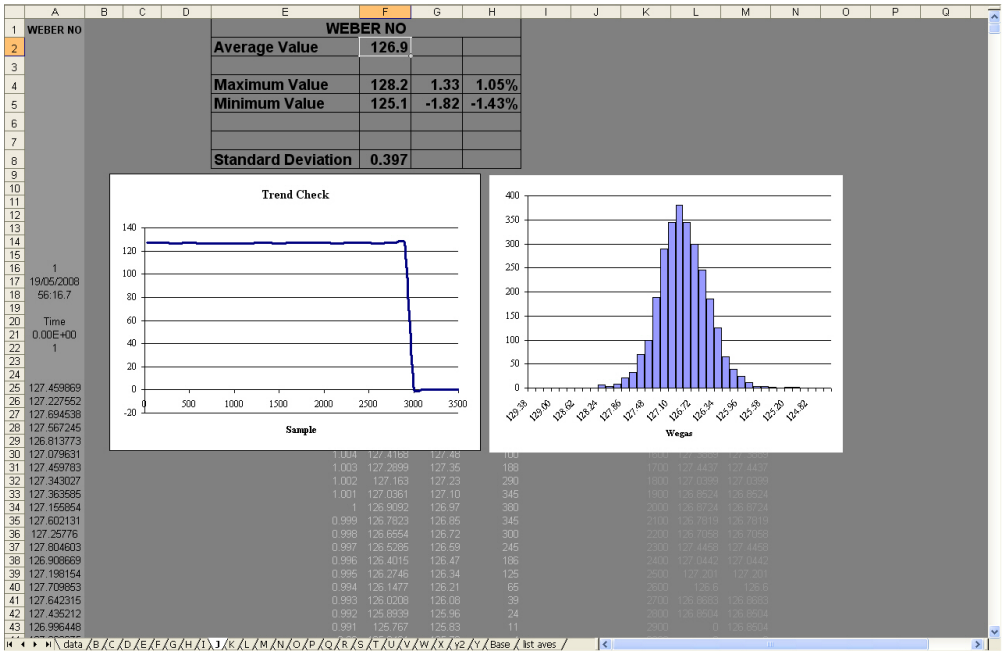

Figure 3.12: Example of an individual parameter tab in the Excel template spreadsheet

Central to the instrumentation hardware was a National Instruments cDaq 9172 console. This device was interfaced with a PC through a Universal Serial Bus (USB) connection. The console had docking slots which accept a variety of National Instrument analogue to digital converter modules. The module selected depended on the physical measurement device to be integrated and the required sampling frequency.

The NI cDac 9172 was installed in a temperature stabilised enclosure. This was to prevent any unwanted draughts across the thermocouple cold junction connections and to maintain them at a stable temperature; the enclosure is shown Figure 3.13.

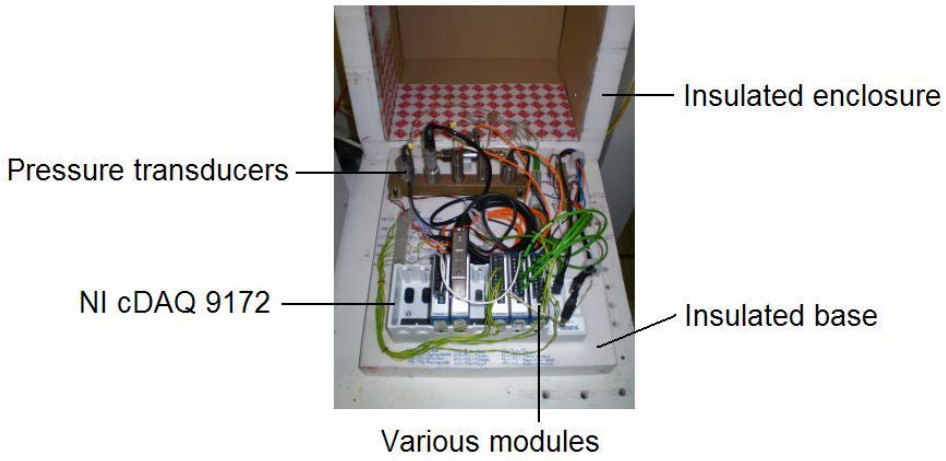

Figure 3.13: Temperature stabilised instrument box

As can be seen in Figure 3.13, the temperature stabilised box also housed the pressure transducers in order to ensure their temperature did not deviate too much from that at which they were calibrated. Auxiliary power was supplied using a regulated, linear, power supply (ISOTECH 1PS2302A).

3.5 Pressure Measurements

There were a total of seven pressure transducers installed in the test facility (locations shown in Figure 3.9). Starting furthest upstream they were: Venturi inlet; Venturi differential (with manometer cross reference); Venturi outlet; plenum chamber; test section absolute; test section gauge and liquid line (with manual gauge cross reference).

As shown in Figure 3.13, the pressure transducers were located in the temperature stabilised enclosure. The only exception to this was the liquid pressure transducer, which was located close to the injector nozzle, to keep hydraulic lines to a minimum length and separate it from the electronics.

The test section pressure was measured twice from the same tapping using both a gauge pressure transducer and an absolute pressure transducer. Since the difference between these measurements was equal to the atmospheric pressure, this approach provided an atmospheric pressure measurement (in real time rather than an input at the beginning of each test). The atmospheric pressure recorded was periodically checked against the laboratory's reference barometer.

The pressure transducers were calibrated against a dead weight tester. Calibrations were carried out with the transducers connected to the cDaq 9172 console (rather than being connected to a separate multimeter) as would be the case in the experimental set-up. The calibrations therefore include the response of the data acquisition system.

The calibration curves were established from twelve separate tests (six with positive stepped graduations and six with negative stepped graduations) and each test included eight pressure elevation levels.

Table 3.1 shows the manufacturer's associated uncertainty details for each of the transducers used.

Location, Range	**Make, Model**	**Temp. error band**	**Linearity and hysteresis**	**From calibration (95% conf.)**	**Zero offset (mbar)**	**Total error band**
Venturi Upstream, 7 bar g	Druck, PDCR 820-0800	0.5% FSO	0.1% BSL	0.05% BSL	0.08% (5)	0.68% FSO
Venturi Δp, d 0.075 bar	Druck, PDCR 4120	0.3% FSO	0.08% BSL	0.02% BSL	0.5% (0.35)	0.88% FSO
Venturi Throat, 7 bar g	Druck, PDCR 820-0800	0.5% FSO	0.1% BSL	0.05% BSL	0.08% (5)	0.68% FSO
Plenum Chamber, 3.5 bar a	Kulite, PT213-342	0.3% FSO	0.35% FSO	0.01% FSO	0.1% (3.5)	0.75% FSO
Test Section, 2 bar g	Keller, 21 R	Not quoted	0.1% FSO	0.04% FSO	Not quoted	1% FSO
Test Section, 3.5 bar a	Kulite, PT213-342	0.3% FSO	0.35% FSO	0.02% FSO	0.1% (3.5)	0.75% FSO
Liquid Delivery, 10 bar g	TI, s2000	1.5% FSO	0.25% FSO	0.2% FSO	0.05% (5)	1.8% FSO

Table 3.1: Pressure transducer manufacturers details (BSL - best straight line, FSO - full scale output)

In this setup the NI cDaq 9172 acts as a voltmeter, its repeatability and accuracy was an order of magnitude better than that of the pressure transducers. Consequently, the uncertainty associated with the NI cDaq 9172 was negligible.

3.6 Temperature Measurements

Temperature measurements were used to identify fluid properties. A total of five temperature measurements were required, all of which used K-type thermocouples, (positions shown in Figure 3.9). Starting furthest upstream they were: Venturi upstream, plenum chamber, test section exit, liquid delivery and instrument box.

Standard correlations embedded in the Labview/NI interface for K-type thermocouples were used. The combined uncertainty of the thermocouples and

acquisition system was ± 1 °C. Noting that, at a fluid temperature of 300 K (room temperature) ± 1 °C represents an uncertainty of ± 0.33% and this was more than adequate precision for the test criteria.

However, for completeness and to show that default standards were achieved, the response of the thermocouples were compared with the laboratory's PRT based ISOTECH TTi-2 reference temperature measurement equipment which has an accuracy of better than 1/100 °C. The temperature measured by the thermocouples through the Labview environment was within ± 1 °C of that measured by the reference equipment (0.293 °C worst single case), for all the thermocouples and at all temperatures tested.

3.7 Volumetric Liquid Flow Measurement

The liquid flow rate was measured using a flow meter which transmitted a current proportional to the flow rate magnitude. The liquid flow rate measurement was used to calculate the liquid jet velocity at the nozzle exit based on continuity, as is the standard approach in sprays in cross-airstream work. This velocity was required to determine the momentum flux ratio (q).

The liquid volumetric flow rate required depends on the nozzle geometry and pressure differential across it. Within this study experiments were completed using two nozzle types:

1. Round nozzle with an orifice area 0.2552 mm^2
2. Slot nozzle with an orifice area 2.6364 mm^2

For the round nozzle used in these tests, the volumetric flow rate was approximately 0.09, 0.16, 0.23 and 0.32 l/min for a differential pressure of 0.5, 1.5, 3.5 and 6.5 bar respectively. For the slot nozzle used in these tests, the volumetric flow rate was approximately 1.05, 1.85, 2.76 and 3.68 l/min for a differential pressure of 0.5, 1.5, 3.5 and 6.5 bar respectively. It was not possible to measure the range of liquid flow rates (0.09 to 3.68 l/min) with a single device and two turbine flow meters were acquired for the task:

1. Kobold DPL-1P05: 0.025 to 0.5 l/min (used with the round nozzle)
2. Kobold DPL-1P20: 0.4 to 12 l/min (used with the slot nozzle)

Both flow meters gave an output current of 4 to 20 mA across their respective measurement ranges. The accuracy of the flow rate defined by the flow meters was compared to a reference flow rate using a measuring flask, scales and a stop watch, as illustrated in Figure 3.14.

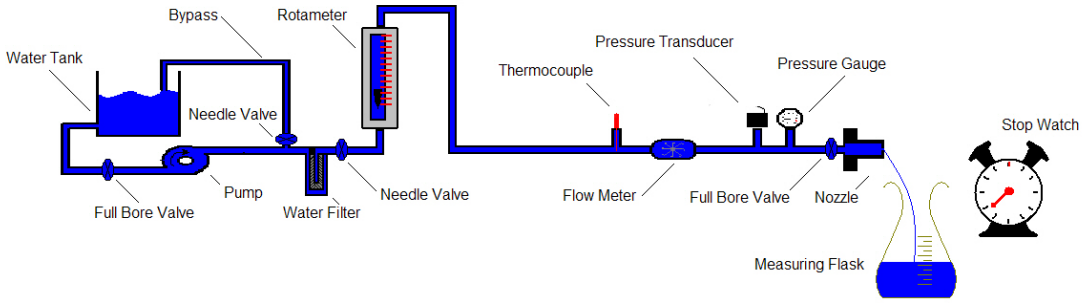

Figure 3.14: Measuring flask and stop watch arrangement

The mass of the water collected was measured on scales with an accuracy of ±1 g (i.e. 0.001 l of water). Each flow meter was connected to the NI cDaq 9172 console, i.e. as in the actual experimental set-up and the calibrations therefore included the response of the data acquisition system.

These tests were repeated on different days, analyses of the results showed that the manufacturers quoted uncertainty of ± 3% was acheived but could not be improved.

So far, this chapter has reported on the instruments assembled to facilitate measurements of the experimental conditions. The following section describes the procedure used to establish the uncertainty levels associated with these key measurements.

3.8 Uncertainty and Stability of the Test Parameters

This section describes the uncertainty associated with Weber number (We_g) and momentum flux ratio (q) calculated and reported herein. Their uncertainty was derived from the uncertainty of the physical measurements that contribute to their definition. The Taylor series uncertainty propagation method[1] provides the basis for the analysis.

3.8.1 Weber Number Uncertainty Analysis

Equation 3.1 shows the relevant derivation of the We_g.
Noting that; $W_g = \frac{\dot{m}_g}{\rho_g A_{TS}^2}$ and $W_l = 0$

$$We_g = \frac{external\ forces}{internal\ forces} = \frac{\rho_g (W_g - W_l)^2 l}{\sigma} = \frac{\dot{m}_g^2 l}{\sigma \rho_g A_{TS}^2} \tag{3.1}$$

$Where: \dot{m} = fn[p_1, (p_1 - p_2), T_1, d_1, d_2]$ and $\rho_g = \frac{p_g}{R T_g}$

Table 3.2 shows the associated uncertainty for each relevant measurement.

Equation Parameter	Measured Parameter	Uncertainty	Source
$\dot{m}_g$	p_1	± 0.68%	manufacturers quoted
	$p_1 - p_2$	± 0.88%	manufacturers quoted
	T_1	± 1.0 °C	manufacturers quoted
	d_1	± 0.5 mm	measured
	d_2	± 0.5 mm	measured
l	l	± 0.01 mm	measurement resolution
σ	σ	± 2%	estimated
ρ_g	p_g	± 1.0%	manufacturers quoted
	T_g	± 3.0 °C	estimated (indirect measurement)
	R	± 0.002 kJ/kgK	estimated
A_{TS}	A_{TS}	± 28 mm^2	measured

Table 3.2: Uncertainty of parameters that contribute to We_g calculation

The Weber number combined uncertainty was calculated as ± 3.37%. Figure 3.15 is a flowchart that shows how the uncertainty of We_g was calculated for a specific case, where the different coloured backgrounds represent:

[1] As defined in ISO ISBN 92-67-01075-1 (1993), UKAS-M300003 (1997) and Taylor and Kuyatt (1994)

1. Grey - an equation to be resolved (i.e. Equation 3.1 at the centre)
2. Yellow - variable *real time measured* parameter and its associated uncertainty
3. Green - constant parameter and its associated uncertainty
4. Blue - a calculated or resultant uncertainty
5. Pink - partial differential equation that results from the equation to be resolved

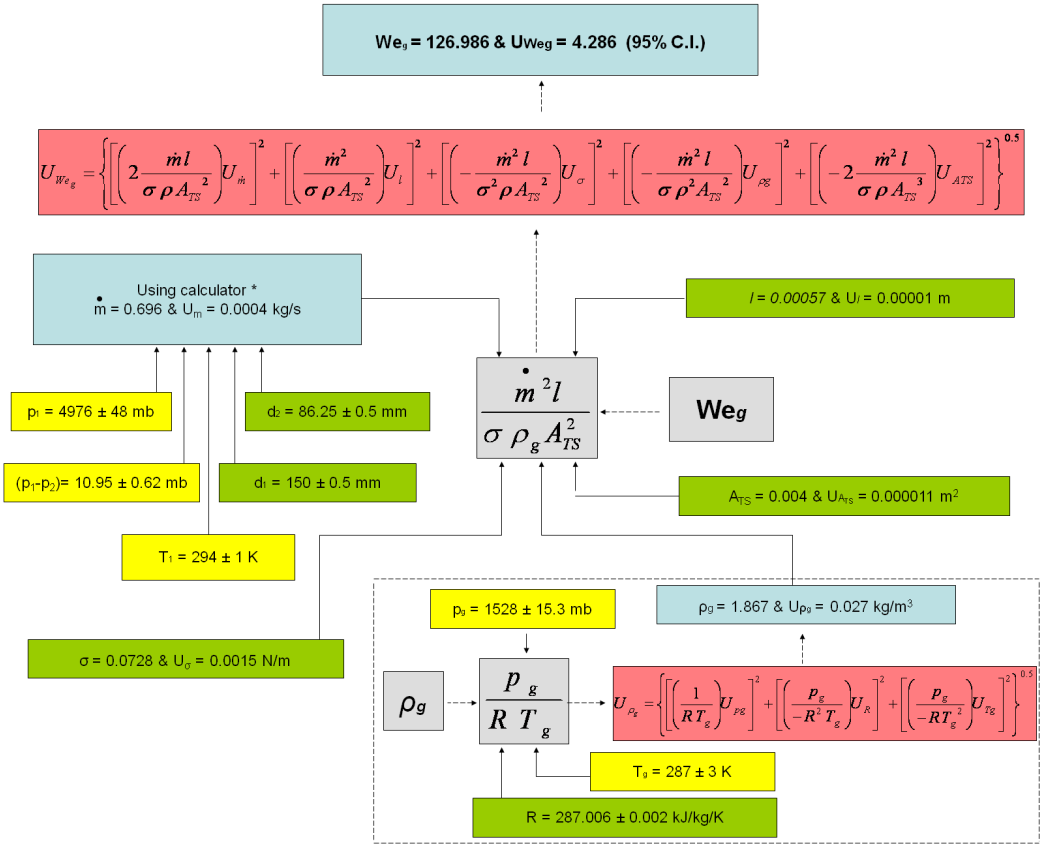

Figure 3.15: Weber number uncertainty analysis (*from **Cooke and Regan (2009)**)

3.8.2 Momentum Flux Ratio Uncertainty Analysis

Equation 3.2 shows the relevant derivation of q.

$$q = \frac{liquid\ momentum}{gas\ momentum} = \frac{\rho_l\, U_l^2}{\rho_g\, W_g^2} = \frac{\rho_l\, \bar{V}_l\, \rho_g\, A_{TS}^2}{\dot{m}_g^2\, A_{noz}} \tag{3.2}$$

Where : $\dot{m} = fn\left[p_1,\ (p_1 - p_2),\ T_1,\ d_1,\ d_2\right]$ *and* $\rho_g = \frac{p_g}{R\,T_g}$

Table 3.3 shows the associated uncertainty for each relevant measurement.

Equation Parameter	Measured Parameters	Uncertainty	Source
ρ_l	ρ_l	± 2.0%	estimated
$\bar{V}$	$\bar{V}$	± 3.0%	manufacturers quoted
ρ_g	p_g	± 1.0%	manufacturers quoted
	T_g	± 3.0 °C	estimated (indirect measurement)
	R	± 0.002 kJ/kgK	estimated
A_{TS}	A_{TS}	± 28 mm^2	measured
$\dot{m}_g$	p_1	± 0.68%	manufacturers quoted
	$p_1 - p_2$	± 0.88%	manufacturers quoted
	T_1	± 1.0 °C	manufacturers quoted
	d_1	± 0.5 mm	measured
	d_2	± 0.5 mm	measured
A_{noz}	A_{noz}	± 0.01 mm^2	measurement resolution

Table 3.3: Uncertainty of parameters that contribute to q calculation

The squared terms in the momentum flux ratio make it naturally sensitive to small changes in liquid and air properties. This, as well as the challenging process of measuring small liquid volumes, makes momentum flux ratio a difficult parameter to measure experimentally. For this test rig and instrumentation arrangement the associated uncertainty was calculated as ± 9.48%, where $q = 32.72$. Figure 3.16 is a flowchart that shows how the uncertainty of q was calculated for this specific case, where (as before) the different coloured backgrounds represent:

1. Grey - an equation to be resolved (i.e. Equation 3.2 at the centre)
2. Yellow - variable *real time measured* parameter and its associated uncertainty
3. Green - constant parameter and its associated uncertainty
4. Blue - a calculated or resultant uncertainty
5. Pink - partial differential equation that results from the equation to be resolved

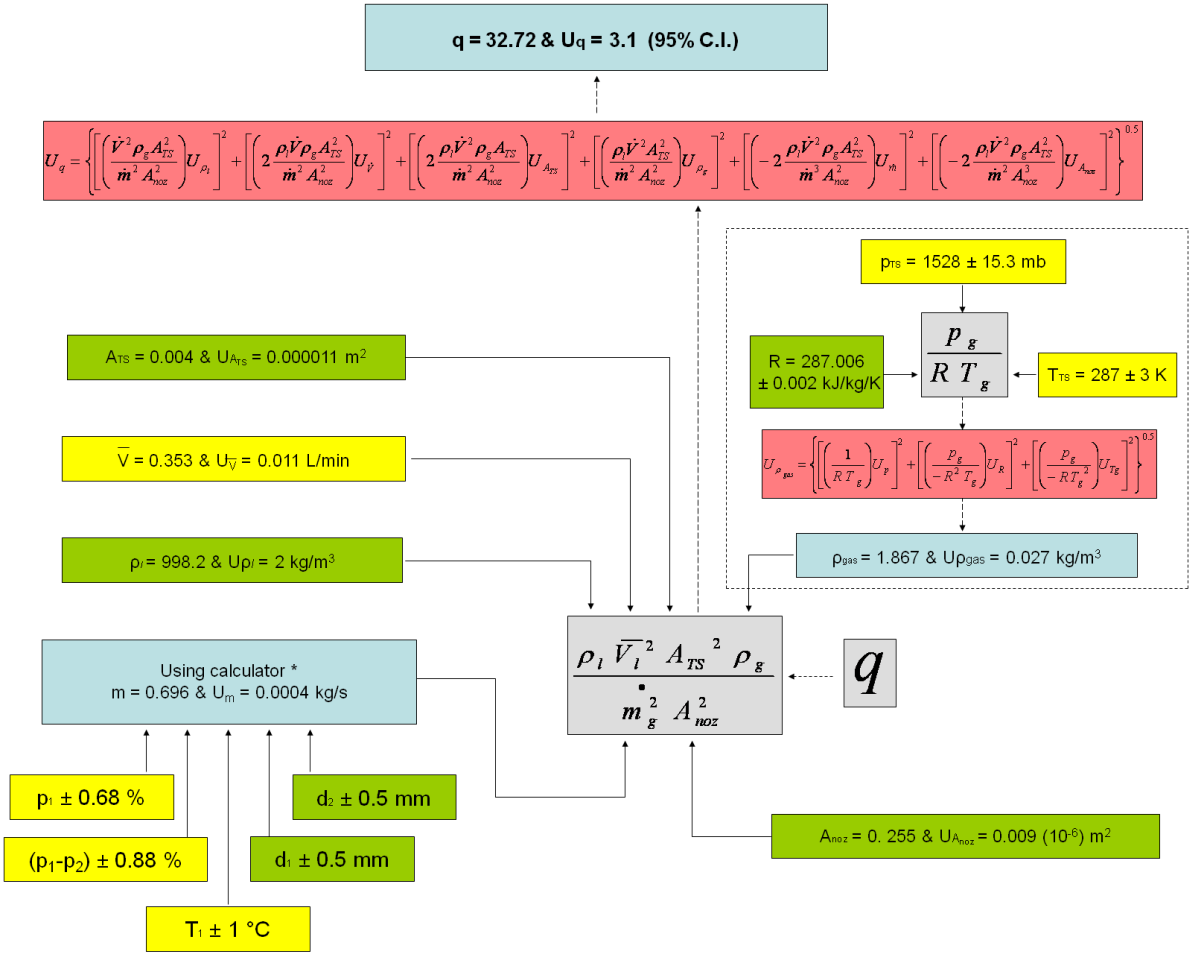

Figure 3.16: Momentum flux ratio uncertainty analysis (*from **Cooke and Regan (2009))**

3.9 Chapter Synopsis

This chapter presented the TFMRC spray test facility which was designed and constructed specifically for this study. The chapter went on to describe the condition monitoring instrumentation and reported the calculated uncertainty levels of the associated measurements. The instruments are used to derive bulk flow rates and mean velocity of both the liquid flow and the cross-airstream.

The instrumentation used to determine the test conditions was independent of the more sophisticated laboratory techniques employed to characterise the local flow field effects. Five different such measurement approaches were used in this study: Laser Doppler Anemometry (LDA), Hot Wire Anemometry (HWA), Phase Doppler Particle Analysis (PDPA), Laser Sheet and Pulsed Digital Camera (LSPDC) and High Speed Video (HSV). The following chapter provides a conspectus for each and defines the relevant set-up used in this work.

Chapter 4

Spray Characterisation Techniques

This chapter describes five different experimental techniques that were used to define the cross-airstream and characterise the spray fields:

1. Laser Doppler Anemometry (LDA)
2. Hot Wire Anemometry (HWA)
3. Phase Doppler Particle Analysis (PDPA)
4. High Speed Video (HSV)
5. Pulsed Laser Sheet with Coupled Digital Camera (PLSCDC)

LDA tests were conducted to define the velocity distribution in the cross-airstream at the axial plane where liquid was injected in the test section. The purpose of this was two fold. Firstly, it demonstrated that the test apparatus operated as intended with a symmetrical airstream and without hot spots. Secondly, the data provides a boundary condition that can be plugged into CFD codes.

HWA tests were conducted define the turbulence levels in the cross-airstream again to provide an input for CFD to set the appropriate boundary conditions.

PDPA was selected for the important process of characterising droplet sizes and velocities. Different approaches for droplet measurements were compared, including a system called shadow-sizing which is based on Particle Image Velocimetry (PIV). However, this system is a field of view technique and does not provide the same level of detail that can be obtained using the point measurement approach of PDPA.

A HSV system was available for a short period during the programme, through an EPSRC loan. The videos produced provide useful macroscopic insight into the steadiness of the spray morphology. The sequential still frames can also be used to determine spray penetration.

The TFMRC's PIV system was used to capture high resolution images of the spray field, although only tests with the round nozzle were conducted. Since the velocimetry capability of this system was not required or used, the application is defined here as a pulsed laser sheet with coupled digital camera.

This chapter describes these five techniques as well as their particular set-up for the spray test facility.

4.1 Laser Doppler Anemometry (LDA)

The local velocities in the cross-airstream were measured to provide the appropriate boundary condition input for CFD codes. The measurements were completed using the TFMRC's LDA system.

The LDA principle relies on the coherence of laser light. A single beam is split into two which are focused towards each other to form an interference region, known as the measurement volume, as illustrated in Figure 4.2.

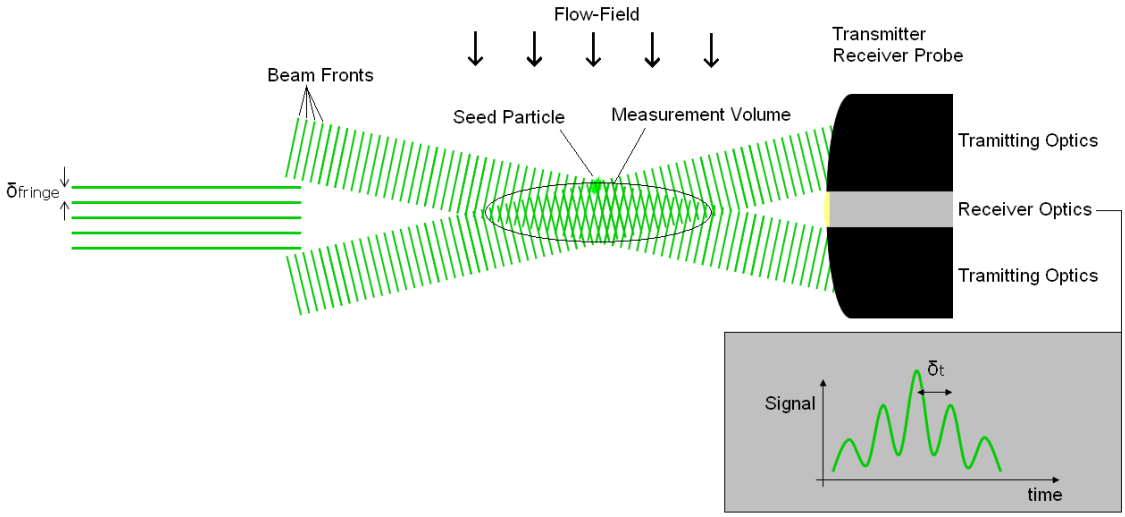

Figure 4.1: LDA basic arrangement

The beam fronts form a set of fringes. As a particle passes through them it reflects light in all directions, producing a series of light pulses as it passes each fringe. The period between these light pulses define the particles velocity.

Hence, assuming the particle has the same velocity as its surroundings the flow velocity can be determined by measuring the time between the light pulses received in a photo-detector and knowing the distance between the fringes.

This basic principle described above is correct but, as an anemometer such a machine could not measure a zero velocity (and would be unstable at low velocities); nor would it be able to differentiate between negative and positive velocities. In order to provide the required level of functionality, one of the beams is manipulated, using a 'Bragg Cell', to slightly shift its frequency. The affect of this is to cause the fringes in the measurement volume to 'roll'. In this way a stationary particle exhibits a series of light pulses as the fringes roll through the particle. The direction and rolling speed of the fringes can be analytically resolved from the geometry of the beam interference, the wavelength and the phase shift.

Using two pairs of perpendicular beams (at different wavelengths), two velocity components can be measured simultaneously.

The TFMRC's LDA system was used to measure the local axial velocity in the test section. These measurements were used to verify the symmetry of the airstream and provide a detailed boundary condition for CFD comparisons. The LDA system was used in the back scatter mode using a 200 mm combined transmitter/receiver probe.

The TFMRC's two component LDA system consisted of: Dantec Burst Spectrum Analyser, Bragg Cell giving a 40 MHz frequency shift, Optical fibre connections to a 250 mm focal length probe. The laser system was a Spectra Physics 5 W Argon - Ion Laser.

Two dimensions of velocity were measured in the spray rig test section simultaneously; the cross airstream direction (z); and, the liquid flow direction (x). The results of these investigations are reported in Chapter 6. Table 4.2 provides a list of the test setup parameters.

Property	U1	U2
Seeding Particles	Olive oil	
Laser Power	< 2 W (typical)	
Wavelength	514.5 nm	488 nm
No of fringes	14	14
Fringe spacing	5.203 μm	4.935 μm

Table 4.1: LDA test set up

4.2 Hotwire Anemometry (HWA)

The turbulence intensity of the cross-airstream was measured to provide a boundary condition input for CFD codes. The measurements were completed using the TFMRC's HWA system.

In HWA a thin ($\approx 5\mu$m diameter) wire is introduced into the flow field. The temperature of the wire varies (cools) as the flow velocity increases. The electrical resistance of the hot wire is related to its temperature and a relationship between electrical resistance and the velocity of the flow it is in can be established.

The system uses a Wheatstone bridge circuit and a differential feedback amplifier. As the hotwire's temperature deviates the current drawn by the WBC changes and velocity is effectively measured by applying the appropriate calibration.

The measurement of turbulence requires a system capable of taking measurements more quickly than the deviations in velocity occur. HWA systems can operate at measurement frequencies up to 450 kHz and, as a result, HWA is a useful tool in turbulence characterisation. The TFMRCs HWA consists of a Dantec 6 Channel Stream Line Constant Temperature Anemometry system and Dantec StreamWare software.

A 1D tungsten wire probe was used in the tests and the system was set up to operate at 100 kHz (i.e. at 100 m/s a measurement is performed in every 1 mm of flow that passes the probe). A mount for the hot-wire was constructed such that the hot-wire could be introduced into the flow using one of the test section's nozzle positions, as shown in Figure 4.2.

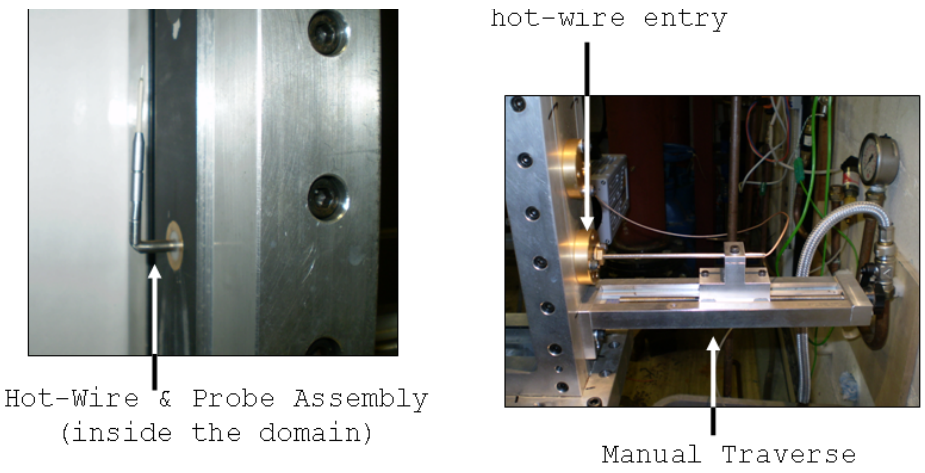

Figure 4.2: Hot-Wire mounting system

Because the aim of the hot-wire measurements was to establish turbulence (rather than absolute values of velocity) the hot wire could be calibrated 'in-situ' using the local LDA velocity data for reference. This was a convenient approach as it negated the need to include density corrections required where a hot-wire is calibrated using flows from the outlet of fixed nozzles at atmospheric pressures.

The results of the turbulence investigation are presented in Chapter 6.

4.3 Phase Doppler Particle Analysis (PDPA)

The method used in this study to characterise droplet sizes and velocities was Phase Doppler Particle Analysis (PDPA). PDPA simultaneously measures the diameter and corresponding velocity of transparent spherical particles. The following provides an overview of the operating principles with some limitations highlighted. After which the details of how PDPA was set-up in these experiments is discussed.

4.3.1 PDPA Operating Principles

The PDPA principle relies on the coherent frequency of a laser light source. A laser is used to generate a pair of light rays are directed such that they intercept to form a small volume of intense light (*known as the measurement volume*). As

a particle passes through the measurement volume, light-rays are scattered in all directions (*scattered-light*). This scattered-light exhibits greatly varying light intensity, corresponding to the mode in which it reflects off or exits the particle, i.e. through reflection, 1^{st} order refraction, 2^{nd} order refraction and so on, as illustrated in Figure 4.3

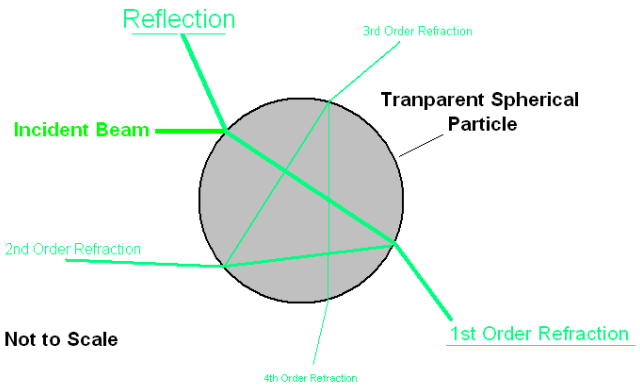

Figure 4.3: Scattered light from transparent spherical particle

The light intensity of each mode is a function of its radial location with respect to the particle, as described by the Mie Light Scattering map in Figure 4.4. The light from a particular mode can be isolated and interrogated; the most powerful modes are typically used, reflected or 1^{st} order refraction.

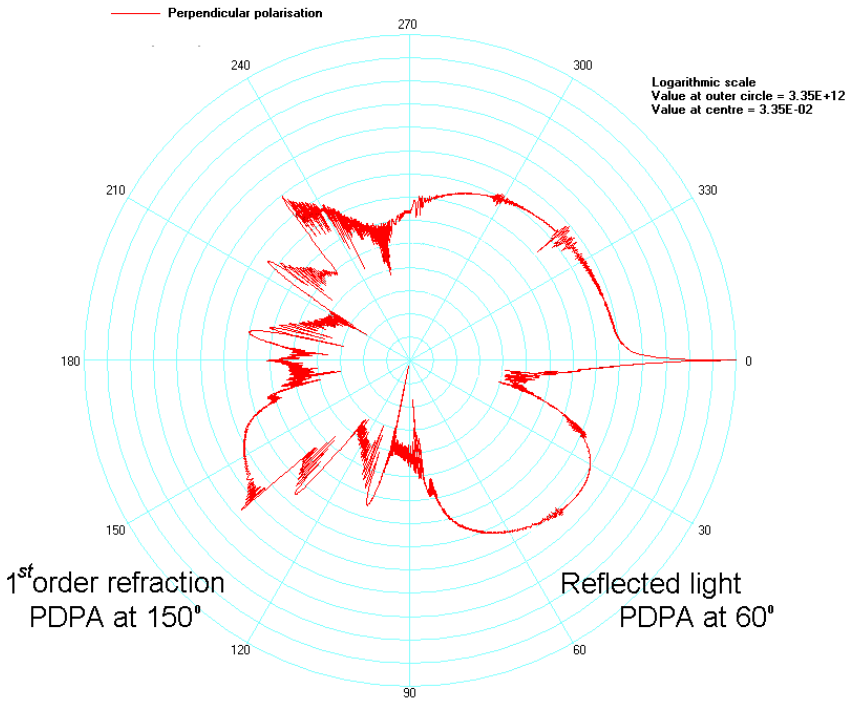

Figure 4.4: Mie-theory light intensity

The PDPA principle measures the size of a particle by measuring the phase-lag of scattered-light received at two photo detectors at different radial locations, as illustrated in Figure 4.5.

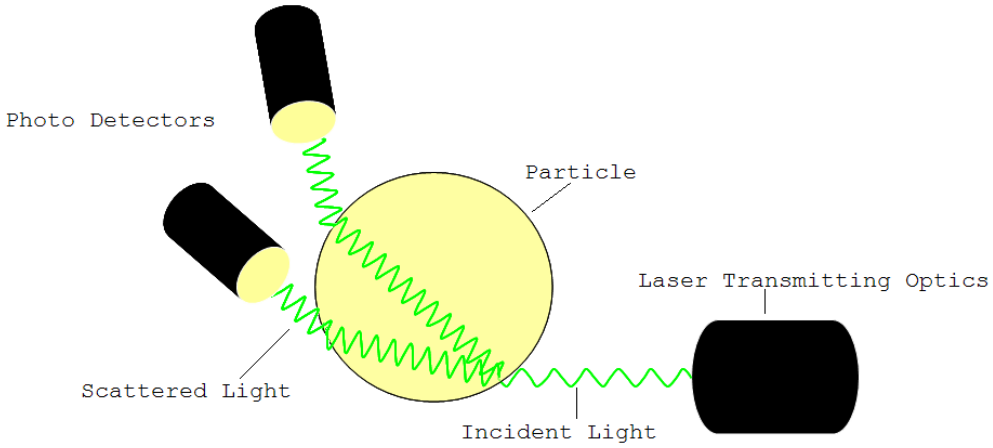

Figure 4.5: PDPA Principle

The phase-lag results because the *speed of light* within the particle is different to that in the surrounding gas. More generally, the speed of light depends on the *refractive index* of the matter through which it travels:

$$n = \frac{c}{v} \tag{4.1}$$

where: v is the incident speed of light; c is the speed of light in a vacuum (299,792,458 m/s); n is the material refractive index (n = 1.0003 for air, n = 1.333 for water).

Because the scattered-light collected in each receiver takes a different route through the particle, there is a phase offset between the signal in each receiver, as illustrated by Figure 4.6. The technique benefits from a perfectly linear relationship between the phase lag and the curvature of the particle surface. If the particle is assumed to be spherical the diameter can be inferred.

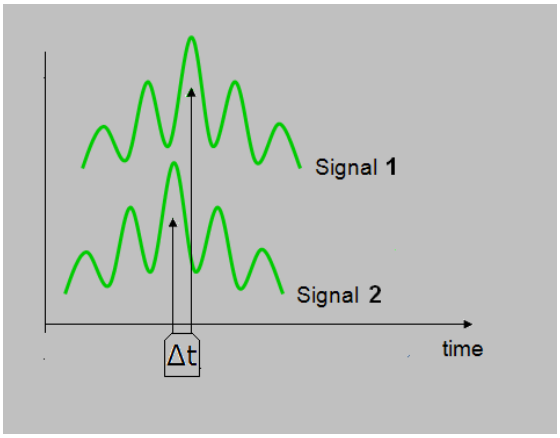

Figure 4.6: PDPA Principle

The application of the basic principle outlined above is in practice a complex process. The Dantec equipment used in this study is, as far as possible, a self-contained system. Crucially this means the receiver optics relative locations are factory fixed. Along with the Dantec software, the complete package provides a reliable measuring device. The main tasks left for the operator are:

- aligning the transmitting and receiving probes with one another and the desired measurement point; and
- fine-tuning the LASER power and signal response in the optical collectors for the particular conditions - to maximise the signal to noise ratio.

In theory a particle size measurement can be obtained from the shift in phase between two photo detectors, however the Dantec system uses three receiving optics and obtains two semi-independent measurements, as can be seen in

Figure 4.7. This approach effectively measures the curvature of the particle at two different circumferential positions. The spherical validity of the droplet can be confirmed by comparing the two measurements and rejecting incidents that do not compare. This method of using three receiving optics also enables a greater range of droplet sizes to be measured with finer resolution.

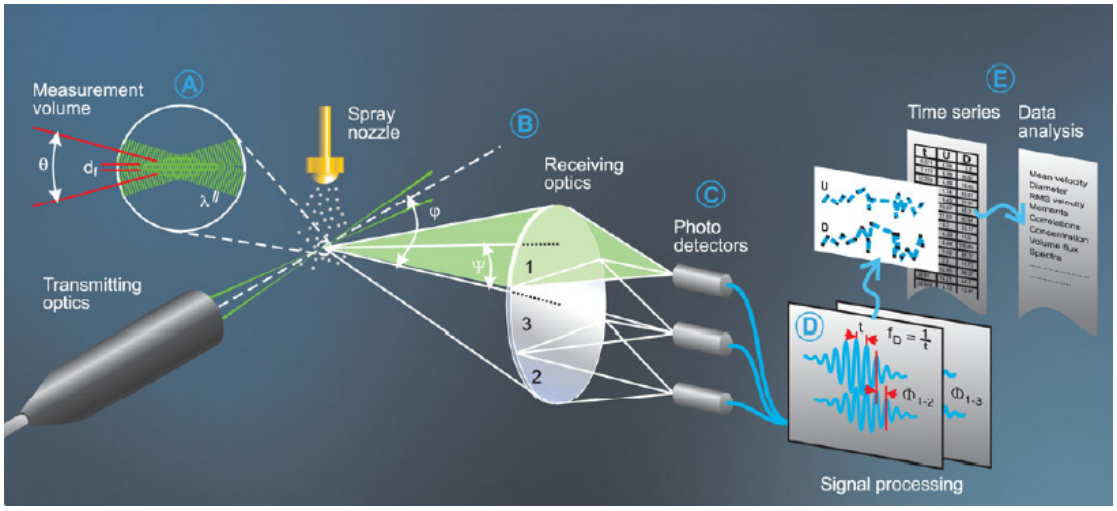

Figure 4.7: PDPA Arrangement (image from www.Dantec.com)

For a droplet to be successfully measured, it must transit the measurement volume on its own, in isolation from its neighbouring droplets. In dense sprays this criterion is often not met and, as a result, PDPA's capability to measure local mass flux is fundamentally inhibited. Consider the two cases in Figure 4.8.

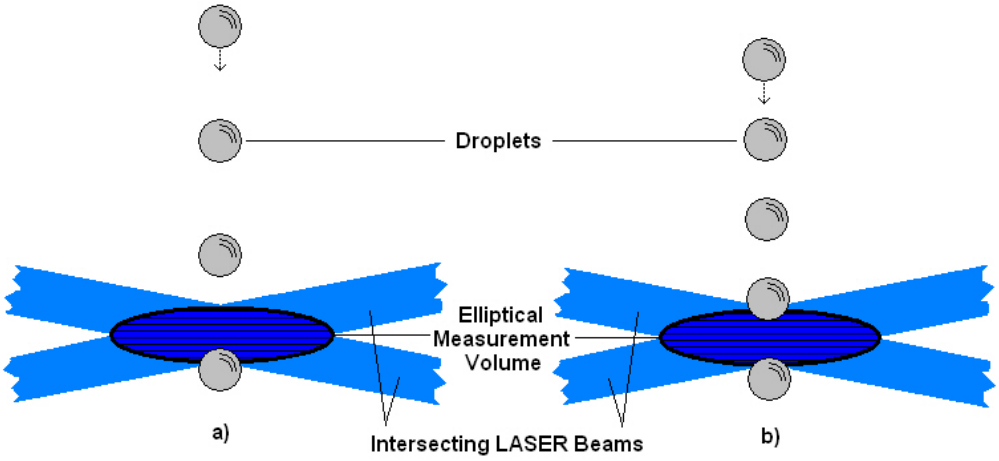

Figure 4.8: Measurement volume and droplet spacing

In case a) the four particles are spaced such that each exits the measurement volume before the next arrives and all four particles can be successfully mea-

sured. Since the droplet diameters are measured and **all** the droplets per unit time are accounted for, the local mass flux can be calculated.

In case b) only one droplet is added, hence the population density has increased by 25%, but now they are too close together. The next droplet enters before the preceding droplet exits. In this hypothetical case no droplets are measured. In practice, droplet spacing is not so uniform and many measurements would be successfully performed. But many droplets are lost to multi-occupancy and the system cannot accurately account for the number of droplets per unit time, the local mass flux cannot be calculated.

Although much of the spray is unaccounted for, in dense sprays, droplets are missed indiscriminately. **Edwards and Marx (1991)** confirmed that mean droplet sizes and velocities are representative even in very dense sprays. They demonstrated that where 80% of the particle and volume flux is lost, the error in mean diameters is less than 5%.

The measurement principle requires the results from two photo-detectors, however, employing a third photo-detector has useful advantages. The Dantec Fibre-smg uses this method. The third detector allows for a second semi-independent measurement and a comparison of the measurements enables the system to operate over a wider range of droplet sizes and also provides a method to check the spherisicity assumption which is critically important.

Where the two measurements do not agree, within an error band, the system rejects the measurement and omits the data. However, the nature of the signal received is such that whenever the light scattered from a particle (or multiple particles in multi-occupancy) is meaningless in terms of the measurement approach, the two measurements do not match and the systems records a non-spherical event. The PDA system displays and logs the number of non-spherical events providing a measure of the systems capability for the given application/point in the spray; i.e. spherical validity falls below 100%, if the measurement volume is in a point where droplets have not yet formed *or* the spray is dense with high multi-occupancy events *or* there is a poor SNR for some other reason.

As a rule of thumb spherical validity is expected to be in excess of 70% for useful measurements to be obtained, lower than this is an indication that the PDA set-up is not appropriate for the application. The sphercal validity associated with droplet size measurements provides a check that the PDA system was operating effectively and the set-up was appropriate for the spray in which the

measurement was made.

It is perfectly possible to adjust the set-up parameters (such as laser power, masks, filters, gain, velocity frame(s), alignment, etc.) of the PDA system to achieve spherical validity of 100%, provided the spray field is not too dense and application is appropriate for PDA. However, where the objective is to define a complete spray field, rather than a single point within a spray, the operator needs to set-up the parameters on the basis of a compromise for what is optimal across a section of the spray. Consequently, the spherical validity varies over a set of measurements over a section of a spray field, as the particular PDA set-up is more and less suited to different parts of the spray field in which the measurements were performed.

The following sub-section describes the specifics of the PDPA setup and its application used in this study.

4.3.2 TFMRC Spray Facility PDPA Configuration

The TFMRC did not previously to this study have particle measurement capability, PDPA was chosen as it is widely accepted as the most accurate method. Furthermore, it was possible to develop the system based on additional hardware (and new application software) to the Dantec LDA system which has been in operation at the TFMRC for a number of years (and described previously in this chapter). The necessary additions were procured from Dantec to assemble the particle measurement capability based on their Dantec FiberPDA system.

Figure 4.9 shows the PDPA transmitting and receiving probes as well as the 3D traverse system on which they were fixed.

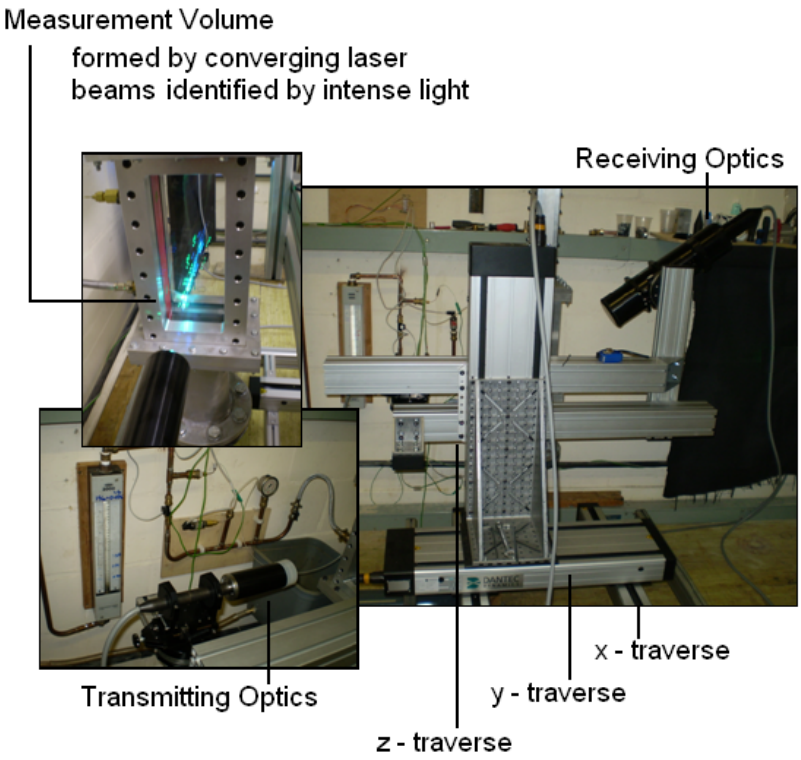

Figure 4.9: PDPA hardware

The transmitting and receiving probes were located on a 3D traverse to enable automated spray-wide measurements. The PDPA measurements were made over a complete cross section of the spray field at four separate axial locations: z = 10, 25, 40 and 70 mm. The PDPA setup parameters are listed at the end of this section in Figure 4.11.

It was possible to perform measurements as close as 2 mm from the nozzle wall, closer than this the incident laser beams interfered with the test section's window frame. Between 2 to 4 mm from the nozzle wall ($2 < x < 4$ mm), the SNR was less reliable than it was for $x > 4$ mm. The step size between each measurement point was varied from 1 to 3 mm depending on the size of the spray field. At each point in the measurement grid, data were acquired for either: 50,000 samples or 1% consolidation on AMD with a wall clock of 4 seconds where these criteria were not met.

Figure 4.10 shows the a typical z plane measurement grid.

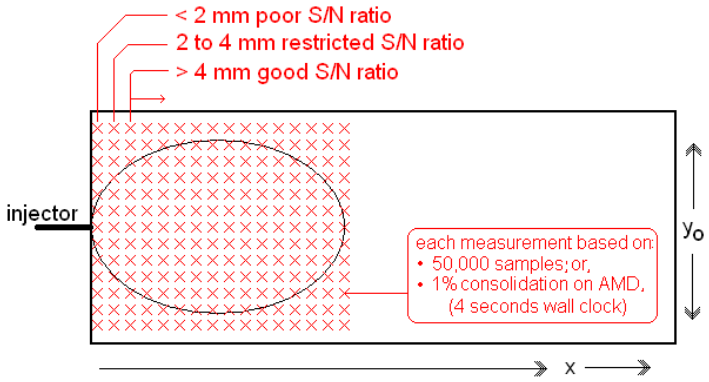

Figure 4.10: Typical z plane PDPA point measurement grid

The uncertainty of the position the measurement volume (i.e. location of the PDPA measurements) is estimated as ± 0.5 mm for the x and y coordinates. Aligning the x and z coordinates is quite straight forward as the laser beams can be physically aligned with a reference surface by eye, on a low power setting.

The y coordinate cannot be lined up by eye because the laser beams are only perpendicular to the y plane and, as a result, accurate alignment is more difficult to achieve. After various attempts at different procedures for lining up the y coordinate, the best method proved to be by traversing the measurement volume through the spray and watching the signal in the PDPA software. The point where the signal reduced to zero defined the edge of the spray; the y coordinate was aligned by assuming $y = 0$ mm was equal-distance from each edge of the spray. The contour plots presented throughout this work show that the spray-fields were always symmetrical across the y origin plane and validate this method of alignment.

Over the entire data set an average of 10^4 samples were taken at each data point. A sensitivity test was carried out to investigate how AMD was affected by the sample count, it showed that the variation in AMD was less than 1 μm where the sample count was greater than 2600 - where typical droplet sizes were of the order of 50 μm.

Figure 4.11 is a list of the typical PDPA setup parameters used in this study, the Figure is screen shot taken from the PDPA software.

Property	Optical PDA System - U1	Optical PDA System - U2
Wavelength	514.5	488
Focal length	300	300
Beam diameter	1.35	1.35
Expander ratio	1.98	1.98
Beam spacing	15	15
Frequency shift	4e+007	4e+007
Number of fringes	14	14
Fringe spacing (um)	5.203	4.935
Beam half-angle (deg)	2.834	2.834
Probe volume - dx (mm)	0.07361	0.06982
Probe volume - dy (mm)	0.07352	0.06974
Probe volume - dz (mm)	1.487	1.411
Receiver type	112 mm Fiber PDA	112 mm Fiber PDA
Scattering angle (deg)	30	30
Receiver focal length	310	310
Receiver expander ratio	1	1
Fringe direction	Positive	Positive
Scattering mode	Refraction	Refraction
Aperture mask	Mask C	Mask C
Spherical validation band (%)	15	15
Spatial filter	Slit: 0.200 mm	Slit: 0.200 mm
Particle name	Water	Water
Particle refractive index	1.334	1.334
Particle specific gravity	1	1
Particle kinematic viscosity	0.001	0.001
Medium name	Air	Air
Medium refractive index	1	1
Medium specific gravity	1	1
Medium kinematic viscosity	0.001	0.001
Eff. scattering mode	Refraction	Refraction
Eff. scattering angle (deg)	30	30
Phase factor P12	4.74	4.74
Phase factor P13	1.022	1.022
Max. diameter (um).	256.9	256.9
Relative refractive index	1.334	1.334
Eff. spatial filter width	0.2	0.2
Critical angle (deg)	82.88	82.88
Brewster angle (deg)	73.71	73.71
Rainbow angle (deg)	138.1	138.1

Figure 4.11: Screen shot of a typical PDPA set-up

4.4 High Speed Video (HSV)

The high speed video equipment was made available through an EPSRC loan arrangement. The camera was a Monochrome Photron SA3 with a frame rate ranged from 2,000 to 120,000 fps. The maximum resolution was 1024 x 1024 pixels available at 2,000 fps, with higher frame rates coming at the cost of frame resolution. The minimum field of view was of the order of 100 x 100 mm.

Figure 4.12 shows the high speed camera focused on the test section, flooded with light through the opposite window that incorporated a diffusive film.

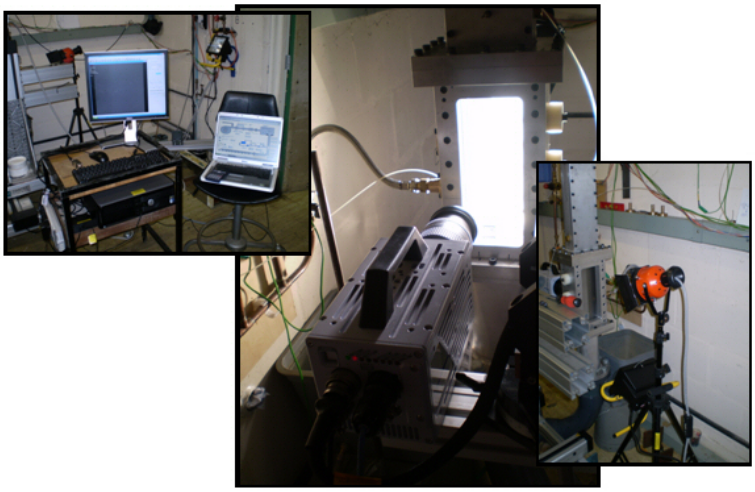

Figure 4.12: High speed video set-up

Extensive high speed video data was collected, the entire test matrix (defined in the Results Chapter) was completed at 2, 10 and 20 kfps. The complete set of images is some 100 Gbytes in size.

4.5 Pulsed Laser Sheet and Coupled Digital Imaging

The high frame rate of the high speed video system has characteristically low resolution. In order to capture detailed images of the spray field, a pulsed laser sheet and coupled digital camera was used. This offers far superior resolution to that of the high speed video. This type of approach has in the past been widely used in jet behaviour investigations. Figure 4.13 shows the arrangement.

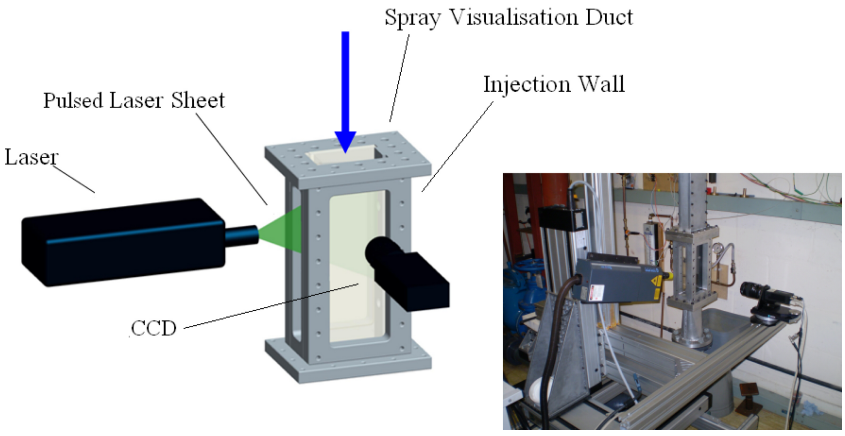

Figure 4.13: PIV set-up

The arrangement was assembled and configured utilising a Dantec Particle Image Velocimeter (PIV) system. A pulsed laser operating at 15 Hz was used to provide sheet illumination of the spray. The images were recorded using a 2 mega pixel CCD camera located at a right angle to the laser sheet. The image pulse duration was 10 ns (for 100 m/s this corresponds to a displacement of 1 μm) which was sufficiently short to effectively freeze the motion.

4.6 Chapter Synopsis

This chapter has reported on the experimental methods used to facilitate spray characterisation. The next chapter discusses preliminary experiments that were conducted for the purpose of providing a base-line data-set using a round nozzle.

Chapter 5

Continuous (Air) Phase and Discrete (Liquid) Phase Flow Properties

The characteristics of the gas and liquid flows, before they combine to form the spray field, have a significant impact on the resulting spray field's characteristics. In the same way, for CFD modeling, the input boundary conditions need to be representative of the actual upstream flows, in order to predict the spray's flow physics. This chapter discusses the upstream flow properties of both the cross-airstream and the liquid injection relevant to these sprays in cross-airstreams experiments.

5.1 Cross-Airstream

During experiments, the bulk mean velocity of the cross-airstream was measured utilising an upstream nozzle to ± 3 m/s. However, in order to define the cross-airstream in greater detail, surveys of the local velocities in the test section were completed using Laser Doppler Anemometry (LDA), as well as turbulence measurements using Hot Wire Anemometry. These definitions provided detailed boundary conditions that could be used in CFD models aimed at predicting the sprays created within this programme of work.

5.1.1 LDA Cross-Airstream Velocity Measurements

LDA measurements were performed at the axial plane coincident with where the liquid injection took place during the spray tests, i.e. $z = 0$. Figure 5.2 shows

the $z = 0$ cross-section as cut-through *A-A*, as well as illustrating the optional insert that could be used to reduce the test section's cross-sectional area, making higher cross-airstream velocities possible.

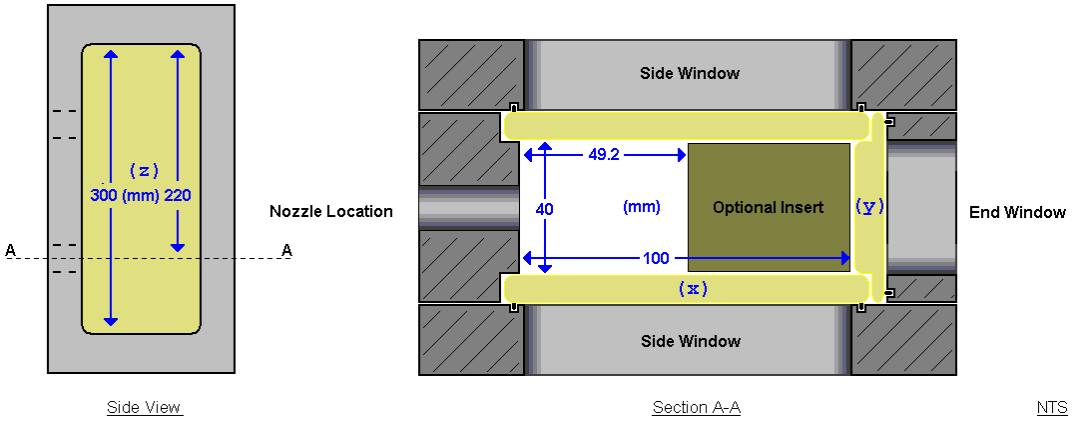

Figure 5.1: Position of local velocity measurements

The following sub-section details the results from the LDA measurements performed in the full working section (i.e. 100 mm x 40 mm), and this is followed by a sub-section that details the same but for the reduced working section (i.e. 49.2 mm x 40 mm).

Full Test Section Configuration

In the full test section configuration the maximum velocity of the cross-airstream that could be attained was approximately 100 m/s. LDA local velocity measurements were carried out at three different levels of bulk mean velocity: W_{mean} = 30 m/s; W_{mean} = 61 m/s; and, W_{mean} = 96 m/s - Figure 5.2 shows contour plots of the results of the LDA measurements.

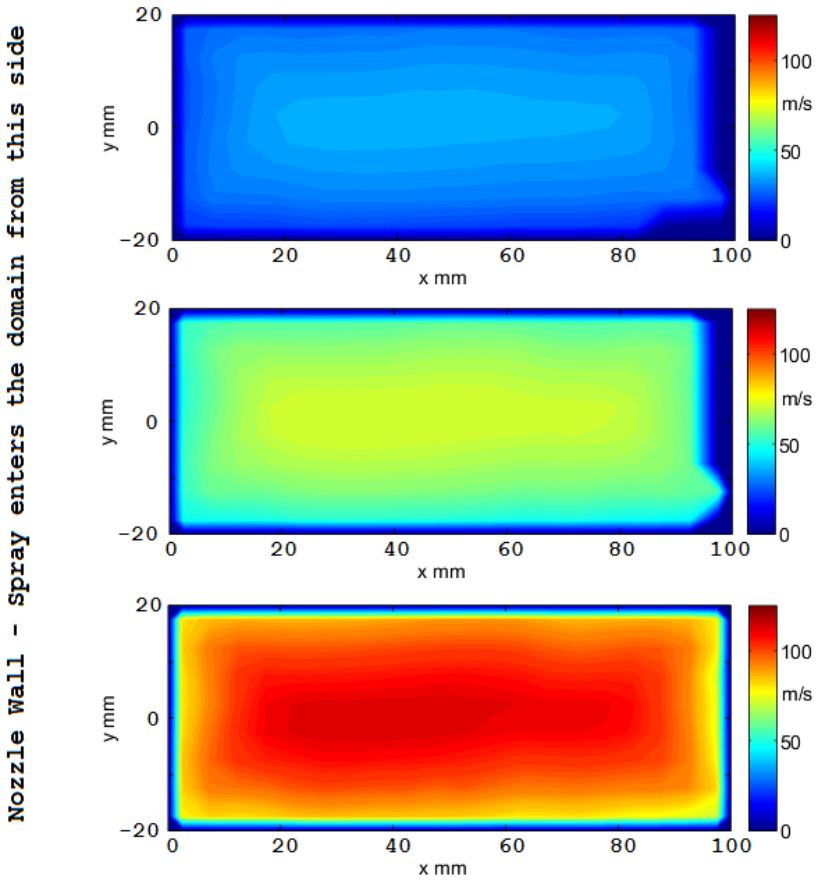

Figure 5.2: Local cross-airstream velocity (at: W_{mean} = 31; 61; and, 96 m/s)

Figure 5.3 shows in greater detail the variation in local cross-airstream velocity on the centre-line (y = 0 mm), i.e. the axis on which liquid was injected during the spray experiments.

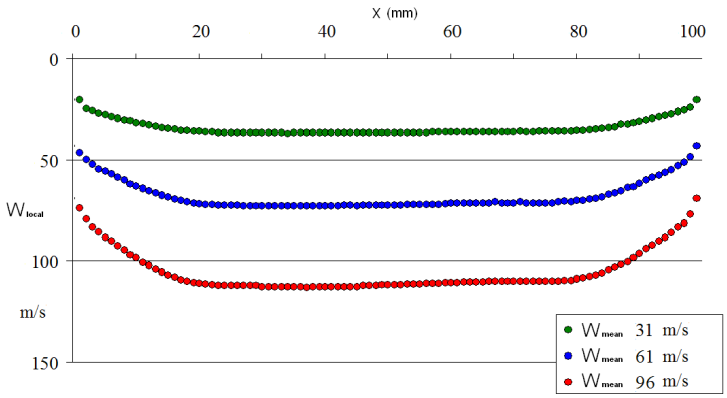

Figure 5.3: Centre-line local cross-airstream velocity

Figure 5.2 and Figure 5.3 show that the velocity profile maintained reasonably mirrored behaviour across all lines of symmetry, free from any unwanted bias.

Reduced Test Section Configuration

In the reduced test section configuration the maximum velocity of the cross-airstream that could be attained was approximately 200 m/s. LDA local velocity measurements were carried out at three different levels of bulk mean velocity: W_{mean} = 95 m/s; W_{mean} = 134 m/s; and, W_{mean} = 195 m/s - Figure 5.4 shows contour plots of the results from the LDA measurements.

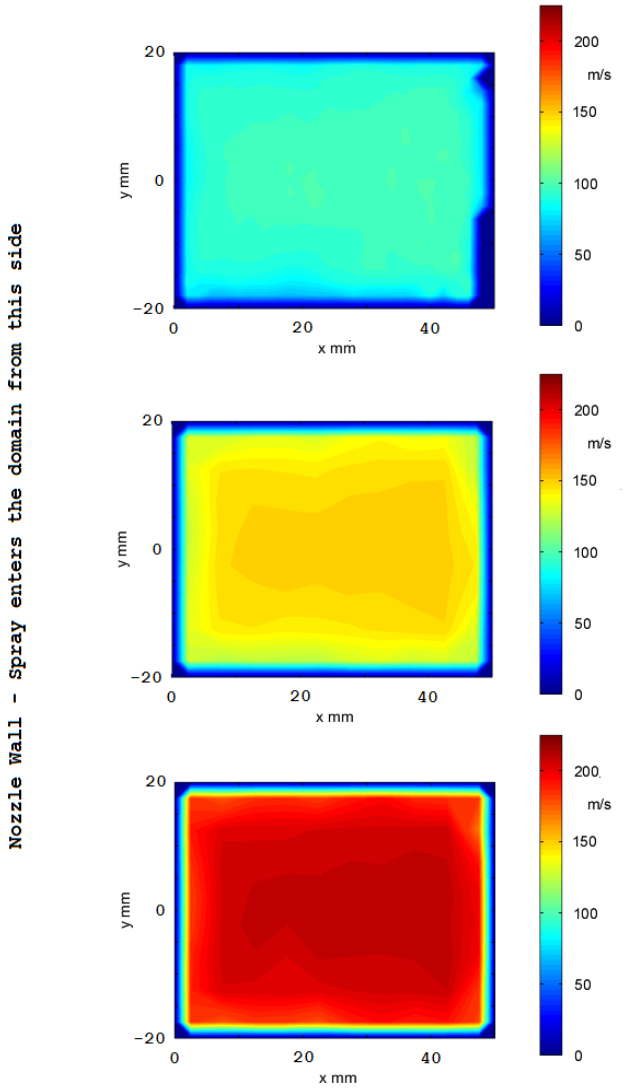

Figure 5.4: Local cross-airstream velocity, (W_{mean} = 95; 134; and, 195 m/s)

The contour plots show that the velocity profile maintains reasonably mirrored behaviour across all lines of symmetry. Figure 5.5 shows in greater detail the variation in local cross-airstream velocity on the centre-line (y = 0 mm), i.e. the axis on which liquid was injected during spray experiments.

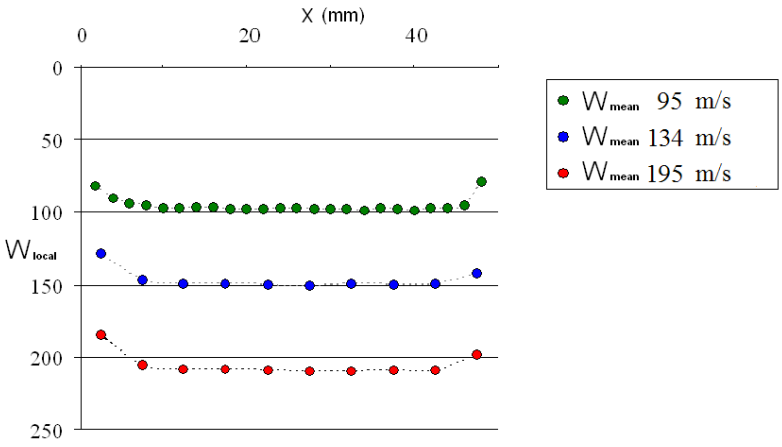

Figure 5.5: Centre-line local cross-flow velocity

The symmetry displayed by the measurements in Figure 5.5 show that the cross-airstream was well balanced and free from any unwanted bias.

5.1.2 Comparison with Bulk Cross-Airstream Velocity

To confirm the mean cross-airstream velocity calculated in the Labview routine, using the pressure differential across the Venturi nozzle, a numerical integration of the LDA results was carried out (a separate test from those shown above). The numerical integration of the local velocities across the complete cross-sectional plane gave W_{mean} = 90.95 m/s which compared to W_{mean} = 92.82 ± 3 m/s returned by Labview during the same test.

5.1.3 Free-stream Turbulence Intensity

The cross-airstream turbulence intensity was measured using a 1D hot-wire system. A mount for the hot-wire was constructed such that the hot-wire could be introduced into the flow using one of the test section's nozzle positions, as shown in Figure 5.6.

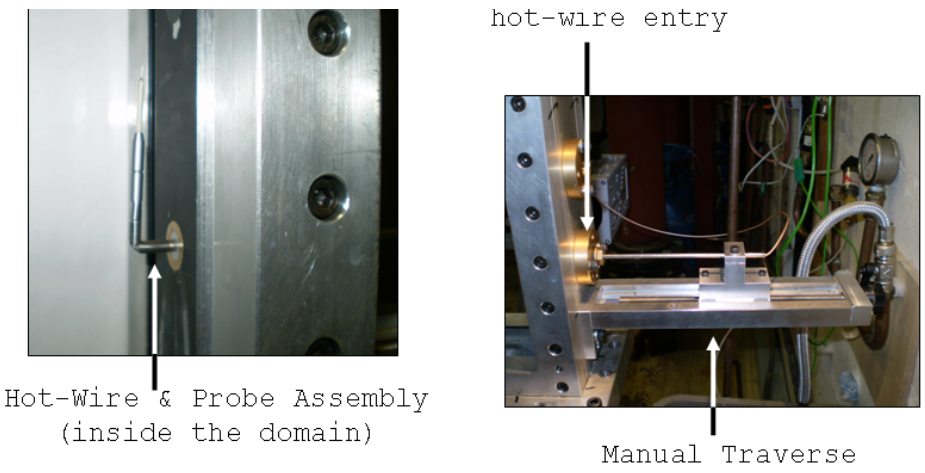

Figure 5.6: Hot-Wire mounting system

Because the LDA measurements already provided accurate local absolute velocities, the hot-wire did not need to measure the absolute amplitude of velocity accurately; only the periodic variation in local flow velocity. The hot wire could be calibrated 'in-situ' using the LDA velocity data as reference. This was a convenient approach as it negated the need to include density corrections (which are required where a hot-wire is calibrated using flows from fixed aperture nozzles at atmospheric pressures but, used to measure flows at pressures other than atmospheric).

The hot wire was traversed across the centre of the test section, y = 0 mm. Figure 5.7 plots the variation in turbulence intensity measured with distance from the nozzle wall where the bulk mean flow was of the order of 200 m/s.

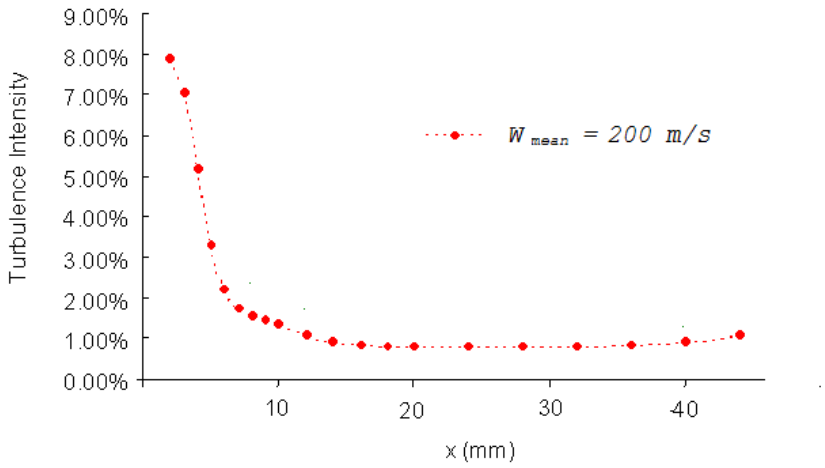

Figure 5.7: Local Turbulence Intensity (on the centre-line at 200 m/s)

Further results showed that the free-stream turbulence was of the order of 1% for all cross-airstream velocities.

5.2 Liquid Nozzle Flow Characteristics

This section starts with an introduction that describes how the liquid flow in the nozzle influences the spray-field and this is followed by an appraisal, as far as was possible, for the round and slot nozzles used in the experiments for this study.

The nozzle through which liquid is injected into the spray domain, incorporates features that influence how the spray develops. Primarily these features can be listed as:

1. Nozzle diameter (or cross-sectional area)
2. Nozzle length to diameter ratio
3. Nozzle inlet (radiused or sharp)
4. Nozzle shape (round, slot or other)

Nozzle Diameter (or cross-sectional area)
The size of the droplets in the downstream spray-field are proportional to the nozzle diameter, particularly at low Weber number conditions. When droplets form from a liquid jet through column break-up, their diameter is related to the diameter of the liquid column from which they came and, in turn, the diameter of the liquid column is proportional to the nozzle diameter from which it came.

Nozzle length to diameter ratio
The length to diameter ratio determines how developed the flow is at the nozzle outlet and whether or not the affects of cavitation are limited to within the nozzle or reach the nozzle exit.

Nozzle inlet (radiused or sharp)
The nozzle entry can be manufactured with a sharp edge or radiused to minimise separation and therefore the possibility of cavitation.

Nozzle shape (round, slot or other)
The shape of the nozzle determines the shape of the liquid continuum that

stems from the nozzle exit and engages with the cross-airstream. The shape of the liquid continuum, with respect to the confluent airstream, has a significant influence on the trajectory of the liquid and, consequently the final location of the spray as well as its the cross-sectional shape. Furthermore, the specific morphology of the confluent liquid/air flows, affects the intensity of the momentum exchange and, importantly, this can influence the distribution of droplet sizes within the spray-field. The subject of nozzle shape is of particular interest in this study which has examined results generated using a round nozzle as well as an aligned and perpendicular slot shaped nozzle.

The following sections report the findings of preliminary experiments that were conducted specifically in order to establish the discharge coefficient of the nozzles that were used in the main experiments. The discharge coefficients found, provide a parameter that can be used as a reference to predict the likely flow behaviour within each nozzle at different injection pressures, using the findings from **Ahn et al. (2006)** as a benchmark (as was reported in detail in subsection 2.5.2).

The following sections are split by nozzle type (and orientation for the slot nozzle), firstly the round nozzle flows are reported and this is followed by broadly similar sections that report the horizontally aligned slot nozzle and then the vertically aligned slot nozzle, i.e. as in Figure 5.8.

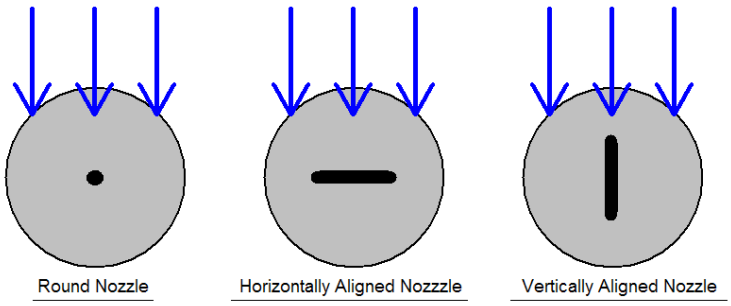

Figure 5.8: Nozzle orientations

5.2.1 Round Nozzle

The dimensions of the round nozzle are presented in Figure 5.9.

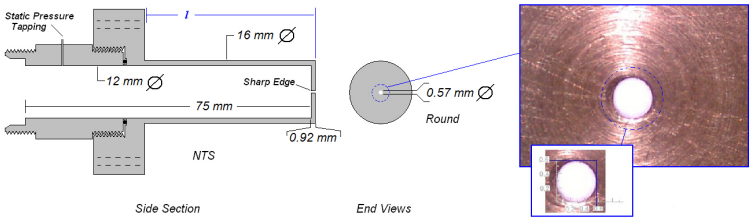

Figure 5.9: Round nozzle injector geometry and digital microscope image

An investigation was carried out to identify the discharge coefficient of the round nozzle, calculated using:

$$Cd = \frac{\bar{V}_{measured}}{A_{nozzle}\sqrt{\frac{2\left(P_{upstream}-P_{downstream}\right)}{\rho\left[1-A_{nozzle}/A_{upstream}\right]}}} \tag{5.1}$$

Figure 5.10 shows the variation of discharge coefficient (C_d) with pressure drop (Δp) across the round nozzle.

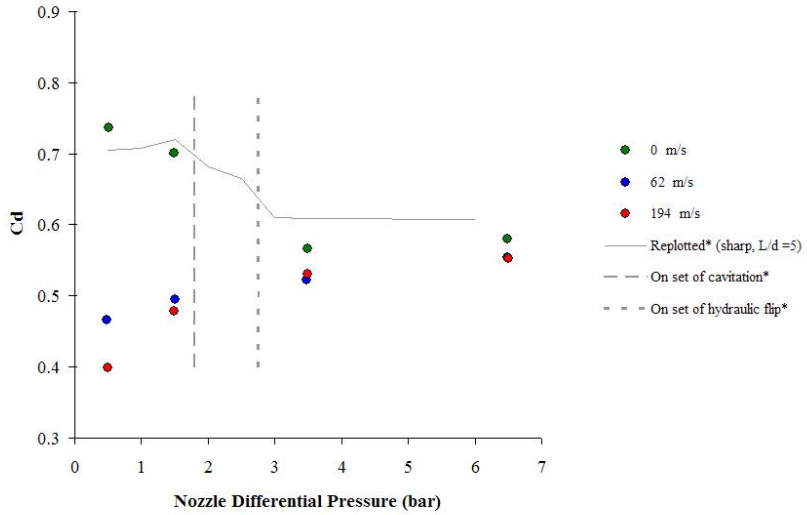

Figure 5.10: Variation of discharge coefficient with pressure differential at static, low and high speed cross-airstream velocity (*plotted with results from **Ahn et al. (2006)** at static condition)

Figure 5.10 presents the discharge coefficient measured at three separate values of cross-airstream velocity: W_{mean} = 0, 62 and 194 m/s.

When there is no cross-airstream, the reduction in discharge coefficient with increasing Δp in the range of $1.5 \leq \Delta p \leq 3.5$ bar indicates cavitation in the nozzle. The reduction in discharge coefficient occurs because of low pressure regions that form as a result of flow separation at the nozzle entry edge. Liquid in this low pressure region evaporates and forms a toroidal region of gas that inhibits the flow of liquid (downstream of the gaseous toroidal region the flow reattaches to the nozzle wall).

For larger values of pressure drop ($\Delta p = 3.5$ and 6.5 bar) the discharge coefficient exhibits very little variation with pressure drop *or* cross-airstream velocity and this indicates a *Hydraulically Flipped Nozzle*, where the liquid remains detached from the wall right up to the nozzle exit.

At the lower values of pressure drop ($\Delta p = 0.5$ and 1.5 bar) increasing the cross-airstream velocity causes a dramatic reduction in the discharge coefficient. This is due to the momentum of the cross-airstream providing a significant resistance to the injection of liquid into it. Figure 5.11 shows the results of a numerical model reported by **Herrmann (2009)**, the cross-airstream can be seen to affect the liquid flow upstream of the nozzle exit in the upper region of the nozzle passage.

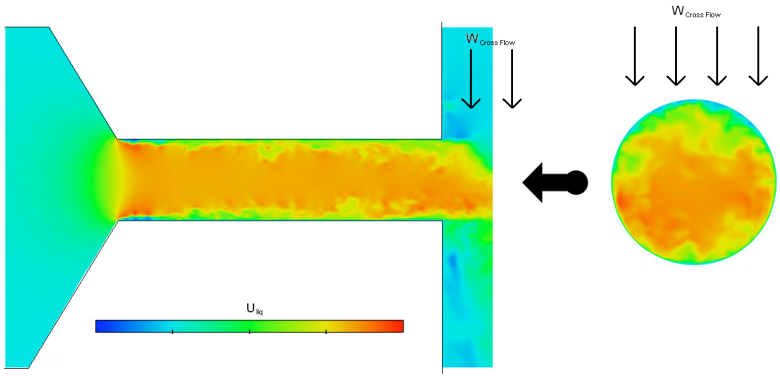

Figure 5.11: Liquid velocity distribution from jet atomisation modelling **Herrmann (2009)**

This numerical study was defined using boundary conditions within the range applicable for this study: liquid velocity of approximately 10 m/s (which approximately equates to a Δp of 1.25 bar for the round nozzle used in this study) and cross-airstream mean velocity of approximately 120 m/s ($q \approx 6.6$ and $We_g \approx 330$).

5.2.2 Horizontal Slot Nozzle

The slot nozzle was arranged such that the long dimension was perpendicular to the direction of the cross-airstream. A horizontally aligned slot maximises the drag experienced by the injected liquid from the cross-airstream and therefore minimises the spray penetration.

The dimensions of the slot nozzle are presented in Figure 5.12.

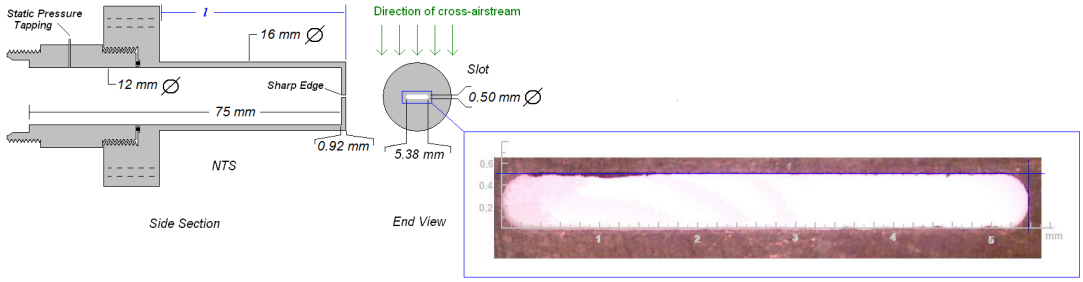

Figure 5.12: Slot nozzle injector geometry and digital microscope image

An investigation was carried out to identify the discharge coefficient of the horizontally aligned slot nozzle. The nozzle discharge coefficient was calculated using Equation 5.1. Figure 5.13 shows the variation of discharge coefficient (Cd) with pressure drop (Δp) across the nozzle.

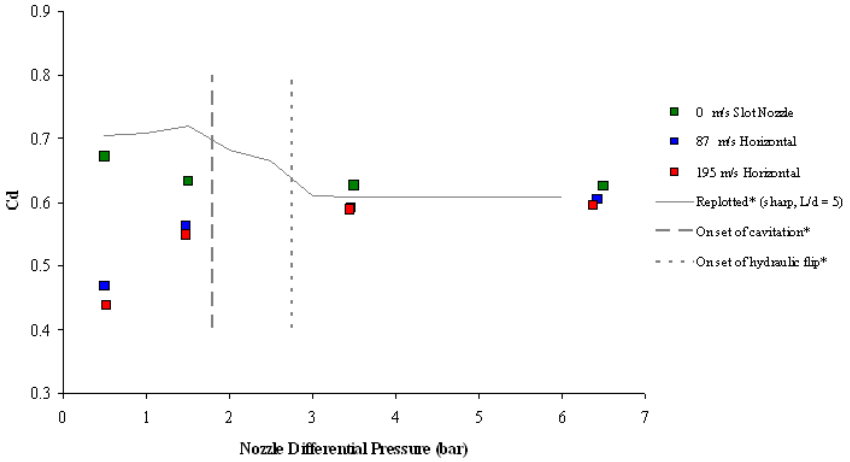

Figure 5.13: Variation of discharge coefficient with pressure differential at static, medium and high speed cross-airstream velocity, *plotted with results from **Ahn et al. (2006)**

For the slot nozzle, at the static cross-airstream condition, the discharge coefficient was approximately constant for Δp = 1.5, 3.5 and 6.5; at a level of 0.63. For a

round nozzle this would indicate a hydraulically flipped nozzle flow, however, given the very different geometry of the slot nozzle - the flow in the slot nozzle cannot be judged by reference to **Ahn et al (2006)**. The reason Ahn's round nozzle data has been plotted alongside the slot nozzle data is to show that the discharge coefficient does appear to follow the same pattern of behaviour, but, at lower differential pressure.

Figure 5.13 also presents two cross-airstream velocity conditions, W_{mean} = 87 and 195 m/s. For larger values of pressure drop (Δp = 3.5 and 6.5 bar) the discharge coefficient shows little variation with pressure drop and is relatively insensitive to the cross-airstream velocity. At lower values of pressure drop (Δp = 0.5 and 1.5 bar), increasing cross-airstream velocity causes a reduction in the discharge coefficient, this is consistent with the behaviour observed for the round nozzle.

5.2.3 Vertically Aligned Slot Nozzle Sprays

The dimensions of the slot nozzle are presented in Figure 5.12. The slot nozzle was arranged such that the long dimension was aligned with the direction of the cross-airstream. A vertically aligned slot minimises the drag experienced by the injected liquid from the cross-airstream and therefore maximises the spray penetration.

An investigation was carried out to identify the discharge coefficient of the vertically aligned slot nozzle. The nozzle discharge coefficient was calculated using Equation 5.1. Figure 5.14 shows the variation of discharge coefficient (Cd) with pressure drop (Δp) across the nozzle.

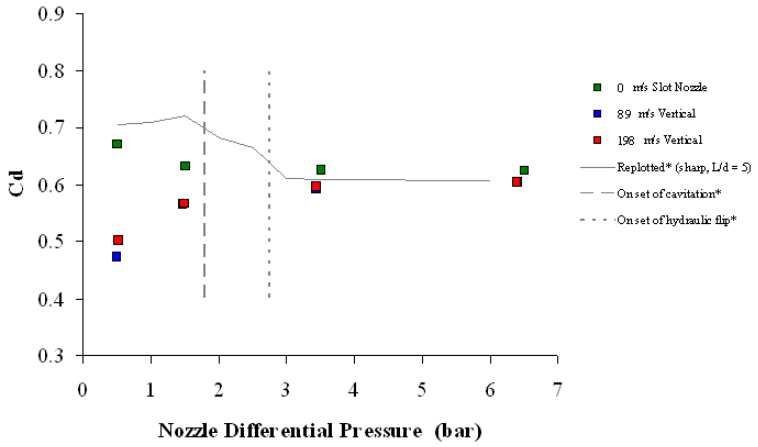

Figure 5.14: Variation of discharge coefficient with pressure differential at static, medium and high speed cross-airstream velocity, *plotted with results from **Ahn et al. (2006)**

The vertically aligned slot nozzle exhibited discharge coefficient levels very similar to those for the horizontally aligned slot. This suggests that the orientation of the slot nozzle had little effect on the nozzle flow. The resistance to the nozzle flow generated by the cross-airstream appears to remain consistent regardless of whether the emanating liquid was broad-side or thin-side.

5.3 Chapter Synopsis

This chapter detailed the cross-airstream velocity distribution, through an LDA assessment, and showed that the flow field was well balanced and free from unwanted bias. Hot-wire tests showed the free-stream turbulence of the bulk of the flow was of the order of 1%. This chapter reported on the nozzle discharge coefficients of the nozzles used in the spray characterisation experiments.

The following chapter presents the results and analysis of some preliminary tests which were completed using a round nozzle to confirm the operation of the TFMRC spray test and the capability of the PDPA system; as well as providing base case data set from a round nozzle.

Chapter 6

Preliminary Tests and Jet Stability

In order to carry out the experiments required in this study, a new test rig needed to be designed and built at the Thermo-Fluid Mechanics Research Centre. Prior to the execution of slot nozzle testing, which was the main aim of this study, a series of round nozzle ⇓⊙ tests were completed. This aspect of the work provided a base case data set and a means of assessing the performance of the new test facility against the extensive open literature for sprays in cross-airstreams from round nozzles. Table 6.1 shows the test conditions covered in the present study compared to previous studies.

Authors	We_g	q	d (mm)	L/d	Liquid
Present study	15 - 594	0.8 - 252	0.57	1.61	Water
Birouk et al. (2003)	1.6 - 14	15 - 284	1.0	not given	Aero engine oil
Becker & Hassa (2002)	360 - 2120	2 - 18	0.45	1.56	Jet-A
Wu et al. (1997)	71 - 1179	3.4 - 148	0.5, 1.0, 2.0	4	Various
Wu et al. (1998)	54 - 217	5.3 - 59	0.50	4	Water
Lubarsky et al. (2007)	33 - 2020	40	0.46	10	Various
Tambe et al. (2004)	51 - 248	0.9 - 10.2	0.38, 0.76	1.33/0.67	Various
Chen et al. (1993)	618 - 1121	3 - 45	0.76, 1.0	not given	Fuel

Table 6.1: Summary of experimental conditions for referenced investigations

This chapter presents the results from the round nozzle experiments and introduces how data is represented in the following main results chapter and, therefore, provides a prelude to it.

A notable feature of sprays in cross-airstreams is the unsteadiness exhibited by the liquid jet, often detectable with the naked eye. An examination of the mechanisms involved reveals that some jet unsteadiness appears to be inevitable. In

addition to presenting the round nozzle test results, this chapter concludes with a summary of the various possible causes of jet unsteadiness.

6.1 Analysis of the Liquid Jet

In order to assess the features of the liquid jet, high resolution images were obtained using a digital camera with a synchronised pulsed laser sheet. Tests were completed at twelve different conditions, listed in Table 6.2.

$$\mathrm{We}_g = \frac{\rho_g \, (W_g - W_l)^2 \, d_{noz}}{\sigma} \tag{6.1}$$

$$q = \frac{\rho_l \, U_l^2}{\rho_g \, W_g^2} \tag{6.2}$$

	$W_{mean} \approx 30$ m/s	$W_{mean} \approx 60$ m/s	$W_{mean} \approx 90$ m/s
Δp $\approx$ 0.5 bar	15 (23)	54 (8.6)	123 (2.8)
Δp $\approx$ 1.5 bar	15 (56)	54 (22)	123 (7.1)
Δp $\approx$ 3.5 bar	15 (129)	54 (35)	123 (16)
Δp $\approx$ 6.5 bar	15 (252)	54 (68)	123 (31)

Table 6.2: $\overset{\Downarrow}{\odot}$ Pulsed laser sheet imaging average test conditions, We_g (q)

At the higher levels of cross-airstream velocity (e.g. W_{mean} = 90 m/s) the corresponding level of surface stripping obscures the detail of the liquid jet. These tests were completed with the test section in the full working section configuration (i.e. the insert used for higher velocity airstreams was not used). This maximises the space available and allowed for long liquid jets traversing considerable distances, in excess of 100 diameters.

For each condition indicated in Table 6.2, 30 images were obtained. A sample of this data is shown in Figure 6.1 with colours inversed for clarity - the injection point can be seen towards the top left hand side.

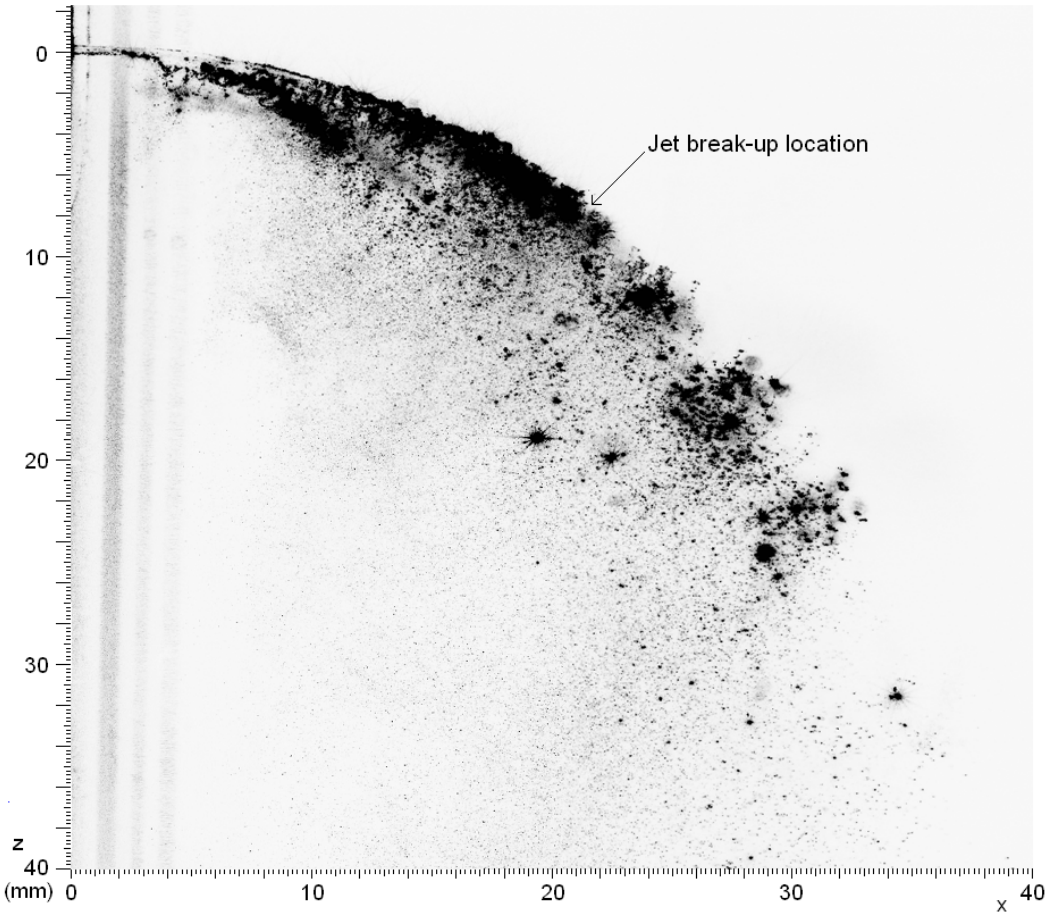

Figure 6.1: ⇊⊙ Pulsed laser image; at y = 0; for Δp = 3.5 bar, W_{mean} = 61 m/s, We_g = 54 and q = 35

Viewing the 30 images in succession for each condition, showed variation in both jet trajectory and break-up length. The cause of this variation *or jet unsteadiness* is not entirely clear. There are several potential causes which are summarised at the end of this chapter.

Jet Break-up Location

The point at which the liquid jet disintegrates, *jet break-up location*, was defined by the respective transverse and axial coordinates x_b and z_b. The estimated break-up location was determined by the point where the light intensity became indicative of ligaments, rather than the continuum of the jet, as highlighted in Figure 6.1.

The break-up location is reasonably evident in some images but more difficult to identify in others. The estimated break-up location for each condition was taken as the mean from four randomly selected images, from the 30 available images. The manual process for determining the point judged to be the jet's

final break-up has an inherent spread which is estimated to be of the order of 2 mm in both x and z directions.

Because the transition from jet to ligaments is subtle, an automated Matlab interrogation routine that reliably picked out the location of final break-up would be difficult to compile; and this was not considered necessary since this does not represent a significant aspect within the wider aims of this study. The jet break-up location results were primarily used to compare the performance of the new test facility with previous studies from other laboratories.

Figures 6.2 and 6.3 show the variation of transverse and axial jet break-up location with momentum flux ratio for the twelve test cases defined in Table 6.2.

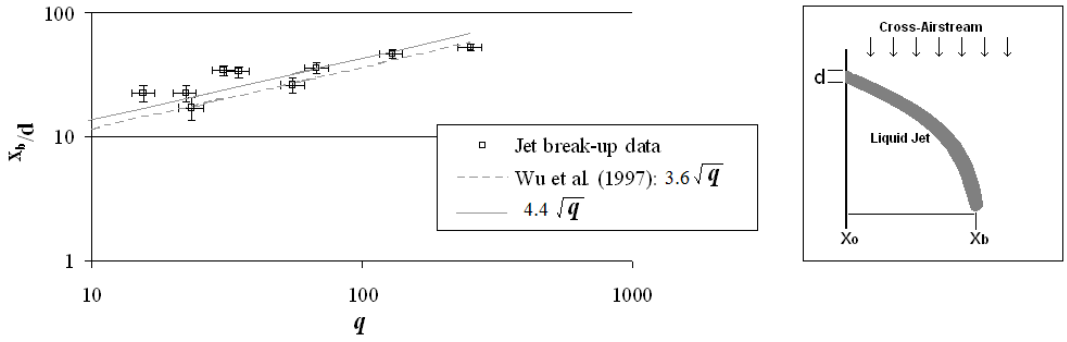

Figure 6.2: ⇓⊙ Transverse liquid jet break-up length; for all test cases (error bars:q ± 9.48%, x_b ± 2 mm)

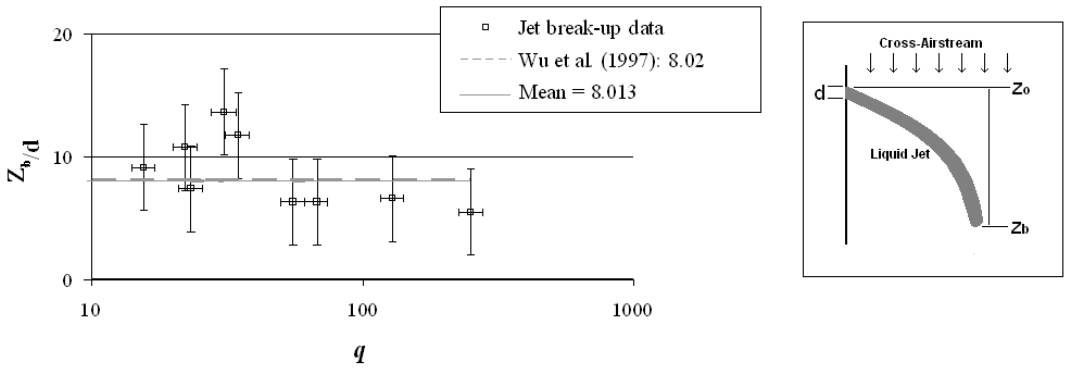

Figure 6.3: ⇓⊙ Transverse liquid jet break-up length; for all test cases (error bars:q ± 9.48%, z_b ± 2 mm)

In Figure 6.2, the transverse location of the break-up point, x_b, is shown to increase with increasing q on a log-log scale. This is because higher q means

a relatively higher liquid momentum and the liquid jet penetrates further into the cross-airstream. The plot of transverse break-up location x_b identifies that the jet break-up in this study was longer than that described in **Wu et al. (1997)**. This difference is believed to be primarily due to the difference in boundary conditions, which gave a reduced cross-airstream velocity over the initial part of the jet. However, turbulence of the water jet, nozzle design and location definition may also be factors. This data yielded a correlation for transverse jet break-up as given in Equation 6.3.

$$x_b/d = 4.4\sqrt{q} \tag{6.3}$$

Where: $15 < We_g < 124$ *and* $2.8 < q < 252$

In contrast the axial location of the break-up point, z_b, is unaffected by q, as shown by Figure 6.3 on a linear-log scale. Although there is a significant spread of data (maximum and minimum values of z_b/d = 13.7 and 4.9), the mean axial break-up was z_{bmean} = 8.02 which is comparable to **Wu et al. (1997)** which reported z_{bmean} = 8.01.

Figure 6.4 is a photographic map of the liquid jet trajectory for the conditions featured in Table 6.2.

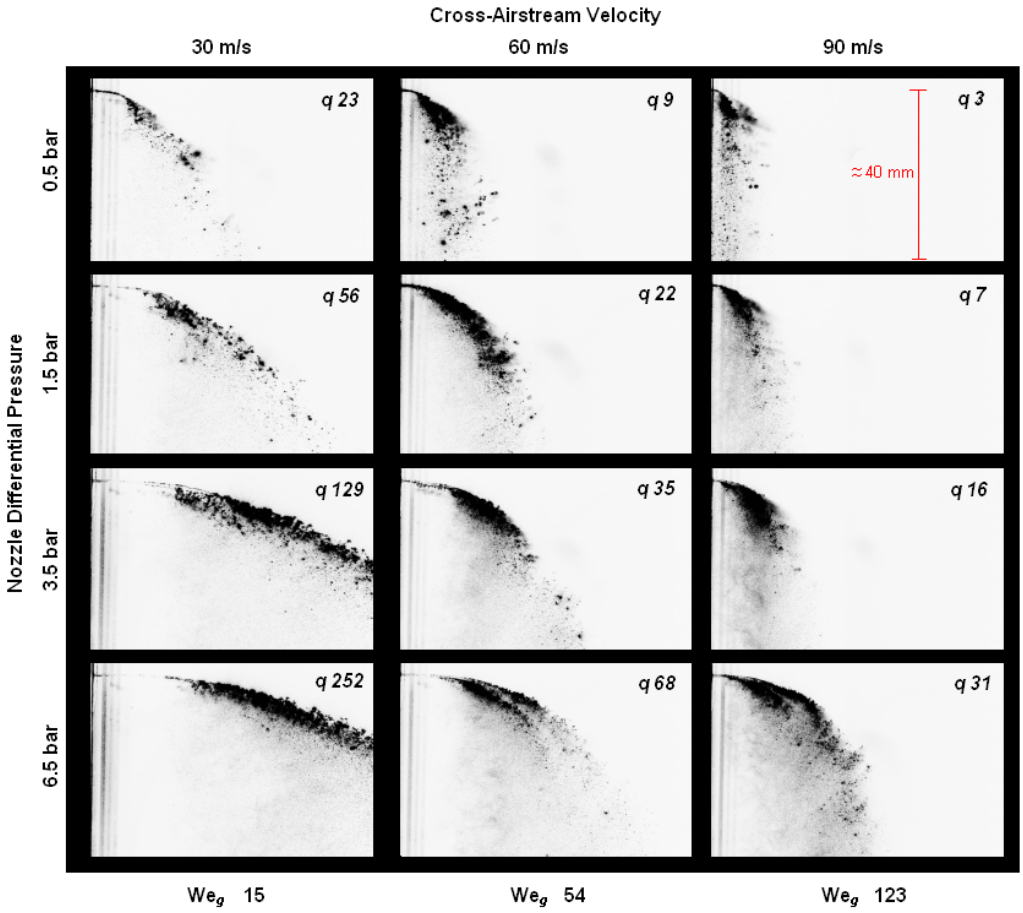

Figure 6.4: ⊙⇊ Pulsed laser sheet imaging map of conditions; at $y = 0$; for all test cases

The relative influence of pressure drop across the nozzle and cross-airstream velocity are clearly seen in Figure 6.4. For example:

- for constant W_{mean}, increasing pressure differential causes the jet to penetrate further into the test section; and,
- for constant Δp, increasing the cross-airstream velocity reduces the extent of the jet penetration.

Although difficult to see in these reduced size images, inspection does reveal that the transverse location of the break-up point, x_b, increases with Δp (i.e. increasing q) and decreases with increasing W (i.e. decreasing q). However, there is little change in z_b with these parameters.

Jet Trajectory

The path followed by the liquid jet, *jet trajectory*, was traced from the pulsed laser and CCD camera images, using the uppermost surface. The mean of the

results from four images was used to determine the trajectory associated with a particular condition. Figure 6.5 shows the results of the jet trajectory analysis for all of the acquired data.

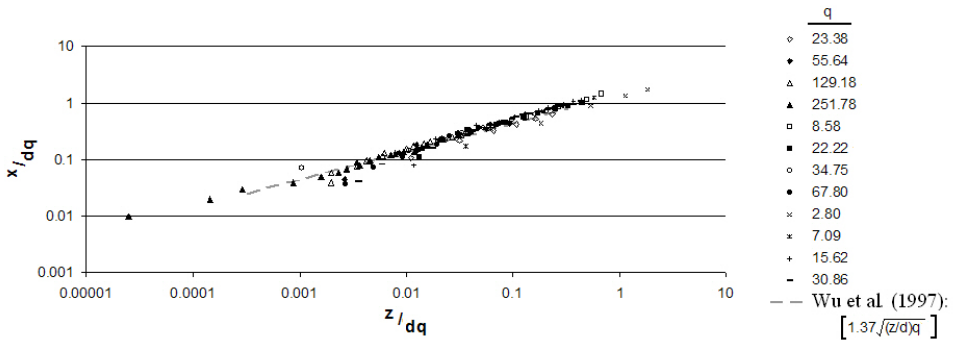

Figure 6.5: ⇓ ⊙ Jet trajectory analysis; at $y = 0$; for $15 < We_g < 124$ *and* $2.8 < q < 252$

Figure 6.5 plots the variation in the penetration of the jet (x) with axial distance downstream (z). The axes were normalised using the nozzle diameter multiplied by the momentum flux ratio. As can be seen, the data tends to a single result demonstrating that momentum flux ratio and nozzle diameter have a controlling influence on the jet's trajectory. The units chosen for the axes in Figure 6.5 were established in **Wu et al. (1997)**. The corresponding correlation from Wu's results has been added to the plot and displays close agreement with the current data. In the current study there was a relatively thick cross-airstream boundary condition and this resulted in a slightly increased transverse jet break-up distance (x_b) compared to **Wu et al. (1997)**. The reason the same discrepancy is not depicted in Figure 6.5 is believed to be because Wu used the centre-line of the liquid jet, rather than the uppermost edge which was used in this analysis.

In conclusion the liquid jet break-up and liquid jet trajectory produced results which met with expectations with reference to **Wu et al. (1997)**. Whilst this work was conducted primarily to underwrite the performance of the TFMRC spray observation test facility, it also provides useful affirmation of previous work.

This chapter continues with an examination of the downstream spray field effects from the round nozzle.

6.2 Round Nozzle Spray Droplet Analysis

A total of twelve PDPA spray characterisation experiments were conducted. Their corresponding test conditions are presented in Table 6.3.

	$W_{mean} \approx$ **90 m/s**	$W_{mean} \approx$ **135 m/s**	$W_{mean} \approx$ **195 m/s**
Δ**p** ≈ **0.5 bar**	Case 1: 118 (2.5)	Case 5: 275 (1.6)	Case 9: 594 (0.8)
Δ**p** ≈ **1.5 bar**	Case 2: 118 (7.1)	Case 6: 276 (3.0)	Case 10: 586 (2.2)
Δ**p** ≈ **3.5 bar**	Case 3: 117 (16)	Case 7: 276 (6.7)	Case 11: 580 (3.3)
Δ**p** ≈ **6.5 bar**	Case 4: 118 (30)	Case 8: 277 (13)	Case 12: 580 (6.5)

Table 6.3: ⇓⊙ PDPA average test conditions We_g (q)

The following subsection is a short introduction which defines the characteristics of a typical spray to provide a foundation understanding, before more complex relationships between the spray characteristics and changing experimental conditions are discussed.

6.2.1 Introduction to Spray Data

Using Case 7 from Table 6.3 as an example, this introduction steps through the measured droplet characteristics and sizes, and discusses how they relate to the flow physics of the spray field.

Figure 6.6 is a contour plot of the axial velocity (W_{drop}) of the droplets in Case 7 at the z = 40 mm plane.

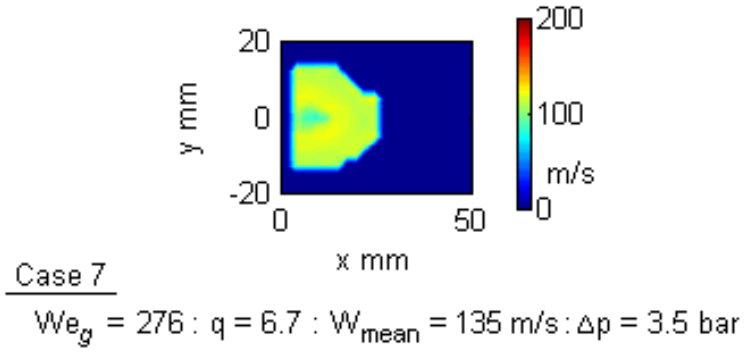

Figure 6.6: ⇓⊙ Variation of axial droplet velocity W_{drop} with cross-sectional location; at the z = 40 mm plane; for We_g = 276 and q = 6.7 (Case 7)

The spray enters the test section at the point $x = y = z = 0$ mm and the cross section displayed by Figure 6.6 is at $z = 40$ mm. Hence, Figure 6.6 shows the cross-sectional variation in the axial component of velocity attained by the droplets (from being accelerated by the cross-airstream) at 40 mm downstream of the injection point.

The axial velocity can be seen to vary over the section of the spray. The most conspicuous variance is the central region of slower moving droplets, as highlighted in in Figure 6.6 below. This region of retarded velocities results from the blockage created by the liquid body which emanates from the injector and combined mass of the spray core leading to what is described as a wake region.

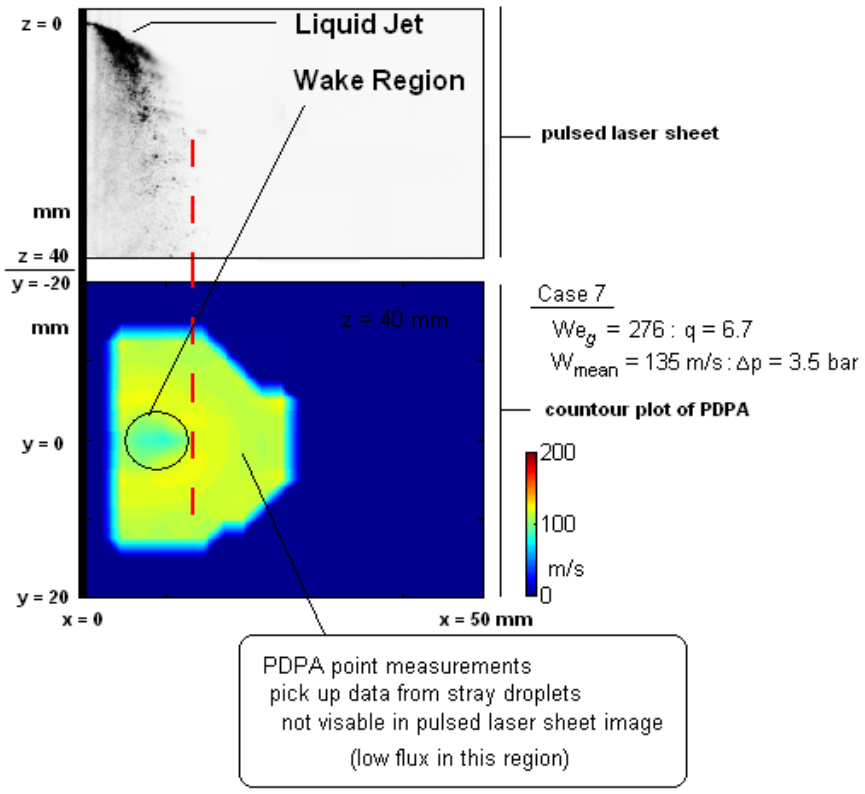

Figure 6.7: ⇊ ⊙ Pulsed laser sheet image and PDPA data comparison; at $z = 40$ mm; for $We_g \approx 276$ and $q \approx 6.7$ (Case 7)

The reason the wake region is associated with spray core density as well as the liquid jet, is because it can be seen at $x = 4$ mm between $y = -5$ to 5 mm (over which the liquid jet passes) the droplet's axial velocities are more consistent with droplets in the spray's general periphery rather than those in the wake region.

Figure 6.6 displays (as would be expected) a reasonable degree of symmetry

of the spray field about the $y = 0$ mm axis. It can also be seen that the spray penetrates to $x = 25$ mm; which is greater than would be expected from **Wu et al. (1998)** findings for spray penetration limit Equation 2.19:

$$x_{limit} = 0.57\left(4.3\,(7)^{0.33}\left(\frac{40}{0.57}\right)^{0.33}\right) = 19 \text{ mm} \tag{6.4}$$

Spray flux drops rapidly away from the spray's core region (**Inamura et al. (1997)** reported 70% of the liquid mass contained within 25% of the wet cross sectional area), therefore, the droplets represented by PDPA measurements in spray's periphery were based on relatively few droplet incidents. Data is obtained becuase the PDPA measurement volume pauses in each location for a finite period, accruing data as-and-when droplets pass through; as a result PDPA produces results from 'stray' droplets which were not captured in the image based measurements. The spray penetration displayed in the image based measurements were in reasonable agreement with Equation 6.4.

Figure 6.8 is a contour plot of the droplet transverse component of velocity (U_{drop}), again from Case 7.

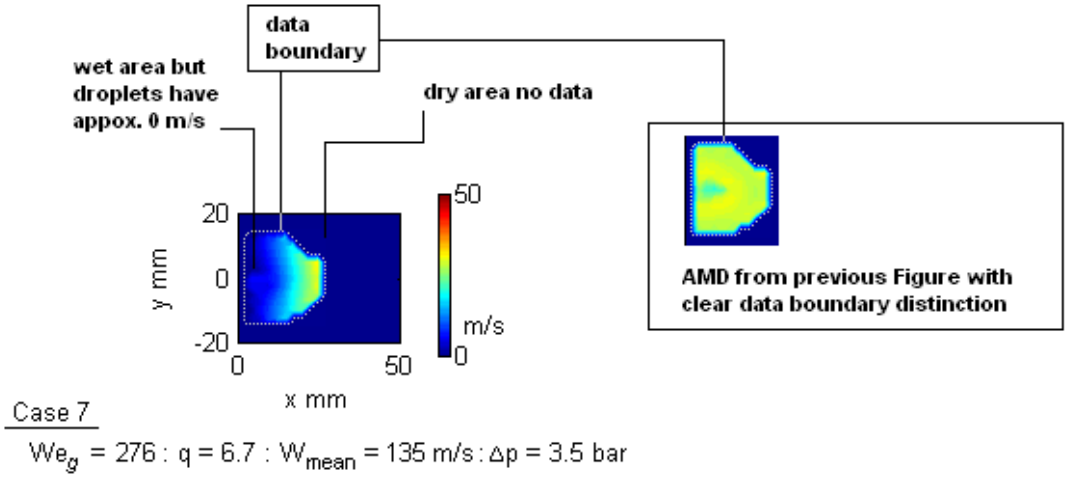

Figure 6.8: ⇓⊙Variation of transverse droplet velocity U_{drop} with cross-sectional location; at the $z = 40$ mm plane; for $We_g = 276$ and $q = 6.7$ (Case 7)

The first thing to note regards the style adopted for the contour plots used throughout this thesis, the background of the plots was set to the same colour as a zero measurement. This provides a neat appearance for the contour plots and is preferable to having a separate colour for the background but, it is important to recognise the difference between zero readings and dry areas.

With familiarity it becomes reasonably obvious where the data boundary is and from understanding that there are **never** dry areas anywhere within the **data boundary**. Hence, a dark blue pixel inside the data boundary represents a low or zero measurement and outside the data boundary a dark blue pixel depicts the area is dry. Figure 6.8 is a good example of this, where it is not immediately obvious where the data boundary is because zero readings and the data boundary coincide. However, referencing a contour plot of the AMD droplet property (for the same droplets) shows the data boundary more clearly and, with this in mind, one can see that there are droplets near the nozzle wall in Figure 6.8 but, they have ≈ zero transverse velocity. For the most part, where contour plots are presented in this thesis, they are done so side-by-side with the corresponding droplet properties and cross-referencing to locate the data boundary is simply a case of looking at an adjacent plot.

Figure 6.8 shows the cross-sectional variation in transverse velocity the droplets retained, 40 mm downstream of the injection point. The droplets transverse component of velocity results from transverse deceleration, as the original transverse momentum (the liquid had at the exit of the nozzle) is overpowered by the cross-airstream momentum - *a momentum exchange*. Hence the droplets lose transverse velocity and gain axial velocity with increasing z.

The left-to-right stratification shown in Figure 6.8, is a result of larger droplets breaking-away from the liquid jet with greater momentum due to their greater mass.

Figure 6.9 shows the distribution of droplet size in AMD [D_{10}] across the same cross section.

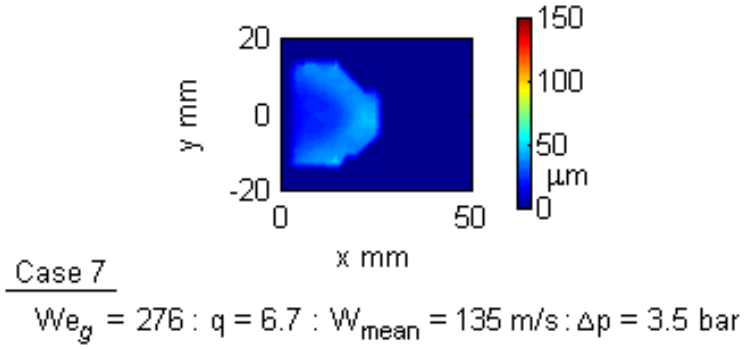

Figure 6.9: ⇓ ⊙ Variation of arithmetic mean diameter AMD [D_{10}] with cross-sectional location; at the z = 40 mm plane; for We$_g$ = 276 and q = 6.7 (Case 7)

The AMD [D_{10}] value across the section is reasonable constant, in Figure 6.9, at We_g = 276. The dynamic forces imposed by the cross-airstream on the liquid compared to its surface tension force mean that droplet size tends to a low value throughout the spray.

Lubarsky et al. (2007) tested over a wide range of Weber number, their test conditions were quite different to this study, nevertheless, their data (in Figure 6.10) is useful to demonstrate that droplet size collapsed towards a minimum value as Weber number increased.

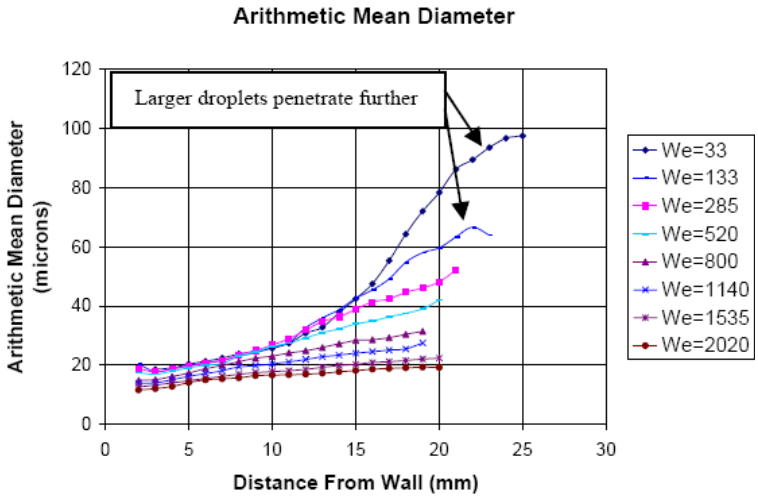

Figure 6.10: ⇓⊙ Variation of arithmetic mean diameter AMD [D_{10}] at x = 0 to 30 mm y = 0, z = 30 mm from **Lubarsky et al. (2007)**

The variation in droplet diameter is more evident at lower levels of Weber number, for example, Figure 6.11 shows the AMD [D_{10}] distribution at We_g = 118 (Case 2).

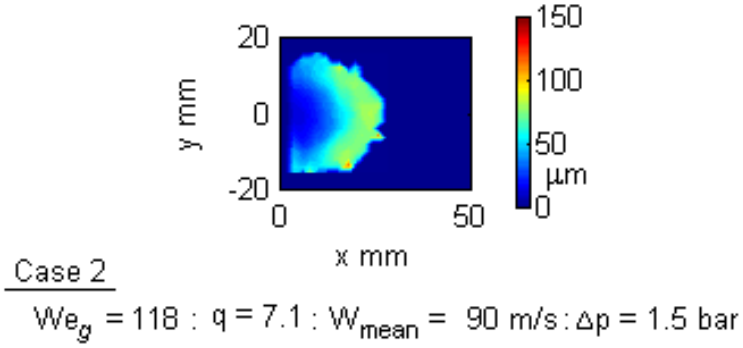

Figure 6.11: ⇓⊙ Variation of arithmetic mean diameter AMD [D_{10}] with cross-sectional location; at the z = 40 mm plane; for We_g = 118 and q = 6.7 (Case 7)

Comparing the left-to-right stratification in Figure 6.8 with Figure 6.11 shows the proportional relationship between U_{drop} and AMD [D_{10}] , albeit they are at different Weber number magnitudes.

This basic introduction to the spray data has described the general structure of a typical spray field. Spray behaviour is most sensitive to We_g and q, in order to assess each's influence it is useful to hold the other constant. Correspondingly, the following analysis is presented in two ways:

- As a Weber number analysis holding momentum flux ratio constant; and,
- As a momentum flux ratio analysis holding Weber number constant.

6.2.2 Weber Number Analysis (Constant q)

Responses of the spray behaviour with variations in We_g are more clearly observed at constant q because spray behaviour is sensitive to q. In these test results, variations in We_g are brought about by variations in cross-airstream velocity W_{mean} (i.e. the liquid *and* air flow rates vary but, the momentum balance between them (q) remains constant). From Table 6.3 it can be seen that two sets of constant q could be used:

1. Cases 1, 6 and 11, $q \approx 3$; and,
2. Cases 2, 7 and 12, $q \approx 6.7$.

This subsection uses the results from Cases 2, 7 and 12. Figure 6.12 shows the distribution of: (a) droplet axial component of velocity; (b) droplet transverse component of velocity; and, (c) droplet diameter in AMD [D_{10}] .

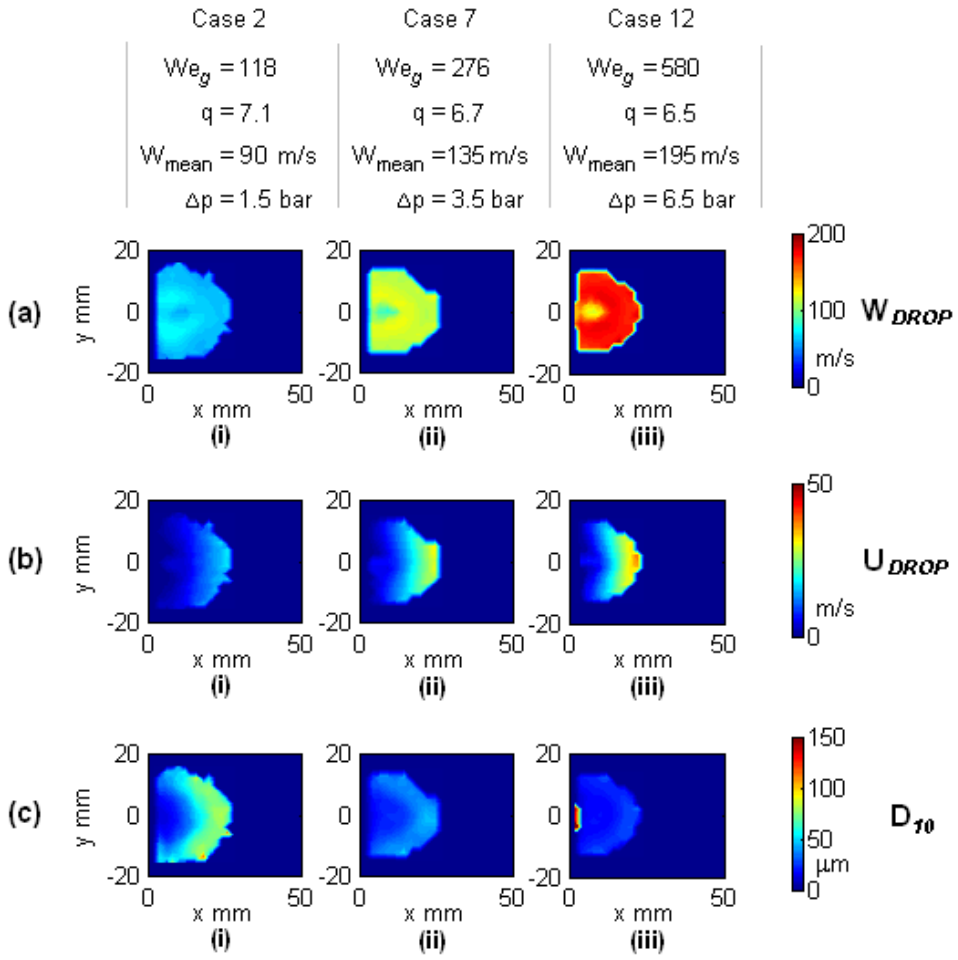

Figure 6.12: ⇊ ⊙ Contour plots of (a) W_{drop}, (b) U_{drop} and (c) AMD [D_{10}] ; at z = 40 mm plane; for We$_g$ = 118, 276 & 580 and constant $q \approx 7$

The plots represent droplets at the z = 40 mm plane; at three We$_g$ levels; and, constant $q \approx 7$. The general increase in U_{drop} *and* W_{drop} (in Cases 2, 7 and 12 respectively) are a result of the associated increases in both the air *and* liquid flow rates.

There is little variation in spray penetration or spread between these three cases. It is noteworthy that a similar spray shape occurs even though in Case 2 the liquid flow rate is less than half of that in Case 12 (0.157 and 0.322 *l*/min respectively). This demonstrates that spray penetration scales with q.

The influence on droplet AMD [D_{10}] from the variation in We$_g$ is evident across the three plots c-i, c-ii and c-iii. The largest AMD [D_{10}] values are at We$_g$ = 118 (Case 2). AMD [D_{10}] is reduced in Cases 7 and 12 where We$_g$ = 276 and 580 respectively (as would be expected from Figure 6.10). There is not much difference between We$_g$ = 276 to 580, this is because droplet size tends to a minimum value as shear break-up dominates, as was illustrated in Figure 2.1.

Apart from the fact that low We_g leads to generally larger droplets, on close inspection it is also apparent that a greater *range* of droplet size is exhibited. The range of droplet sizes recorded for all the test cases is shown in Figure 6.13.

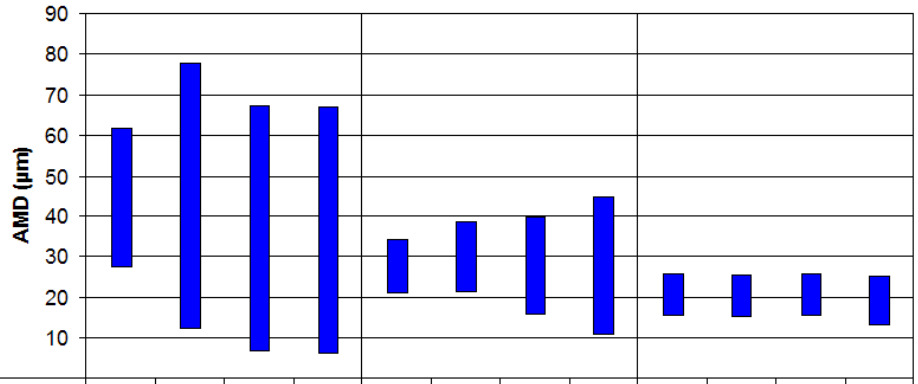

Case no.	1	2	3	4	5	6	7	8	9	10	11	12
q	2.5	7.1	16	30	1.6	3.0	6.7	13	0.8	2.2	3.3	6.5
We_g	118				276				586			

Figure 6.13: ⇊⊙ Droplet size range; at z = 40 mm; for all test cases

For the four cases at We_g = 118, a smaller range of AMD [D_{10}] was measured where q = 2.5 than where q = 7.1, 16 and 30. Equation 2.17 shows that increasing q promotes surface break-up which leads to smaller droplets being produced, as is seen for We_g = 118 in Figure 6.13.

At We_g = 276, again the droplet size lower limit decreases from 22 to 12 μm as q increases from 1.6 to 13 respectively. However there also appears to be a trend for the upper limit to increase (i.e. from 35 to 45 μm across the four cases), it is not clear why this was.

In Cases 9 to 12 where $We_g \approx 587$, the cross-airstream velocity dominates the break-up process and, as a result, there is little variation in droplet size, with a range of 15 to 25 μm measured for q = 0.8, 2.2, 3.3 and 6.5.

Figure 6.12 row (c) showed the distribution of AMD [D_{10}] over a complete cross-sectional plane. Figure 6.14 is a line plot using the same data but, only showing the centre-line distributions.

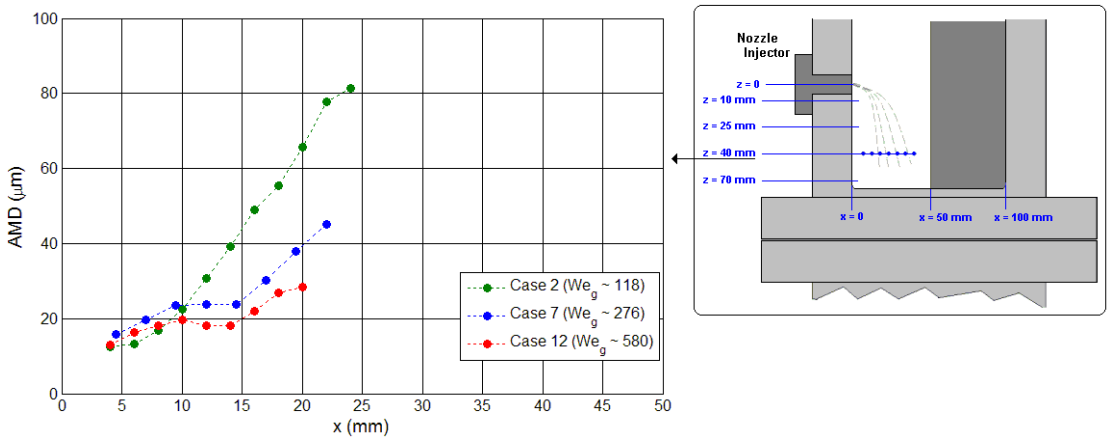

Figure 6.14: ⇓⊙ Variation of centre-line AMD [D_{10}] with distance from the nozzle wall; at x = 0 to 50 mm, y = 0 mm, z = 40 mm; for We$_g$ = 118, 276 & 580 and nominally constant $q \approx 6.7$ (Cases 2, 7 and 12)

The increase in AMD [D_{10}] with distance from the nozzle wall for We$_g$ = 118 and 276 (Cases 7 and 12) exhibit inflections in the general trend between x = 10 to 15 mm. **Wu et al. (1998)** also found this inflection behaviour but, at low levels of q, as shown in Figure 6.15 (c), for q = 9.5.

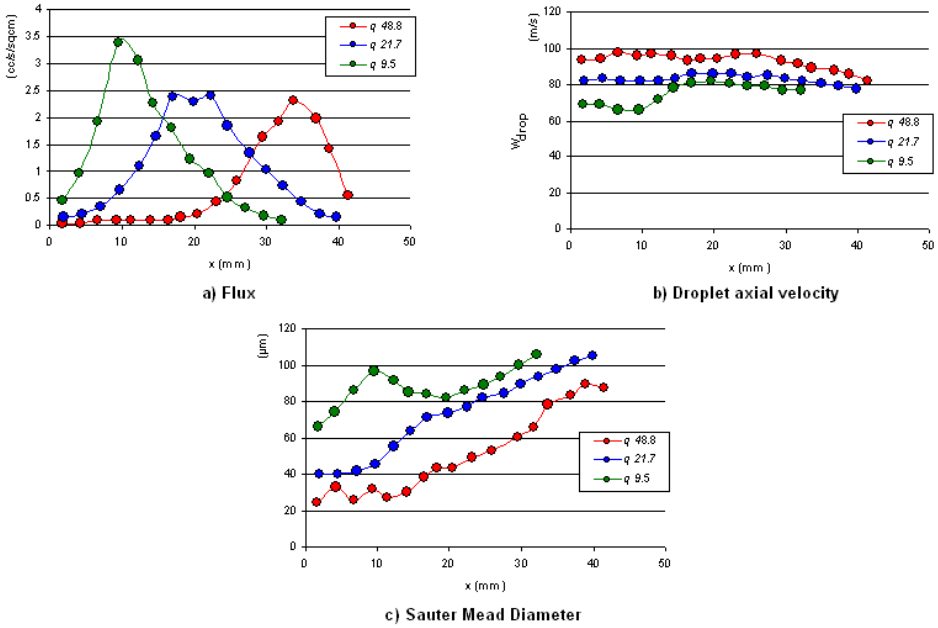

Figure 6.15: ⇓⊙ Plots of flux, W_{drop} and SMD replotted from **Wu et al. (1998)**; at x = 0 to 50 mm, y = 0 mm & z = 150 mm; for q = 48.8, 21.7 & 9.5, W_{mean} = 103 m/s, d$_{noz}$ = 0.5 mm and water injectant

In general, droplets break away from the liquid body with transverse momentum proportional to their mass, with the result of droplet size increasing away

from the nozzle wall, as illustrated in Figure 6.16.

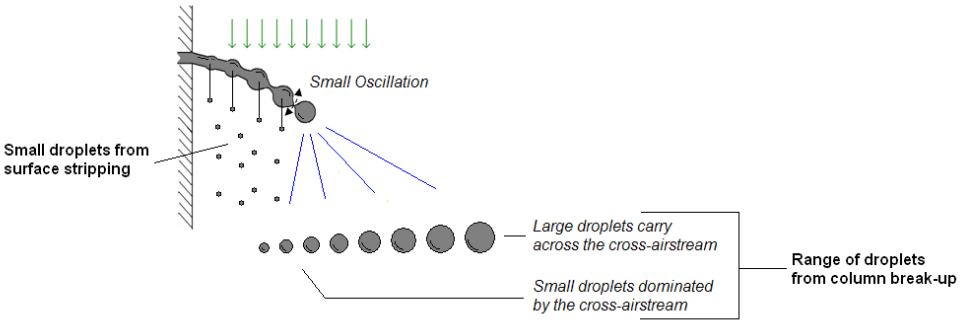

Figure 6.16: General droplet size distribution

Figure 6.16 shows the general principle for droplet size distribution applicable to sprays in cross-airstreams. For the conditions tested in this study there is always at least an underlying trend of droplet size increasing away from the nozzle wall corresponding to the illustration above. However, other factors can contribute to the droplet size trend away from the nozzle wall and, as a result, the basic distribution described above can have additional features, such as Wu's inflected trend in Figure 6.15 (c).

Wu associated his inflected trend with low q conditions, however, the trends in Figure 6.14 are all at similar q but, in Case 2 it is clear that no inflection occurred - with AMD [D_{10}] steadily increasing across the spray field. The three trends at $q \approx 6.7$, in Figure 6.14 suggest that an inflection, cannot be predicted by q alone.

Low q conditions generally create a relatively dense spray, because the low liquid momentum restricts the dispersion of the injected liquid and, as a result, the liquid tends to be confined to a small cross-sectional area. The more dense the spray-field is, the more intense the blockage is to the cross-airstream and the more significant the wake region.

Respectively, Cases 2, 7 and 12 in Figure 6.14 represent increasingly dense sprays, due to the increase in liquid flow rate in-conjunction with constant spray penetration. The more dense sprays give rise to a more significant wake region (as can be identified in row a in Figure 6.12) and the droplet AMD [D_{10}] inflection appears to result from this rather than low momentum flux ratio *per se*.

Figure 6.17 below plots Wu's data for flux, W_{drop} and droplet size for his inflected case where $q = 9.5$, the data has been normalised to allow each trend to be plotted together.

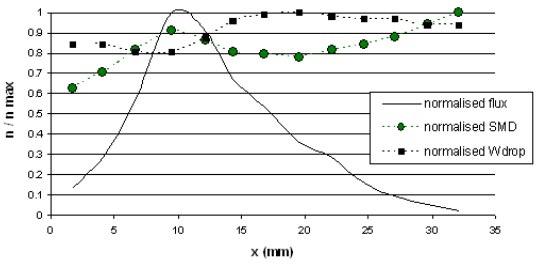

Figure 6.17: ⇊⊙ Plots of flux, W_{drop} and SMD replotted from **Wu et al. (1998)**; at x = 0 to 50 mm, y = 0 mm & z = 150 mm; for q = 9.5

It can be seen in Wu's data that the peak in flux (i.e. the spray core) was located at $x \approx 10$ mm and, this coincided with the initial peak in droplet diameter. Hence, the droplet size and flux peaked together where the droplet size distribution exhibited an inflection. It can also be seen that where droplet size peaked, W_{drop} was a minimum, the lower droplet velocities are indicative of lower cross-airstream velocity in the wake region and, therefore, the increased droplet size in this location could be due to low local Weber number, as illustrated in Figure 6.18.

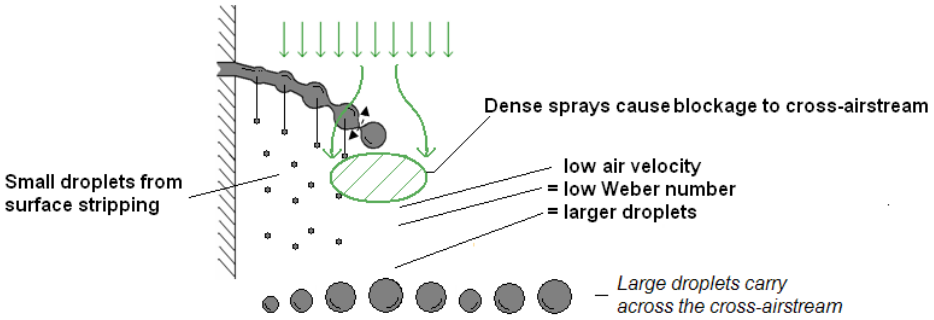

Figure 6.18: General droplet size distribution

Hence, a conclusion of this analysis is that inflections in the general droplet size trend are caused by spray core density rather than low q specifically. This section has examined the round nozzle data with respect to changes in Weber number, the following section examines the round nozzle data with respect to changes in momentum flux ratio.

6.2.3 Momentum Flux Ratio Analysis (Constant We_g)

Responses of the spray field behaviour due to changes in q are more clearly observed at constant We_g. From Table 6.3, the test matrix provides three **sets** of experiments that satisfy this constraint

- Cases 1 to 4 $We_g \approx 118$;
- Cases 5 to 8 $We_g \approx 276$; and
- Cases 9 to 12 $We_g \approx 586$.

This subsection uses the results from Cases 5 to 8, Figure 6.19 is the plot of variation of AMD [D_{10}] with distance from the nozzle wall.

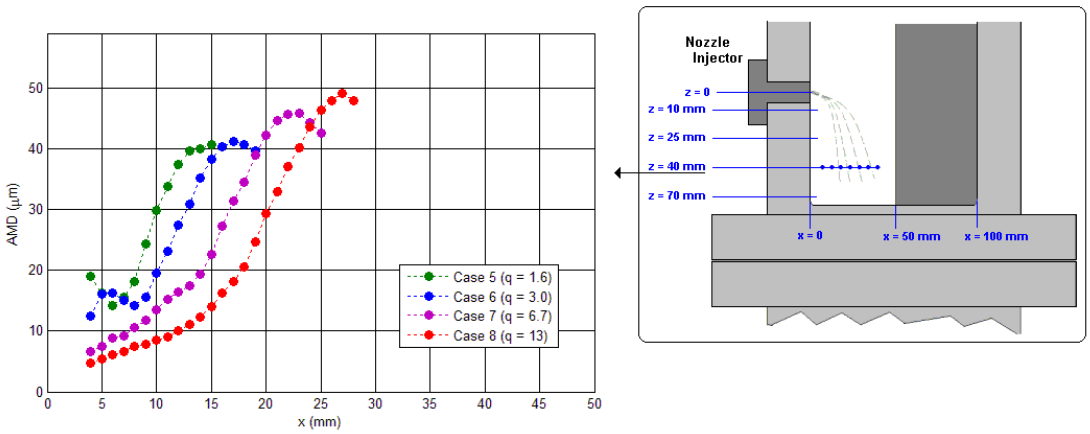

Figure 6.19: ⇊⊙ Variation of AMD [D_{10}] on the centre-line with distance from the nozzle wall; at x = 0 to 50 mm, y = 0 mm & z = 40 mm; for q = 1.6, 3.0, 6.7 & 13 and $We_g \approx 276$

Figure 6.19 shows the variation in measured values of AMD [D_{10}] along the centre-line at the z = 40 mm. The four trends all have $We_g \approx 276$ and the four trends show q = 1.6, 3.0, 6.7 and 13. It is immediately apparent that increasing momentum flux ratio (q) increased the spray penetration into the test section. The plot also demonstrated (as did Figure 6.13 at $We_g = 276$) increasing q extended the range of AMD [D_{10}] measured.

For q = 3.0, the distribution of AMD [D_{10}] in the near wall region ($4 < x < 8$ mm) exhibits a small inflection as was discussed at end of the previous subsection. For q = 1.6, the distribution in the near wall region ($4 < x < 6$ mm) appears to exhibit the *tail* of an inflection in the distribution - it seems likely that if it had

been possible to obtain reliable data between $0 < x < 6$ mm a complete inflection would be depicted.

Figure 6.20 shows the distribution of: (a) droplet axial component of velocity; (b) droplet transverse component of velocity; and, (c) droplet diameter in AMD [D_{10}] .

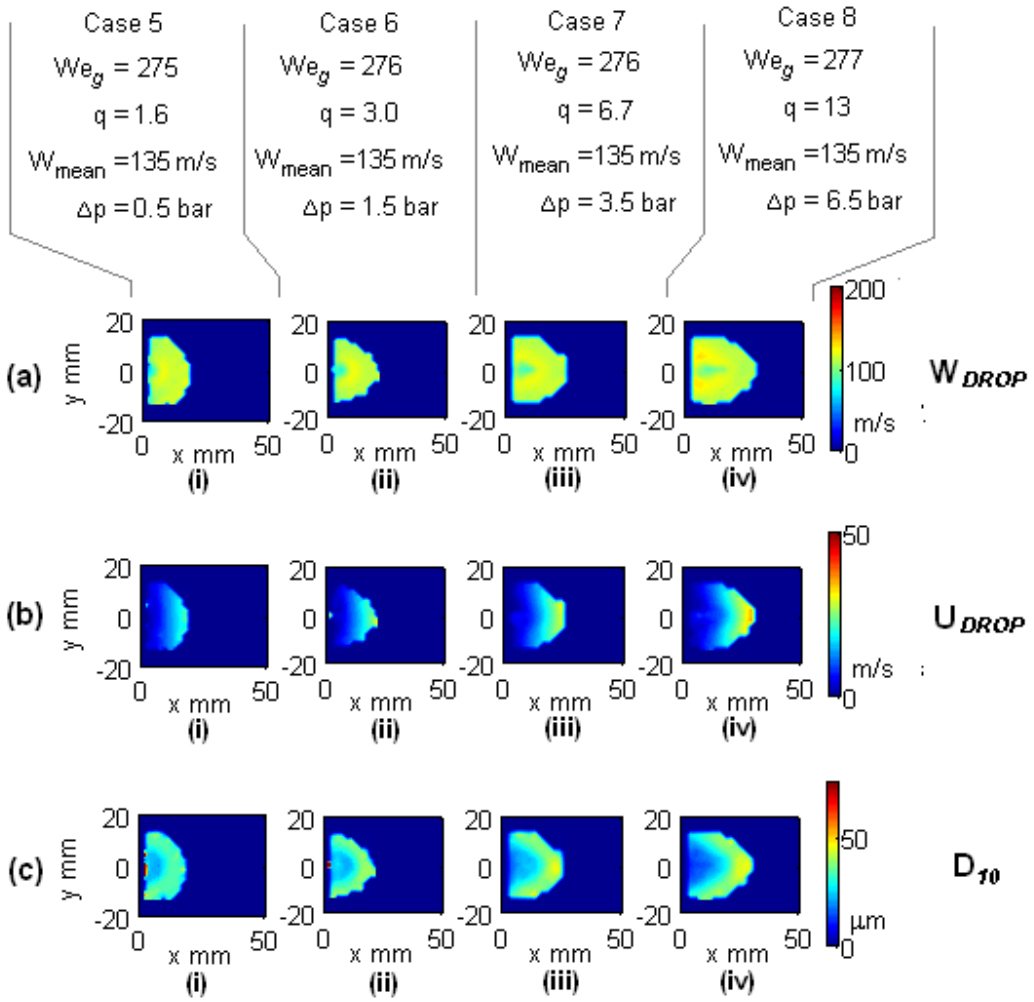

Figure 6.20: ⇊⊙ Contour plots of (a) W_{drop}, (b) U_{drop} and (c) AMD [D_{10}] characteristics; at z = 40 mm; for q = 1.6, 3.0, 6.7 & 13 and We$_g$ ≈ 276

The contour plots represent the spray at the $z = 40$ mm plane, the wet area can be seen to increase with the increase in q. The increase is mostly due to extended penetration into the test section, there is only a small amount of spread (i.e. extensions in the ± y). This is to be expected from Equations 2.14 and 2.15.

The contour plots in row a show the droplet's axial component of velocity (W_{drop}). Since (W_{drop}) results from the droplets being accelerated by the cross-airstream, which is constant across a-i, a-ii, a-iii and a-iv, there is a high degree of consistency across the four plots.

The contour plots in row b show the droplet transverse component of velocity (U_{drop}). The origin of transverse velocity is the liquid injection into the test section through the nozzle; U_{drop} is the transverse component of velocity that remains, in this case at 40 mm downstream of the injection point. The droplets near to the nozzle wall have low U_{drop} velocity and this is why they are near the nozzle wall rather than in the periphery. It is only the droplets in the periphery that exhibit appreciable U_{drop} velocity. Across b-i, b-ii, b-iii and b-iv, the increasing injection pressure (Δp = 0.5, 1.5, 3.5 and 6.5) leads to increasing q and this manifests as increasing U_{drop} across the plots that make up row (b) in Figure 6.20.

The contour plots in row c show the droplet diameter expressed as AMD [D_{10}] . The droplet size is reasonably constant as would be expected for constant Weber number.

This and the previous subsection have introduced the data presentation approaches adopted in this study and these approaches are emulated for the slot nozzle sprays in the main results chapter which follows this. The aim was also to build on the understanding of the general spray field physics and the variations in droplet properties that can be expected for different conditions.

Part of the reason for the preliminary testing was to compare the results generated by the TFMRC spray facility with previous studies, the following subsection compares the droplet sizes measured using the TFMRC apparatus with data from **Wu et al. (1998)**.

Drop Size Comparison

Figure 6.21 plots the variation in SMD[1] with distance from the nozzle wall for data obtained in this study with **Wu et al. (1998)**

[1]SMD is often used in studies where evaporation rate is an important parameter, Wu's data was presented in SMD and hence this has been used as the benchmark for the purpose of this comparison

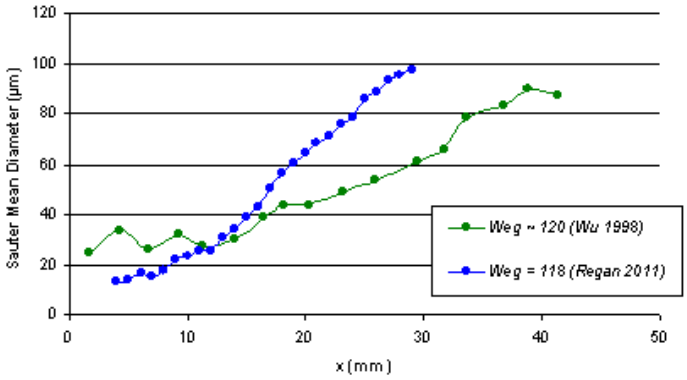

Figure 6.21: ⇓⊙ Variation in SMD with distance from the nozzle wall from **Wu et al. (1998)** and data obtained in this study

The two trends are both at $We_g \approx 120$ and $q \approx 50$. Both trends are on the centre-line $x = 0$ to 50 mm and $y = 0$. However they are at different downstream locations, Wu's data was taken at $z = 150$ mm, whereas the current data was taken closer to the nozzle exit at the $z = 40$ mm and hence there is a spray penetration deficit. This is why Wu's data is offset and exhibits greater x values. However, the SMD ranges and distributions are in good agreement.

The preliminary testing using the round nozzle confirmed the operation of the test facility and the PDPA system. Characteristic droplet trends were in-line with previous studies.

The following section in this chapter provides a summary of the various potential causes of liquid jet unsteadiness. The reason this is included in this chapter, rather than the literature review, is because the jet unsteadiness became more apparent through conducting experiments.

6.3 Jet Unsteadiness

Within the body of open literature for the subject of sprays in cross-airstreams, jet unsteadiness is often overlooked even though at low q values it is clearly visible. There are a number of different sources for the jet unsteadiness none of which can easily be isolated. The following text lists six flow features which potentially provide sources of unsteadiness and that contribute to a greater or lesser extent to the general instability of the liquid jet as it enters the test section.

1) Nozzle Exit Expansion

As the liquid flows axially along the nozzle passage, the nozzle's wall constrains radial flow. At the nozzle exit plane the liquid flow, which becomes a liquid jet at that point, experiences a step change as the nozzle's radial constraint abruptly ends. Surface tension serves to tend liquid bodies to a minimum surface area, a sphere. As the liquid exits the nozzle the 'free' cylindrical liquid body attempts to expand radially to form a sphere. Such radial expansion maybe small but, the imbalance sets up an instability which may grow (or decay).

2) Liquid Jet Acceleration in the Cross-Airstream Direction

As the liquid flow exits the confinement of the nozzle, its exposure to the cross-airstream is immediate - a step change. This normal acceleration was reported in **Schetz et al. (1980**) to be the cause of the inception of the familiar surface waves, which lead to the eventual collapse of the liquid jet.

3) Cavitation Periodic Shedding

Cavitation can occur at the nozzle entry. The cavitation mechanism produces a toroidal shaped vapour region at the nozzle entry. It is possible that this toroidal vapour region clings to the nozzle entry edge and acts as a smooth entry. Hence the cavitation reaches a maximum and does not develop downstream; the effect is simply to restrict the flow a little.

On the other hand, as **Ahn (2009)** reported it could be possible that the cavitation mechanism is continuous, the vapour region grows steadily and at a critical point the vapour region is shed downstream from the nozzle entry - and, the process repeats as illustrated in Figure 6.22.

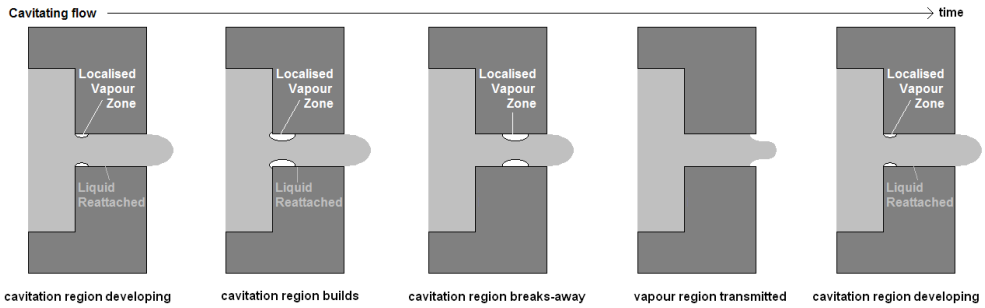

Figure 6.22: Development and shedding of a local vapour region

In this way the nozzle restriction caused by cavitation is cyclical and therefore so is q. Since the liquid jet trajectory is very sensitive to q, the emanating liquid jet must tend to move between limits in tune with the cyclical nozzle restriction.

4) Von K*á*rm*á*n Vortex Street

As the liquid jet traverses the cross-airstream, the situation is much like a cylindrical protrusion in a flow situation. Vortex shedding would be expected, with the wake characteristically alternating from side-to-side (as illustrated by Figure 6.23) at frequency that can be defined by the Strouhal number. However, since the liquid jet is fluid and dynamic, rather than solid and stationary, the situation is more convoluted than in the widely studied fundamental case. It seems likely that, as the free-stream flow bias alternates side-to-side, the vortex street could cause the liquid jet to wobble in tune.

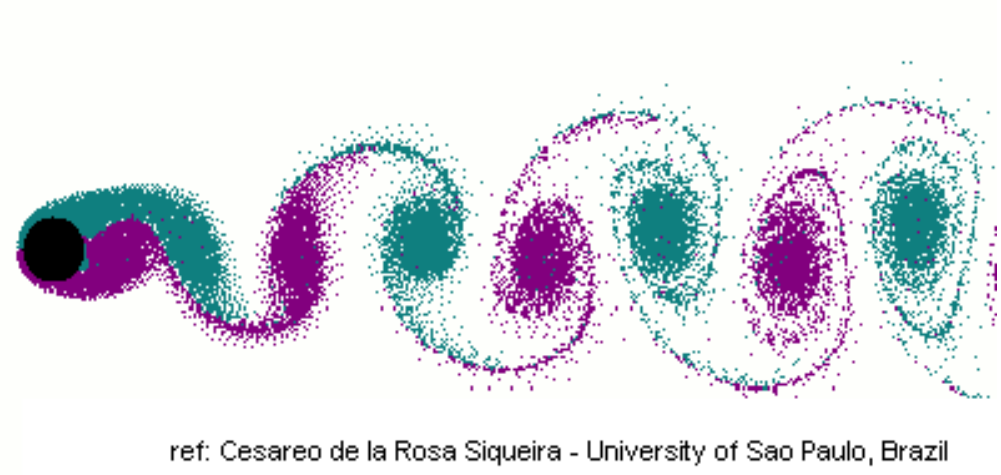

Figure 6.23: Development of a Von K*á*rm*á*n vortex street

Further downstream the liquid column turns in the direction of the cross-airstream and no longer resembles a perpendicular cylinder in a flow and, as a result, the vortex street flow mechanism must be limited to the upstream section of the liquid jet.

5) Vortex Pair within the Turning Liquid Jet

As the liquid jet turns through 90° in the direction of the cross-airstream, a counter rotating vortex pair can develop - due to the static pressure deficit leading to the flow field turning *in* on itself, as illustrated in 6.24 from **Friq and Roche (1994)**.

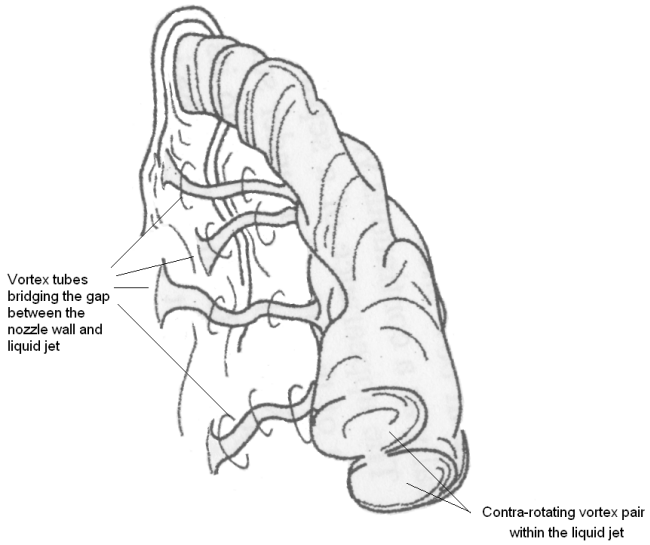

Figure 6.24: Vortex pair in turning liquid jet from **Fric and Roche (1994)**

6) Trailing Vortex in the Liquid Jet Wake

A possible factor in jet unsteadiness is believed to be the existence of an unsteady trailing vortex which forms in the jet's wake. This behaviour was first reported by **Chen et al. (1998)**, as illustrated in Figure 6.25.

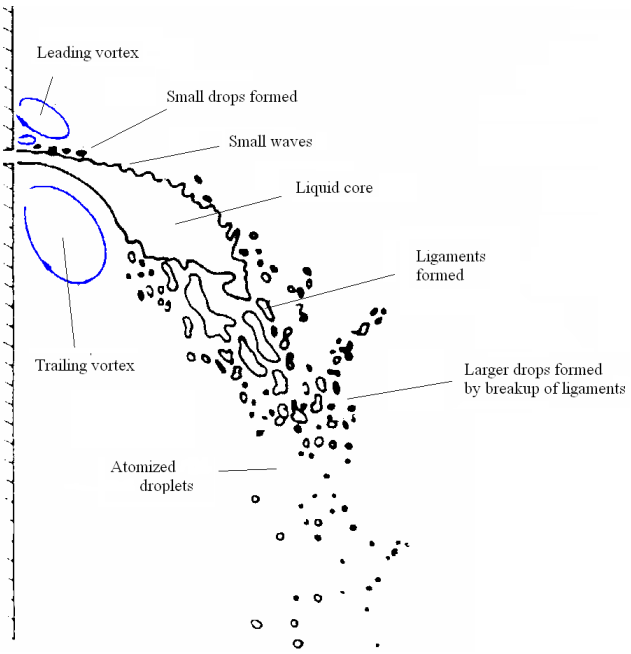

Figure 6.25: Spray structure and trailing vortex **Chen et al. (1998)**

Figure 6.25 shows a small leading vortex and counter rotating dependent vortex on the upper surface of the liquid column and a larger trailing vortex in the

region under the liquid column. These vortices are driven by the interaction of the air with the liquid jet flow, as illustrated in Figure 6.26.

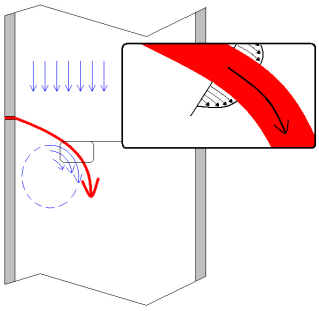

Figure 6.26: Trailing vortex driven by liquid flow

A *leading vortex*, on the upper surface of the liquid column, can not easily develop because the cross-airstream dynamic pressure dominates. In contrast, as the cross-airstream passes around the relatively dense liquid jet, a wake region is formed and a strong *trailing vortex* may develop.

Based on the pulsed laser sheet images taken in the preliminary testing for this study, it was possible to confirm the existence of airflows consistent with a trailing vortex, by applying Particle Image Velocimetry (PIV). The wake region of the jet is populated with small droplets, these small droplets can be used as seeds for a vector analysis. Figure 6.27 shows a result of such a PIV vector analysis. The vectors under the liquid jet show that droplets in this region turn through more than 90 degrees and support the possibility of an intermittent/permanent trailing vortex.

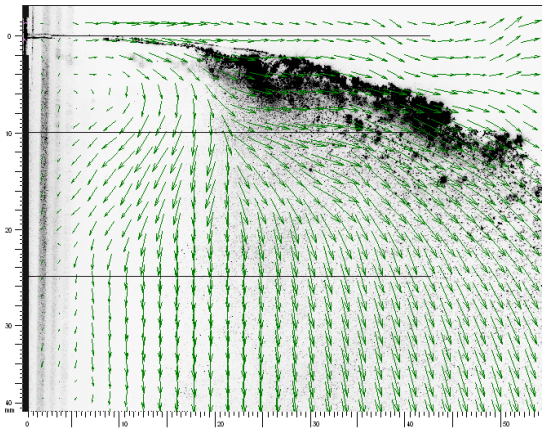

Figure 6.27: ⇊⊙ PIV analysis showing flow vectors under a round nozzle jet at $We_g = 54$ and $q = 68$

PIV vector analysis was applied to a series of consecutive images which showed

that the two phase flow in the wake region exhibits a high degree of unsteadiness. Since the PIV vector analysis uses droplets of the spray, rather than seeding, it is not of sufficient quality/accuracy to provide a reliable measurement of the angular velocity for a vortex. It is not clear whether the unsteadiness is inherent in the vortex and disturbs the liquid column or the other way round.

The six mechanisms above have been described with qualitative reference and illustrate the interrelated nature of the flows that occur with the spray in cross-airstreams situation. Considering the joint influence of the six mechanisms, it is clear that liquid jet unsteadiness should be expected. As a general observation of the tests, the liquid jet's oscillations about a mean path were most obvious when q was low.

6.4 Chapter Synopsis

In this chapter it has been shown that the test facility operated in-line with expectations. Six possible causes for the unsteadiness exhibited by the liquid jet were described. The next chapter discusses the unique results from this study.

Chapter 7

Slot Nozzle Spray Characterisation

This chapter has four sections. Firstly, an introduction sets out the test conditions chosen for the slot nozzle tests. This is followed by an assessment of the sprays generated from the horizontally aligned ⇊ slot tests for variations in Weber number and momentum flux ratio, in the format established for the round nozzle tests ⇊ in the previous chapter. This is repeated for the vertically aligned ⇊ slot nozzle tests. This chapter is completed with a comparison of the spray characteristics from the two slot orientations in relation to one another.

7.1 Introduction

The experimental test matrix was established on We_g and q. A total of twelve points with three We_g levels and six q levels. The magnitudes of these parameters were defined according to the levels expected to occur in gas turbine engine oil leak scenarios.

In round nozzle sprays in cross-airstreams work, the characteristic length scale required in the We_g definition is based on the nozzle diameter - on the basis that the emanating liquid jet should have the same diameter. Since a slot nozzle does not have a diameter, a different approach is required. **Schetz and Padhye (1977)** worked with slot nozzles and used the equivalent diameter (d_{eq}), as in Equation 7.1.

$$We_{g\,deq} = \frac{\rho_g \left(W_{air} - W_{liquid}\right)^2 d_{eq}}{\sigma} \tag{7.1}$$

(noting that $W_{liquid} = 0$ at the nozzle exit for perpendicular injection)

However, the particular definition of d_{eq} was not listed. There are several different definitions for equivalent diameter, Equation 7.2 is taken from **Koch (2008)** who concluded that this is the most appropriate version.

$$d_{eq} = 1.453 \frac{Area^{0.6}}{Perimeter^{0.2}} \tag{7.2}$$

Schetz and Padhye's approach of using d_{eq} has also been adopted here and the data is presented in this way. However, there is no specific qualification for using d_{eq}. The best length scale to use, would of course be one that unifies the results from non-round and round injector geometries - whether this can be achieved with a standard diameter representation such as d_{eq} or d_h is not currently known. In order, to advance this particular aspect would require testing over a small number of test points but, with multiple slot nozzle specimens. As only a single slot specimen has been used in this study, the results cannot be used to develop a universal length scale for We_g.

Figure 7.1 shows the relevance of the test sprays with respect to those expected in the engine. The region in blue represents the range possible in the engine, assuming oil leaking through a crack measuring 0.1 by 0.5 mm or d_{eq} = 0.602 mm (noting that; the slot nozzle used in these tests had d_{eq} = 1.6 mm).

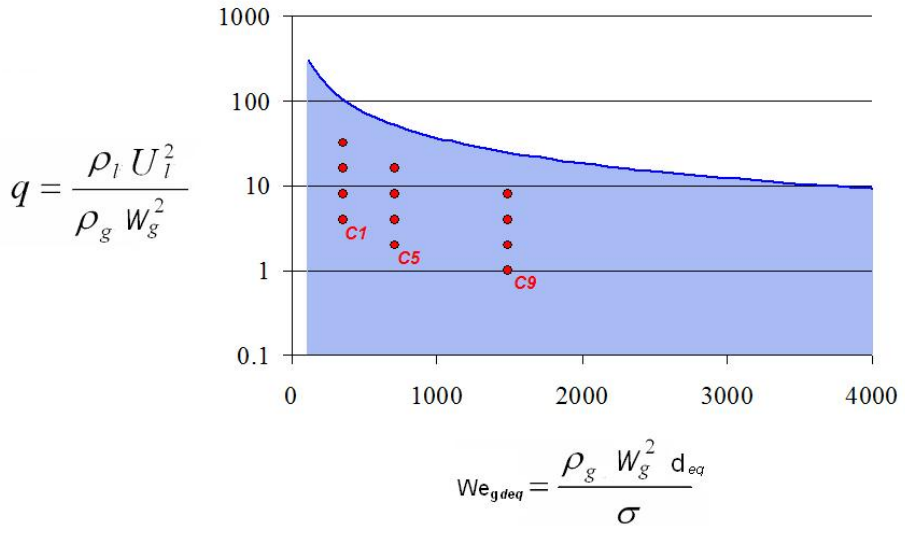

Figure 7.1: Engine relevant momentum flux ratio and Weber number (in blue) and test points (in red), with Cases 1, 5 and 9 highlighted

Figure 7.2 below shows how the experimental data produced by this project extends from the test points covered by previous studies.

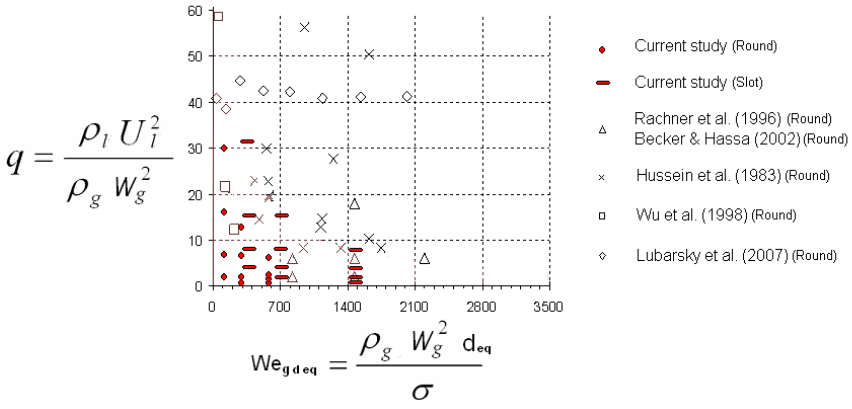

Figure 7.2: Momentum flux ratio and Weber Number data from previous research and this study, replotted from **Hart, Hutcheson and Regan (2009)**

This project included twelve different test points based on:

- **Three cross-airstream velocities, W_g = 90, 135, 195 m/s**; and,
- **Four liquid flow velocities, U_l = 7.8, 11.0, 15.6 and 22.0 m/s.**

The required liquid velocities (U_l) required nozzle differential pressures of **0.5, 1.5, 3.5 and 6.5 bar** respectively; based on the measured volumetric flow rate and assuming continuity. Table 7.1 shows the test matrix nominal values of $We_{g\,deq}$ and q with respect to the cross-airstream velocity and nozzle differential pressure.

	W_{mean} = 90 m/s $We_{g\,deq} \approx 354$	W_{mean} = 135 m/s $We_{g\,deq} \approx 714$	W_{mean} = 195 m/s $We_{g\,deq} \approx 1490$
Δp = 0.5 bar	Case 1: q ≈ 4	Case 5: q ≈ 2	Case 9: q ≈ 1
Δp = 1.5 bar	Case 2: q ≈ 8	Case 6: q ≈ 4	Case 10: q ≈ 2
Δp = 3.5 bar	Case 3: q ≈ 16	Case 7: q ≈ 8	Case 11: q ≈ 4
Δp = 6.5 bar	Case 4: q ≈ 32	Case 8: q ≈ 16	Case 12: q ≈ 8

Table 7.1: Test matrix (nominal values)

The test matrix was completed using the slot nozzle (0.5 by 5.38 mm, as described in 3.2.11) in two different orientations with the nozzle's major dimension: per-

pendicular (*or horizontal alignment*) to the cross-airstream and parallel (*or vertical alignment*) to the cross-airstream, as in Figure 7.3.

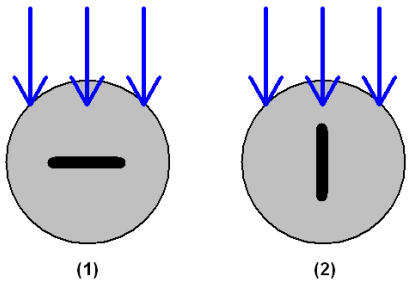

Figure 7.3: Orientation of the slot nozzle to the cross-airstream (1) horizontally aligned and (2) vertically aligned

For clarity symbols have been developed to designate and differentiate between the nozzles and orientations as follows:

Horizontal slot nozzle: ⇊⊖
Vertical slot nozzle: ⇊⌽
Round nozzle: ⇊⊙

The overall experimental programme is made up of 36 different spray conditions, from three test groups, *round nozzle, horizontal slot nozzle and vertical slot nozzle* - each test group consisted of twelve test conditions. The round nozzle experiments were discussed in the previous chapter and this chapter focuses on the slot nozzle tests.

PDPA analysis was conducted for each test case at three downstream planes, z = 10, 25 and 40 mm, for the wet area at each level (in some cases z = 70 mm was also run as can be seen from the data presented in Appendices A, B and C). Typically, each z plane required of the order of 100 to 200 individual measurements points and, therefore, each spray was subjected to perhaps 500 PDPA measurements in total. In addition, the complete test matrix was also conducted with a High Speed Video (HSV) applied. Overall, there is a considerable amount of data that has been generated by this study. The full spectrum of tests provides a useful data base that can be interrogated in many different ways to develop understanding for the flow physics involved with sprays from slot and round nozzles in cross-airstreams.

The PDPA system generated a number of different droplet property outputs and, as a result, the scope for different analysis is considerable. To put some perspec-

tive on this, Figure 7.4 shows a tree of the test variables and the corresponding potential outputs.

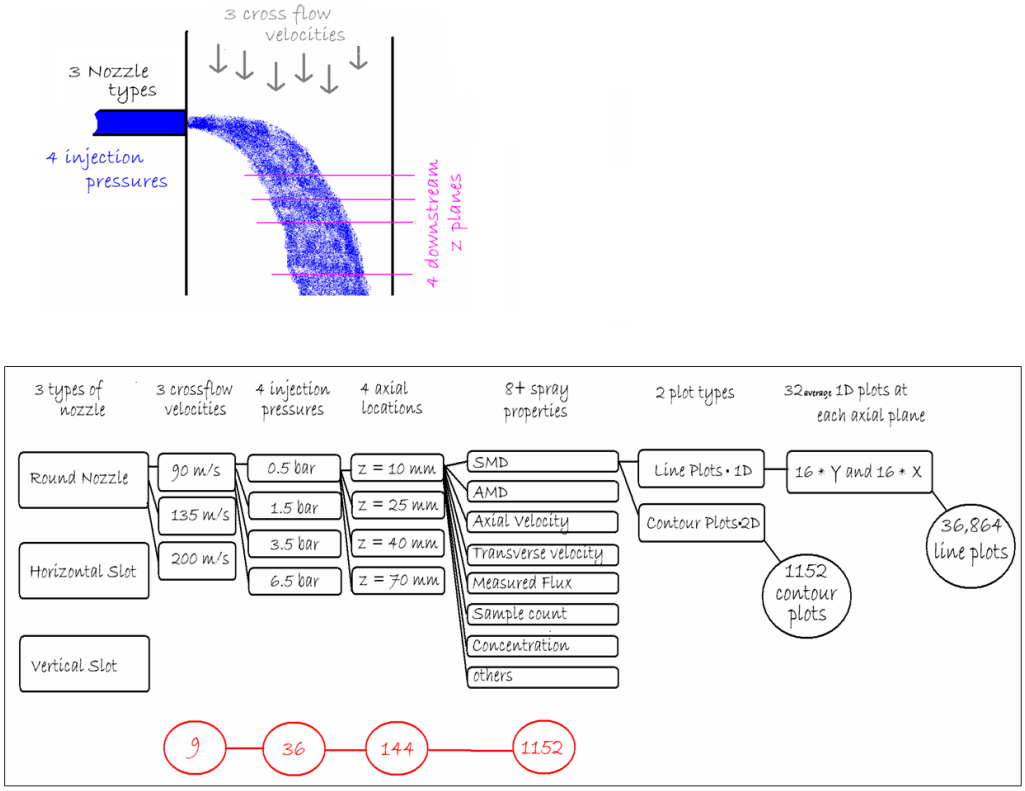

Figure 7.4: Tree of test variables and potential outputs

In order to aid the process of data interrogation a menu based Matlab routine was developed, structured on Figure 7.4, to access the data and return contour plots or line plots. Line plots could be built up by adding data from the various test cases to compare the sprays' characteristics and, in doing so, develop understanding of the relationships. The Matlab routine played an important role in developing the analysis presented in this chapter.

The following two sections are an appraisal of the results of the horizontally and vertically aligned nozzle tests respectively.

7.2 Horizontally Aligned Slot ⇓⊖ Nozzle Sprays

The slot nozzle was mounted in the test section with its long dimension in a horizontal alignment, perpendicular to the cross-airstream direction, as illustrated in Figure 7.5.

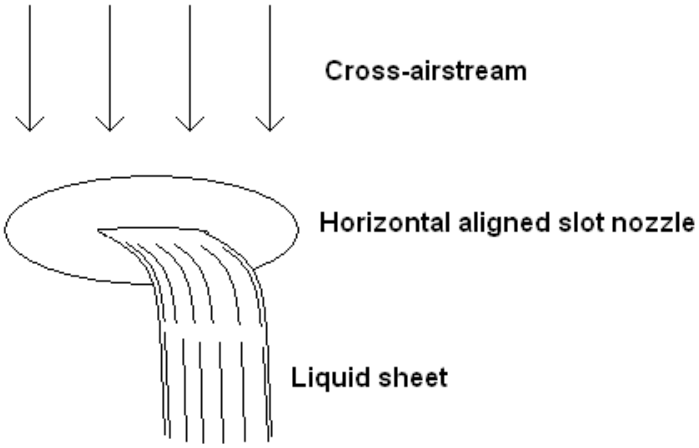

Figure 7.5: Horizontally aligned slot ⇓ and liquid sheet

This configuration maximises the liquid surface area that is directly exposed to the cross-airstream direction. Consequently, this reduces sheet penetration into the test section to a minimum (based on orientation of a slot nozzle).

7.2.1 Spray-Field Characteristics

Table 7.2 shows the conditions measured during the horizontal aligned slot tests.

	$W_{mean} \approx$ **90 m/s**	$W_{mean} \approx$ **135 m/s**	$W_{mean} \approx$ **195 m/s**
Δ**p ≈ 0.5 bar**	Case 1: 310, (2.7)	Case 5: 727, (1.2)	Case 9: 1520, (0.5)
Δ**p ≈ 1.5 bar**	Case 2: 304, (7.5)	Case 6: 699, (3.3)	Case 10: 1531, (1.8)
Δ**p ≈ 3.5 bar**	Case 3: 297, (20.4)	Case 7: 704, (8.6)	Case 11: 1444, (4.1)
Δ**p ≈ 6.5 bar**	Case 4: not possible	Case 8: 709, (15.8)	Case 12: 1263, (8.6)

Table 7.2: ⇓ PDPA average test conditions, $We_{g\,deq}$ (q)

The conditions in Case 4 led to a large spray field that impinged on the test section windows, through which it proved impossible to obtain data. Although it was possible to obtain data in the large sprays produced by Cases 3 and 8, a considerable amount of the spray periphery impinged on the windows at the downstream planes z = 40 and 70 mm. In contrast in Case 9 the entire

spray-field remained in close proximity to the nozzle wall and, as a result, it is reasonable to assume that a significant proportion of the spray existed in an area inaccessible to the PDPA measurement volume (i.e. less than 4 mm from the nozzle wall). Cases 4 and 9, represent the two extremes of these tests. Case 4 represents a limitation due to the size of the test section. Whilst Case 9 represents a fundamental limitation due to the nozzle wall, although it is acknowledged that an alternative test section design and/or PDPA arrangement could allow for measurements much closer to the nozzle wall than was possible for these tests.

In Cases 9 and 10, $We_{g\,deq}$ is a little over 1500, however, as the liquid injection rate was increased for Cases 11 and 12, the blockage it created to the cross-airstream was such that it was not possible to maintain the air flow's mean velocity. As a result, $We_{g\,deq}$ was reduced to 1444 in Case 11 and further still, down to 1263 for Case 12. Again this demonstrates that the test section was at the limits of its operational capacity at the higher end of the fluid flow rates tested.

The following analysis is split into two subsections. Firstly, the horizontal slot data is discussed with respect to changes in Weber number value ($We_{g\,deq}$), with momentum flux ratio (q) nominally constant. Secondly, the horizontal slot ⇊ data is discussed with respect to changes in momentum flux ratio (q), where Weber number ($We_{g\,deq}$) is nominally constant.

Weber Number Analysis (constant q)

As a result of the spray's sensitivity to q, the responses of the spray behaviour with variations in $We_{g\,deq}$ are more clearly observed across tests with constant q. Variations in $We_{g\,deq}$ were brought about by changing the cross-airstream velocity W_{mean}. In order for tests to possess the same q value, the liquid flow rate must remain in proportion with W_{mean}. From the test matrix, it is possible to form two sets of three cases that provide constant q conditions:

- Cases 1, 6 and 11, where $q \approx 3.5$; or,
- Cases 2, 7 and 12, where $q \approx 8$.

The following analyses focuses on Cases 2, 7 and 12, where $q \approx 8$ and $We_{g\,deq}$ = 304, 704 and 1263, respectively. Figure 7.6 shows the distribution of: (a) droplet axial component of velocity; (b) droplet transverse component of velocity; and, (c) droplet diameter in AMD [D_{10}] .

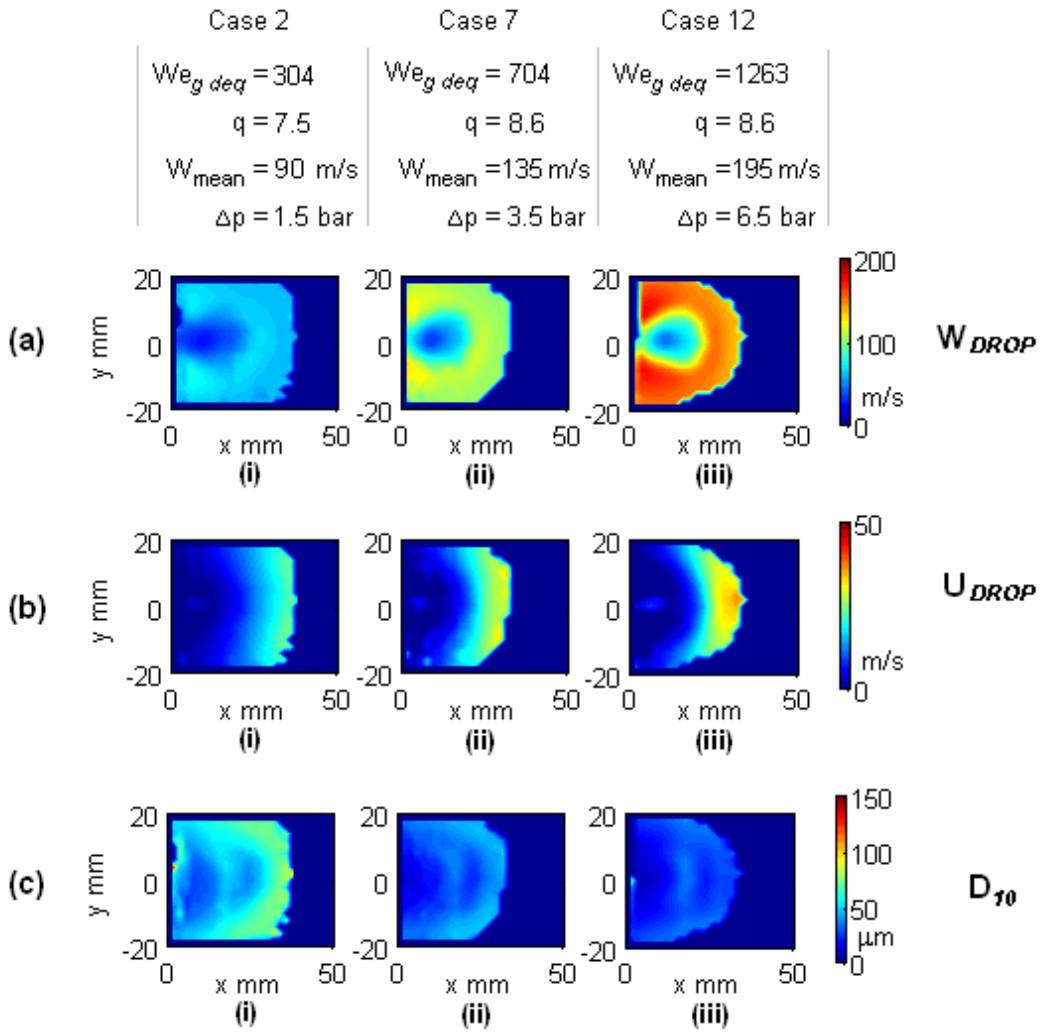

Figure 7.6: ⇓ Contour plots of (a) W_{drop}, (b) U_{drop} and (c) AMD [D_{10}] ; at the z = 40 mm plane; $We_{g\,deq}$ = 304, 704 and 1263 and constant $q \approx 8$

For round nozzles, it is established that q provides a good indicator for spray penetration. In these contour plots the overall penetration is relatively constant with the spray's maximum penetration into the test section reaching $x \approx 34$ mm. This indicates that q should provide a reasonable basis for predicting spray penetration for a horizontally aligned slot nozzle. However, it is important to point out that this does not mean the relationship of q with spray penetration established for round nozzles is relevant to non-round nozzle geometries or different aspect ratios of slot nozzles. Spray penetration is very sensitive to nozzle size, shape, aspect ratio and orientation.

The droplet's axial and transverse components of velocity are presented in rows a and b in Figure 7.6.

At the point where liquid exits the nozzle and enters the spray-field domain, it

does so with maximum transverse velocity and without any axial velocity. The liquid continuum emanating from the nozzle exit experiences a momentum exchange with the cross-airstream. As the liquid progresses downstream, so it attains axial (W) velocity and sheds transverse (U) velocity. At some time t_∞ the liquid, now in droplet form, will exhibit axial velocity equal to the cross-airstream that surrounds it and all its initial transverse velocity will be gone:

$$\begin{array}{ccc} \textcircled{1}\ t = 0 & (U_l = U_{noz}) & (W_l = 0) \\ \textit{momentum exchange} & \Downarrow & \Downarrow \\ \textcircled{2}\ t_\infty & (U_l = 0) & (W_l = W_{air}) \end{array}$$

The droplet's axial component of velocity distributions (row a) show how much axial velocity the droplets have attained at the z = 40 mm plane. Scanning from left to right across the contours plots in row a, it is clear there was a general increase in the droplet's axial velocity, as would be expected from the increase in cross-airstream velocity (90, 135 and 195 m/s respectively). These plots also clearly display a significant wake region (as described in Figure 6.7) of suppressed droplet axial velocity as highlighted in Figure 7.7 below. Figure 7.7 also shows how the the droplet's axial component of velocity increases with axial distance z, by presenting data from three downstream planes, z = 25, 40 and 70 mm; for $We_{g\,deq}$ = 1263 and q = 8.6 (Case 12).

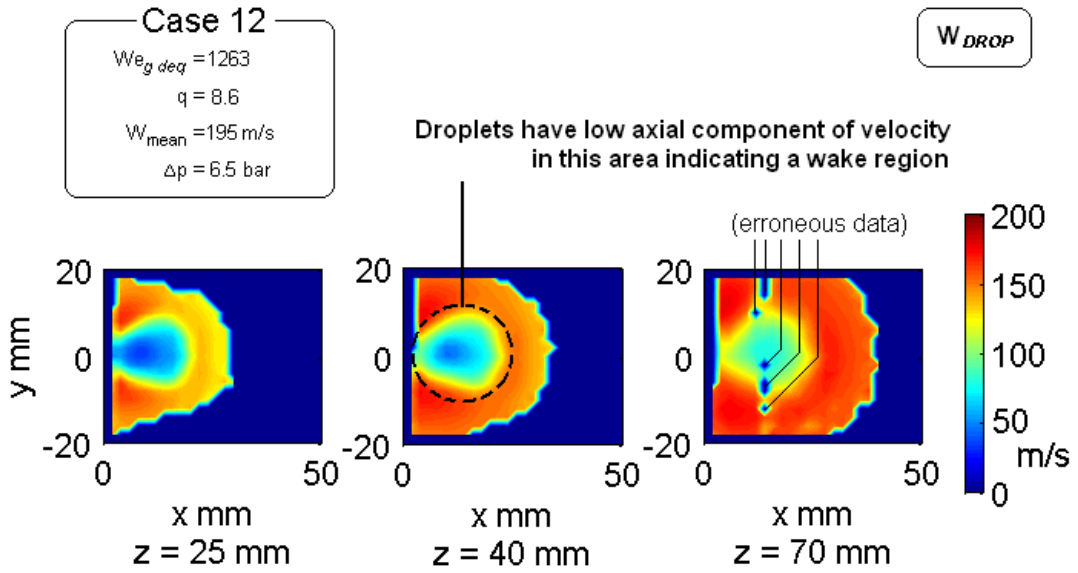

Figure 7.7: ⇓ Contour plots of W_{drop}; at the z = 25, 40 and 70 mm planes; for $We_{g\,deq}$ = 1263 and q = 8.6

These plots show that the effects of the wake region remained evident at z = 70 mm, the furthest downstream distance tested.

Row b in Figure 7.6 shows the droplet's transverse component of velocity U_{drop}. As has been explained previously, the distribution of U_{drop} contour plots show how much transverse velocity has been retained by the droplets, in this case at the $z = 40$ mm plane; from continuity the mean nozzle exit velocity, at $z = 0$ mm, was 11.0, 15.6 and 22.0 m/s (for Cases 2, 7 and 12 respectively). Droplets near to the nozzle wall must have low or zero U_{drop}, in order for them to be close to the nozzle wall. Similarly, the droplets with the highest U_{drop} occupy the far periphery of the spray field (i.e. $x \gtrsim 20$ mm for $q \approx 8$ at $z = 40$ mm)

Row c in Figure 7.6 shows distributions of AMD [D_{10}] and shows similar trends to those seen for round nozzles, in general, with larger droplets tending to the far periphery. Figure 7.8 shows the asymptotic nature of droplet size with increasing We_g for round nozzle sprays from **Lubarsky et al. (2007)**.

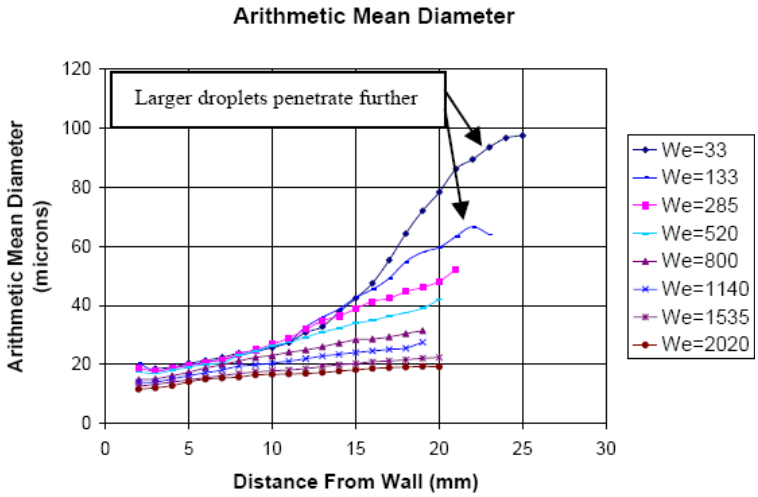

Figure 7.8: ⇊ ⊙ Variation of arithmetic mean diameter AMD [D_{10}] at $x = 0$ to 40 mm $y = 0$, $z = 30$ mm from **Lubarsky et al. (2007)**

From Lubarsky's graph, droplet size is relatively constant across the centre-line in the spray for $We_g \gtrsim 800$. Row c in Figure 7.6 suggests this was also true for these horizontal slot tests, where it is evident there is a greater differential in droplet size between $We_{g\,deq}$ 304 and 704; than there was between $We_{g\,deq}$ 704 and 1263.

The AMD [D_{10}] can be seen, particularly in plot 'C-i', to exhibit an inflection (between $20 \gtrsim x \gtrsim 27$ mm) in the the general trend of increasing AMD [D_{10}] with distance from the nozzle wall (increasing x), as illustrated in Figure 7.9.

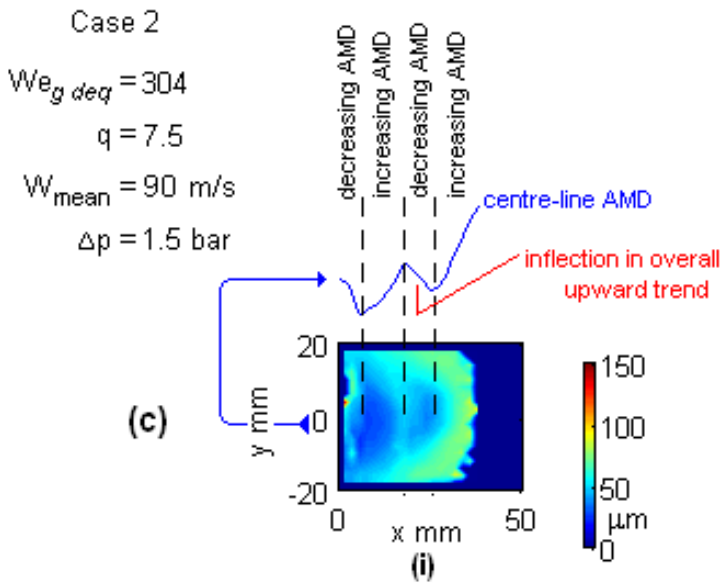

Figure 7.9: ⇓ Contour plot of AMD [D_{10}] with inflection identified; at z = 40 mm; $We_{g\,deq}$ = 304 and q = 8.6 Case 2

The inflection has been identified for round nozzles (e.g. as was shown Figure 6.17) and was previously associated with low q conditions, however, Figure 6.14 showed that the density of the spray core appears to be the important factor. The slot nozzle used in this study has d_{eq} = 1.6 mm compared to d = 0.57 mm for the round nozzle used. Hence the flow rate is considerably greater for the slot nozzle and the sprays produced are, relatively, very densely populated. Consequently, the inflected AMD [D_{10}] trend in Figure 7.9 was to be expected. Figure 7.10 shows the variation of AMD [D_{10}] with distance from the nozzle wall (x = 0 to 50 mm) on the centre-line (y = 0) mm at the z = 40 mm plane for each case featured in row c of Figure 7.6. This more clearly shows the extent of the inflection exhibited in the overall increasing AMD [D_{10}] with distance from the nozzle wall and all cases exhibit an inflection.

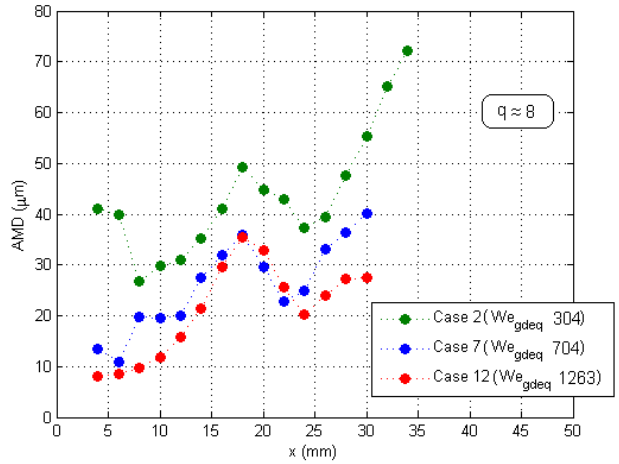

Figure 7.10: ⇓ Variation of centre-line AMD [D_{10}] with distance from the nozzle wall; at x = 0 to 50 mm, y = 0 mm and z = 40 mm; for $We_{g\,deq}$ = 304, 704 and 1263 and $q \approx 8$ (Cases 2, 7 and 12)

Figure 7.10 again shows the general shift in droplet size brought about the variation in $We_{g\,deq}$ (304, 704 and 1263 respectively), with a larger shift in drop size for $We_{g\,deq}$ 304 → 704; than for, $We_{g\,deq}$ 704 → 1263.

Figure 7.11 shows the range of droplet sizes measured for each of the Cases 1 to 12.

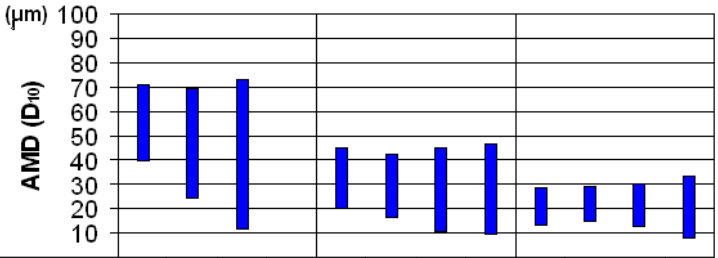

Case no.	1	2	3	4	5	6	7	8	9	10	11	12
q	2.7	7.5	20.4		1.2	3.3	8.6	15.8	0.5	1.8	4.1	8.6
We_{gdeq}	310	304	297		727	699	704	709	1520	1531	1444	1263

Figure 7.11: ⇓ AMD [D_{10}] ranges; at z = 40; for all test cases

The ranges depicted, in Figure 7.11, have been filtered to exclude data which was based on less than 2600 individual measurements, as this level was shown to produce repeatability within $\pm 1\,\mu m$ (described in Section 4.3.2). The variation in AMD [D_{10}] depicted in Figure 7.11 follows a very similar pattern to that of the

round nozzle Figure 6.13, with the AMD [D_{10}] **range** widening with increasing q within each level of Weber number.

The increasing AMD [D_{10}] range is most obvious where Weber number was lowest, $We_{g\,deq} \approx 300$ (Cases 1 to 3), particularly at the lower end with smaller droplets being produced.

This could be due to an increase in **transverse Weber number**. As the liquid injection rate increases, the transverse velocity deficit between the liquid flow and the cross-airstream increases (noting that the mean liquid flow velocity in the nozzle for Cases 1, 2 and 3 was U_{liquid} = 7.8 m/s; 11.0 m/s; and, 15.6 m/s respectively; whilst the cross-airstream's transverse velocity is always zero, i.e. $U_{air} = 0$).

Figure 7.12 illustrates how a transverse Weber number could be calculated, in the same way that the axial Weber number, typically used, is.

$$\underline{\text{Axial Weber number}} \qquad \underline{\text{Transverse Weber number}}$$

$$We_{g\,deq} = \frac{\rho_g\,(W_{air} - W_{liquid})^2\,d_{eq}}{\sigma} \quad \textbf{or} \quad We_{g\,deq} = \frac{\rho_g\,(U_{liquid} - U_{air})^2\,d_{eq}}{\sigma}$$

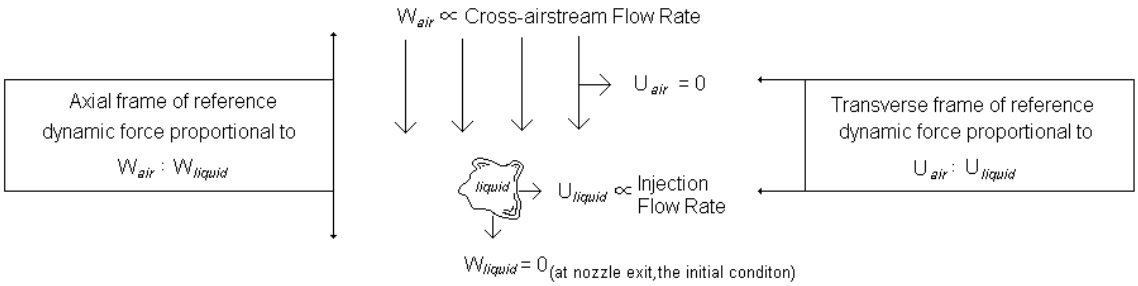

Figure 7.12: Diagram of axial and transverse frame of reference

The influence on the AMD [D_{10}] range with increasing q would be expected to diminish with the higher $We_{g\,deq}$ test levels (Cases 5 to 12), as the dynamic forces from the cross-airstream velocity increasingly dominated the break-up of the liquid continuum (i.e. $W_{air} - W_{liquid} \gg U_{liquid} - U_{air}$).

Generally for sprays in cross airstreams this is the case, the axial velocity deficit is much greater than the transverse velocity deficit. The dynamic forces generated from the transverse velocity deficit are often negligible by comparison, hence Weber number is calculated with an axial frame of reference. However, as q increases, $U_{liquid} - U_{air}$ becomes greater and, at some point, will influence the break-up process - with smaller droplets being produced as a result of the transverse velocity deficit.

For these tests (as with most spray in cross-airstream experimental setups), at the nozzle exit plane U_{air} and W_{liquid} both equal zero, so the axial and transverse velocity deficits at the nozzle exit plane were nominally:

$$W_{air} - \cancelto{0}{W_{liquid}} = \text{90 m/s; 135 m/s; or, 195 m/s;}$$

$$U_{liquid} - \cancelto{0}{U_{air}} = \text{7.8 m/s; 11.0 m/s; 15.6 m/s; or, 22.0 m/s.}$$

Table 7.3 shows the axial and transverse based Weber numbers for the horizontal slot tests, as well as the relative proportionality.

Case	$We_{g\,deq}$ (Axial f.o.r.)	$We_{g\,deq}$ (Transverse f.o.r.)	Ratio
1	310	2.4	0.8%
2	304	4.7	1.6%
3	297	9.5	3.2%
4	dnr		
5	727	2.4	0.3%
6	699	4.7	0.7%
7	704	9.5	1.4%
8	709	18.9	2.7%
9	1520	2.4	0.2%
10	1531	4.7	0.3%
11	1444	9.5	0.7%
12	1263	18.6	1.5%

Table 7.3: $\Downarrow$ $\ominus$ Axial Weber number compared to transverse Weber number; at $x = y = z = 0$; for all test cases

Table 7.3 highlights how the transverse Weber number is, respectively, a greater proportion of the axial Weber number for Cases 1 to 3, than for Cases 5 to 8 which in-turn are greater than for Cases 9 to 12. This can be seen to generally correspond with the increases in range of AMD [D_{10}] presented in Figure 7.11.

However, it should also be noted that with increasing q, the liquid continuum becomes more defined, more stable and physically larger which increases the opportunity for surface stripping (the break-up process that leads to smaller droplets) and this could also be a factor in the smaller droplets measured with increasing q.

This examination of the horizontally aligned slot nozzle data at varying Weber number ($We_{g\,deq}$) and constant momentum flux ratio (q), has shown that $We_{g\,deq}$ is the primary determinant in the resultant droplet sizes; as it is for round nozzles.

Overall, this suggests that although the spray structure from a horizontal slot nozzle is quite different to that from a round nozzle, the fundamental break-up mechanisms applicable to round nozzles also apply to the horizontally aligned slot nozzle tested in this study. However, attention is drawn to the importance of the Weber number parameter ($We_{g\,deq}$) in droplet size prediction and in particular defining an appropriate length scale. Here d_{eq} was used but, it is not clear if this is appropriate to unify droplet size predictions between round and horizontal slots because the testing was too limited with just a single slot specimen featuring in the tests.

This subsection focused on the horizontal slot data with reference to changes in $We_{g\,deq}$ with q held constant, in contrast the following subsection looks at the horizontal slot ⇊ data with reference to changes in q across tests with constant $We_{g\,deq}$ value.

Analyses of Momentum Flux Ratio (constant $We_{g\,deq}$)

The variation in spray characteristics with changes in q are more clearly identified across tests with constant $We_{g\,deq}$. In these tests, changes in q are brought about by varying the liquid delivery rate. In order to hold $We_{g\,deq}$ constant, W_{mean} must be a constant value.

From the test matrix, it is possible to form three sets of tests that satisfy this condition:

- Cases 1, 2 and 3, where $We_{g\,deq} \approx 300$;
- Cases 5, 6, 7 and 8, where $We_{g\,deq} \approx 700$; or,
- Cases 9, 10, 11 and 12, where $We_{g\,deq} \approx 1450$.

The following analyses focuses on Cases 5 to 8, where q = 1.2, 3.3, 8.6 and 15.8 respectively and $We_{g\,deq} \approx 700$. Figure 7.13 shows the distribution of: (a) droplet axial component of velocity; (b) droplet transverse component of velocity; and, (c) droplet diameter in AMD [D_{10}] at the z = 40 mm plane.

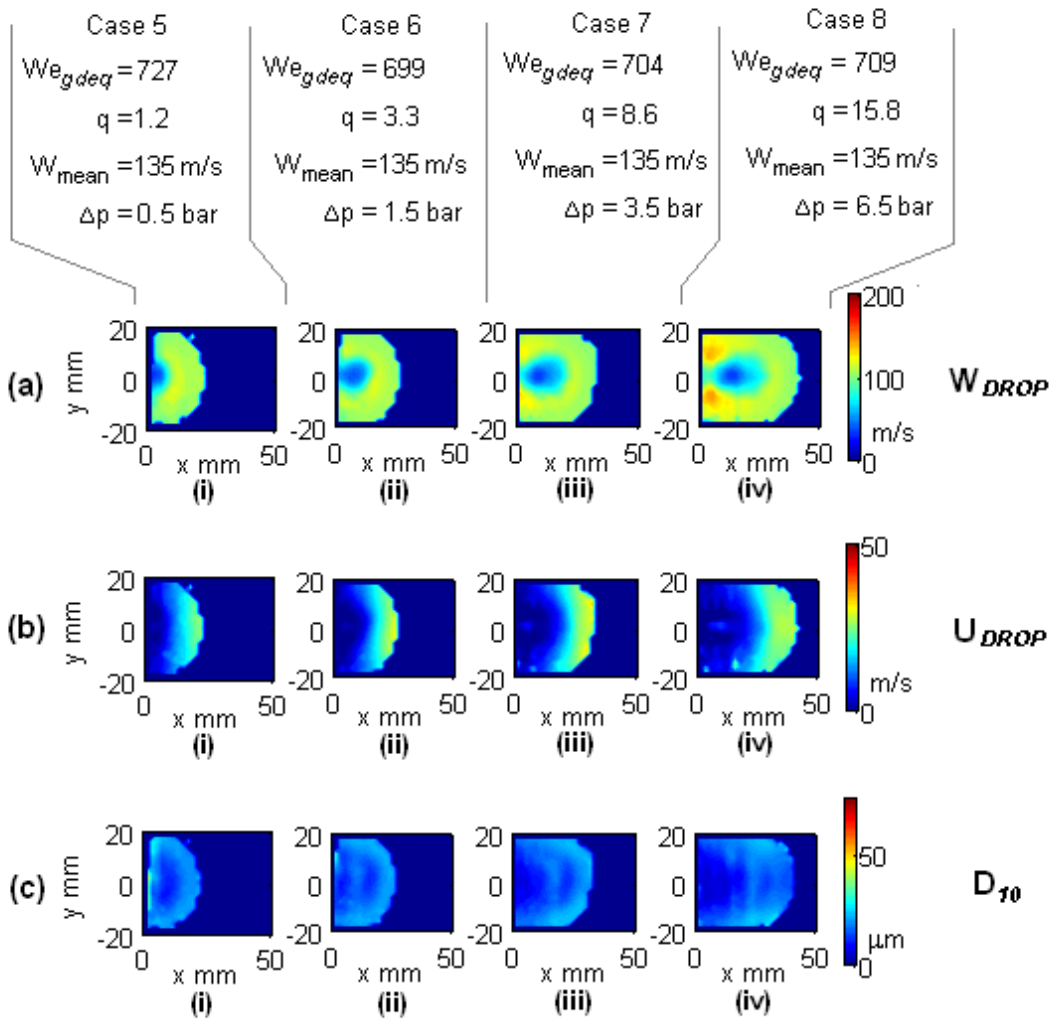

Figure 7.13: ⇓ Contour plots of (a) W_{drop}, (b) U_{drop} and (c) AMD [D_{10}] ; at the z = 40 mm plane; for q = 1.2, 3.3, 8.6 & 15.8 and constant $We_{g\,deq} \approx 710$

From Figure 7.13 it is evident that the area occupied by the spray field increases with increasing q, as would be expected from increasing injection pressure but, constant cross-airstream velocity. The liquid flow rate = 1, 1.6, 2.6 and 3.6 l/min respectively for Cases 5, 6, 7 and 8.

The data shows there was some spray interference with the side windows (i.e. the test section was too narrow), although not ideal, this is not considered to be influential on any of the findings presented. The fact that good measurements were obtained indicates that light rays passed through the side-windows cleanly and without unwanted refraction. This is only possible with small/occasional liquid impinging on the test section side-windows, representing a small fraction of the overall liquid mass transfer.

Row a in Figure 7.13 shows the axial component of velocity the droplets have obtained by the z = 40 mm plane. A wake region can be identified in all four plots and it can be seen how this wake region migrates away from the injector wall with increasing q.

Row b in Figure 7.13 shows the transverse component of velocity (U_{drop}) the droplets have retained at the z = 40 mm plane. As was discussed previously these plots of transverse velocity adopt a stratified pattern with the highest U_{drop} values found in the far periphery, furthest from the nozzle wall, and these plots also exhibit this behaviour.

Row c in Figure 7.13 shows the results of AMD [D_{10}] measured at the z = 40 mm plane. AMD [D_{10}] appears to be reasonably constant for q = 1.2, 3.3, 8.6 and 15.8; as would be expected for approximately constant Weber number and with reference to Figure 7.11.

The horizontally aligned slot nozzle ⇊ has been shown to closely follow the behaviour exhibited by a round nozzle ⇓ in terms of the connection between Weber number and droplet sizes and how spray location was defined by q. The following section discusses the data for the slot nozzle in the vertical orientation ⇊.

7.3 Vertically Aligned ⇓ Slot Nozzle Sprays

The slot nozzle was arranged such that the long dimension was aligned with the direction of the cross-flow direction, as illustrated in Figure 7.14.

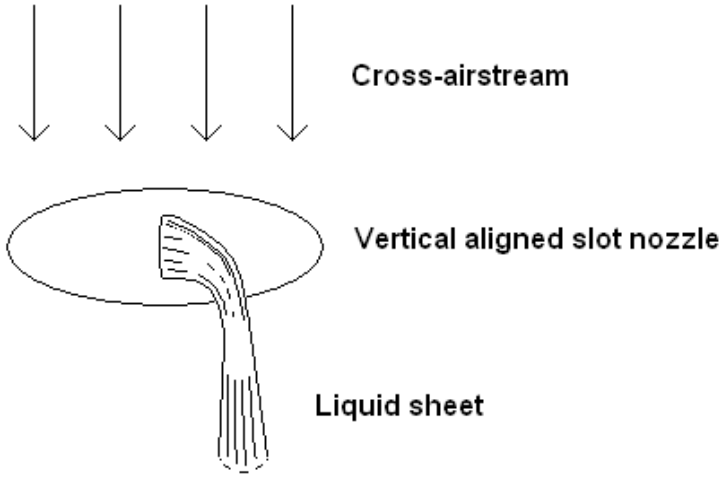

Figure 7.14: Vertically aligned ⇓ slot and liquid sheet

A vertically aligned slot ⇓ minimises the drag experienced by the cross-airstream and therefore maximises penetration depth.

7.3.1 Spray-Field Characteristics

Previously Table 7.1 showed the target test conditions, Table 7.4 shows the measured conditions for the PDPA tests completed with the vertically aligned nozzle.

	$W_{mean} \approx$ **90 m/s**	$W_{mean} \approx$ **135 m/s**	$W_{mean} \approx$ **195 m/s**
Δ**p ≈ 0.5 bar**	Case 1: 320, (3.4)	Case 5: 699, (1.6)	Case 9: 1630, (0.6)
Δ**p ≈ 1.5 bar**	Case 2: 331, (9.1)	Case 6: 721, (4.2)	Case 10: 1661, (1.8)
Δ**p ≈ 3.5 bar**	Case 3: 321, (20.3)	Case 7: 710, (9.4)	Case 11: 1604, (4.2)
Δ**p ≈ 6.5 bar**	Case 4: not possible	Case 8: not possible	Case 12: 1581, (7.5)

Table 7.4: ⇓ PDPA average test conditions vertical slot, $We_{g\,deq}$ (q)

The conditions in Cases 4 and 8 led to a large spray field that impinged on the test section windows, through which it proved impossible to obtain data. Although it was possible to obtain data in the large spray produced by Case 3, a considerable amount of the spray periphery impinged on the windows at the downstream planes $z = 40$ and 70 mm. In contrast in Case 9 the entire spray-field remained in close proximity to the nozzle wall and it is reasonable to assume that a significant proportion of the spray existed in an area inaccessible to the PDPA measurement volume (i.e. less than 4 mm from the nozzle wall refer to Figure 4.10). Cases 4 and 9, represent the two extremes of these tests.

As in the previous section for the horizontal slot nozzle data, the following discussion of the vertical nozzle data is divided into two categories: firstly, the response of the spray behaviour to changes in Weber number ($We_{g\,deq}$) at constant momentum flux ration (q) are examined; and secondly, the response of the spray behaviour to changes in momentum flux ration (q) at constant Weber number ($We_{g\,deq}$) are examined.

Weber Number Analysis (constant q)

As was discussed previously, the responses of the spray to variations in $We_{g\,deq}$ are more clearly identified across tests with the same momentum flux ratio. In these tests, variations in $We_{g\,deq}$ are brought about by changing the cross-airstream velocity W_{mean}. In order for tests to possess the same q value, the liquid flow rate must remain in proportion with W_{mean}. From the test matrix, it is possible to form two sets of three cases that satisfy this condition:

- Cases 1, 6 and 11, where $q \approx 3.9$; or,
- Cases 2, 7 and 12, where $q \approx 8.7$.

The following analyses focuses on Cases 2, 7 and 12, where $q \approx 8.7$ and $We_{g\,deq} =$ 331, 710 and 1581, respectively. Figure 7.15 shows the distribution of: (a) droplet axial component of velocity; (b) droplet transverse component of velocity; and, (c) droplet diameter in AMD [D_{10}] .

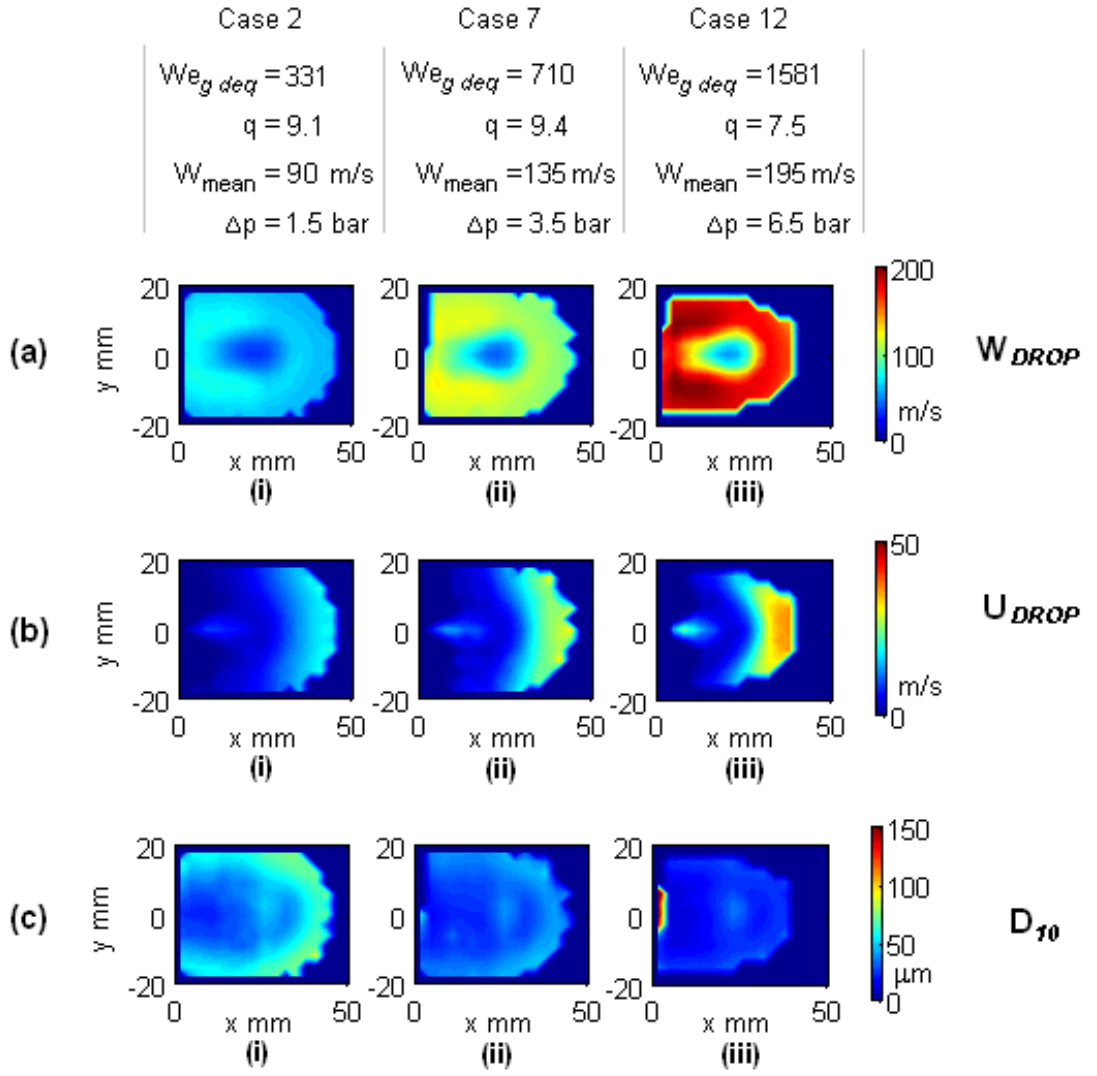

Figure 7.15: ⇊ Contour plots of (a) W_{drop}, (b) U_{drop} and (c) AMD [D_{10}] ; at the z = 40 mm plane; for $We_{g\,deq}$ = 331, 710 & 1581 and constant $q \approx 8.7$

For round nozzles, it is well established that q provides a good indicator for spray penetration. In these distributions the overall penetration is relatively stable indicating that q should provide a reasonable basis for predicting spray penetration for a vertically aligned slot nozzle. However it is important to recognise this does not imply that the relationship of q with spray penetration established for round nozzles is relevant to non-round nozzle geometries. Spray penetration is very dependent on nozzle geometry and orientation.

The distributions in row a show how much cross-airstream velocity has been attained by the droplets at the z = 40 mm plane. As one scans, from left to right across the contours plots, W_{drop} obtains higher values corresponding with increases in W_{mean} (90, 135 and 195 m/s respectively) across the three different

Weber number test conditions. Similarly to the horizontal nozzle plots in the previous section, a significant wake region can easily be identified in all cases.

In row b the distributions U_{drop} show how much transverse velocity has been retained by the droplets at the z = 40 mm plane, where the theoretical (from continuity) mean nozzle exit velocity, at z = 0 mm, was 11.0, 15.6 and 22.0 m/s (respectively). As would be expected, given these different injection rates, the intensity of U_{drop} can be seen to increase across the three test conditions. In plot 'b-iii', compared to plots 'b-i' and 'b-ii', the greater transverse velocity could be interpreted to mean that downstream penetration will also be greater; which is counter to the theory that penetration is controlled by q. However, since the cross-airstream is also greater, downstream penetration will remain proportional, as is clearly the situation upstream as penetration is comparable at z = 40 mm.

In row c the AMD [D_{10}] distribution plots show similar trends to those for round nozzles, in general, with larger droplets tending to the far periphery. An inflection in the droplet AMD [D_{10}] increase with distance from the wall is clearly evident, as was the case for the horizontal nozzle tests described in the previous section.

Figure 7.16 shows the variation of AMD [D_{10}] with distance from the nozzle wall (x = 0 to 50 mm) for the centre-line (y = 0) mm at the z = 40 mm plane. This shows more clearly the extent of the inflection exhibited in the overall increase in AMD [D_{10}] with distance form the nozzle wall.

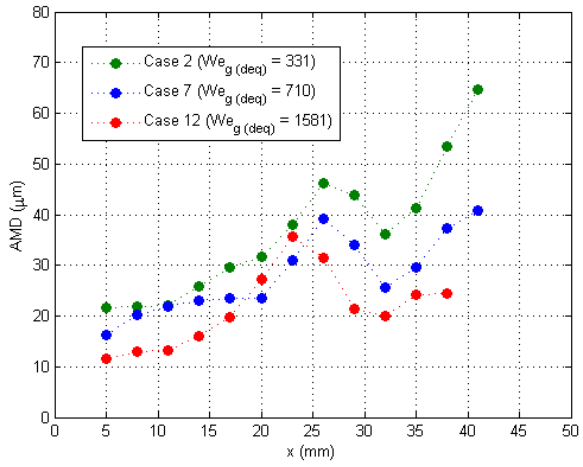

Figure 7.16: ⇓ Variation of centre-line AMD [D_{10}] with distance from the nozzle wall; x = 0 to 50 mm, y = 0 mm & z = 40 mm; for $We_{g\,deq}$ = 331, 710 and 1581; and, nominally constant $q \approx 8.7$ (Cases 2, 7 and 12)

In Case 12, q was lower at 7.5 than it was for Cases 2 and 7 at 9.1 and 9.4, respectively. As a result, for Case 12 (q = 7.5) AMD [D_{10}] peaks initially at x = 23 mm; where as for Cases 2 and 7 (q = 9.1 and 9.4) AMD [D_{10}] peaks initially at x = 26 mm. This gives some indication of the sensitivity of spray location to q. Nevertheless, Figure 7.16 shows the general shift in droplet size brought about the variation in $We_{g\,deq}$ over the three tests.

Figure 7.17 shows the range of AMD [D_{10}] measured for each of the test conditions (Cases 1 to 12).

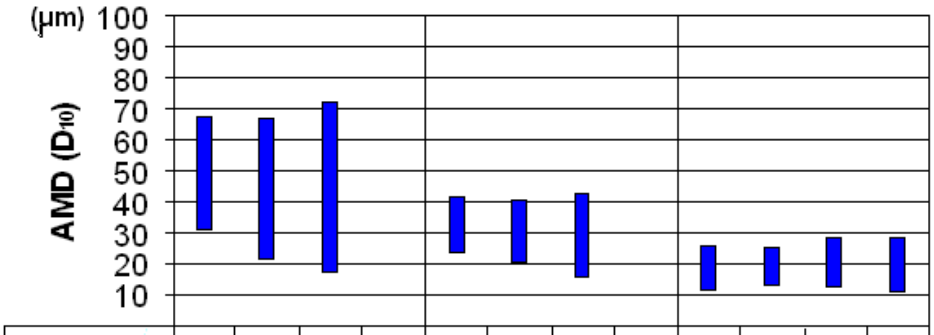

Case no.	1	2	3	4	5	6	7	8	9	10	11	12
q	3.4	9.1	20.3		1.6	4.2	9.4		0.6	1.8	4.2	7.5
We_{gdeq}	320	331	321		699	721	710		1630	1661	1604	1581

Figure 7.17: ⇊ AMD [D_{10}] range; at z = 40 mm; for all test cases

The ranges depicted, in Figure 7.17, have been filtered to exclude data which was based on less than 2600 individual measurements, as this level was shown to produce repeatability within ± 1 μm (described in Section 4.3.2). There is, as was the case for the horizontal nozzle tests and discussed in the previous section, evidence that increasing q widened the range of droplets measured.

It can be seen from Figure 7.17, overall, $We_{g\,deq}$ is the primary determinant in droplet size prediction with q providing a secondary influence. Although as was described in the previous section the smaller droplets produced with increasing q, is more likely to result from increasing transverse Weber number than from changes in the momentum balance.

This subsection examined the vertical slot nozzle data with reference to changes in $We_{g\,deq}$ with q held constant, the following sub-section focuses on this data with reference to changes in q across tests with nominally constant $We_{g\,deq}$.

Momentum Flux Ratio Analysis (constant $We_{g\,deq}$)

The variation in spray characteristics with changes in q are more clearly identified across tests with constant $We_{g\,deq}$. In these tests, changes in q are brought about by varying the liquid delivery rate. In order to hold $We_{g\,deq}$ constant, W_{mean} must remain constant.

From the test matrix, it is possible to form three sets of tests that satisfy this condition:

- Cases 1, 2 and 3, where $We_{g\,deq} \approx 331$;
- Cases 5, 6 and 7, where $We_{g\,deq} \approx 710$; or,
- Cases 9, 10, 11 and 12, where $We_{g\,deq} \approx 1538$.

The following analyses focuses on Cases 9 to 12, where q = 0.6, 1.8, 4.2 and 7.5 respectively and $We_{g\,deq} \approx 1538$. Figure 7.18 shows the distribution of: (a) droplet axial component of velocity; (b) droplet transverse component of velocity; and, (c) droplet diameter in AMD [D_{10}] at the z = 40 mm plane.

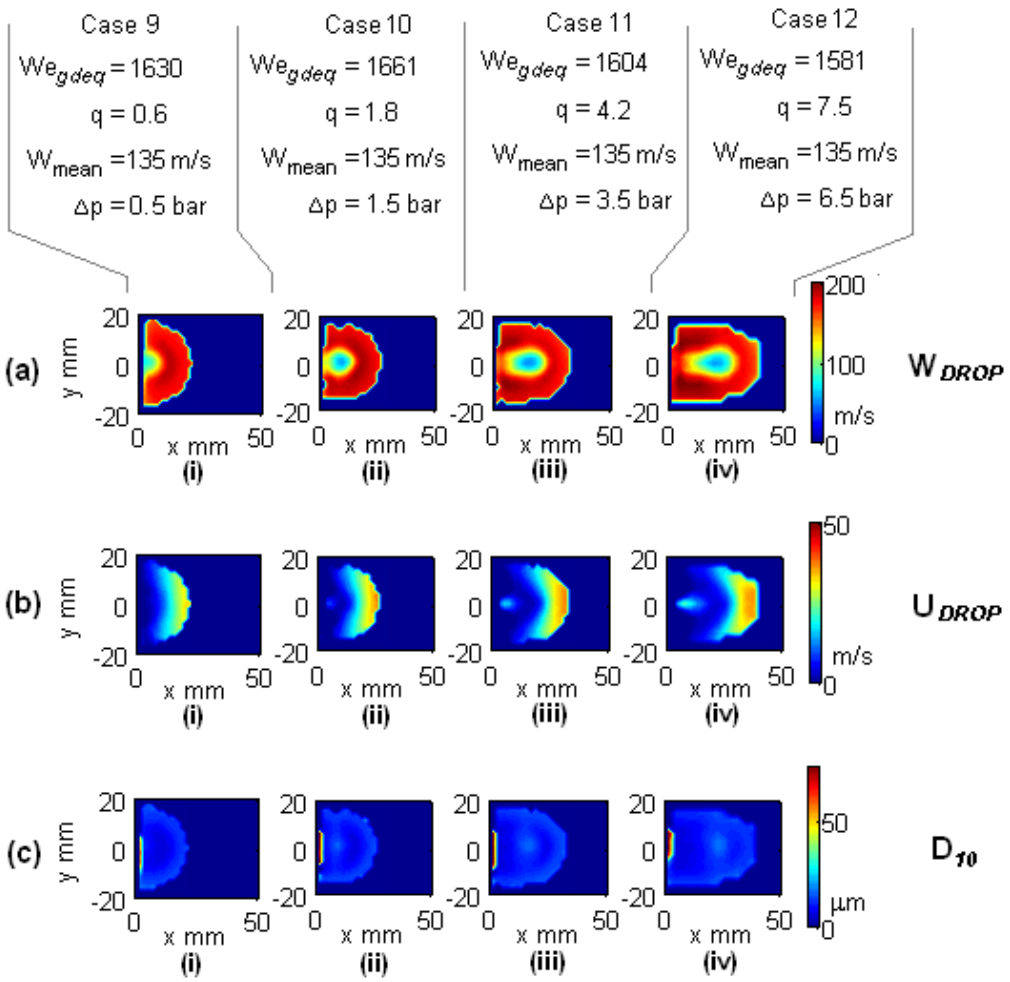

Figure 7.18: ⇊ Contour plots of (a) W_{drop}, (b) U_{drop} and (c) AMD [D_{10}] ; at z = 40 mm, q = 0.6, 1.8, 4.2 and 7.5 and constant We$_{g\,deq} \approx 1538$

From Figure 7.18 it is evident that the area occupied by the spray field increases with increasing q, as would be expected from increasing the liquid flow rate.

The data appears to suggest some spray interference with the side windows (i.e. the test section was too narrow), although not ideal, this is not considered to be influential on the findings presented. The fact that good measurements were obtained indicates that light rays passed through the side-windows cleanly and without unwanted refraction. This is only possible with small/occasional liquid impinging on the test section side-windows, representing just a small fraction of the overall liquid mass transfer.

Row a in Figure 7.18 shows the axial component of velocity (W_{drop}) the droplets have obtained by the z = 40 mm plane. A wake region can be identified in all

four plots and it can be seen how this region migrates away from the injector wall with increasing q. This shows that the wake region is associated with the blockage created by the combined mass of the spray core rather than the liquid sheet. Since the liquid sheet extends from the nozzle wall and the droplet's axial velocities close to the nozzle wall can be seen to be almost equal to the cross-airstream mean velocity $\approx$ 195 m/s, rather than having retarded velocity indicative of the wake region.

Row b in Figure 7.18 shows the transverse component of velocity (U_{drop}) the droplets have retained at the z = 40 mm plane. As was discussed previously, these plots of transverse velocity adopt a stratified pattern with the highest U_{drop} values found in the far periphery furthest from the nozzle wall.

Row c in Figure 7.18 shows the results of AMD [D_{10}] measured at the z = 40 mm plane. AMD [D_{10}] appears to be reasonably constant for q = 0.6, 1.8, 4.2 and 7.5; as would be expected for approximately constant Weber number.

This and the previous sections in this chapter, for the most part, have focused on sprays from each slot nozzle orientation without cross reference or comparison between orientations - the aim was to establish each set of tests in isolation. The following section focuses on the commonalities and differences of the spray characteristics between different nozzle types and orientations.

7.4 Comparison of Horizontal and Vertical Slot Tests

The previous sections in this chapter focused on the spray characteristics for the horizontal and vertical slot nozzle tests in isolation. This section builds on this and focuses on the differences between the sprays from the horizontal and vertical slot nozzle tests.

The different nozzle arrangements led to very different looking liquid flows emanating from the nozzle exit, e.g. as can be seen in Figure 7.19.

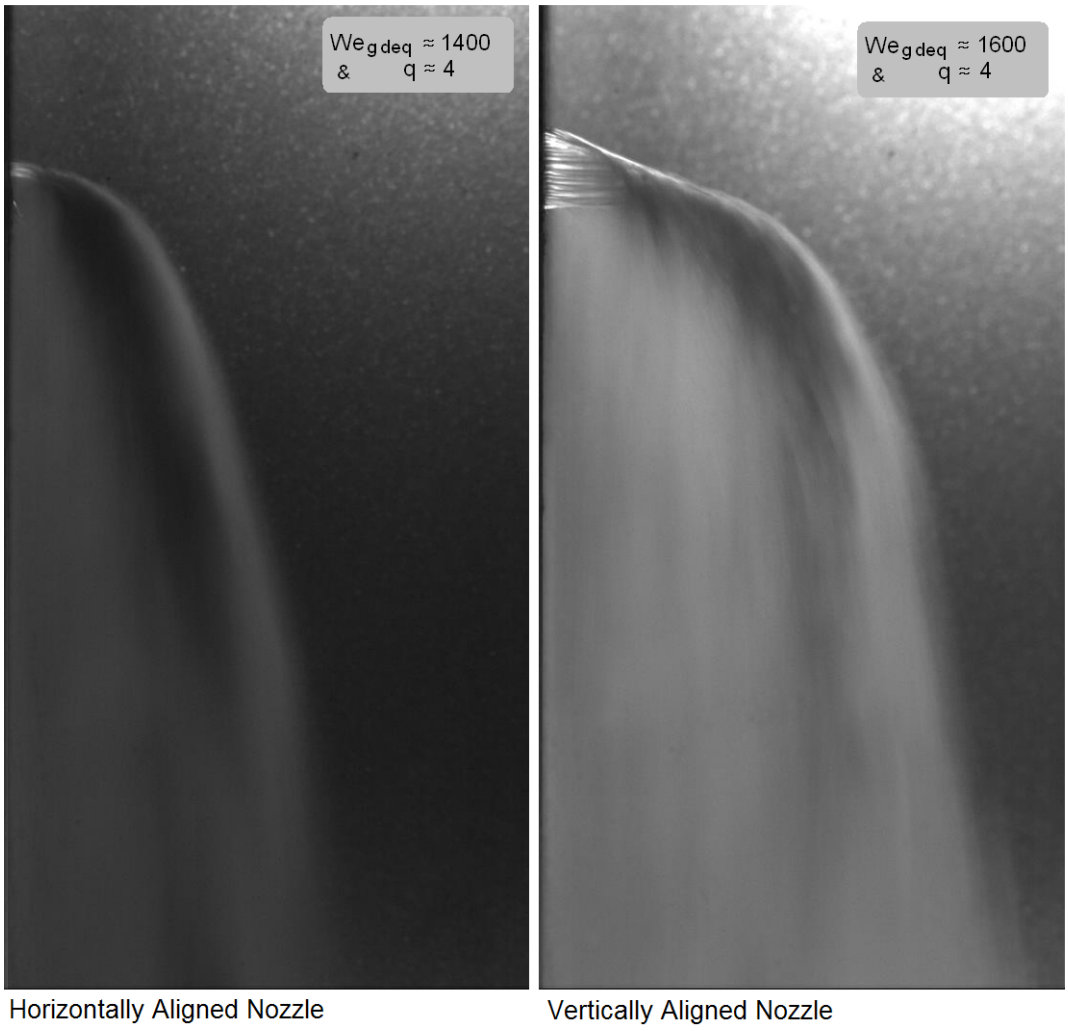

Figure 7.19: ⇊⇊ Liquid flow emanating from the nozzle exit

The horizontal slot spray appears to be quite similar to a round nozzle spray (e.g. Figure 6.1), however, it is important to consider these pictures only provide a side-on view; from an end-on view horizontal and round nozzle sprays look quite different because the slot nozzle has much greater depth. Nevertheless,

there are clearly similarities between the shape and penetration of the liquid jet from a round nozzle and the liquid sheet from a horizontal slot nozzle. The emanating horizontal liquid sheet appears to behave as one might expect a horizontal row of round nozzles would.

In contrast, the vertically aligned slot nozzle is very different in its format. As the vertical liquid sheet extends away from the nozzle exit, it *rolls over* toward the observer (out of the page). Although no visual evidence is provided here, the vertical liquid sheet's deformation is symmetrical across the y_{origin} plane and the *rolling over* occurred on both sides simultaneously, rather than being heavily biased to one side or flipping from one side to the other.

The vertical liquid sheet converges away from the nozzle, as identified in Figure 7.20.

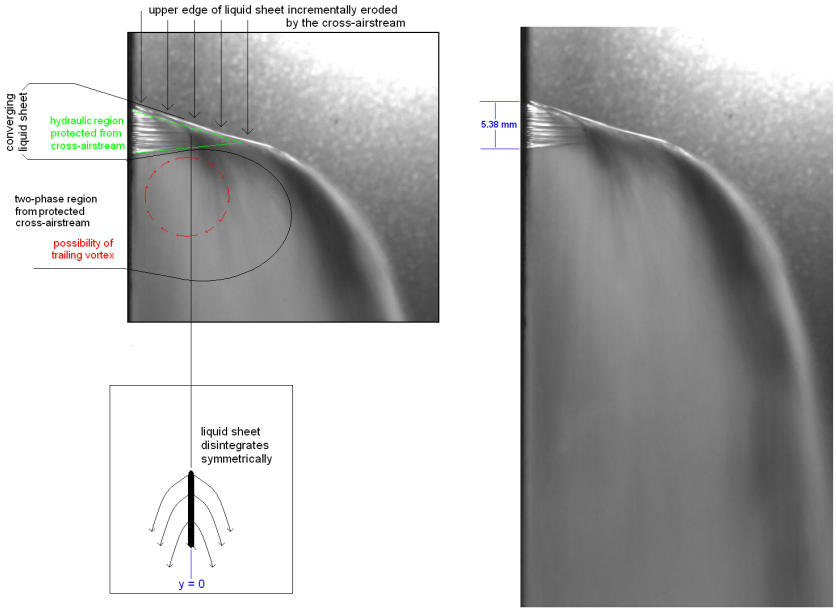

Figure 7.20: ⇓ⓘ Structure of vertical liquid sheet; for, $We_{gdeq} \approx 1600$ and $q \approx 7.5$ (Case 12)

The convergence of the liquid sheet could be the result of surface tension, acting to reduce the surface area of the liquid body to a minimum, therefore, the flowing liquid sheet will naturally tend to a cylindrical form. As the lower side of the liquid sheet is protected from the cross-airstream by the upper side, the lower half of the liquid sheet is able to flow slightly upwards against the direction of the cross-airstream. However, the flow field in the two-phase region directly under the liquid continuum is highly complicated, a 'trailing vortex' can form within this region (as illustrated in Figure 6.26 in Chapter 6) and therefore the

convergent liquid flow exhibited from the vertical slot may be the result of a combination of factors.

The vertical liquid sheet's disintegration was a more gradual process than it was for the horizontal sheet. The liquid's *direct* exposure to the cross-airstream is incremental along the upper edge of the liquid sheet. Because of this incremental exposure, the vertical liquid sheet appears to break-up in a relatively ordered fashion and, overall, the flow field was generally more steady for the vertical slot sprays than it was for the horizontal slot sprays.

For Case 12 presented in Figure 7.20, from $x = 0$ to ≈ 12 mm, as the upper edge of the liquid sheet was eroded by the engaging cross-airstream, so the hydraulic lower section of the sheet appears to replenish the upper edge, maintaining the sheet as a complete liquid body. As a result, the vertical liquid sheet exhibited a strikingly straight line along its upper edge, before there is a more definite collapse - from which point the outer edge of the spray appears to adopt a trajectory more consistent with both the horizontal slot and round nozzle. The progressive nature of the vertical liquid sheet break-up, offsets the spray-field in the x direction and leads to greater spray penetration than for the horizontal slot at the same air and liquid flow rates (i.e. same q).

From the assessment above it is clear that the disintegration of the horizontal and vertical liquid sheets were quite different. However, the range of AMD [D_{10}] measured in the corresponding spray fields was similar for both orientations, as can be seen in Figure 7.21.

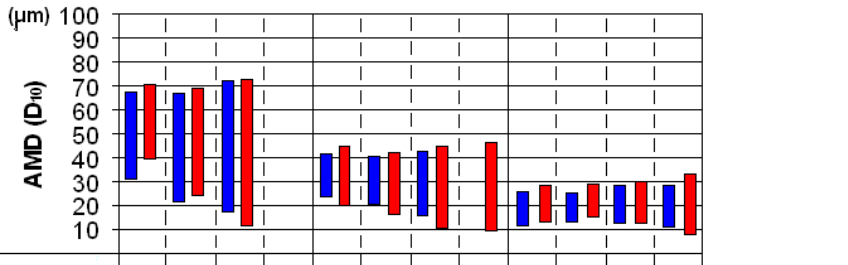

Case no.	1	2	3	4	5	6	7	8	9	10	11	12
q	3.4	9.1	20.3		1.6	4.2	9.4		0.6	1.8	4.2	7.5
We_{gdeq}	320	331	321		699	721	710		1630	1661	1604	1581
q	2.7	7.5	20.4		1.2	3.3	8.6	15.8	0.5	1.8	4.1	8.6
We_{gdeq}	310	304	297		727	699	704	709	1520	1531	1444	1263

Figure 7.21: ⇊⊖ ⇊⊕ AMD [D_{10}] ranges for all test cases completed; at the $z = 40$ mm plane

Figure 7.21 is a somewhat basic comparison because it only highlights the mini-

mum and maximum values of AMD [D_{10}] measured in the sprays, nevertheless, it is interesting that there is such close agreement in the droplet size ranges for the two slot orientations.

The main reason Figure 7.21 is not a rigorous comparison is because it does not address the mass transfer associated with each AMD [D_{10}] measurement. The dense sprays produced by the slot nozzle prevented the PDPA system returning reliable flux measurements because of multi-occupancy problems as described in Figure 4.8. Manual flux measurements were considered but there was not time available to complete them, however, the location of the spray core can be estimated from the various data that was acquired. Hence, an extension of Figure 7.21 is to examine and compare the AMD [D_{10}] measured in the spray core (where the bulk of the mass transfer occurs).

The Dantec PDPA system measures the droplet in the *measurement volume* twice at two different circumferential locations of the droplet (as described in Section 4.3.1), the software compares the two measurements and rejects the result if they do not agree (within a tolerance). In theory, where the two measurements do not agree it proves the droplet was not spherical. However, where multi-occupancy in the measurement volume occur, the two measurements do not agree and the incident is often rejected also as a non-spherical incident - hence through the spray core a reduction in signal to noise ratio results in lower spherical validity.

Figure 7.22, is a series of plots and an image of the corresponding spray field from HSV. The line plots (row C) show AMD [D_{10}] on the centre-line as well as the *spherical validity* that was associated with the measurements. Using spherical validity as a guide, two red vertical lines have been superimposed over the plots to highlight the region where spherical validity fell below 80% and this provides an estimate for the location of the spray core at z = 40 mm.

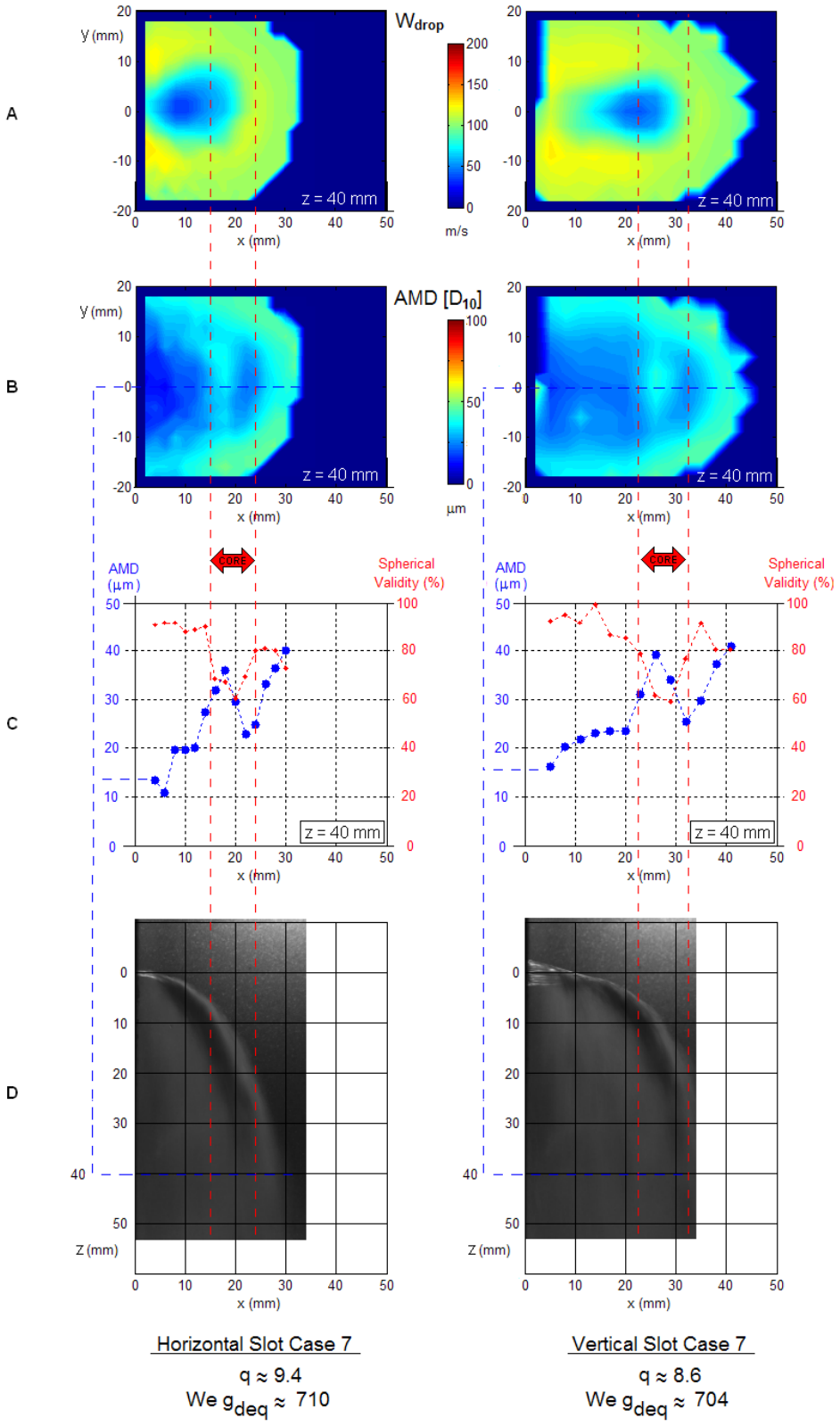

Figure 7.22: ⇊⇊ (A) contour plot of W_{drop}, (B) contour plot of AMD [D_{10}] , (C) line-plots of AMD [D_{10}] & spherical validity and (D) HSV image; for $We_{g\,deq} \approx 710$ & 704 & $q \approx 9.4$ & 8.6 (Case 7)

Both cases exhibit a double peak in the AMD [D_{10}] trend (in row C), i.e. $\Downarrow x$ = 18 & 30 mm and $\Downarrow x$ = 26 & 41 mm, the initial peak was described (in Chapter 6) as an inflection for round nozzle sprays and attributed to occur where the spray was sufficiently dense, rather than a direct feature of low q conditions. In these slot nozzle experiments, the spray density was extreme by comparison and so is the inflection in the AMD [D_{10}] trend, to the extent that it no longer appeared as an inflection within the general trend away from the nozzle wall, as it did for the round nozzle sprays, but a more disconnected and distinct region of droplets.

In Chapter 6, Figure 6.17, showed that **Wu et al. (1998)** found the center of the spray core coincided with the initial peak in droplet size, for round nozzle sprays that exhibited an inflected AMD [D_{10}] trend away from the nozzle wall. Although specific flux measurements would be required to categorically confirm this is also true for both horizontal and vertical slot sprays, row C, in Figure 7.22 does indicate that the initial peak was within the spray core and could be the spray core centre as it is for round nozzles (recalling that the reduction in spherical validity is only a guide for the spray core location). Hence, with a degree of caution, the initial peak in AMD [D_{10}] can by extension be used as a guide for the location of the spray core. In addition, the images in row D in Figure 7.22 support the observation.

Based on spherical validity, the spray core for the horizontal orientation at the z = 40 mm plane, was estimated to be between x = 15 to 24 mm, the corresponding AMD [D_{10}] in this x section ranged from 22 to 37 μm. For the vertical nozzle spray the core was estimated to be located from x = 23 to 33 mm and the AMD [D_{10}] ranged between 26 to 39 μm. Therefore, as well as the overall AMD [D_{10}] ranges being similar for the two nozzle orientations, so was the AMD [D_{10}] associated with the spray cores - with the vertical nozzle's spray core AMD [D_{10}] being marginally higher than that of the horizontal nozzle.

Because the vertical slot orientation provides greater spray penetration than the horizontal slot, it is perhaps intuitive to think the spray from the vertical nozzle would be more dispersed. However, if this were the case then one would expect AMD [D_{10}] to be smaller in the core of the spray for the vertical slot spray as droplets would be more exposed to the dynamic force of cross-airstream.

It is not entirely clear why the vertical nozzle spray appeared to have a marginally greater AMD [D_{10}] through the spray core, however, one explanation is as follows.

In the horizontal orientation ⇊⊖ the liquid is injected over $y \approx$ -2.5 to +2.5 mm and $z \approx$ -0.25 to +0.25 mm and, as a result, the liquid injectant is efficiently exposed to the cross-airstream. In the vertical slot configuration ⇊⊕ the liquid is injected over $y \approx$ -0.25 to +0.25 mm and $z \approx$ -2.5 to +2.5 mm and, as a result, the liquid is largely protected from the cross-airstream.

The contour plots of W_{drop}, in row A in Figure 7.22, show the wake region (as identified by the distinct region of suppressed axial velocities, as described in Figure 7.7) appears to have occupied a slightly larger area for the horizontal slot. This supports the concept that the vertical nozzle provided a slightly reduced dispersion (i.e. greater spray density through the spray core), albeit offset in x and with a larger plane-wide wet area overall.

On this basis, the AMD [D_{10}] peak which occurs in the spray core should be greater for the vertical slot than for the horizontal slot in all cases. To examine this further, Figure 7.23 presents a map of AMD [D_{10}] centre-line distribution for horizontal ⇊⊖ and vertical ⇊⊕ slot sprays for all cases tested.

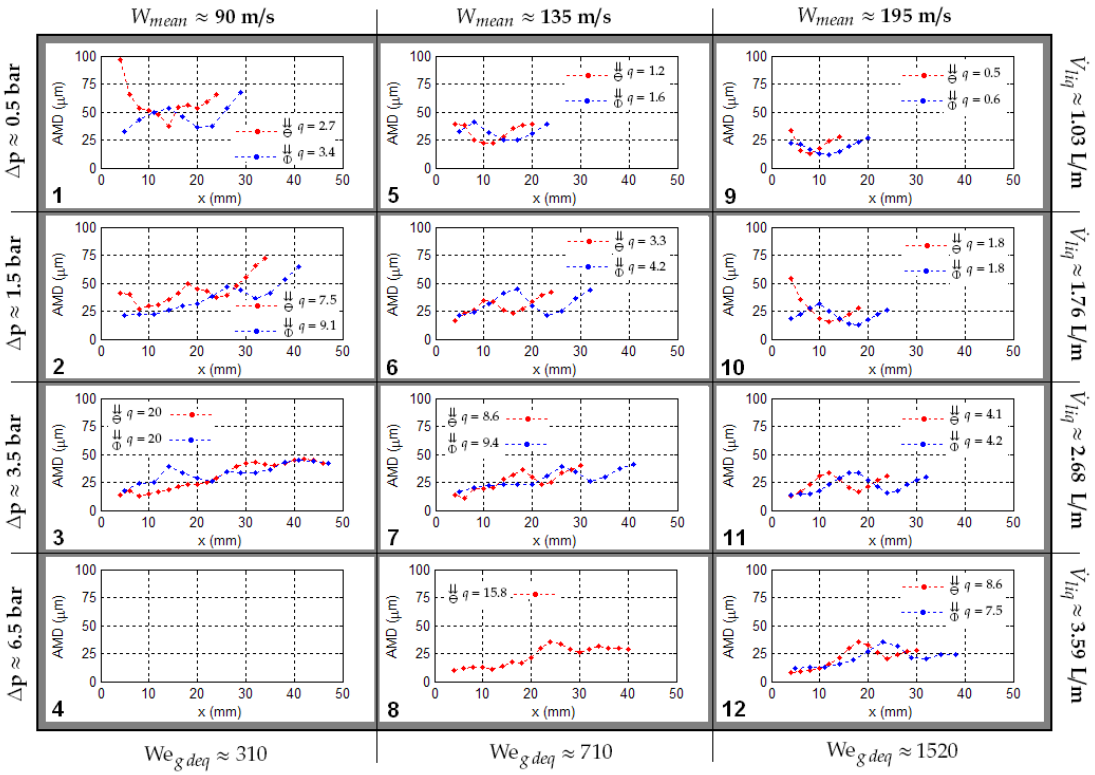

Figure 7.23: ⇊⊖ ⇊⊕ Line-plots of AMD [D_{10}] ; at x = 0 to 50 mm, y = 0 mm & z = 40 mm; for Cases 1 to 12

There is a considerable amount of information in Figure 7.23, and inspection of it provides several insights into the flow physics. The plots are positioned in

the same way as the test matrix was presented in Table 7.1. The basis is that looking left-to-right across plots shows the effect of increasing $We_{g\,deq}$. Looking down the plots shows the effect of increasing q. Looking diagonally, e.g. Plots 2, 7, and 12 shows the effects of increasing $We_{g\,deq}$ and increasing liquid flow rate with constant q (i.e. constant penetration).

In Plot 3 for the vertical ⇊ nozzle spray, there is some apparently erroneous data. The AMD [D_{10}] measurements from x = 4 to 30 mm appear to lack consistency and in particular the AMD [D_{10}] measurement of approximately 40 μm at x = 14 mm cannot be explained.

In Plots 1 and 2, it can be seen that the periphery of the spray field for the ⇊ spray penetrated some 8 mm further than it did for the corresponding ⇊ spray. In Plot 3 the ⇊ measurements extend to x = 46 mm and hence, for the ⇊ slot the spray would be expected to reach $x \approx 54$ mm, which is beyond the spray domain available.

It is likely therefore, the questionable ⇊ AMD [D_{10}] measurements in Plot 3 are a result of too much liquid interference with the test section boundary. This also demonstrates why ⇊ Case 8, with an increased liquid flow rate compared to Case 3, could not produce useful results, and the experiment being abandoned.

For the ⇊ spray in Plot 3, the AMD [D_{10}] trend is generally flatter, and it appears the spray is tending to the basic droplet distribution mechanism described in Figure 6.16, with increasing q and increasing dispersion. This also being a characteristic of sprays from round nozzles.

An overview of Figure 7.23 shows how the spray core and spray periphery for the ⇊ slot penetrated further into the test section domain than the ⇊ in all cases. Further inspection reveals clearly the cases where the spray core was to close to the nozzle wall for the measurement approach to obtain comprehensive coverage of the spray field.

For example, in Plot 9 the ⇊ AMD [D_{10}] distribution does not display the characteristic double peak defining the position of the spray core. However, setting a straight edge against a line that cuts-through the ⇊ spray core peaks in plots 10, 11 and 12 and extending the line upwards to Plot 9, shows where the spray core is likely to be for ⇊ q = 0.6, doing so reveals that in Plot 9 the ⇊ spray core would be outside the measurable domain - too close to the nozzle wall.

Hence, Figure 7.23 shows that a detailed investigation for ⇊ $q \lesssim 1.5$ would require a modified test apparatus and PDPA setup; and, $q \lesssim 4$ for ⇊ sprays.

This information demonstrates that it is necessary to be selective with the data available. For example, conditions that led to sprays that could not be fully characterised would be unlikely to be useful for CFD validation, but it is these sprays that widen the scope of the tests and whilst there is information missing - the information there is - can be used to develop understanding for the flow physics.

Previously, Figure 7.22 (row C) showed that for the spray core peak AMD [D_{10}] in the vertical ⇊ spray was greater than it was in the corresponding horizontal ⇊ spray (for Case 7). It was hypothesized that this could be due to the efficient way the ⇊ nozzle exposes the liquid sheet to the cross-airstream leading to the ⇊ sprays having a slightly less densely populated spray core (than the ⇊ sprays), resulting in a less intense blockage and wake region for the ⇊ sprays and, hence, AMD [D_{10}] ⇊ > AMD [D_{10}] ⇊ in the spray core.

However, whilst Plots 6 and 7 in Figure 7.23 support the hypothesis, none of the other plots do, in particular Plots 2, 3, 11 and 12 show the spray core peak AMD [D_{10}] ⇊ ≅ AMD [D_{10}] ⇊. On this basis, in general, the data shows spray core AMD [D_{10}] was similar between the slot orientations for a given condition.

The most striking deviation from the general trends is observed in Plot 1 for the ⇊ at $x < 10$ mm - with an extreme rise in the AMD [D_{10}] measured in this region. Further inspection shows that Plots 2, 3, 9 and 10 all display a degree of increased AMD [D_{10}] in the measurements nearest to the nozzle wall for the horizontal slot ⇊ results.

In Plot 10, the AMD [D_{10}] measured in the near wall region ($x \leq 6$ mm) for the horizontal spray is much larger than anywhere in Plots 11 or 12. In Plot 9, much of the spray from the horizontal nozzle was inaccessible for the PDPA setup, however, the apparent trend for $x < 6$ mm is again for increased AMD [D_{10}] and whilst the data is too limited to claim it confirms the high AMD [D_{10}] value measured in Plot 10, it does support the possibility of large droplets in the near wall region. Therefore, at $We_{g\,deq} \approx 1520$, there appears to be a significant change in the break-up physics between $q = 4.1$ and 1.8 for the horizontal slot nozzle.

At $We_{g\,deq} \approx 710$ and $q = 1.2$ (Plot 5) the large droplets at $x < 6$ mm appear to be the increase one would expect going into the spray core - so it is not clear whether or not the effect is present. Plot 1, clearly exhibits increased AMD [D_{10}] for the ⇊ spray in the near wall region. Although the $x < 10$ mm increase in ⇊ AMD [D_{10}] in Plot 1 appears out of place compared to the other plots, closer inspection shows that Plots 1 and 10 are quite similar - allowing for the difference in $We_{g\,deq}$.

Given the large ⇊ AMD [D_{10}] measurements in the near nozzle wall region reappear in several, generally low q conditions, they are more likely to be physical than measurement anomalies. Large droplets in the near wall region are not evident for any of the vertical ⇊ nozzle sprays.

Although not quantified, **Wu et al. (1998)** also noted increased diameters (but for round nozzle sprays) near to the injector wall, at low q conditions. They were considered to result from liquid impingement with the downstream edge of the nozzle exit. Because, the process is somewhat independent of the more general break-up physics, droplet sizes can be quite different from those appearing elsewhere in the spray-field.

At low q conditions the liquid jet emanating from the nozzle turns through a tight radius as the cross-airstream is the more dominant of the confluent fluids. The downstream edge of the nozzle exit 'gets in the way' of the natural path of the liquid body and, consequently, the interference causes liquid fragments to break off from the liquid body and this process is called impingement. Since impingement occurs at the lower (or downstream) nozzle exit edge, the fragments/droplets generated in this way are hidden from the cross-airstream by the liquid body itself and, as a result, they experience low Weber number conditions locally; the fragments/droplets are accelerated relatively gradually and can survive as large droplets downstream. Hence, it is the combination of two factors (impingement coupled with low local We_g) that combine to enable the relatively large droplets that can be found in the near wall region at low q conditions.

A perpendicular slot nozzle ⇊ (*i.e. horizontally aligned in the TFMRC arrangement*) maximises the length of the edge against which impingement occurs and, *in addition*, the normal liquid sheet emanating from the nozzle maximises the blockage to the cross-airstream. This could be expected to lead to a relatively high production of large droplets from impingement that are also relatively well protected from the dynamic forces of the cross-airstream.

As q decreases, so the impingement process becomes increasingly active and, simultaneously, the spray core (where the bulk of the mass transfer occurs) becomes increasingly closer to the nozzle wall - so at very low q conditions the spray core AMD [D_{10}] must be influenced by impingement, as appears to be the case in Plots 1 and 10 in Figure 7.23 for the horizontal nozzle. Of course at the extreme low end of the q spectrum, the liquid will simply dribble out of the nozzle exit and down the nozzle wall - hence at some threshold of q the situation can no longer be described as a spray.

This is an important point, not only for understanding the flow physics, but because it is clear that CFD codes developed to replicate the physics of an archetypal spray in cross-airstream, require a further level of sophistication to capture the flow physics at low q conditions where impingement becomes increasingly significant in the spray's droplet sizes.

To further demonstrate the existence of the large droplets created by impingement, Figure 7.24 is an image from HSV of a spray field from the horizontal nozzle which clearly shows large droplets near the nozzle wall.

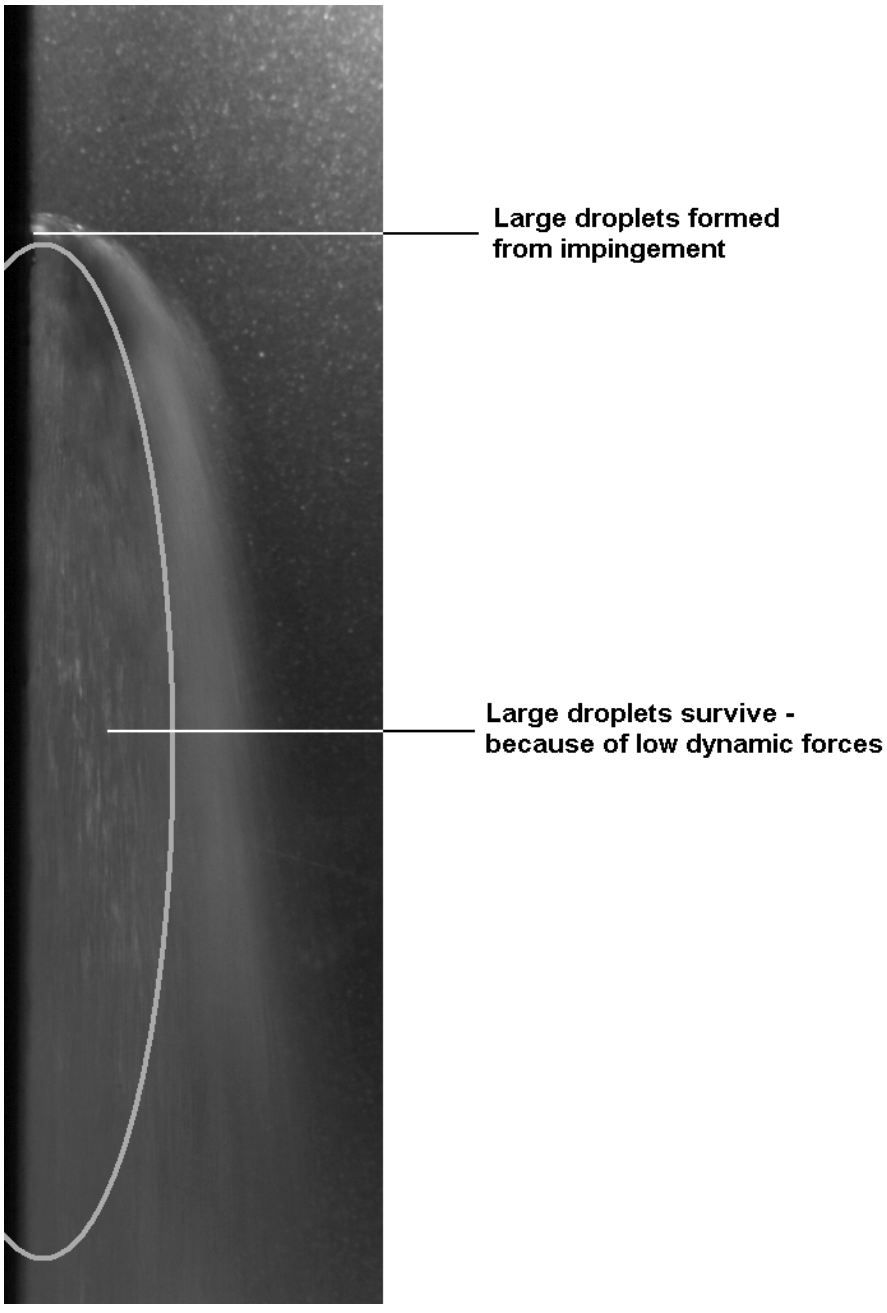

Figure 7.24: ⇊ Enlarged view of spray from HSV; for $We_{g\,deq}$ = 727 and q = 1.2 (Case 5)

Figure 7.24 confirms the existence of the large droplets that were measured by the PDPA system for the horizontal slot. Hence, where impingement is active the process can be illustrated as in Figure 7.25 (with cross reference to the previous Figures 6.18 and 6.16).

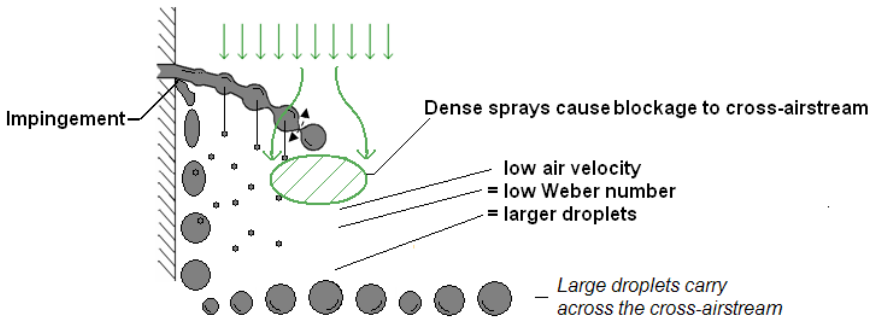

Figure 7.25: Illustration of droplet size distribution with impingement

For a round nozzle the plane-wide extent of droplets from impingement would not generally be expected to be significant and, as a result, impingement has not had a great deal, if any, of previous study. For the vertical nozzle, and its unique structure at the nozzle exit (as presented in Figure 7.20), it seems unlikely that impingement would ever be a feature of the resultant spray field. However, in contrast, the configuration of the horizontal nozzle promotes the onset and influence of impingement.

In order to show the plane-wide extent of the influence of impingement, for all nozzles ⇊⇊⇊, Figures 7.26, 7.27 and 7.28 show a plane-wide analysis of AMD [D_{10}] for Case 10. Each figure shows a contour plot of the recorded data without any filtering, whilst the corresponding histograms are presented with measurements based on less than 2500 samples removed.

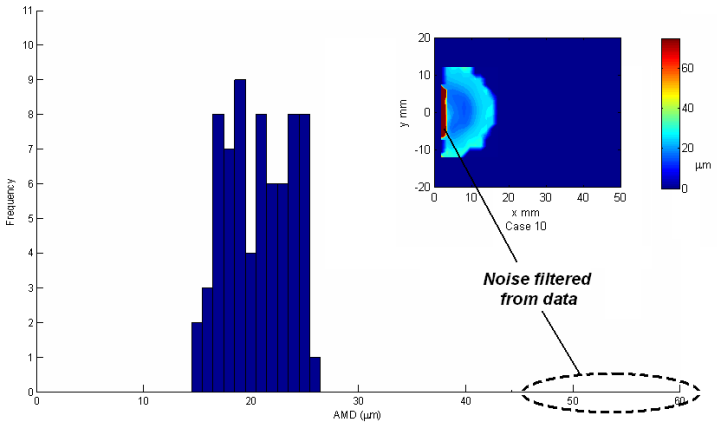

Figure 7.26: ⇓⊙ Plane-wide AMD; at $z = 40$ mm; for $We_g = 586$ and $q = 2.2$ (Case 10)

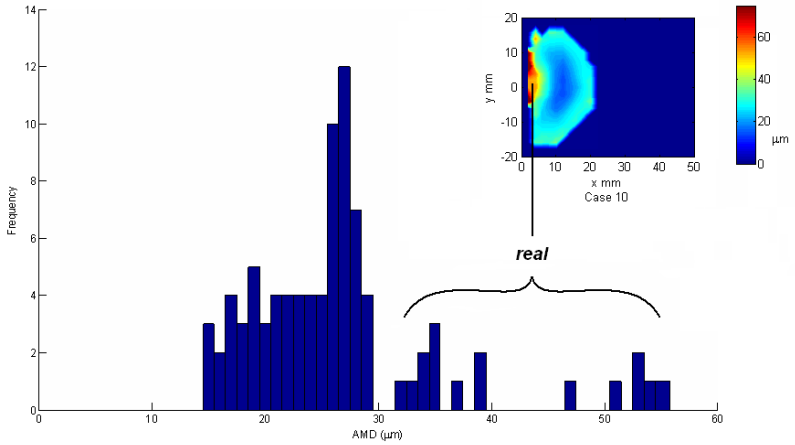

Figure 7.27: ⇓⊖ Plane-wide AMD; at $z = 40$ mm; for $We_{g\,deq} = 1531$ and $q = 1.8$ (Case 10)

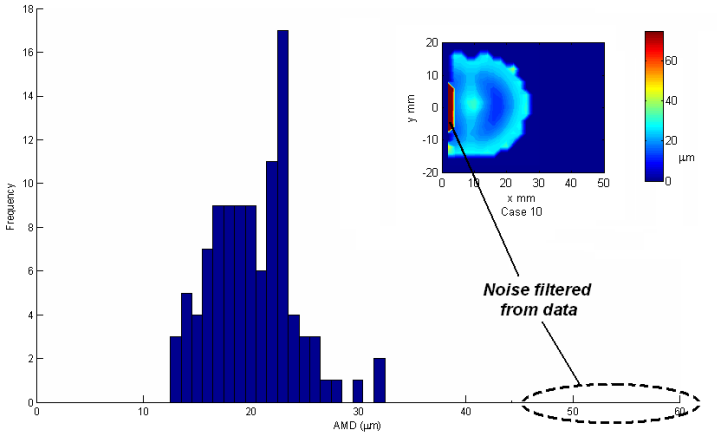

Figure 7.28: ⇓⊘ Plane-wide AMD; at $z = 40$ mm; for $We_g = 1661$ and $q = 1.8$ (Case 10)

The plane-wide histograms and corresponding contour plots within Figures 7.26, 7.27 and 7.28 show that the main body of the spray field yield similar AMD [D_{10}] characteristics for all three nozzle arrangements. For the round and vertical slot arrangements, the apparently incongruent measurements close to the nozzle wall are attributed to a poor signal to noise ratio as the proximity of the wall interferes with the measurement process at x = 2 - hence, these are erroneous measurements that should be ignored, easily filtered out, as it has been in the histograms.

However, in the horizontal slot arrangement the region of increased AMD [D_{10}] near the wall is more prominent and results from reliable measurements which do not get discarded by a sample count threshold limit. Figure 7.29 demonstrates the individual droplet measurements that contributed to a measurement at an affected location; using (x = 4 mm, y = 2 mm & z = 40 mm) as an example.

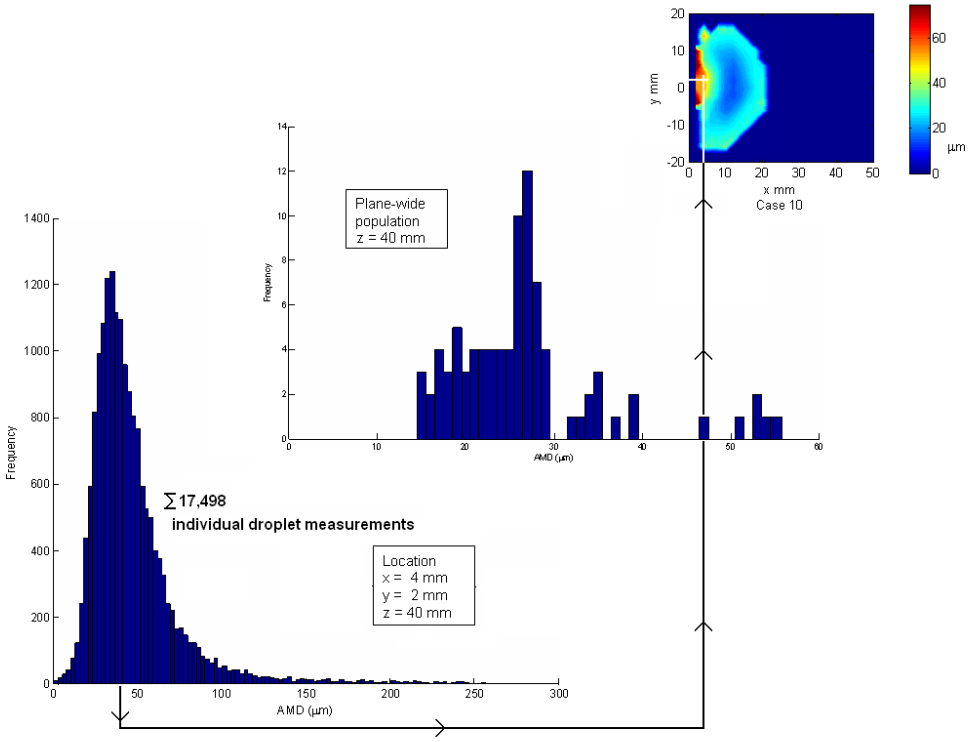

Figure 7.29: Breakdown of data path that contributes to the spray characteristics

The AMD [D_{10}] result of 47 μm at the location of (x = 4 mm, y = 2 mm & z = 40 mm) was based on over seventeen thousand successful individual droplet measurements, clearly demonstrating that although the value is somewhat greater than the measurements in the main body of the spray, the measurement has a high degree of statistical support.

With specific regard to the situation of a fractured oil pipe in a gas turbine engine, the results of impingement demonstrated in the TFMRC experiments are very much a result of the test arrangement. Although it is important to note that a perpendicular ⇊ aligned slot is particularly prone to the impingement mechanism, in the TFMRC tests it is the proximity of the injector wall that allows a protected region to become established and this allows the large droplets to maintain their mass downstream. In an engine scenario it is hard to say whether or not a leak arrangement could occur with the appropriate configuration to produce similar results.

Whilst it is probably impossible to design out the possibility of impingement occurring in an engine oil leak - it may be possible to arrange pipes in such a way that the region in which impingement could occur is exposed to the airstream. For example, offsetting oil pipes from surfaces would be expected to help expose the large droplets produced by impingement to the airstream.

It is apparent that a slot nozzle orientation with its major axis aligned with the cross-airstream ⇊ is much less prone to impingement. This, as well as greater penetration and stability would be expected to improve the match between CFD prediction and experiment.

However, engineers should also be aware that the horizontal nozzle ⇊ provides an effective solution to directly exposing a large liquid surface area to the dynamic forces of cross-airstream which break-up the liquid body. In contrast, the vertical alignment ⇊ minimises the injected liquid's direct exposure to the cross-airstream but, provides greater penetration as a result.

An important extension of this, and one that is perhaps counterintuitive, is to recognise that the greater penetration and larger wet area associated with vertical nozzle ⇊ sprays did not appear to produce a more dispersed spray core.

Based on the current data, droplet size in the spray core and the far periphery was similar between the vertical nozzle ⇊ and horizontal nozzle ⇊. It is possible that the greater penetration of the vertical nozzle ⇊ provides adequate dispersion to largely cancel out the comparatively reduced exposure of its liquid sheet to the cross-airstream and, on balance, droplet sizes in sprays from vertical and horizontal slot sprays are characteristically similar - as was the finding for this study, where impingement was not a feature of the corresponding horizontal nozzle ⇊ spray. Nevertheless, it is worth noting that where the spray core is dense larger droplets would be expected to prevail - according to the theory that was used to explain the inflected AMD [D_{10}] trend.

Chapter 8

Conclusions and Recommendations for Future Work

The purpose of this study was to provide insight into the sprays that develop when oil leaks occur in commercial gas turbine engines. This objective was pursued by creating experimental sprays formed from non-round nozzle geometries, injecting liquid into subsonic airstreams. This required the installation of a new purpose built test facility. The key spray characteristics of droplet size and velocity were measured using a Dantec PDPA system. Further characterisation of the spray field including upstream features were completed using high-speed video and pulsed laser sheet digital imaging.

It was shown that plain tap water provided an acceptable substitute for engine oil; this allowed for simplified test apparatus, compared to testing with engine oil, and an extensive programme of testing was possible as a result. Testing was repeated over a twelve point test matrix with a round nozzle (d = 0.57 mm) and a slot nozzle (Aspect Ratio = 0.5 x 5.38 mm) in two orientations, 36 test points in total.

The test matrix was aimed at conducting experiments at engine representative conditions. Figure 8.1 shows the relevance of the test conditions with respect to those expected to occur in the engine. The region in blue represents the range deemed possible in the engine, assuming oil leaking through a crack measuring 0.1 by 0.5 mm or d_{eq} = 0.602 mm (noting that the slot nozzle used in these tests had d_{eq} = 1.6 mm).

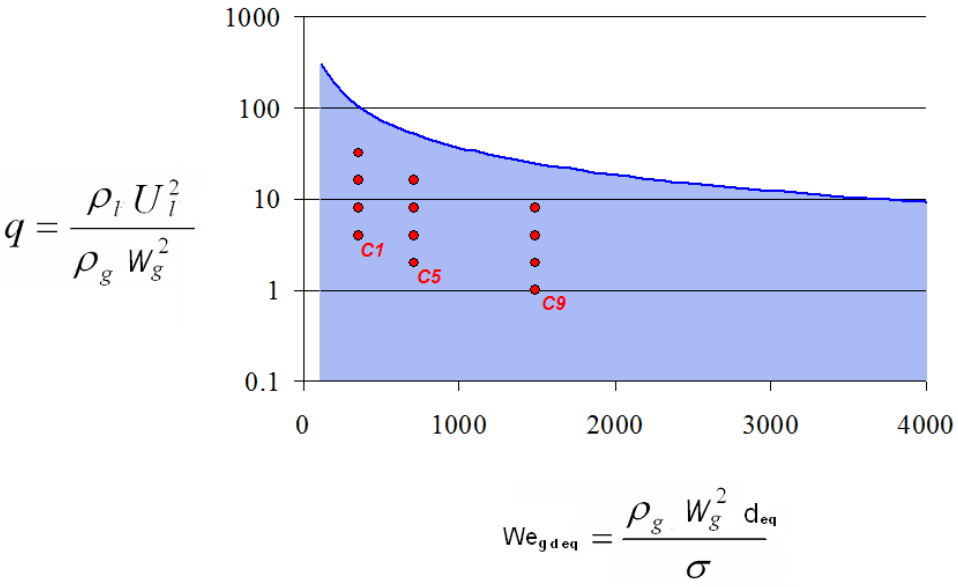

Figure 8.1: Engine relevant momentum flux ratio and Weber number (in blue) and test points (in red), with Cases 1, 5 and 9 highlighted

Figure 8.2 shows the test points covered in this study alongside some previous researchers' work which used round nozzles - where Weber number is based on d_{eq}.

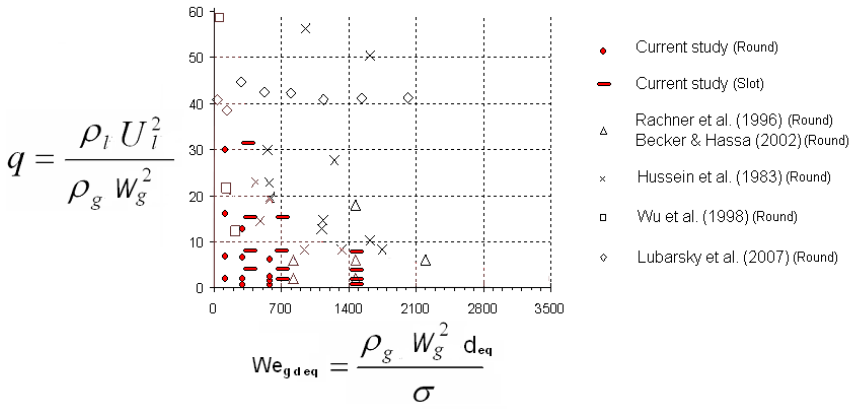

Figure 8.2: Momentum flux ratio and Weber Number data from previous research and this study, replotted from **Hart, Hutcheson and Regan (2009)**

The twelve point test matrix generated a large amount of data and whilst this thesis is considered to provide some useful analysis from it, it is clear there is scope for further analysis. The data can be interrogated from different perspectives depending on the particular interest, whether it is purely academic and

concerned with fundamental flow physics or more commercially based interests with specific requirements. In view of this, a considerable amount of data has been included in the Appendices - such that further analysis by third parties, with potentially different agendas to the current interest, could be achieved in the future.

The analysis completed represents new insight for sprays in cross airstreams from non-round nozzles. In particular, the distribution of droplet sizes was extensively evaluated as this was considered to underpin the measurements in a general way and provide insight into the relevant flow physics.

8.1 Conclusions

The image based data generated in this study showed the liquid body emanating from the nozzle exit is a shadow of the nozzle geometry and, hence, varies considerably between the horizontal ⇊⊖ and vertical ⇊⊘ orientations of the slot nozzle tested. However, the PDPA results showed that this had little influence on the range of AMD [D_{10}] measured in the spray plume, as presented in Figures 8.3.

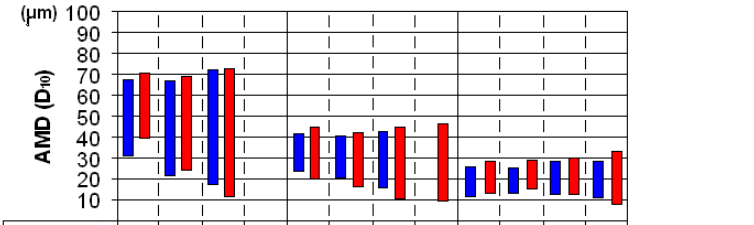

Case no.	1	2	3	4	5	6	7	8	9	10	11	12
q	3.4	9.1	20.3		1.6	4.2	9.4		0.6	1.8	4.2	7.5
We_{gdeq}	320	331	321		699	721	710		1630	1661	1604	1581
q	2.7	7.5	20.4		1.2	3.3	8.6	15.8	0.5	1.8	4.1	8.6
We_{gdeq}	310	304	297		727	699	704	709	1520	1531	1444	1263

Figure 8.3: ⇊⊖ ⇊⊘ AMD [D_{10}] ranges for all test cases completed; at the z = 40 mm plane

In general, the slot nozzle tests produced spray fields fundamentally similar to those from round nozzles. The spray fields of both the horizontal slot ⇊⊖ sprays and vertical slot ⇊⊘ sprays respond to changes in Weber number and momentum flux ratio (the most influential non-dimensional parameters in spray in cross-airstreams) in the same way that round nozzle sprays do - i.e with smaller

droplet sizes in the spray with increasing Weber number and increasing spray penetration with increasing momentum flux ratio.

Further similarities lay in the distribution of droplet size recorded. On the centre plane ($y = 0$) of the spray field, droplet size increased away from the nozzle wall ($0 < x < 50$), this is because droplets break-up from the liquid continuum with transverse velocity proportional to their mass. This provides an underlying structure for droplet distribution for sprays in cross-airstreams, however, local flow conditions manipulate this underlying structure and inflections in the general trends are experienced at certain conditions.

In particular, where the spray field is densely populated, the spray core causes a blockage and, as a result, droplets in the spray core experience lower engaging cross-airstream velocities (and correspondingly lower local Weber number) leading to larger droplet diameters and this results in a double-peak in droplet size distribution. This spray morphology, which has been previously established for round nozzle sprays, for example in **Wu et al. (1998)**, was shown to occur in both the horizontal and vertical slot nozzle tests. Hence the spray droplet distribution away from the nozzle wall exhibits a droplet size peak in the spray's core and another in the spray's periphery.

It was hypothesized that the efficient way in which the horizontal ⇊ configuration of the slot nozzle exposes the emanating liquid sheet to the cross-airstream may lead to smaller droplets in the spray field, compared to the vertical ⇊ orientation, which in contrast efficiently minimises the liquid sheet's direct exposure to the cross-airstream. However, on balance the data did not support this hypothesis. The data showed that AMD [D_{10}] in the spray core and spray periphery were broadly similar for vertical ⇊ and horizontal ⇊ alignment of the slot nozzle.

For the horizontal slot ⇊, at low q conditions where the liquid jet/sheet turns about a tight radius, large droplets were identified in the region near to the nozzle wall and were deemed to result from impingement. This process has been identified for round nozzles in previous studies, such as **Wu et al. (1998)**, and therefore is not unique to the horizontal slot sprays, however, the mechanism is more prevalent with a horizontal slot ⇊ nozzle. For the vertical slot ⇊ tests, large droplets due to impingement were not recorded, examination of high speed video images show the vertical ⇊ liquid sheet which emanated from the nozzle exit retains its transverse momentum for longer, causing the liquid body to extend away from the nozzle exit before it turns into the direction of the cross-airstream. Consequentially, unless q is very low, the nozzle exit geometry does not interfere with the path of the liquid sheet and impingement does not

occur.

Where impingement was present for the horizontal slot tests, the large droplets generated survive downstream because of the proximity of the nozzle wall in the test facility. It is not clear whether a configuration that enables impingement is possible within engine geometries and the relative positions of potential leak sources. Nevertheless, the droplets produced by impingement represent a potential for incongruence between experiment and simulation that needs to be taken into consideration when constructing/running CFD models to predict sprays in which impingement could be significant.

Although not reported in this thesis, CFD models have been constructed to simulate the experiments carried out in this study and detailed comparisons have been made, by the Thermo-Fluid Systems UTC laboratory at the University of Surrey. The comparisons were reported in **Hart, Hutcheson and Regan (2009)** and a detailed account is available in **Hutcheson (2011)**.

This thesis focused on the experiments and the data generated by them, but as a general point in relation to the CFD simulations in the wider programme of work, there was better correlation between experiment and simulation at higher Weber numbers. At higher Weber numbers the shear regime dominates the break-up process - producing smaller droplet diameters and, also, a smaller range of droplet diameters. Where Weber number was low, and particularly where momentum flux ratio was also low, there was less agreement between experiment and simulation.

As momentum flux ratio reduces so the spray field has a less defined structure - at sufficiently low momentum flux ratio the system can no longer be considered to be a spray at all, because the liquid body collapses at the nozzle exit and liquid simply dribbles down the nozzle wall.

However, low Weber number with low momentum flux ratio conditions also present greater challenges from an experimental point of view. Low Weber number sprays contained a wider range of droplet diameters and required a more forgiving PDPA setup, i.e. with a wider acceptance band. For low momentum flux ratio sprays, a significant proportion of the spray was located near to the injector wall where it is less accessible to the PDPA measurement volume. But also, the liquid does not dissipate and spread out so well (as it does at high momentum flux ratio), resulting in relatively densely populated sprays and the PDPA system's signal-to-noise ratio is to some extent constrained by spray density.

Hence it is reasonable to conclude that sprays at low Weber number and low momentum flux ratio levels present greater challenges both experimentally and for simulation; this provides an area of the study that could be further investigated both from the experimental and modelling perspectives.

In general with respect to the current data, the experiments which produced sprays that developed centrally in the test section, i.e. $3 \lesssim q \lesssim 10$, yielded experimental results that are likely to be more useful in CFD validation analysis, because at these levels of q all the spray field could be characterised.

This work programme has made significant contributions to the understanding of the situations that may result when oil leaks occur in gas turbine engines. The project has enhanced the validation status of Fluent CFD code when used for modelling the break-up of liquid flows injected into a cross-airstream. The work has contributed to the development of a CFD based tool which is required to predict the risk of an engine fire - in the aim of assessing current engine designs as well as improving future engine designs.

8.2 Recommendations for Future Work

The progress of this study has developed new understanding but also new questions, as is often the case in the pursuit of knowledge. Listed below are some areas where it is considered that extensions to the current work could be particularly beneficial in developing further understanding.

1. **Manual mass flux measurements**
   Some work towards this objective was completed with the design and construction of a test section attachment to facilitate manual mass flux measurements also known as 'iso-kinetic tubes'. A single test was completed and proved the concept but, this also demonstrated that the time required to complete such tests over the established test matrix would be considerable and was not available.

2. **Round nozzle tests matched for $\mathbf{d}_{eq}$**
   Within this study a set of round nozzle tests were completed, the round nozzle used had a diameter of nominally 0.5 mm which matched the short dimension of the slot nozzle. The choice for this dimension was based on the need to run a set of experiments that could be compared with previous studies, and 0.5 mm diameter nozzles have been widely used in the past,

Wu et al. (1998) for example. It also provided a relatively low density of droplets in the spray field which helped in the commissioning of the PDPA system.

The main objective for this study was to establish droplet size ranges associated with slot nozzles and the test programme reflected this. However, in a wider context the comparison between sprays from slot and round nozzles is of interest. Completing the test matrix using a round nozzle with matching d_{eq} would generate data directly comparable to that collated for the slot nozzle.

However, the data set would still be limited to a single incident of d_{eq} limiting the understanding that could be gained. Testing with several nozzle specimens - varying d_{eq} - would provide further insight and potentially provide the basis for establishing a universal correlation between round and slot nozzle geometries.

3. **Low Weber numbers and momentum flux ratios testing**
   Modifications to the test apparatus to provide improved near wall characterisation, followed by experimental runs and CFD modelling over the low range of Weber numbers and momentum flux ratios.

4. **Viscosity range**
   Investigation into the effect of liquid viscosity on droplet break-up to cover a range of engine oil temperatures. Produce a small set of tests to investigate discrepancies between sprays produced using water and sprays produced using working temperature oil.

5. **Angled slot injection**
   Injection of liquid into the cross-airstream with upstream and downstream components of velocity rather than perpendicular.

6. **Oil pipe failures**
   Assessment of actual cracked pipe specimens to better understand the differences between a manufactured nozzle compared to an in-service pipe crack. Develop understanding of typical discharge coefficients. Conduct a series of experiments using an actual failed pipe over a range of Weber numbers and momentum flux ratios, with the crack direction at various orientations to the cross-airstream. Further analyse the likelihood and effects of cavitation within the pipe crack on oil droplet formation.

7. **Rotating geometries**
   A new test facility to investigate the behaviour of injection into a high

speed air flow in a rotating cavity. An investigation into the behaviour of oil entering low air speed stationary cavities via a rotating labyrinth seal. An investigation into the behaviour of oil entering high air speed rotating cavities via a rotating labyrinth seal.

References

Ahn B., Ismalov M., Heister S.D., (2009)
Forced excitation of swirl injectors using a Hydro-mechanical pulsator
AIAA 2009-5043

Ahn K., Kim J., Yoon Y., (2006)
Effects of orifice internal flowe on traverse injection into subsonic crossflows: cavitation and hydraulic flip
Atomisation and Sprays, vol.16, pp.15-34,

Aisa L., Garcia J.A., Cerecedo L.M., Garcia Palacin I., Clavvo E., (2002)
Particle concentration and local mass flux measurements in two phase flows with PDA. Application to a study on the dispersion of spherical particles in a turbulent air jet
International Journal of Multiphase Flow, vol. 28, pp.301-324

Ali S.K., Foss J.K., (1997)
Experimental determination of discharge coefficient in a two dimensional slit jet
ASME FEDSM97-3048

Asma C.O., Masuttti D., Chazot O., (2009)
Experimental investigation of liquid fragmentation in hypersonic crossflow
AIAA 2009-3506

Azzopardi B.J., (1997)
Drops in annular two phase flow
International Journal of Multiphase Flow, vol. 23, pp.1-53

Bagshaw N.M, Beck S.B.M., Yates J.R., (1999)
Identification of fluid flow regimes in narrow cracks
Institute of Mechanical Engineers, vol. 214, part C

Becker J., Hassa C., (2002)
Breakup and atomisation of a kerosene jet in crossflow at elevated pressure
Atomisation and Sprays, vol.12, pp.363-369,

Bell J.H., Mehta R.D., (1989)
Boundary-Layer predictions for small low-speed contractions
AIAA Journal, vol 27, No. 3, pp. 372-374

Bidone G., (1829)
Experience sur la forme et sur la direction des veines et des courants d'eau lances par diverses ouvertures
Imprimerie Royal, Turin, pp. 1136

Birouk M., Azzopardi B. J., Stabler T., (2003)
Primary breakup of a viscous liquid jet in a cross airflow
Particle and Particle Systems Characterization, vol. 20, Issue 4, pp. 283289

Birouk M., Azzopardi B. J., Stabler T., (2003)
An experimental study of liquid jets interacting with cross airflows
Particle and Particle Systems Characterization, vol. 20, Issue 1, pp. 3946

Borisov A.A., Gel'fand B.E., Natanzon M.S., Kossov O.M., (1979)
Droplet breakup regimes and criteria for their existance
Institute of Chemical Physics - USSR, vol. 40, No. 1, pp. 64-70

Brandt M., Rachner M., (1998)
An experimental and numerical study of kerosine spray evaporation in a premix duct for gas turbine combustors at high pressure
Combustion Sci. and Tech., vol. 138, pp. 313-348

Cavaliere A., Ragucci R., Noviello C., (2003)
Bending and breakup of a liquid jet in a high pressure airflow
Experimental Thermal and Fluid Science, vol. 27, Issue 4, Pages 449-454

Chelko L.J., (1953)
Penetration of liquid jets into a high-velocity airstream
NACA RM E50F21

Chen, T. H., Smith, C. R., Schommer, D. G., Nejad, A. S., (1993)
Multi-zone behaviour of traverse liquid jet in a high speed flow
AIAA, Aerospace Sciences Meeting and Exhibit, 31st, Reno, NV, pp. 11

Chivers T.C., (2002)
The influence of surface roughness on fluid flow through cracks
Fatigue Fract. Engng. Matrt. Struct., vol. 25, pp. 1095-1102

Chryssakis C.A., Assanis D.N., (2005)
A secondary Atomisation model for liquid droplet deformation and breakup under high weber conditions
ILASS, Liquid Atomisation and Spray Systems

Cooke A., Regan N.J. (2010)
The production of a Microsoft Excel tool to assist the teaching of the use of venturi tubes to calculate mass flow rates and their associated uncertainties
IJMEE, vol. 38, No. 1, pp. 56-72

Coren D. D., (2008)
Windage due to protrusions in rotor-stator systems
D.Phil Thesis, University of Sussex

Costa M., Melo M.J., Sousa J.M.M., Levy Y., (2006)
Spray characteristics of angled liquid injection into subsonic crossflows
AIAA Journal, vol 44, No. 3, pp. 646-652

Cristini V., Blawzdziewicz J., Loewenberg M., Collins L.R., (2003)
Break up in stochastic stokes flow: sub-kolmogrov drops in isotropic turbulence
Journal of Fluid Mechanics, vol 492, pp. 231-250

Dai Z., Faeth G.M., (2001)
Temporal properties of secondary drop breakup in the multimode breakup regime
International Journal of Multiphase Flow, vol. 27, pp.217-236

Deckker B.E.L., (1978)
Compressible flow through square edge recangular orifices
Institute of Mechanical Engineers, vol. 192,

Dullenkopf K., Willmann M., Wittig S., Schone F., Stieglmeier M., Tropea C., Mundo C., (1998)
Comparative mass flux measurements in sprays using a patternator and the phase Doppler technique
Part. Syst. Charact., vol 15, pp. 81-89

Edwards C. F., Marx K. D., (1991)
Analysis of the ideal phase-Doppler system: limitations imposed by the single-particle constraint
Sandia Report SAND91-8560

Fric T.F., Roshko A., (1994)
Vortical structure in the wake of a traverse jet
J. Fluid Mech., vol 35, No. 2, pp. 27-64

Fuller R.P., Wu P.K., Kirkendall K.A., Nejad A.S., (2000)
Effects of injection angle on atomisation of liquid jets in traverse airflow
AIAA Journal, vol 38, No. 1, pp. 64-72

Glahn A., Busam S., Blair M.F., Allard K.L., Wittig S., (2002)
Droplet generation by disintegration of oil films at the rim of a rotating disc
Journal of Eng. for Gas Turbines and Power, vol. 124, 117-124

Glahn A., Kurreck M., Willmann M., Wittig S., (1996)
Feasibility study on oil droplet flow investigations inside aero engine bearing chambers
Journal of Eng. for Gas Turbine and Power, vol. 118, pp. 749-755

Hart K.J., Hutcheson P.S., Regan N.J., (2009)
Investigations into the break-up of liquid injected into an air cross-flow stream in support of gas turbine oil fire prediction
Rolls-Royce Plc. Internal Proprietary Report

Herrmann M., (2009)
Detailed Numerical simulations of the primary atomisation of a turbulent liquid jet in crossflow
ASME GT2009-59563

Hojnacki J.T., (1972)
Ramjet engine fuel injection studies
Air force aero propulsion laboratory, Ohio

Hsiang L.P., Faeth G.M., (1992)
Near-limit drop deformation and secondary breakup
International Journal of Multiphase Flow, vol. 18, pp. 635-652

Hussein G.A., Jasuja A.K., Fletcher R.S., (1983)
Penetration and Break-up Behaviour of a Discrete Liquid Jet in a Cross-flowing Airstream - A Further Study
In Proceedings of ASME 28th International Gas Turbine Conference, Phoenix, AZ, US.

Hutcheson P.S., (2008)
A comparison of CFD and experimental data for a round water jet in crossflow
Thermo Fluid Systems UTC, University of Surrey

Hutcheson P.S., (2007)
A literature review of the breakup of liquid jets and sheets
Thermo-Fluid Systems UTC, University of Surrey

Hutcheson P.S., Chew J.W., Thorpe R.B., Young C., (2008)
Assessment of models for liquid jet breakup
Power for Land, Sea and Air, GT2008-50649.

Hutcheson P.S. (2011)
Modelling of oil leakage sprays in gas turbine engine cavities
Ph.D thesis, Thermo-Fluid Systems UTC, University of Surrey.

Inamura T., Nagai N., (1997)
Spray Characteristics of liquid jet traversing subsonic airstreams
AIAA, Vol. 13, No. 2, pp. 250-256

Ingebo R. D., (1967)
Penetration of drops into high-velocity airstreams
Lewis Research Center, Cleveland, Ohio, NASA TM-X-1363

Ingebo R. D., (1979)
Atomisation of water jets and sheets in axial and swirling airflows
Lewis Research Center, Cleveland, Ohio, NASA TM-79043

Joseph D.D., Belanger J., Beavers G.S., (1999)
Breakup of a liquid drop suddenly exposed to a high speed airstream
International Journal of Multiphase Flow, vol. 25, pp.1263-1303

Joshi P.B., Schetz J.A., (1975)
Effect of injector shape on penetration and spread of liquid jets
AIAA, vol. 13, No. 9. pp. 1137-1138

Kashdan J.T., Shrimpton J.S., Whybrew A., (2006)
A digital image analysis technique for quatative characterisation of high speed sprays
Optics and Lasers in Engineering, vol. 45, pp.106-114

Koch P., (2008)
Equivalent diameters of rectangular and oval ducts
Building Serv. Eng. Res. Technol., Vol. 29,

Koivula T., (2000)
On cavitation in fluid power
1st FPNI-PhD Symp. Hamburg, pp. 371-382

Lasheras J.C., Hopfinger E.J., (2000)
Liquid jet instability and atomisation in a coaxial gas stream
Annu. Rev. Fluid Mech., vol 32, pp. 275-308

Lasheras J.C., Villermaux E., Hopfinger E.J., (1998)
Break-up and atomisation of a round water jet by a high-speed annular air jet
Journal of Fluid Mechanics, vol 357, pp. 351-379

Liu Z., Reitz R.D., (1997)
An analysis of the distortion and breakup mechanisms of high speed liquid drops
International Journal of Multiphase Flow, vol. 23, pp.631-650

Lefebvre, (1989)
Atomization and sprays
Taylor Francis Group, ISBN 0-89116-603-3

Leong, M. Y., McDonell V. G., Samuelsen G. S., (2001)
Effect of Ambient pressure on an airblast spray injected into a crossflow
J. Propul Power, vol. 17, No. 5, pp.1076-1084.

Lubarsky, E., Reichel J. R., Zinn B. T. and McAmis R., (2007)
Spray in crosflow - dependence on weber number
Power for Land, Sea and Air, GT2007-27645.

Mehta R.D., Bradshaw P., (1979)
Design rules for small low speed wind tunnels
The Aeronautical Journal

Meister B.J., Scheele G.F., (1969)
Drop formation from cylindrical jets in immiscible liquid systems
AIChE Journal, pp. 700-706

Mikhail M.N., (1979)
Optimum Design of Wind tunnel contractions
AIAA Journal, vol 17, No. 5, pp. 472-477

Nejad A. S., Schetz J. A., (1983)
Effects of properties and location in the plume on droplet diameter for injection in a supersonic stream
AIAA, vol. 21, No. 7. pp. 956-961

Obot N.T., Trabold T.A., Graska M.L., Ghandi F., (1986)
Velocity and temperature fields in turbulent jets issuing from sharp edged inlet round nozzles
Ind. Eng. Chem. Fundam. vol. 25, pp. 425-433

Ohadi M.M., Sparrow E.M., Walavalkar A., Ansari A.L., (1990)
Pressure drop characteristics for turbulent flow in a straight circular tube situated downstream of a bend
Journal of Heat Mass Transfer, vol. 33, No. 4, pp. 583-591

Perurena J.B., Asma C.O., Theunissen R., Chazot O., (2008)
Experimental investigation of liquid jet injection into Mach 6 hypersonic crossflow
Exp. Fluids DOI 10.1007/s00348-008-0566-5

Price J.B., (2008)
Modelling discontinuities and KelvinHelmholtz instabilities in SPH
Journal of Computational Physics, vol 227, issue 24, pp 10040-10057

Rachner M., Becker J., Hassa C., Doerr T., (2002)
Modelling of the atomisation of a plain liquid fuel jet in crossflow at gas turbine conditions
Aerosp. Sci. Technol., vol 6, Issue 7, pp. 495-506

Rachner M., Brandt M., Eickhoff H., Hassa C., Braumer A., Kramer H., Ridder M., Sick., (1996)
A numerical and experimental study of fuel evaporation and mixing for lean premixed combustion at high pressure
Twenty Sixth Symposium on Comb., pp. 2741-2748

Ramond A., Millan P., (2000)
Measurements and treatments of ldaa signals comparison with hot wire signals
Experiments in Fluids, vol. 28, pp. 58-663

Ranger A.A., Nicholls J.A., (1969)
Aerodynamic shattering of liquid drops
AIAA Journal, vol 7, No. 2

Lord Rayleigh F. R. S., (1878)
On the stability of Jets

Ragucci R., Cavaliere A., D'Amico, R., (2000)
Atomization of a liquid jet in gas-turbine configuration
Proceedings of the Eighth International Conference on Liquid Atomization and Spray Systems, Pasadena, pp. 957-964

Saffman M., (1987)
Automatic calibration of LDA measurement volume size
Applied Optics, vol. 26, No. 13,

Savart F., (1833)
Ann. Chim. Phys., vol. 53, pp. 337-386,

Schetz J. A., Kush E. A., Joshi P. B., (1980)
Wave phenomena in liquid jet breakup in a supersonic crossflow
AIAA, vol. 18, No. 7. pp. 774-778

Schetz J. A., Padhye A., (1977)
Penetration and breakup of liquids in subsonic airstreams,
AIAA, vol. 15, No. 10. pp. 1385-1390

Sharma N.Y., Datta A., Som S.K., (2001)
Influences of spray and operating parameters on penetration of vapourising fuel droplets in agas turbine combustor
Applied Thermal Engineering, vol. 21, pp. 1755-1768

Sherman A., Schetz J., (1971)
Liquid sheets and jets in a supersonic gas stream
AIAA LOOK UP pp. 667-671

Sparrow E.M., Altemani C.A.C., Chaboki A., (1984)
Jet impingement heat transfer for a circular jet impinging in crossflow on a cylinder
Journal of Eng. for Gas Turbines and Power, vol. 106, 570-577

Spilhaus A.F., (1947)
Raindrop size shape and falling speed
Journal of Meteorology, vol. 5, 108-110

Sung Wook Park, Sayap Kim, Chang sik Lee, (2006)
Breakup and atomisation characteristics of mono-dispersed diesel droplets in a cross flowair stream
International Journal of Multiphase Flow, vol. 32, pp.807-822

Taylor J.J., Hoyt J. W., (1983)
Water jet photography - techniques and methods
Experiments in Fluids, vol. 1, pp. 113-120

Taylor B.N., Kuyatt C. E., (1994)
Guidelines for evaluating and expressing the uncertainty of NIST measurement results
National Institute of Standards and Technology (NIST), Technical Note 1297

Tambe S. B., Jeng S. M., Mongia H., Hsiao G.,. (2004)
Liquid jets in subsonic cross flow: Master of Science Thesis
AIAA-2005-731.

Tolpadi A.K., Aggarwal S.K., Mongia H.C., (2000)
An advanced spray model for application to the prediction of gas turbine combustor flow fields
Numerical Heat Transfer, Part A, vol. 38, pp. 325-340

Trabold T.A., Esen E.B., Obat N.T., (1987)
Entrainment by turbulent jets issuing from sharp edged inlet round nozzles
Journal of Eng. for Gas Turbines and Power, vol. 109, pp. 248-254

Varga C.M., Lasheras J.C., Hopfinger E.J., (2003)
Initial break up of a small diameter liquid jet by a (COAXIAL) high speed gas stream
Journal of Fluid Mechanics, vol 497, pp. 405-434

Viall E.N., Zhang Q., (2000)
Determining the discharge coefficient of a spool valve
AACC 0-7803-5519-9/00

Widmann J.F., Charagundla S.R., Presser C., Yang G.L., Leigh S.D., (2000)
A correction method for spray intensity measurements obtained via phase doppler interferometry
Aerosol Science and Tech., vol. 32, pp. 584-601

Wigley G., Goodwin M., Pitcher G., Blondel D., (2002)
Imaging and pda analysis of gdi spray in the near nozzle region
Aeronautical and Automotive Engineering, Loughborough University

Wigley G., Heath J., Pitcher G., Whybrew A., (2001)
Experimental analysis of the response of a laser/phase doppler anemometry system to a partially atomised spray
Part. Part. Syst. Charact., vol 18, Issue 4, pages 169 - 178

Willenborg K., (2004)
Rolls-Royce Technical Note

Wu P-K., Kirkendall K. A. and Nejad A. S., (1997)
Break up processes of liquid jets in subsonic crossflows
Journal of Propulsion and Power, 1997, vol. 13, No. 1.

Wu P-K., Kirkendall K.A., Fuller R.P., (1998)
Spray structures of liquid jets atomised in subsonic crossflows
Journal of Propulsion and Power, vol. 14,

Wu P-K., Miranda R.F., Faeth G.M., (1995)
Effects of initial flow conditions on primary breakup of non turbulent and turbulent round liquid jets
Atomisation and Sprays, vol. 5, pp. 175 - 196

Young C., (2002)
Rolls-Royce Technical Note

Zhang Zh., Ziada S. (2000)
PDA measurement of droplet size and mass flux in the three-dimensional atomisation region of water jet in air cross-flow
Experiments in Fluids, vol. 18, pp. 29 - 35

Zhu Y., Wan Y., Huang Y., Peng X., (2006)
Study on the breakup lengths of free round liquid jets
2006-ISJPPE-1014

List of Figures

List of Tables

Appendices

Appendix A

Round Nozzle Plots

	$W_{mean} \approx$ **90 m/s**	$W_{mean} \approx$ **135 m/s**	$W_{mean} \approx$ **195 m/s**
Δ**p** ≈ **0.5 bar**	Case 1: 118 (2.5)	Case 5: 275 (1.6)	Case 9: 594 (0.8)
Δ**p** ≈ **1.5 bar**	Case 2: 118 (7.1)	Case 6: 276 (3.0)	Case 10: 586 (2.2)
Δ**p** ≈ **3.5 bar**	Case 3: 117 (16)	Case 7: 276 (6.7)	Case 11: 580 (3.3)
Δ**p** ≈ **6.5 bar**	Case 4: 118 (30)	Case 8: 277 (13)	Case 12: 580 (6.5)

Table A.1: $\overset{\Downarrow}{\odot}$ PDPA average test conditions, We_g (q)

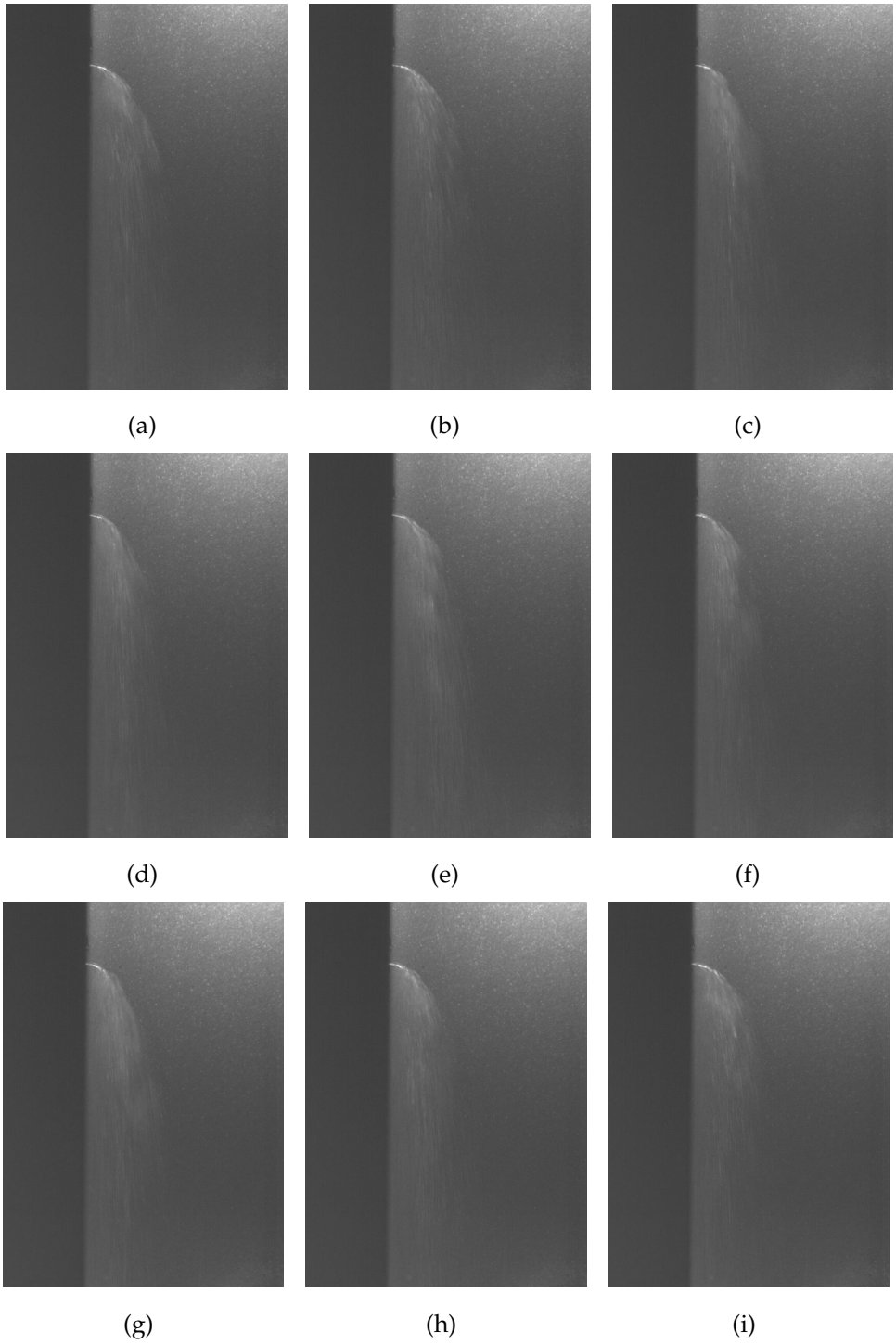

Figure A.1: ⇓⊙ Selection of images extracted from HSV; Case 1 $We_g \approx 118$ and $q \approx 2.5$

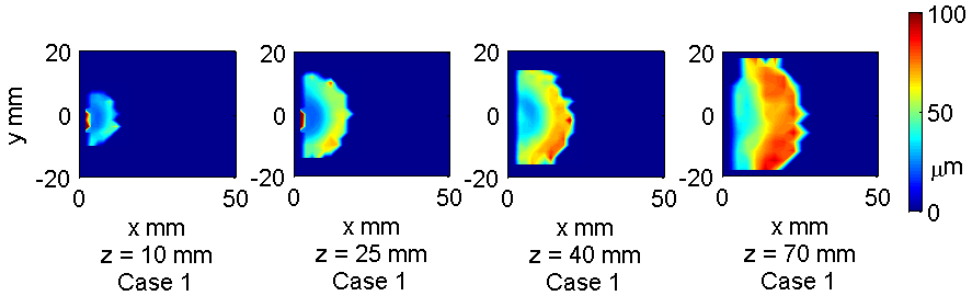

Figure A.2: ⇓⊙ Distribution of AMD; Case 1 $We_g = 118$ and $q = 2.5$

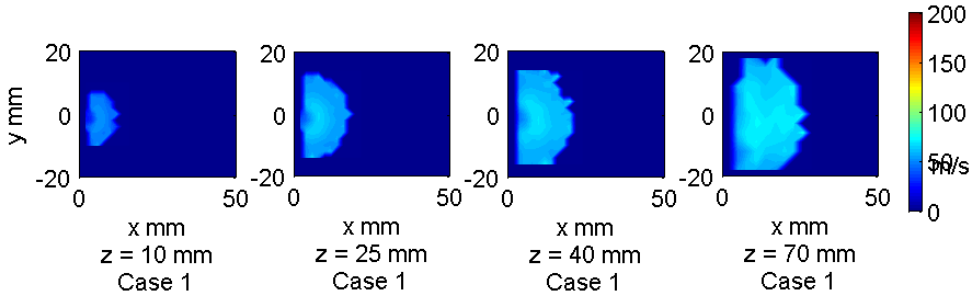

Figure A.3: ⇓⊙ Distribution of W_{drop}; Case 1 $We_g = 118$ and $q = 2.5$

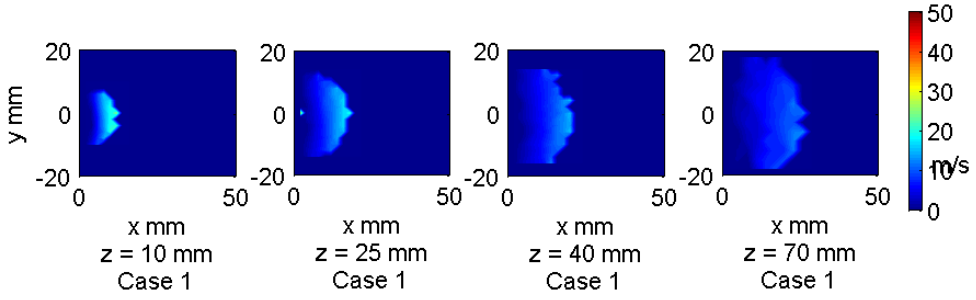

Figure A.4: ⇓⊙ Distribution of U_{drop}; Case 1 $We_g = 118$ and $q = 2.5$

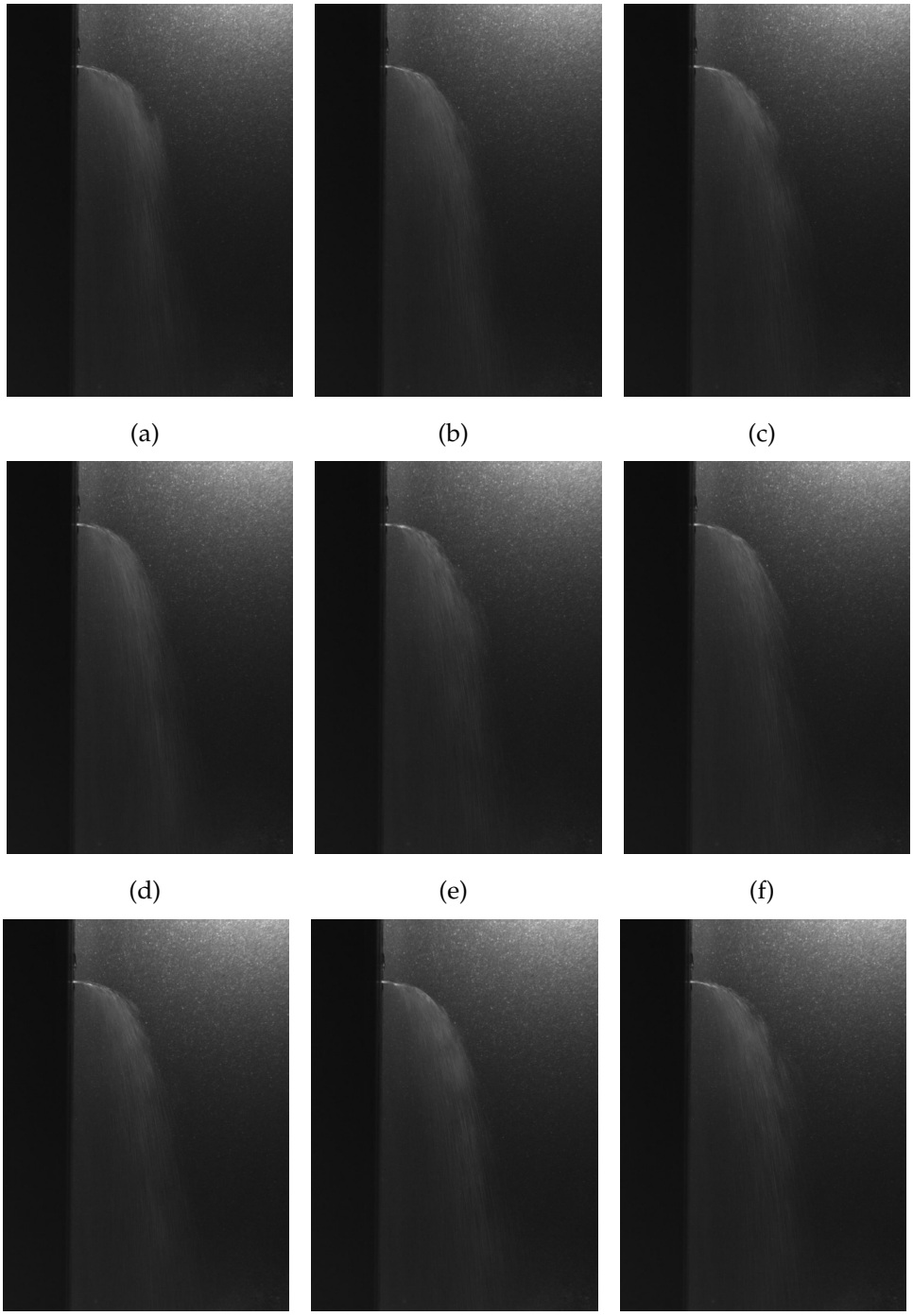

Figure A.5: $\overset{\Downarrow}{\odot}$ Selection of images extracted from HSV; Case 2 $We_g \approx 118$ and $q \approx 7.1$

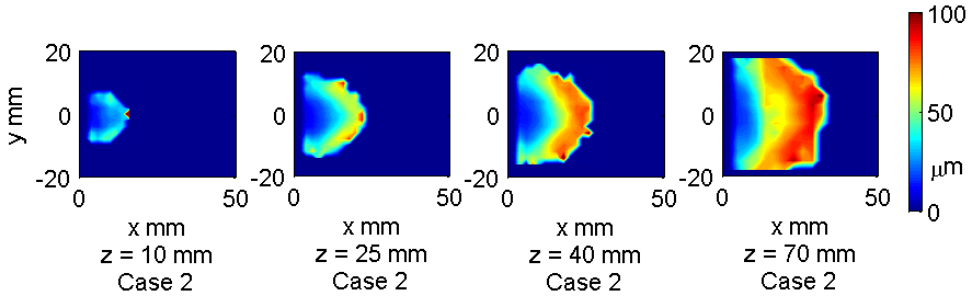

Figure A.6: ⇓⊙ Distribution of AMD; Case 2 $We_g = 118$ and $q = 7.1$

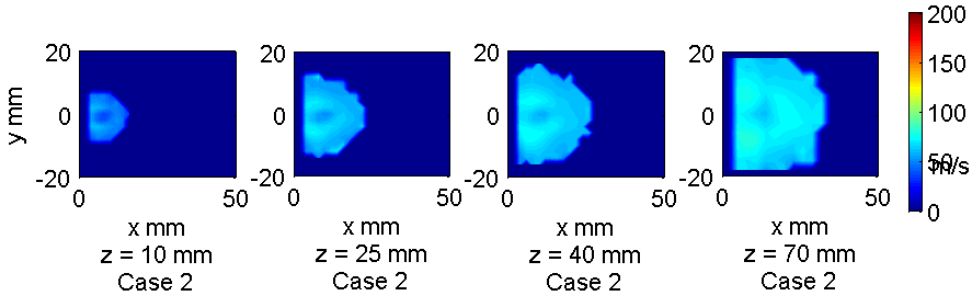

Figure A.7: ⇓⊙ Distribution of W_{drop}; Case 2 $We_g = 118$ and $q = 7.1$

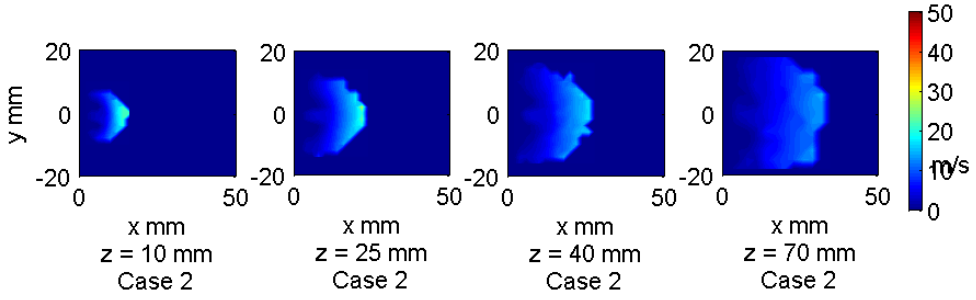

Figure A.8: ⇓⊙ Distribution of U_{drop}; Case 2 $We_g = 118$ and $q = 7.1$

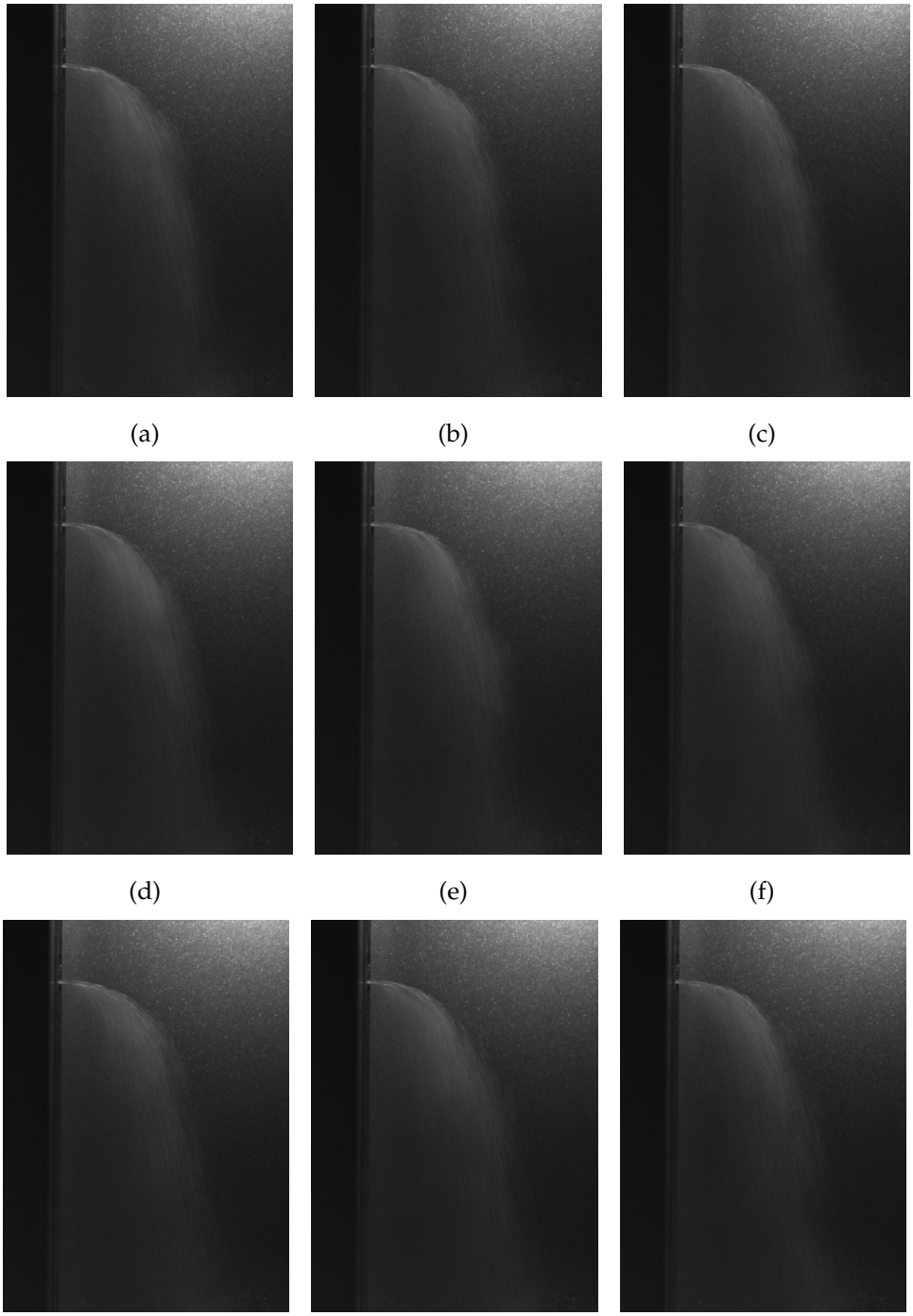

(a) (b) (c)

(d) (e) (f)

(g) (h) (i)

Figure A.9: $\overset{\Downarrow}{\odot}$ Selection of images extracted from HSV; Case 3 $We_g \approx 117$ and $q \approx 16$

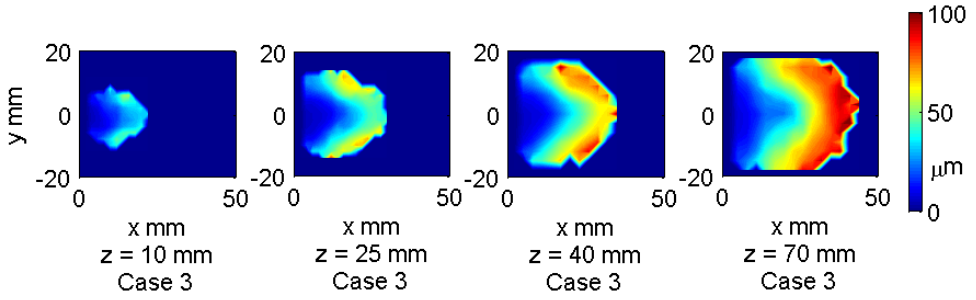

Figure A.10: ⊙ Distribution of AMD; Case 3 $We_g = 117$ and $q = 16$

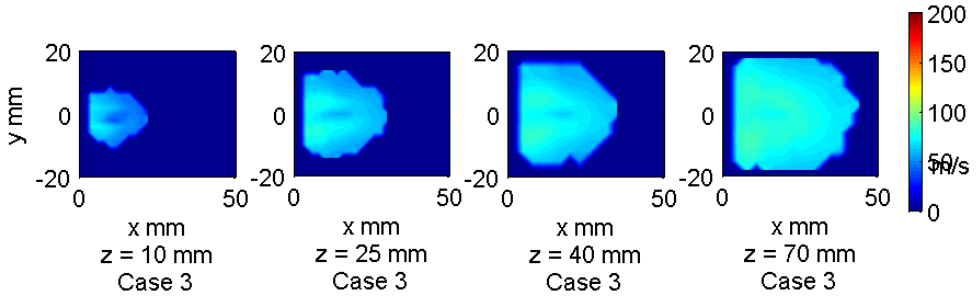

Figure A.11: ⊙ Distribution of W_{drop}; Case 3 $We_g = 117$ and $q = 16$

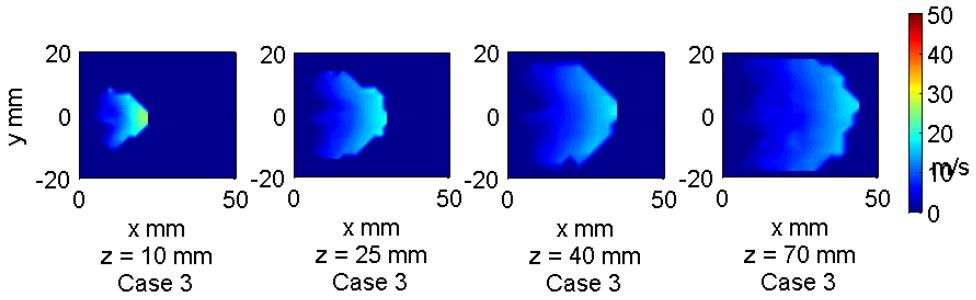

Figure A.12: ⊙ Distribution of U_{drop}; Case 3 $We_g = 117$ and $q = 16$

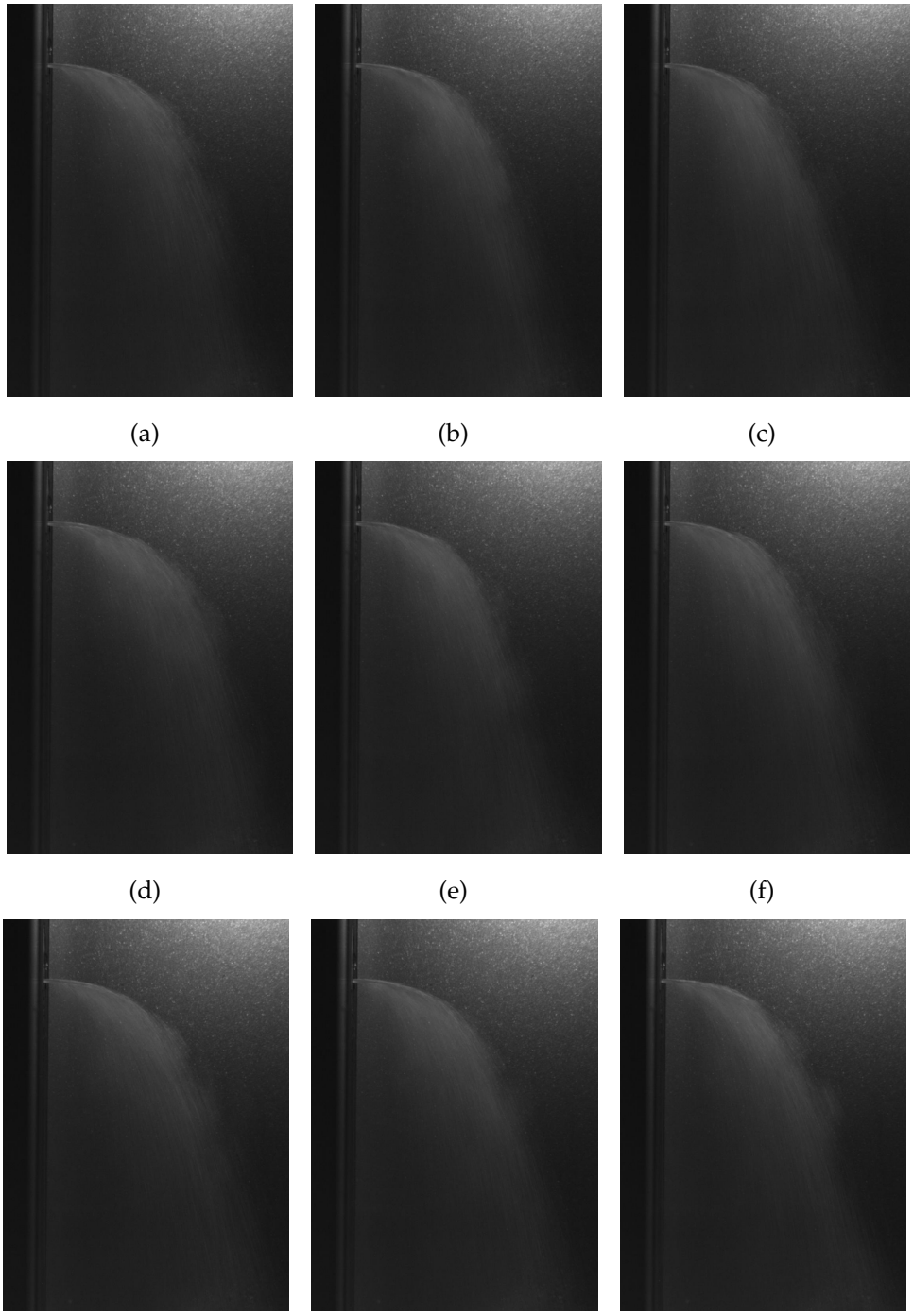

(a) (b) (c)

(d) (e) (f)

(g) (h) (i)

Figure A.13: ⇓⊙ Selection of images extracted from HSV; Case 4 $We_g \approx 118$ and $q \approx 30$

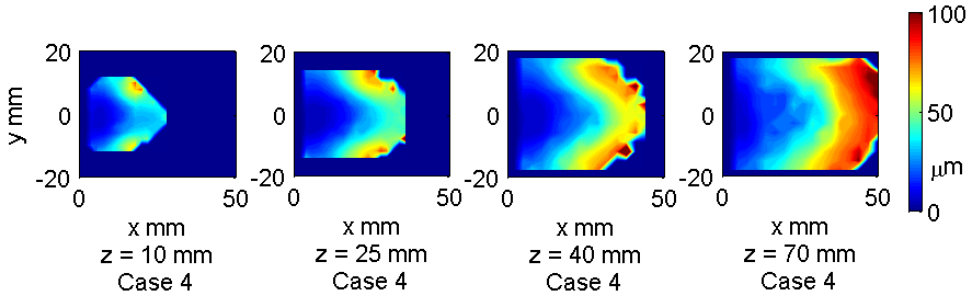

Figure A.14: ⇊⊙ Distribution of AMD; Case 4 $We_g = 118$ and $q = 30$

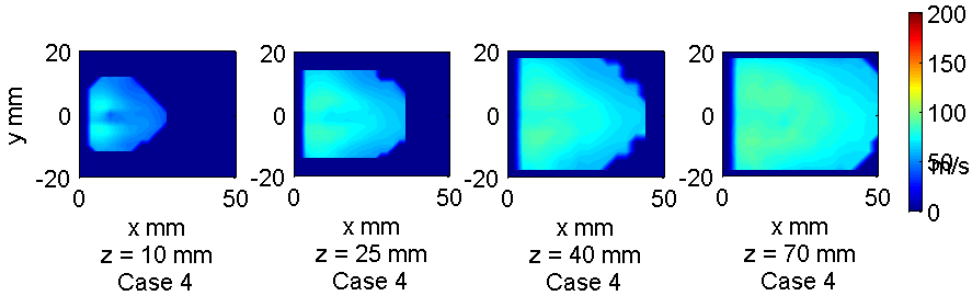

Figure A.15: ⇊⊙ Distribution of W_{drop}; Case 4 $We_g = 118$ and $q = 30$

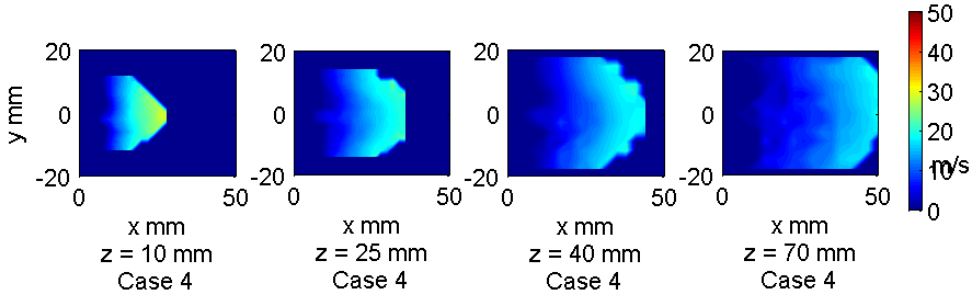

Figure A.16: ⇊⊙ Distribution of U_{drop}; Case 4 $We_g = 118$ and $q = 30$

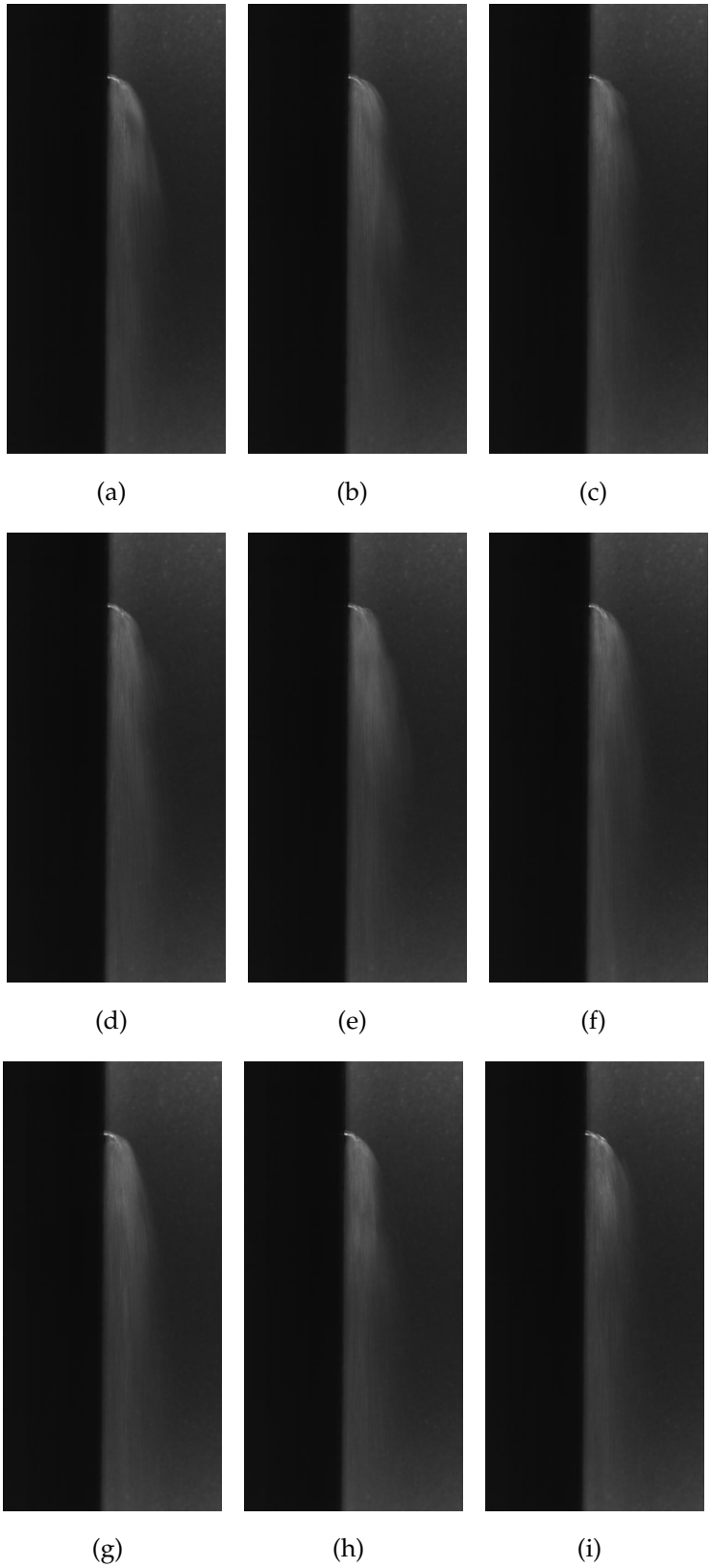

(a) (b) (c)

(d) (e) (f)

(g) (h) (i)

Figure A.17: ⇓⊙ Selection of images extracted from HSV; Case 5 $We_g \approx 275$ and $q \approx 1.6$

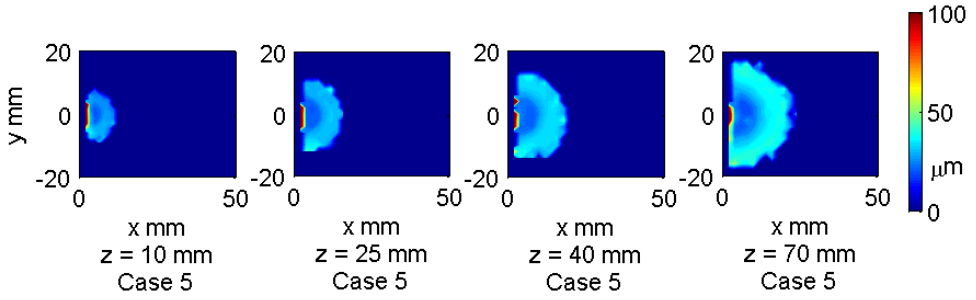

Figure A.18: ⇓⊙ Distribution of AMD; Case 5 $We_g = 275$ and $q = 1.6$

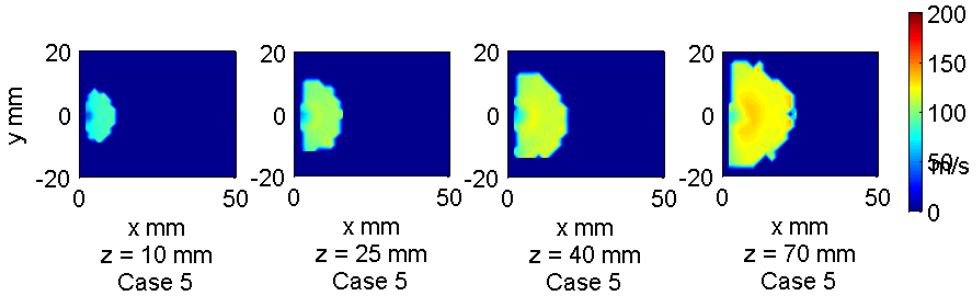

Figure A.19: ⇓⊙ Distribution of W_{drop}; Case 5 $We_g = 275$ and $q = 1.6$

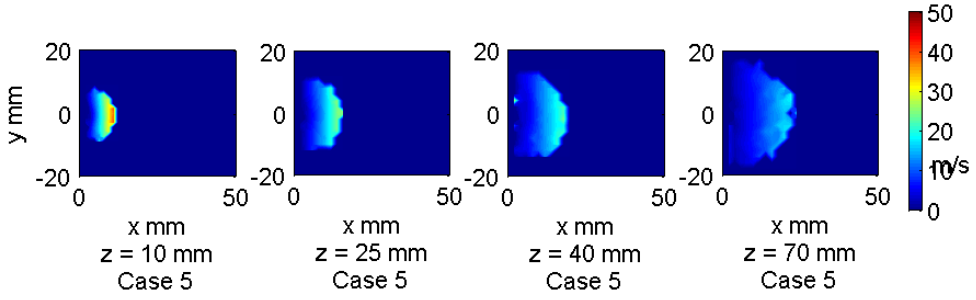

Figure A.20: ⇓⊙ Distribution of U_{drop}; Case 5 $We_g = 275$ and $q = 1.6$

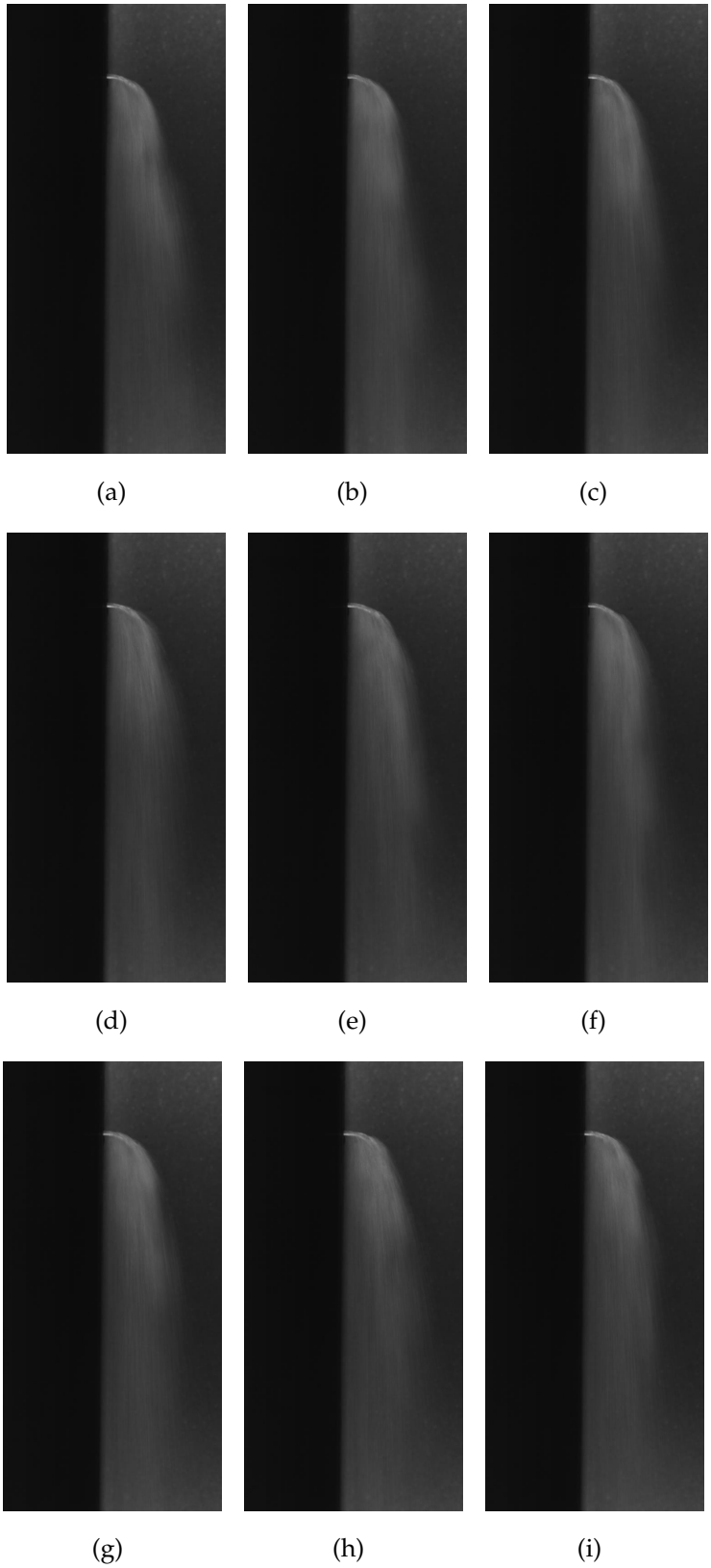

(a) (b) (c)

(d) (e) (f)

(g) (h) (i)

Figure A.21: ⇓⊙ Selection of images extracted from HSV; Case 6 $We_g \approx 276$ and $q \approx 3.0$

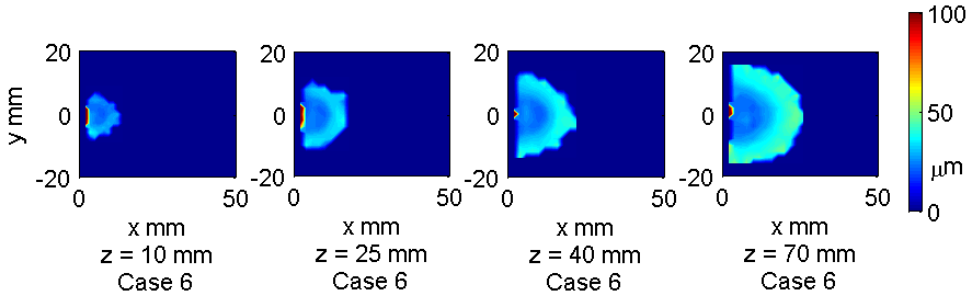

Figure A.22: ⇓⊙ Distribution of AMD; Case 6 $We_g = 276$ and $q = 3.0$

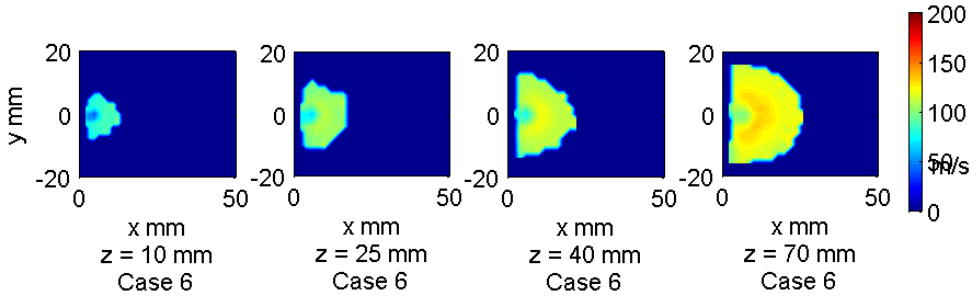

Figure A.23: ⇓⊙ Distribution of W_{drop}; Case 6 $We_g = 276$ and $q = 3.0$

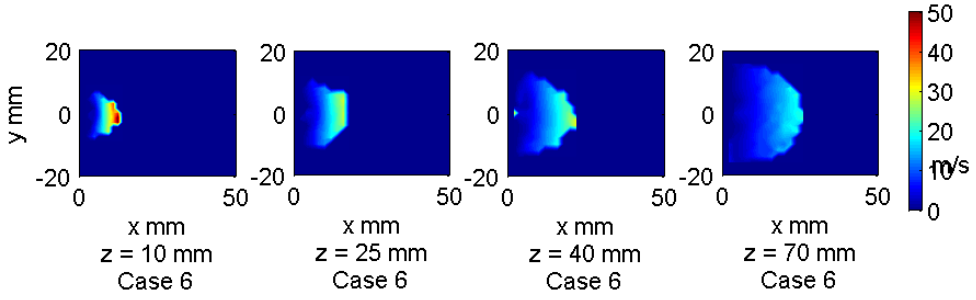

Figure A.24: ⇓⊙ Distribution of U_{drop}; Case 6 $We_g = 276$ and $q = 3.0$

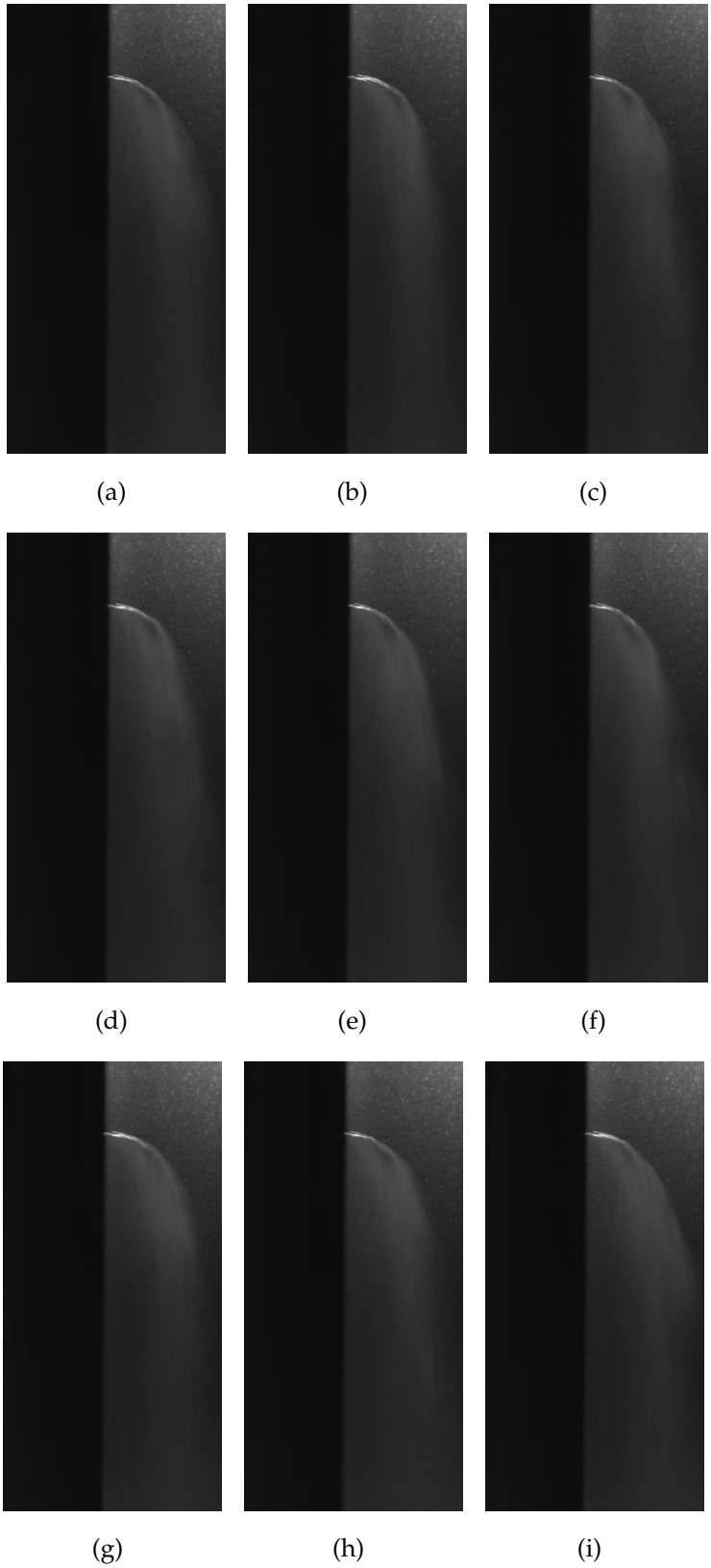

(a) (b) (c)

(d) (e) (f)

(g) (h) (i)

Figure A.25: ⇓⊙ Selection of images extracted from HSV; Case 7 $We_g \approx 276$ and $q \approx 6.7$

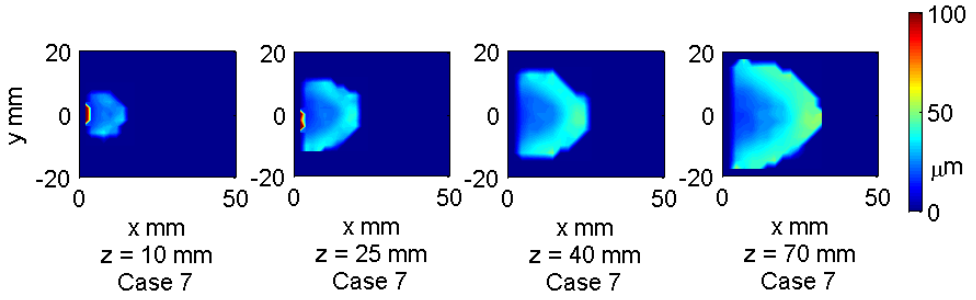

Figure A.26: ⇓⊙ Distribution of AMD; Case 7 $We_g = 276$ and $q = 6.7$

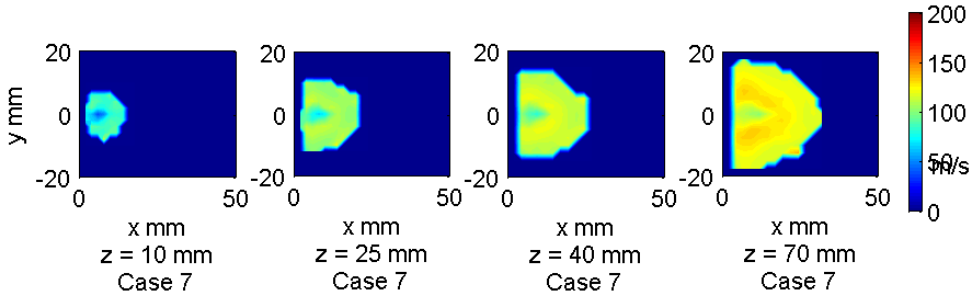

Figure A.27: ⇓⊙ Distribution of W_{drop}; Case 7 $We_g = 276$ and $q = 6.7$

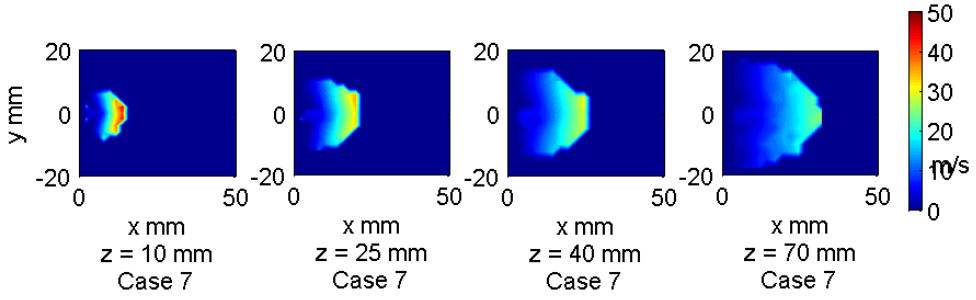

Figure A.28: ⇓⊙ Distribution of U_{drop}; Case 7 $We_g = 276$ and $q = 6.7$

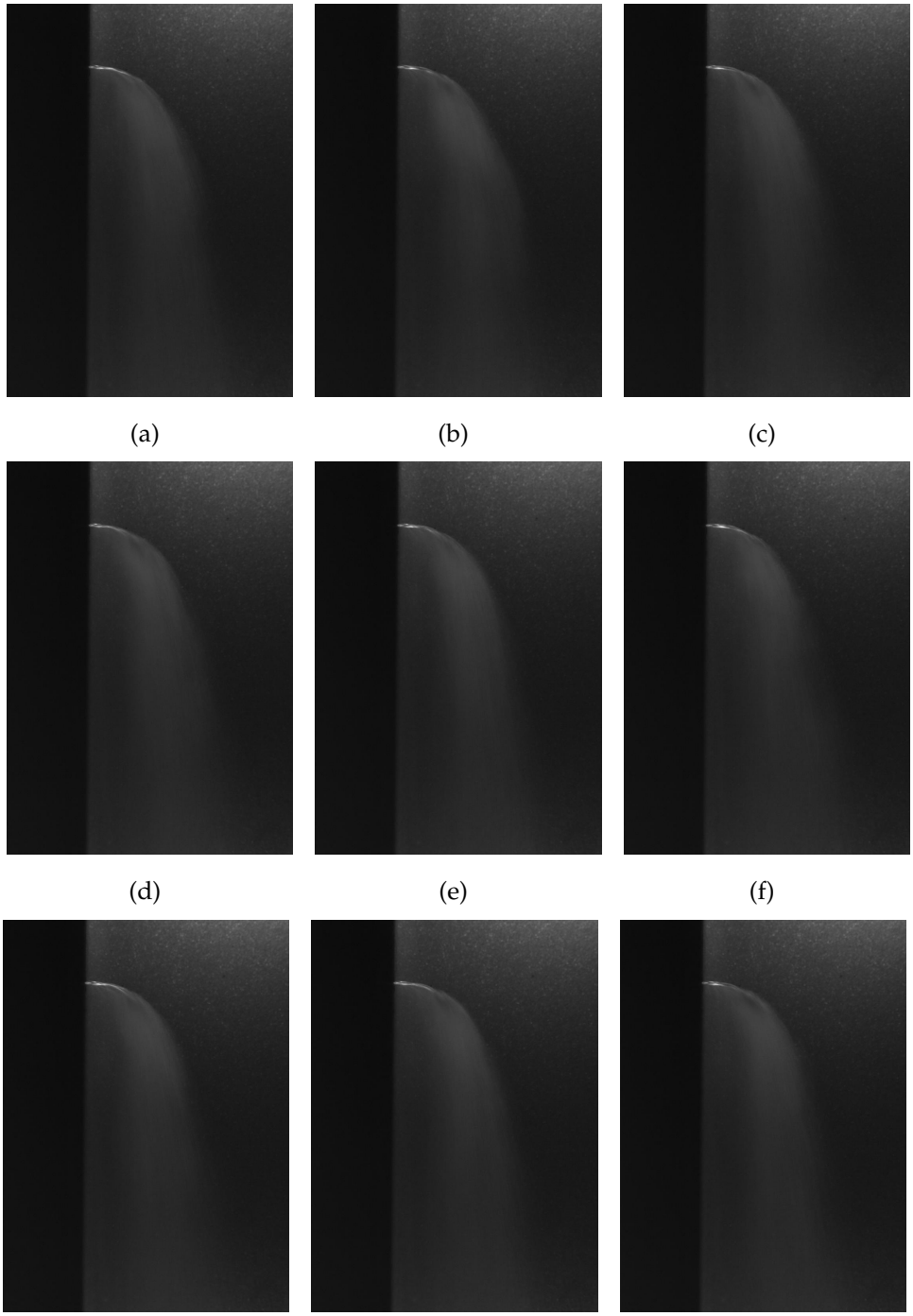

(a) (b) (c)

(d) (e) (f)

(g) (h) (i)

Figure A.29: $\overset{\Downarrow}{\odot}$ Selection of images extracted from HSV; Case 8 $We_g \approx 277$ and $q \approx 13$

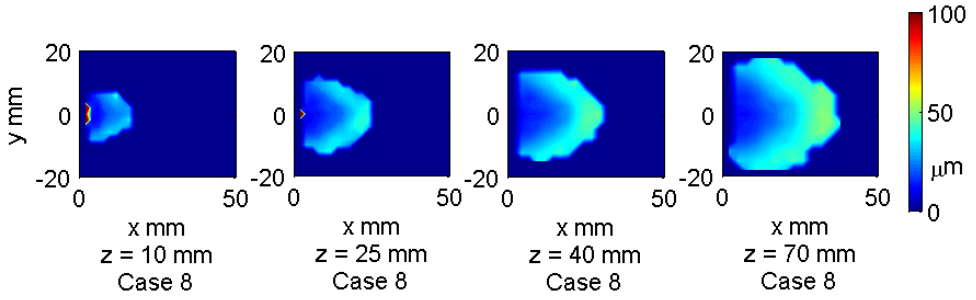

Figure A.30: ⇊⊙ Distribution of AMD; Case 8 $We_g = 277$ and $q = 13$

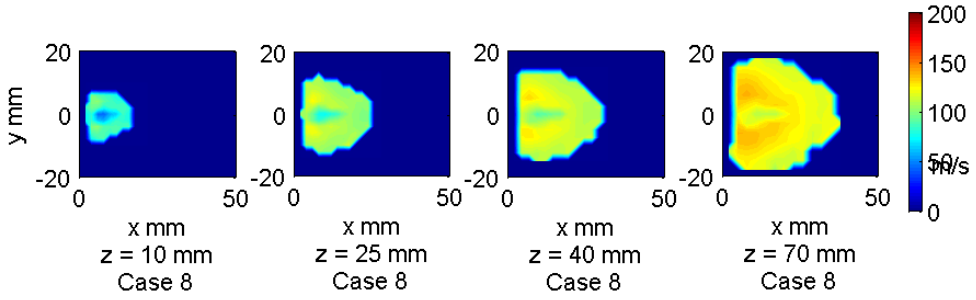

Figure A.31: ⇊⊙ Distribution of W_{drop}; Case 8 $We_g = 277$ and $q = 13$

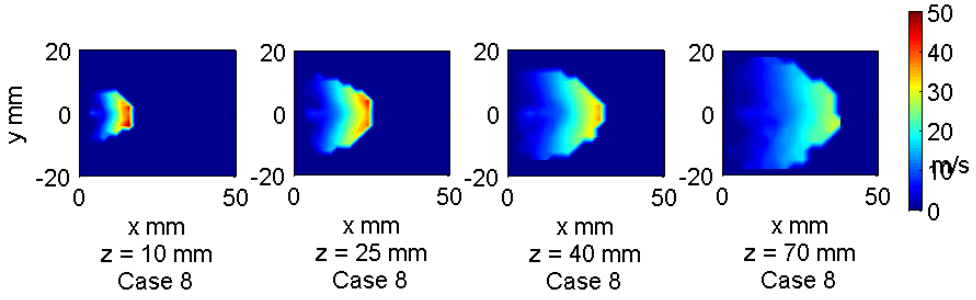

Figure A.32: ⇊⊙ Distribution of U_{drop}; Case 8 $We_g = 277$ and $q = 13$

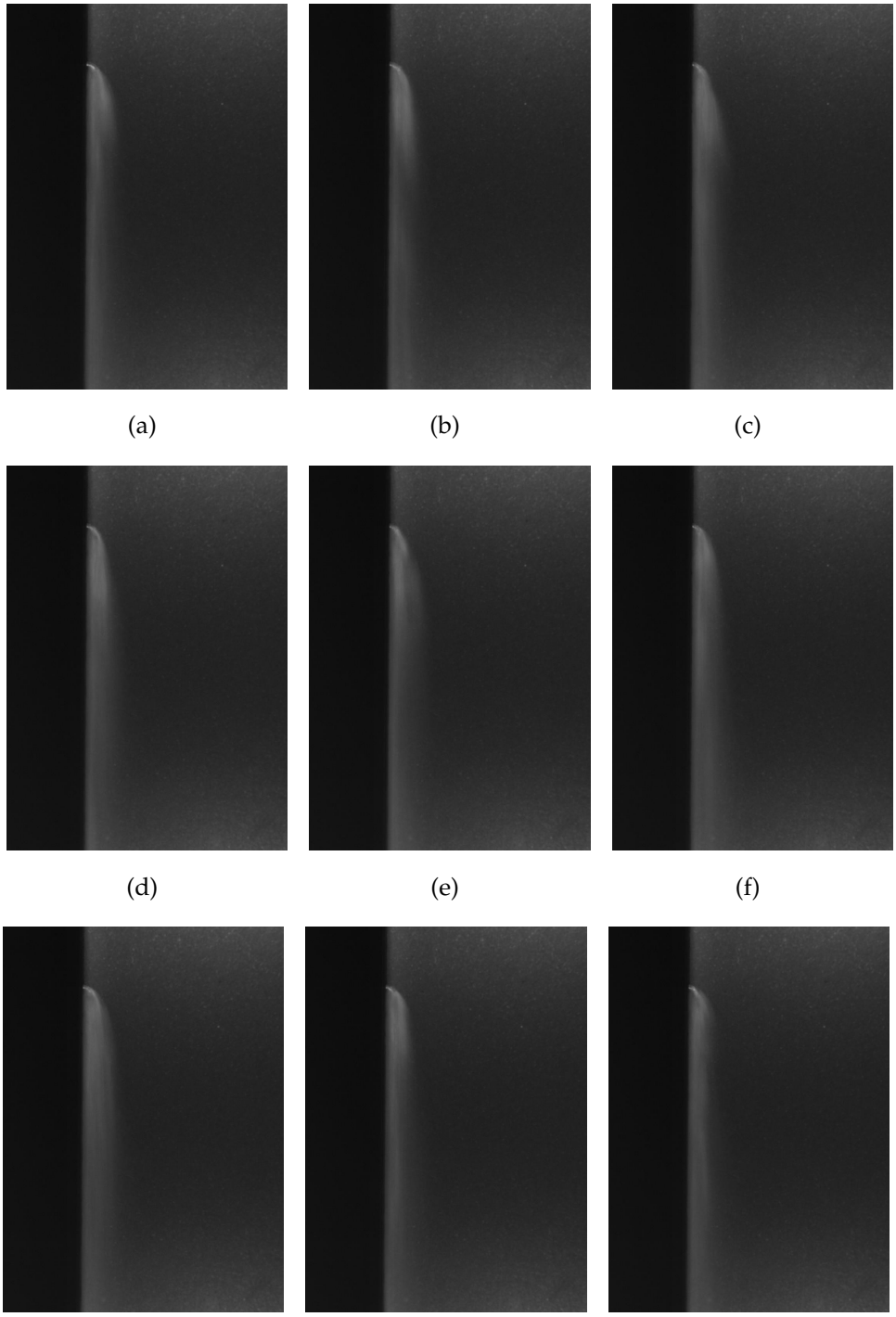

(a) (b) (c)

(d) (e) (f)

(g) (h) (i)

Figure A.33: ⇓⊙ Selection of images extracted from HSV; Case 9 $We_g \approx 594$ and $q \approx 0.8$

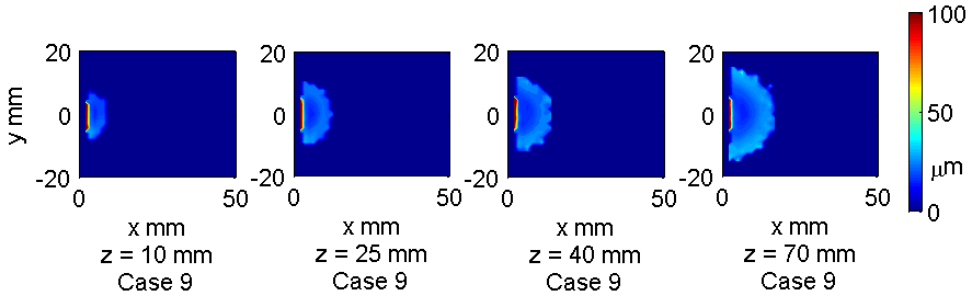

Figure A.34: ⇓⊙ Distribution of AMD; Case 9 $We_g = 594$ and $q = 0.8$

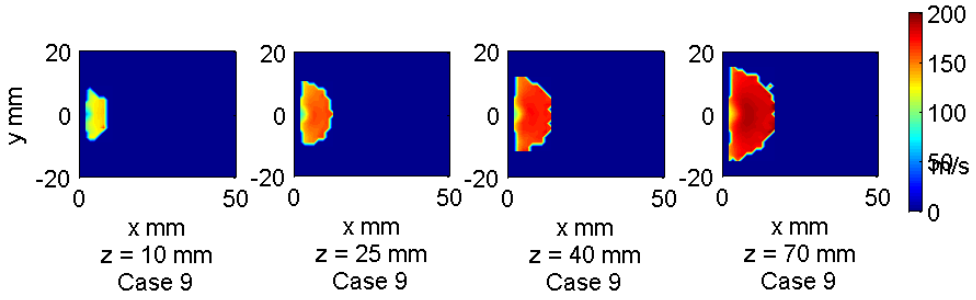

Figure A.35: ⇓⊙ Distribution of W_{drop}; Case 9 $We_g = 594$ and $q = 0.8$

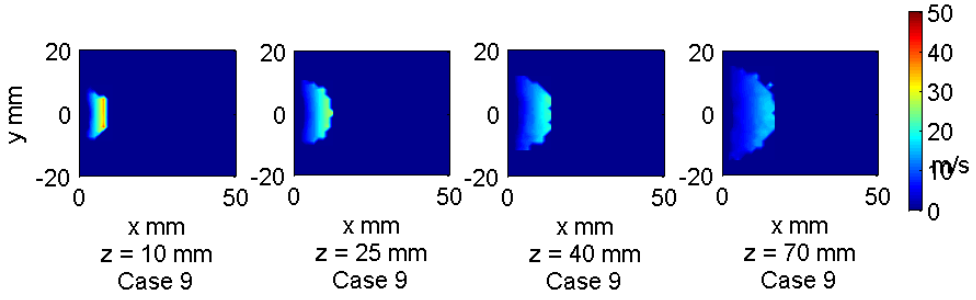

Figure A.36: ⇓⊙ Distribution of U_{drop}; Case 9 $We_g = 594$ and $q = 0.8$

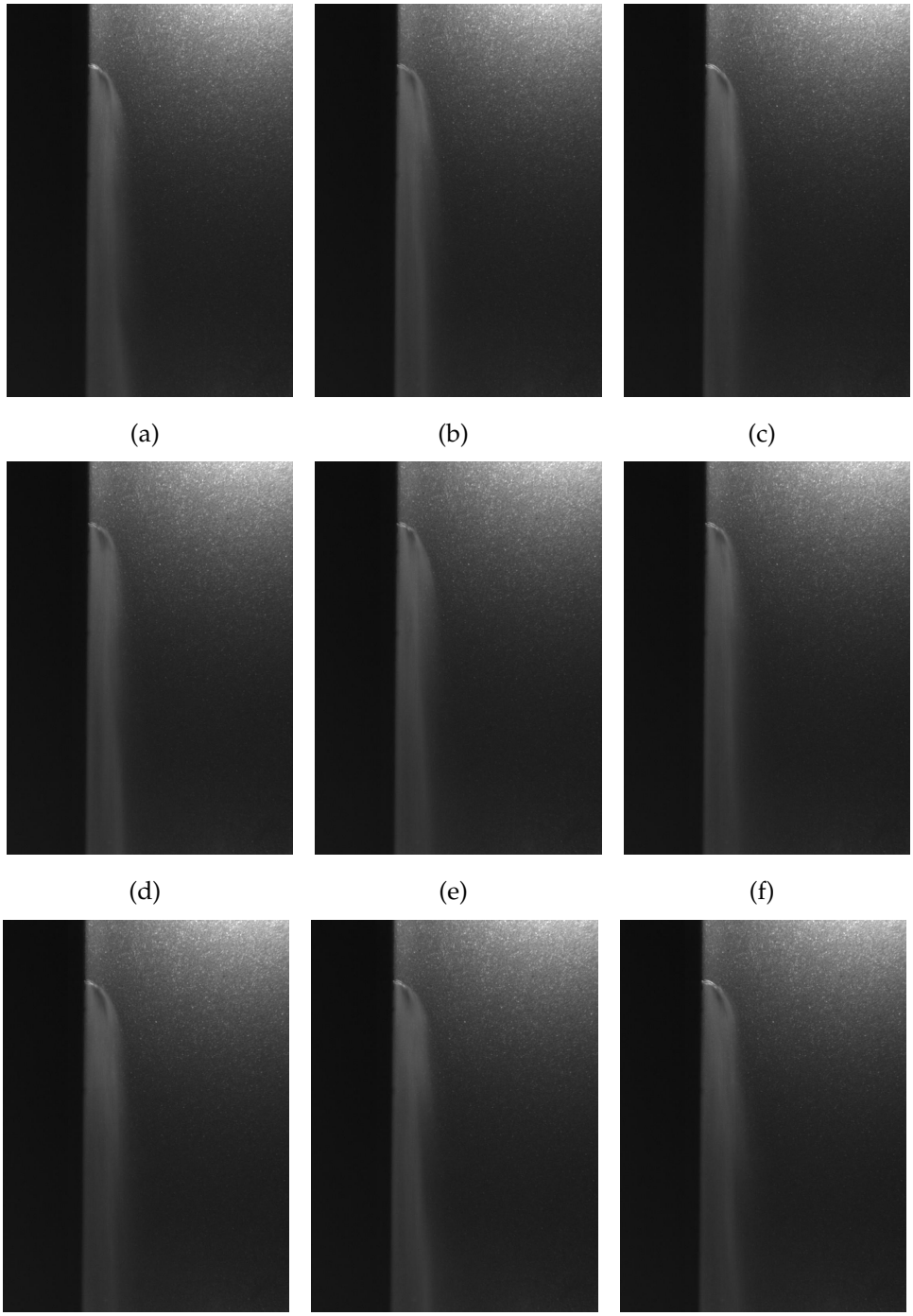

(a) (b) (c)

(d) (e) (f)

(g) (h) (i)

Figure A.37: ⇓⊙ Selection of images extracted from HSV; Case 10 $We_g \approx 586$ and $q \approx 2.2$

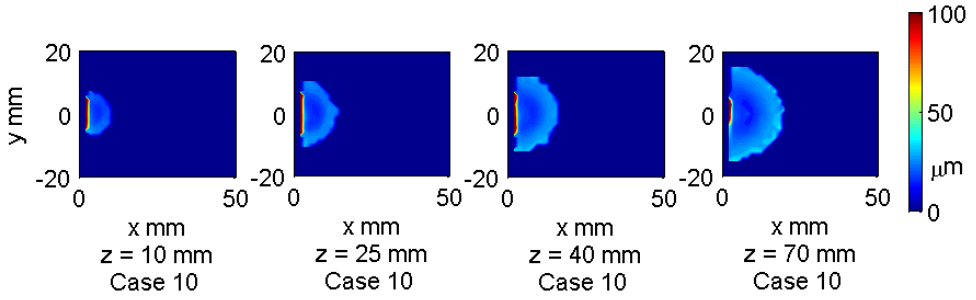

Figure A.38: ⇓⊙ Distribution of AMD; Case 10 $We_g = 586$ and $q = 2.2$

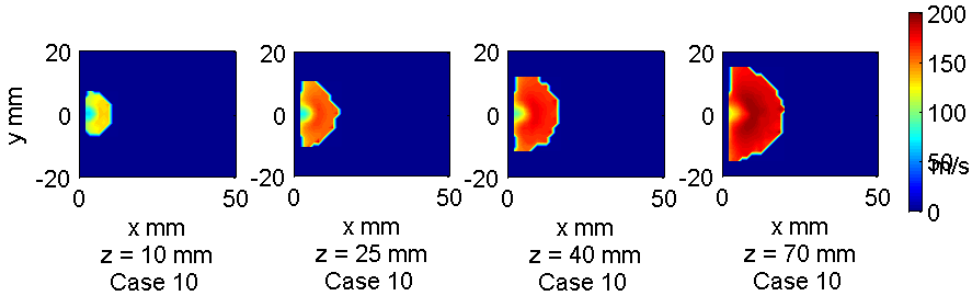

Figure A.39: ⇓⊙ Distribution of W_{drop}; Case 10 $We_g = 586$ and $q = 2.2$

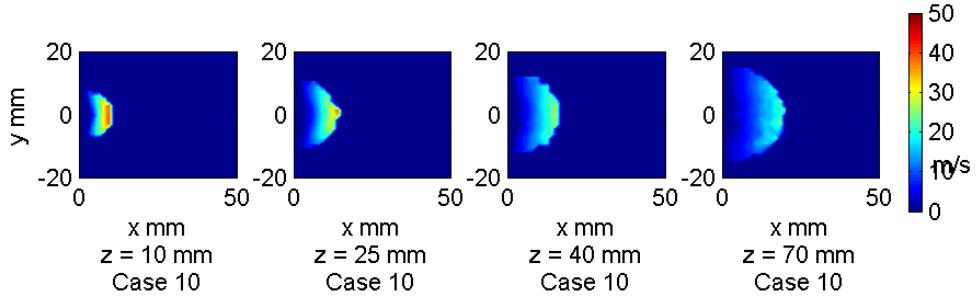

Figure A.40: ⇓⊙ Distribution of U_{drop}; Case 10 $We_g = 586$ and $q = 2.2$

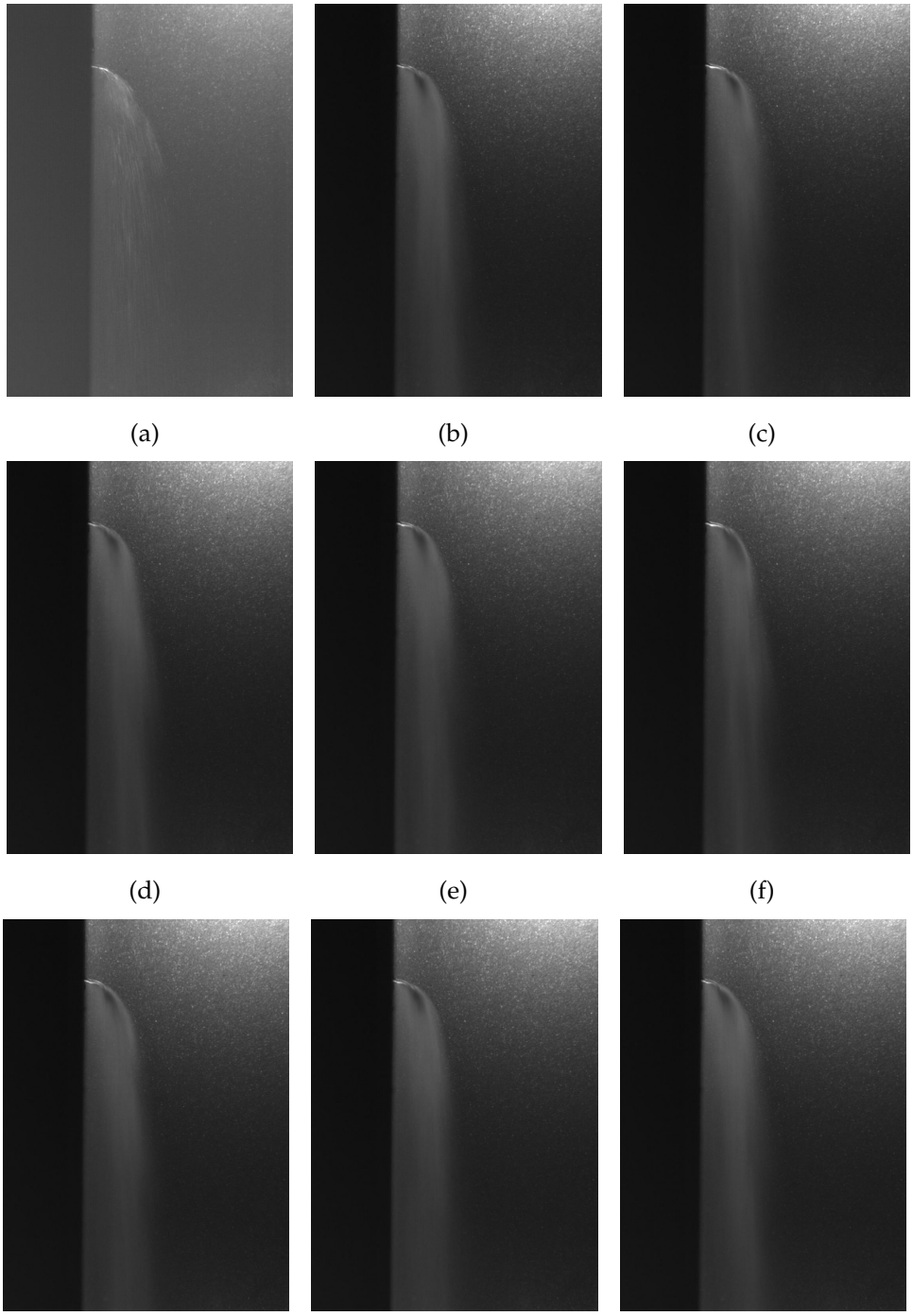

(a) (b) (c)

(d) (e) (f)

(g) (h) (i)

Figure A.41: $\overset{\Downarrow}{\odot}$ Selection of images extracted from HSV; Case 11 $We_g \approx 580$ and $q \approx 3.3$

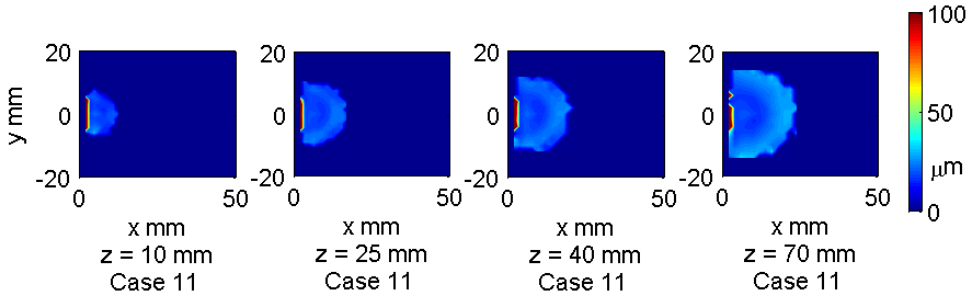

Figure A.42: ⇓⊙ Distribution of AMD; Case 11 $We_g = 580$ and $q = 3.3$

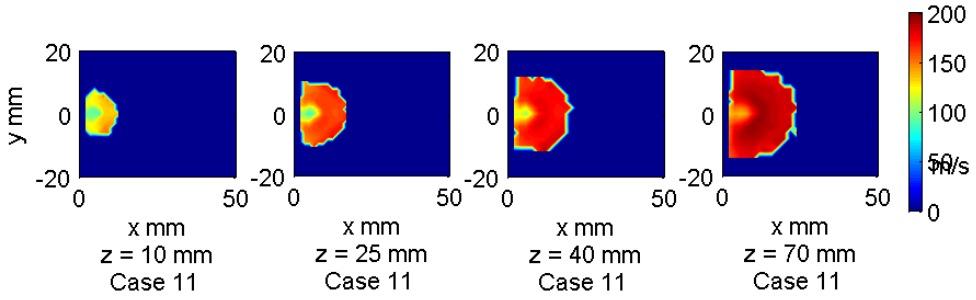

Figure A.43: ⇓⊙ Distribution of W_{drop}; Case 11 $We_g = 580$ and $q = 3.3$

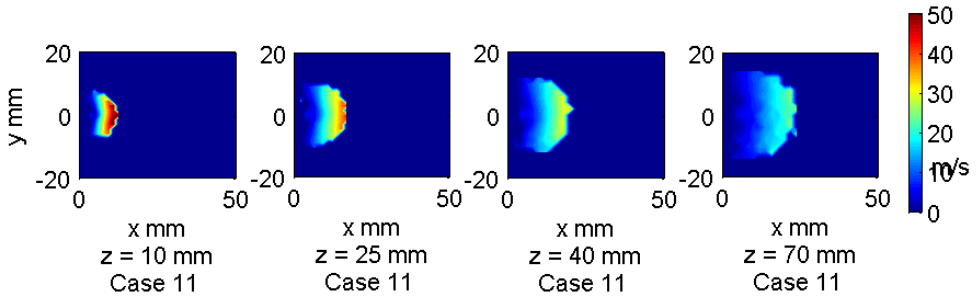

Figure A.44: ⇓⊙ Distribution of U_{drop}; Case 11 $We_g = 580$ and $q = 3.3$

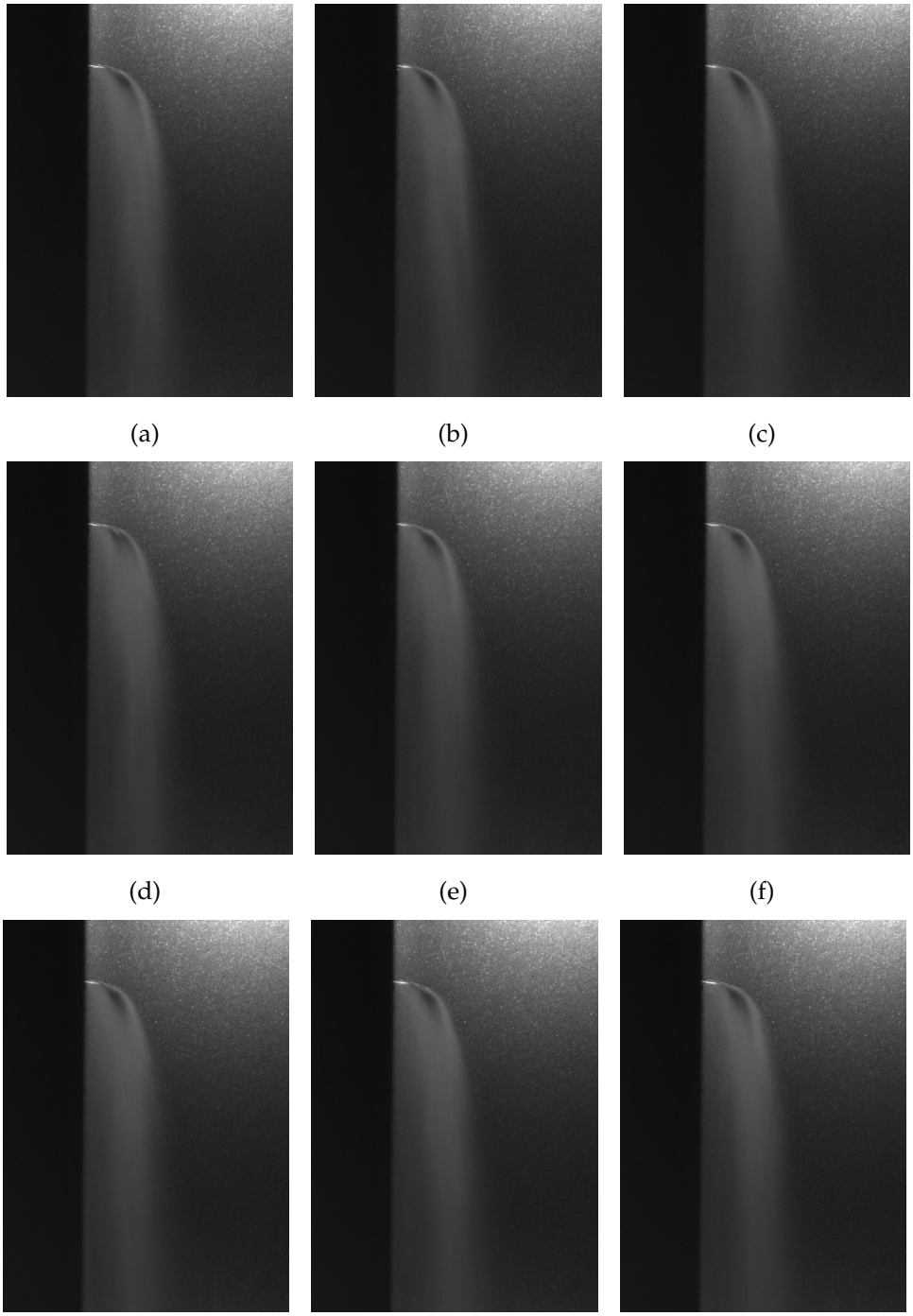

(a) (b) (c)

(d) (e) (f)

(g) (h) (i)

Figure A.45: $\overset{\Downarrow}{\odot}$ Selection of images extracted from HSV; Case 12 $We_g \approx 580$ and $q \approx 6.5$

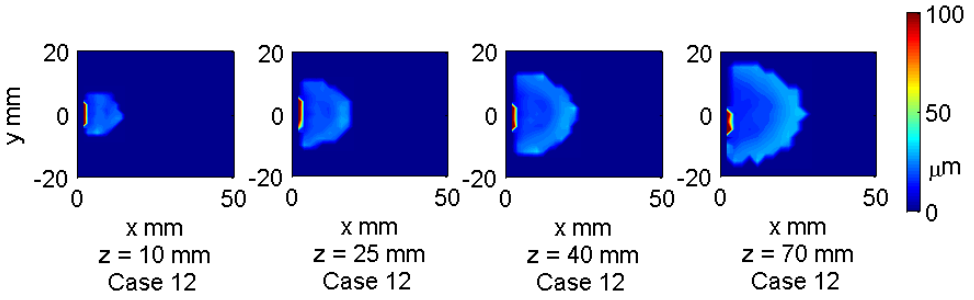

Figure A.46: ⇓⊙ Distribution of AMD; Case 12 $We_g = 580$ and $q = 6.5$

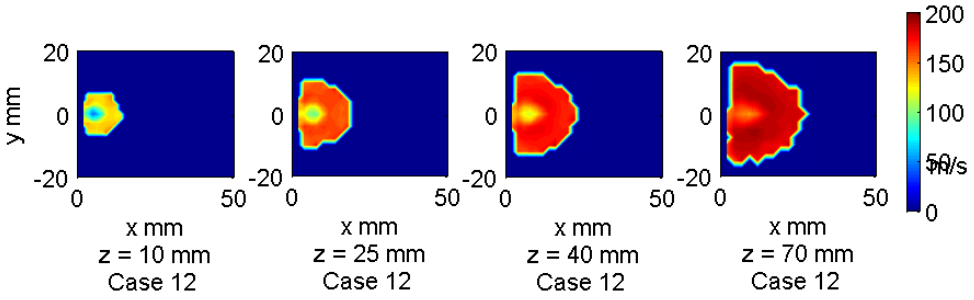

Figure A.47: ⇓⊙ Distribution of W_{drop}; Case 12 $We_g = 580$ and $q = 6.5$

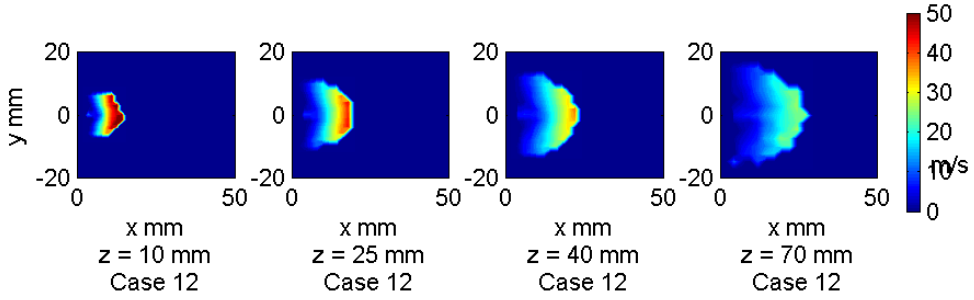

Figure A.48: ⇓⊙ Distribution of U_{drop}; Case 12 $We_g = 580$ and $q = 6.5$

Appendix B

Horizontal Slot Nozzle Images and Plots

	$W_{mean} \approx$ **90 m/s**	$W_{mean} \approx$ **135 m/s**	$W_{mean} \approx$ **195 m/s**
Δ**p** ≈ **0.5 bar**	Case 1: 310, (2.7)	Case 5: 727, (1.2)	Case 9: 1520, (0.5)
Δ**p** ≈ **1.5 bar**	Case 2: 304, (7.5)	Case 6: 699, (3.3)	Case 10: 1531, (1.8)
Δ**p** ≈ **3.5 bar**	Case 3: 297, (20.4)	Case 7: 704, (8.6)	Case 11: 1444, (4.1)
Δ**p** ≈ **6.5 bar**	Case 4: not possible	Case 8: 709, (15.8)	Case 12: 1263, (8.6)

Table B.1: $\overset{\Downarrow}{\ominus}$ PDPA average test conditions, $We_{g\,deq}$ (q)

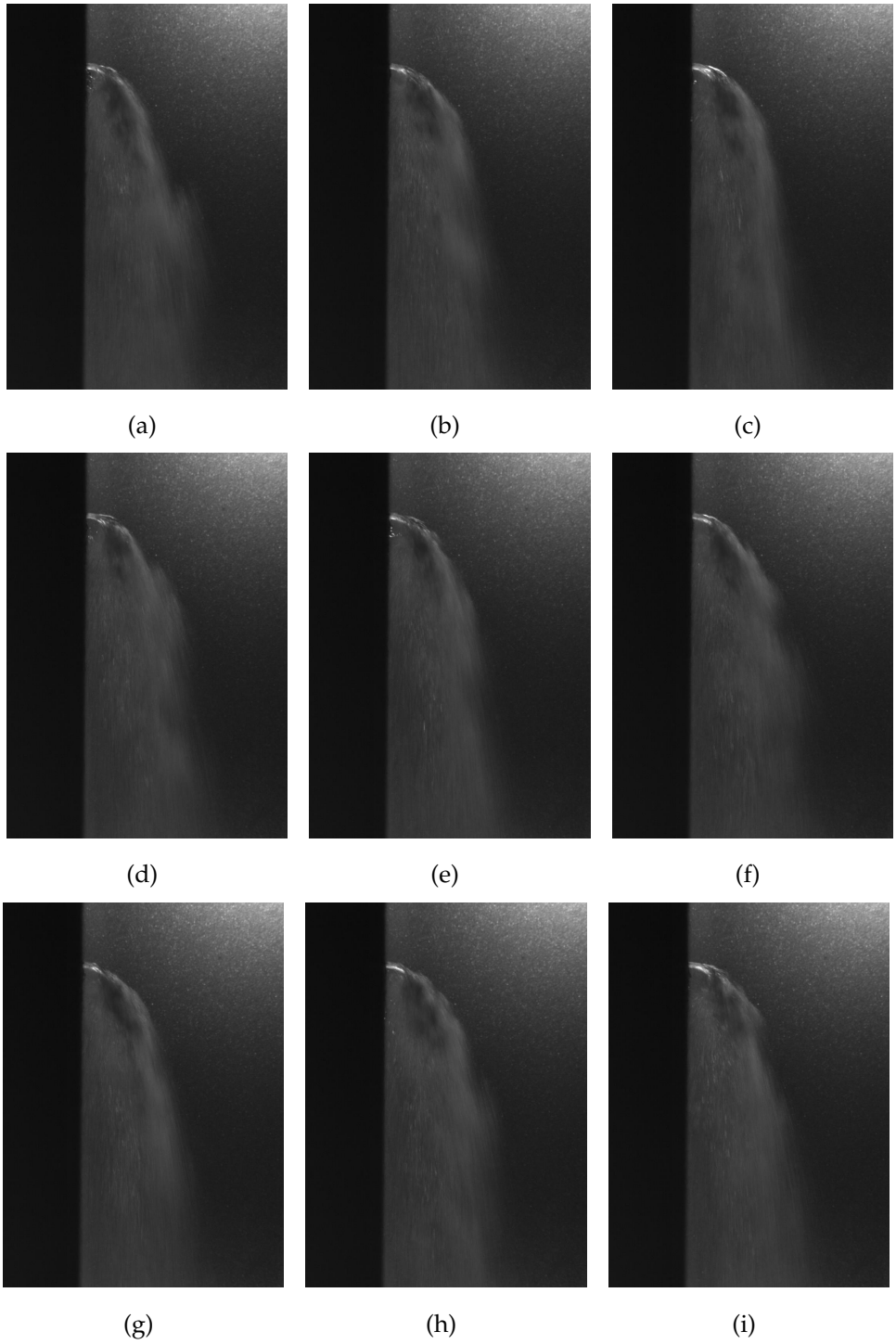

(a) (b) (c)

(d) (e) (f)

(g) (h) (i)

Figure B.1: ⇓ Selection of images extracted from HSV; Case 1 $We_{g\,deq} \approx 310$ $q \approx 2.7$

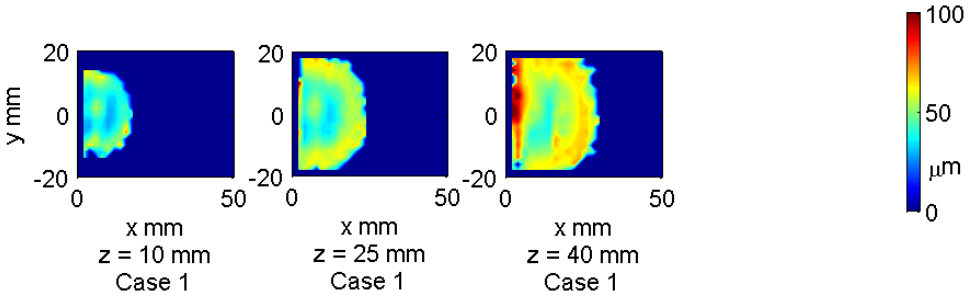

Figure B.2: ⇓ Distribution of AMD [D_{10}] ; Case1 $We_{g\,deq}$ = 310 q = 2.7

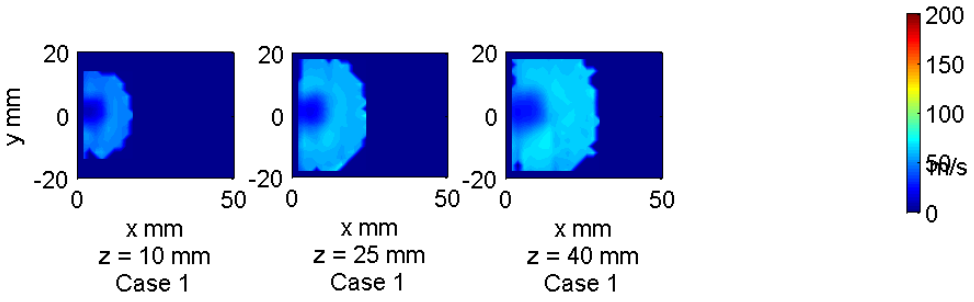

Figure B.3: ⇓ Distribution of W_{drop}; Case1 $We_{g\,deq}$ = 310 q = 2.7

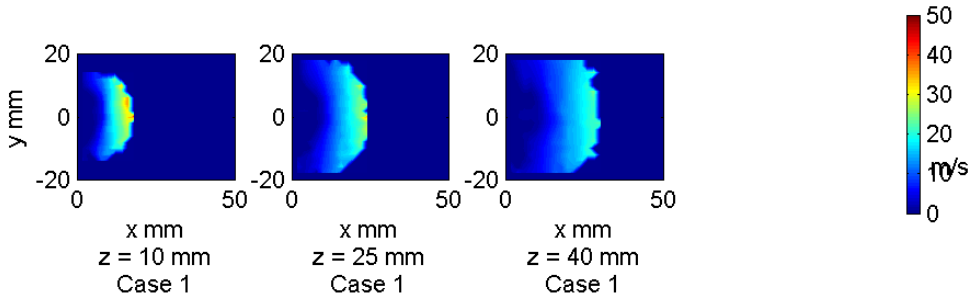

Figure B.4: ⇓ Distribution of U_{drop}; Case1 $We_{g\,deq}$ = 310 q = 2.7

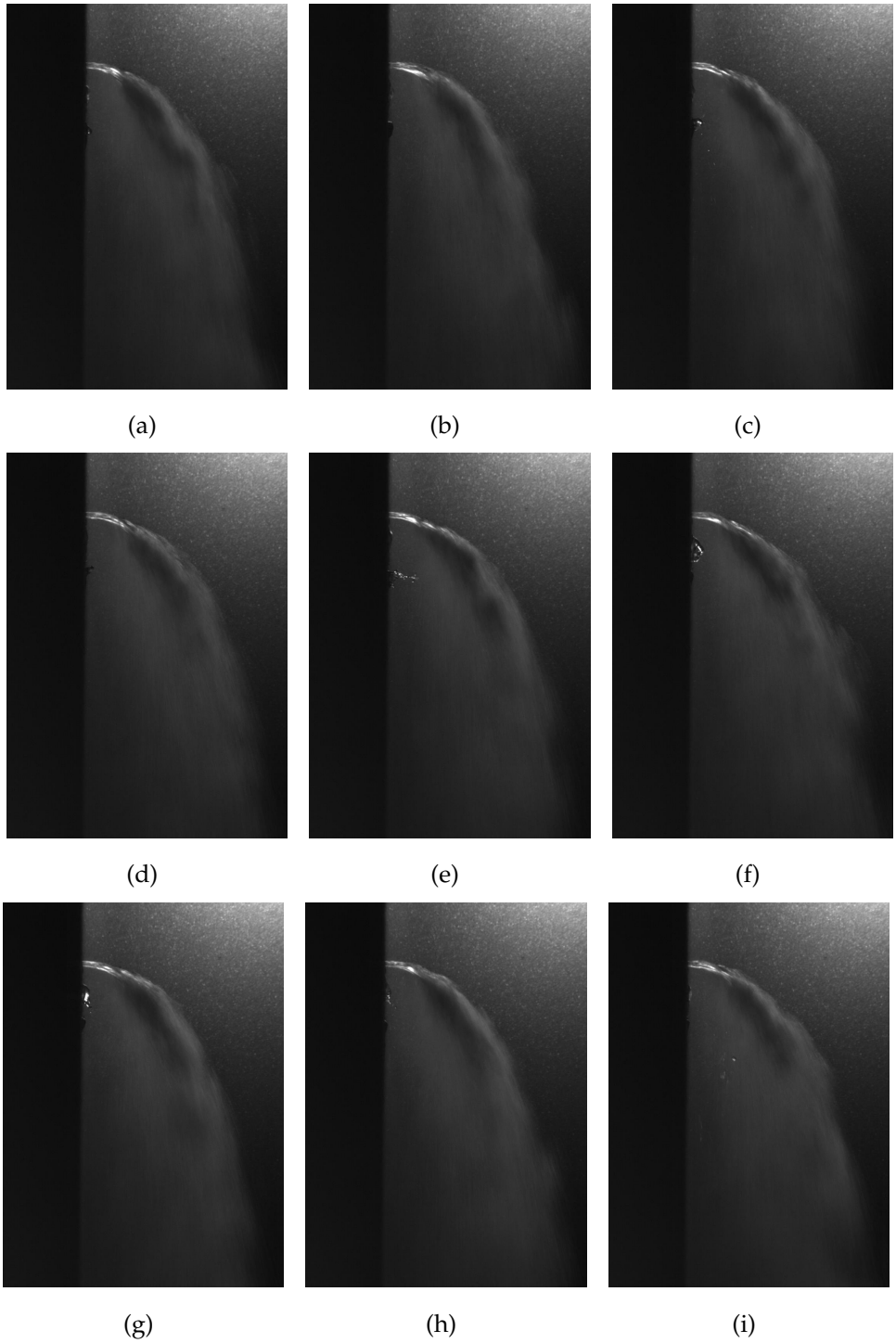

(a) (b) (c)

(d) (e) (f)

(g) (h) (i)

Figure B.5: $\overset{\Downarrow}{\ominus}$ Selection of images extracted from HSV; Case2We$_{g\,deq} \approx 304$ $q \approx 7.5$

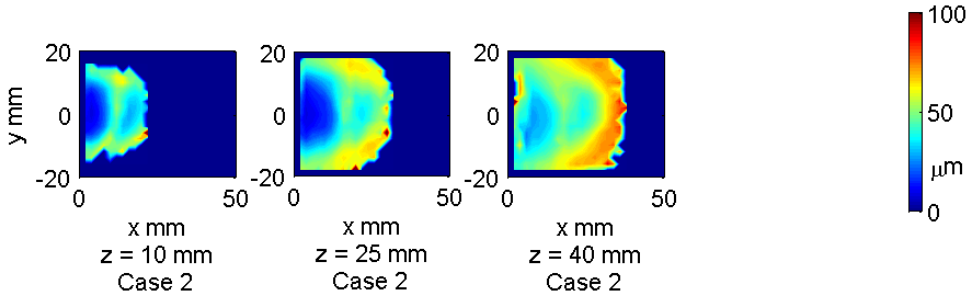

Figure B.6: ⇓ Distribution of AMD [D_{10}] ; Case2We$_{g\,deq}$ = 304 q = 7.5

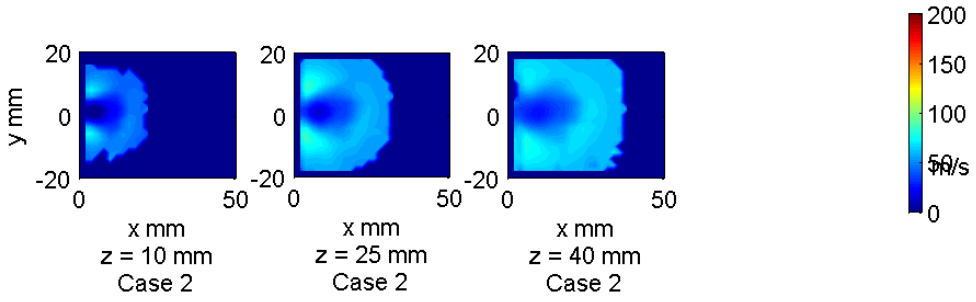

Figure B.7: ⇓ Distribution of W_{drop}; Case2We$_{g\,deq}$ = 304 q = 7.5

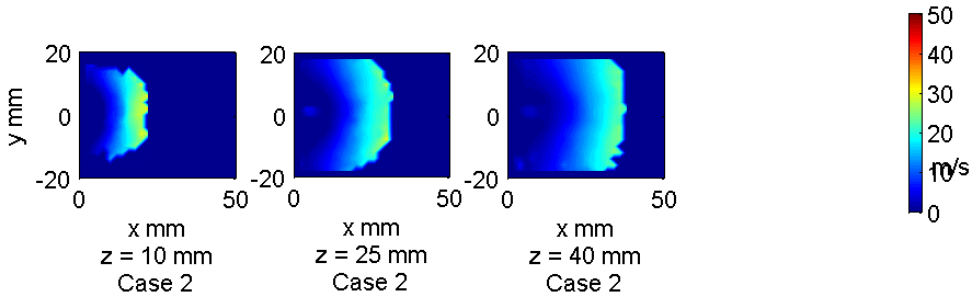

Figure B.8: ⇓ Distribution of U_{drop}; Case2We$_{g\,deq}$ = 304 q = 7.5

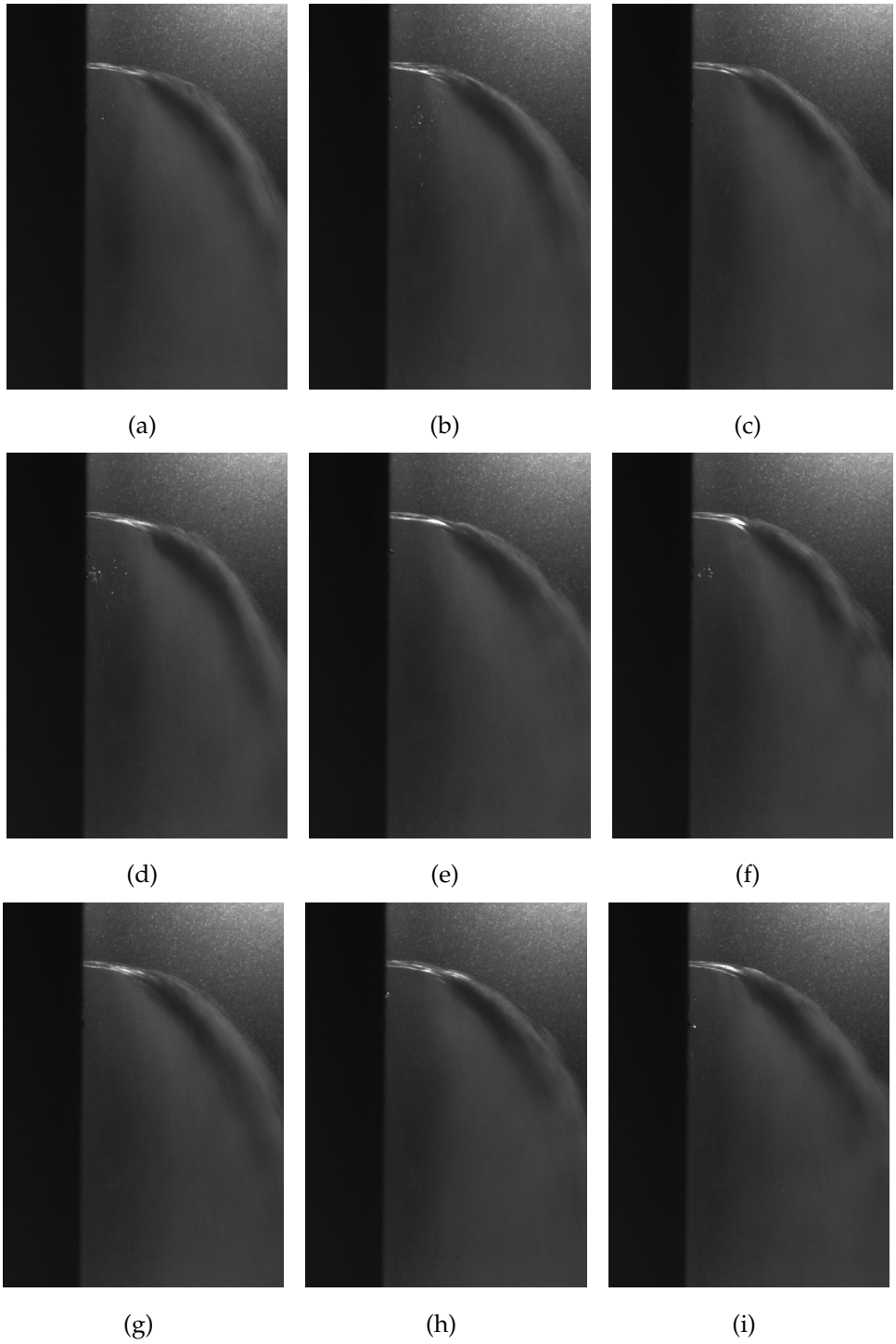

(a) (b) (c)

(d) (e) (f)

(g) (h) (i)

Figure B.9: ⇓ Selection of images extracted from HSV; Case 3 $We_{g\,deq} \approx 297$ $q \approx 20.4$

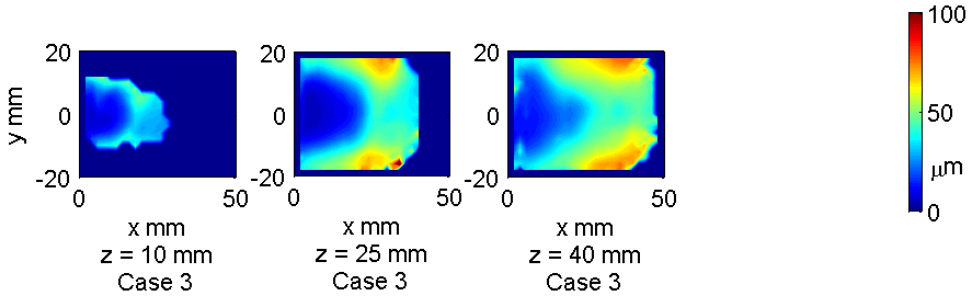

Figure B.10: ⇓ Distribution of AMD [D_{10}] ; Case 3 $We_{g\,deq} = 297$ $q = 20.4$

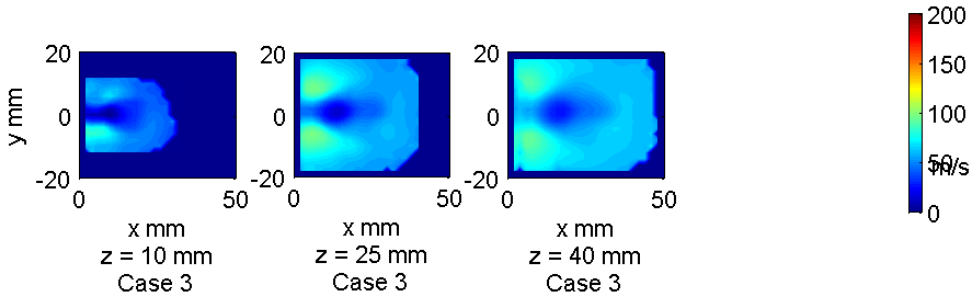

Figure B.11: ⇓ Distribution of W_{drop}; Case 3 $We_{g\,deq} = 297$ $q = 20.4$

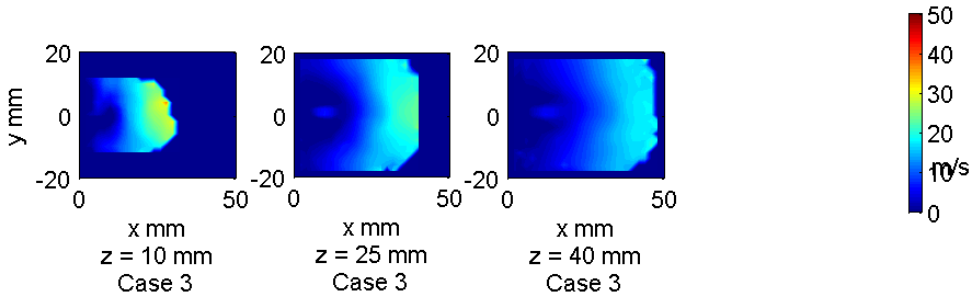

Figure B.12: ⇓ Distribution of U_{drop}; Case 3 $We_{g\,deq} = 297$ $q = 20.4$

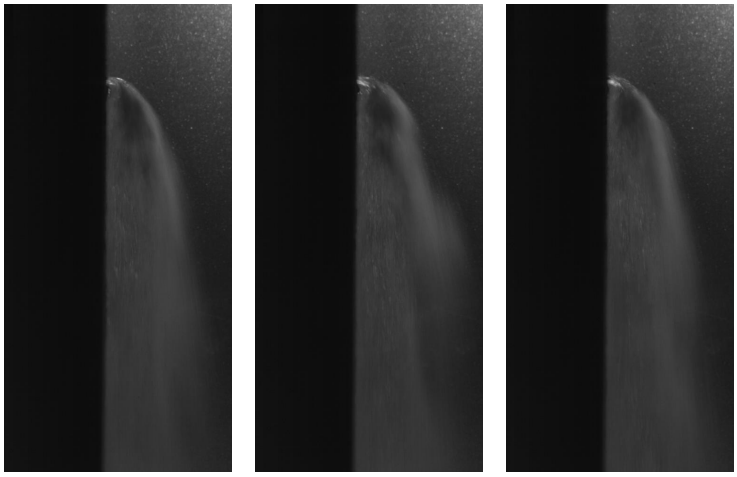

(a) (b) (c)

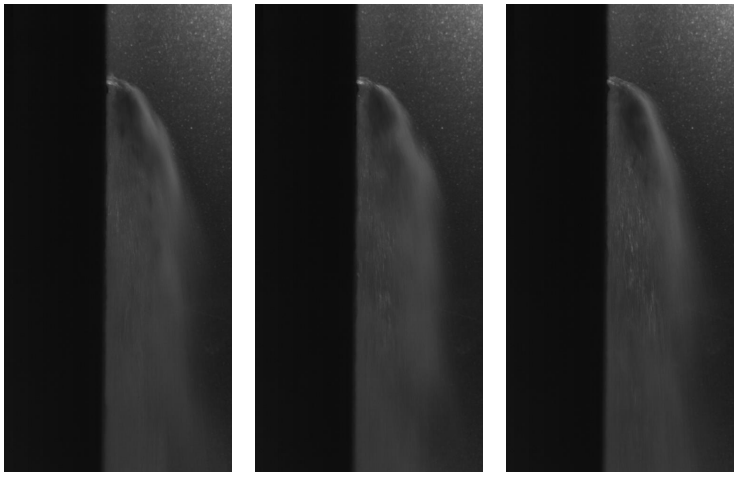

(d) (e) (f)

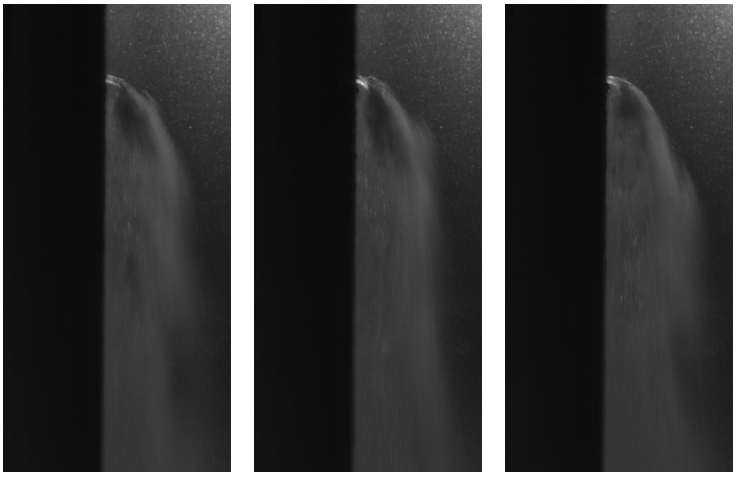

(g) (h) (i)

Figure B.13: ⇊ Selection of images extracted from HSV; Case 5 $We_{g\,deq} \approx 727$ $q \approx 1.2$

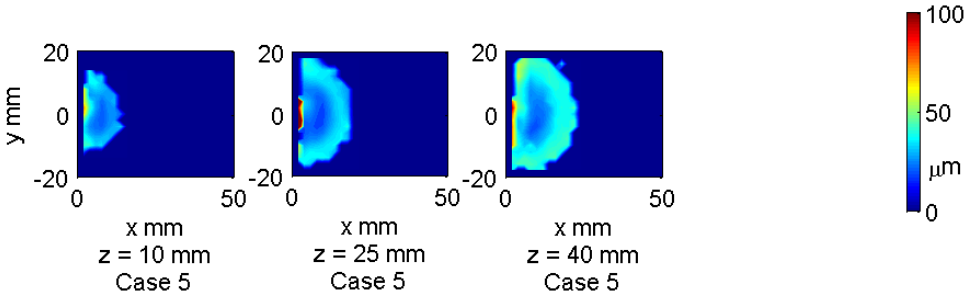

Figure B.14: ⇓ Distribution of AMD [D_{10}] ; Case 5 $We_{g\,deq} = 727$ $q = 1.2$

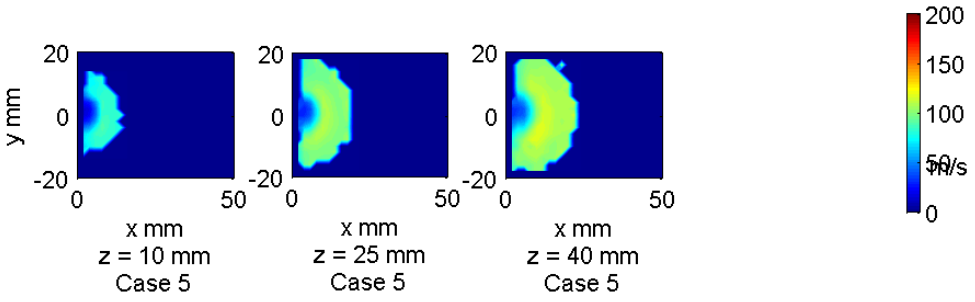

Figure B.15: ⇓ Distribution of W_{drop}; Case 5 $We_{g\,deq} = 727$ $q = 1.2$

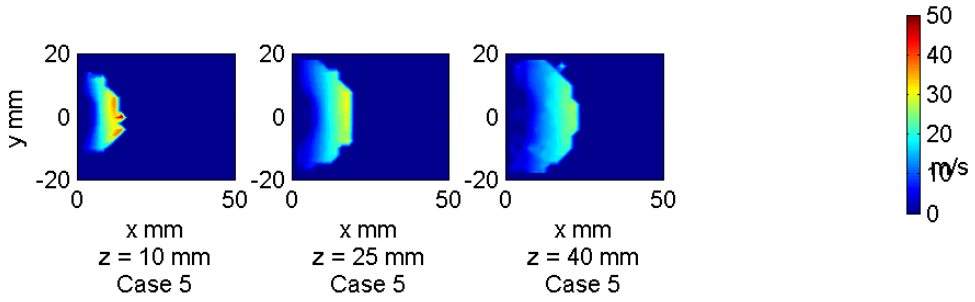

Figure B.16: ⇓ Distribution of U_{drop}; Case 5 $We_{g\,deq} = 727$ $q = 1.2$

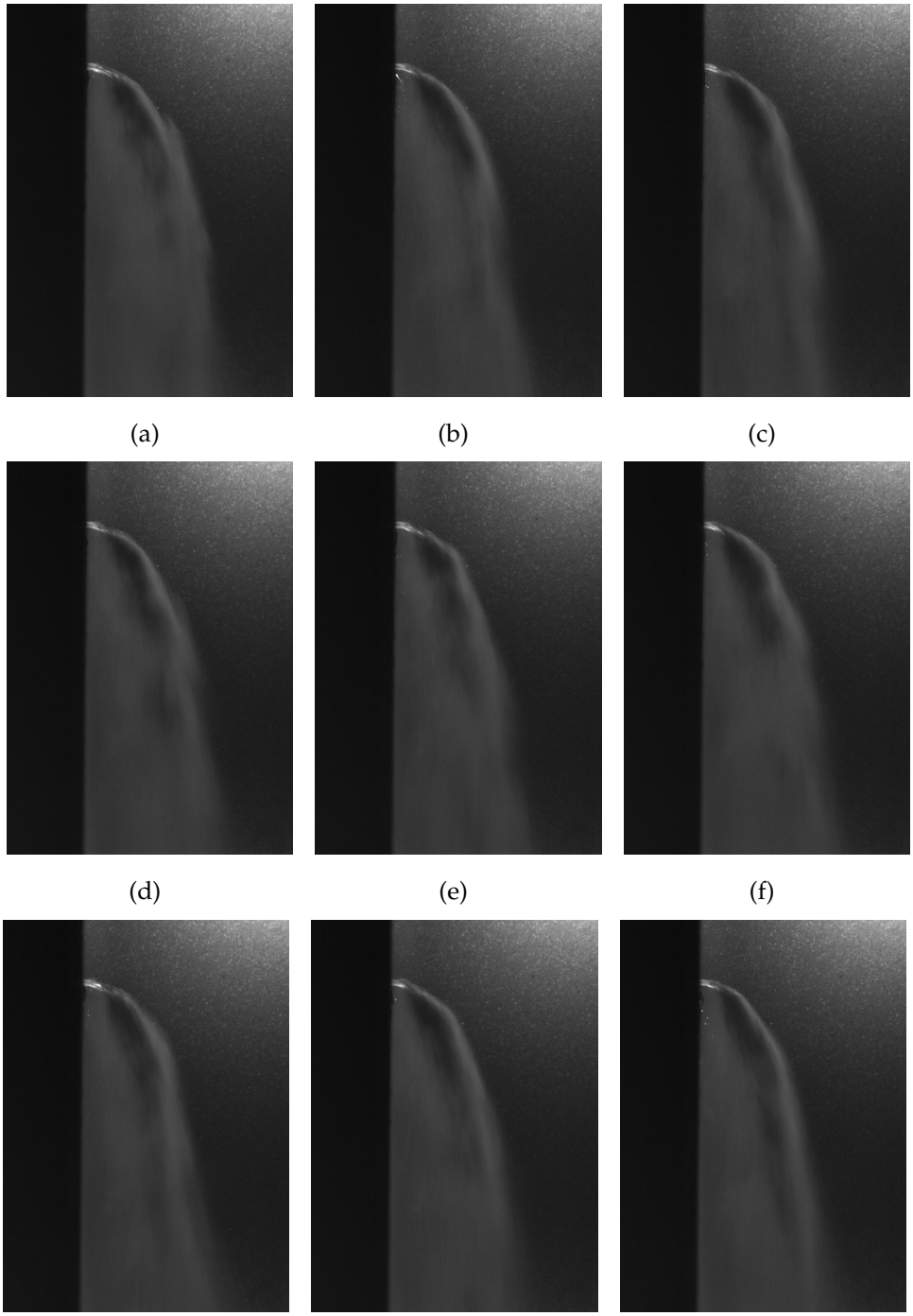

(a) (b) (c)

(d) (e) (f)

(g) (h) (i)

Figure B.17: $\overset{\Downarrow}{\ominus}$ Selection of images extracted from HSV; Case 6 $We_{g\,deq} \approx 699$ $q \approx 3.3$

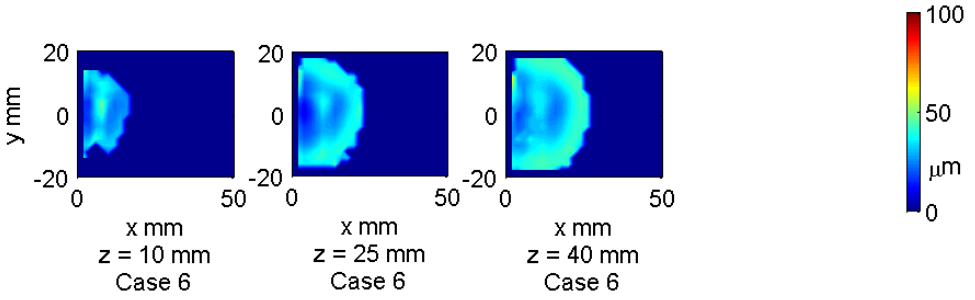

Figure B.18: ⇓ Distribution of AMD [D_{10}] ; Case 6 $We_{g\,deq} = 699$ $q = 3.3$

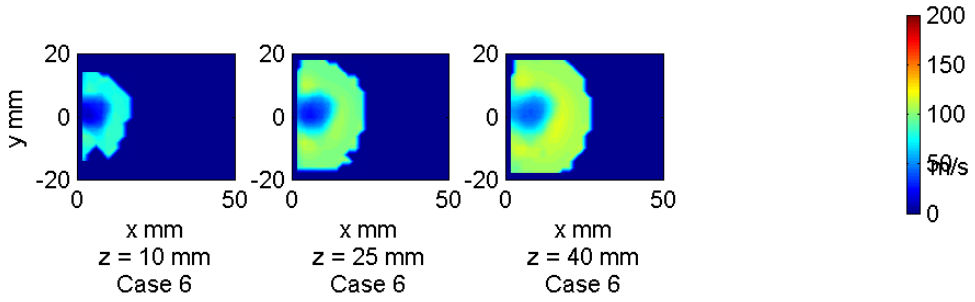

Figure B.19: ⇓ Distribution of W_{drop}; Case 6 $We_{g\,deq} = 699$ $q = 3.3$

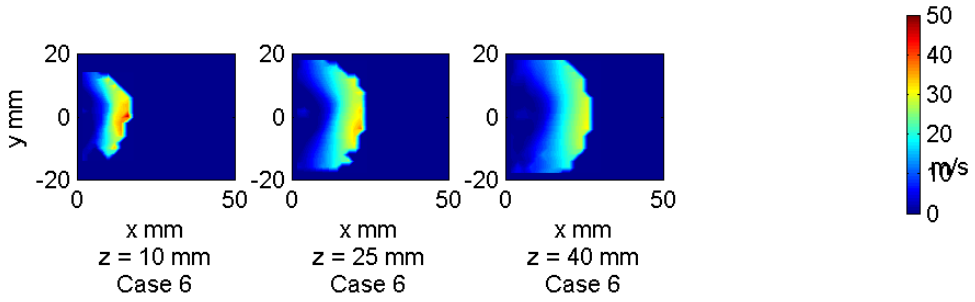

Figure B.20: ⇓ Distribution of U_{drop}; Case 6 $We_{g\,deq} = 699$ $q = 3.3$

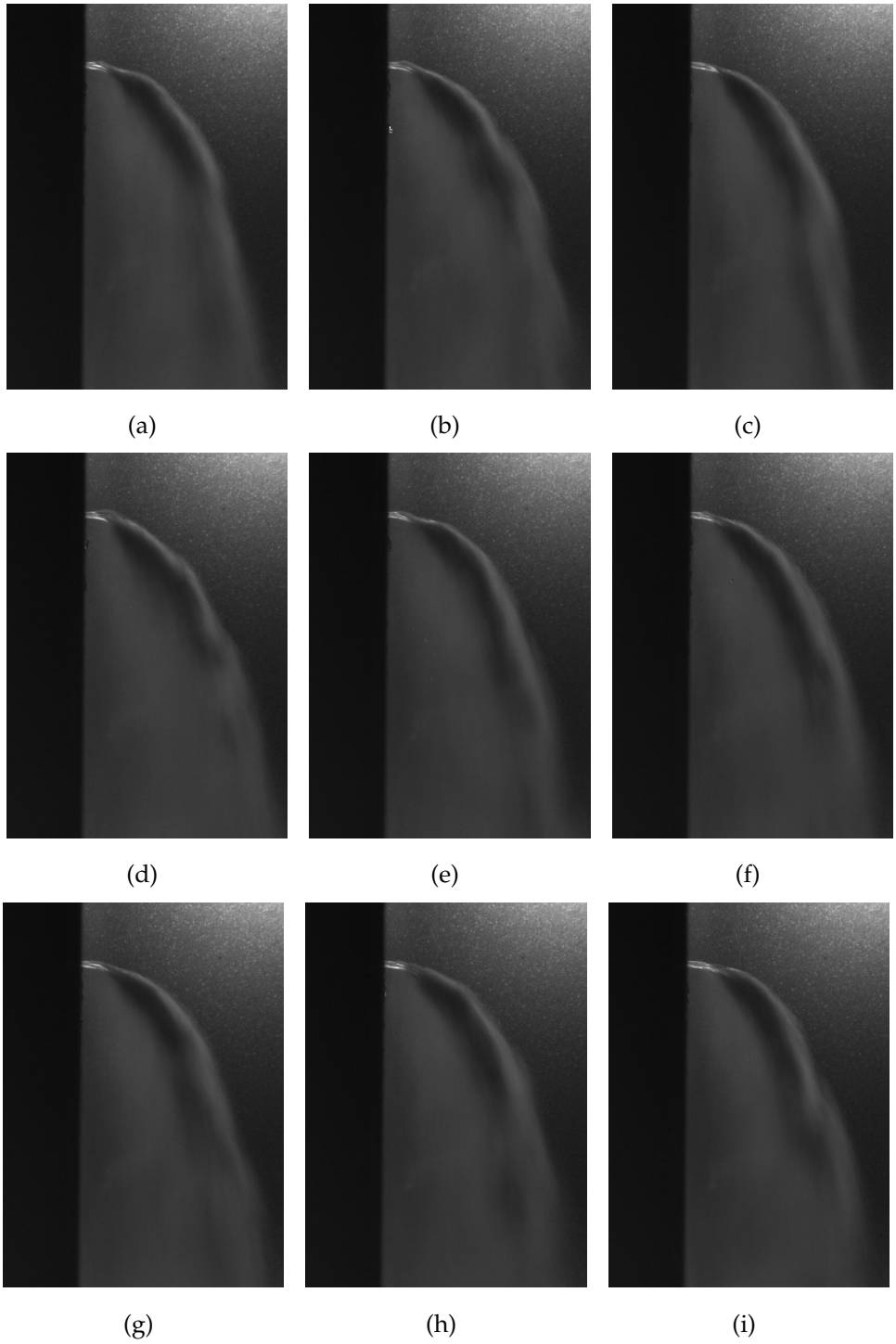

(a) (b) (c)

(d) (e) (f)

(g) (h) (i)

Figure B.21: ⇓ Selection of images extracted from HSV; Case 7 $We_{g\,deq} \approx 704$ $q \approx 8.6$

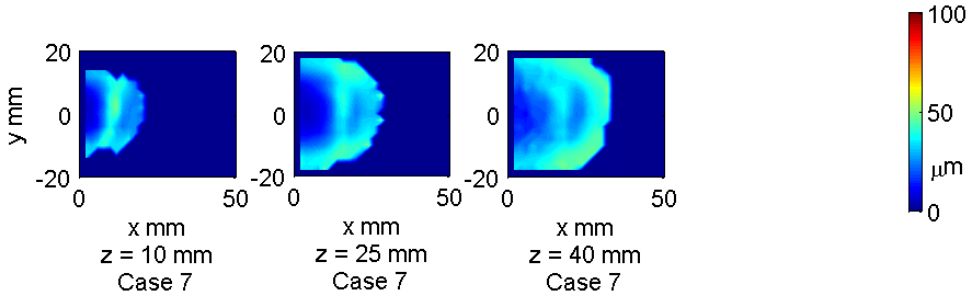

Figure B.22: ⇓ Distribution of AMD [D_{10}] ; Case 7 $We_{g\,deq}$ = 704 q = 8.6

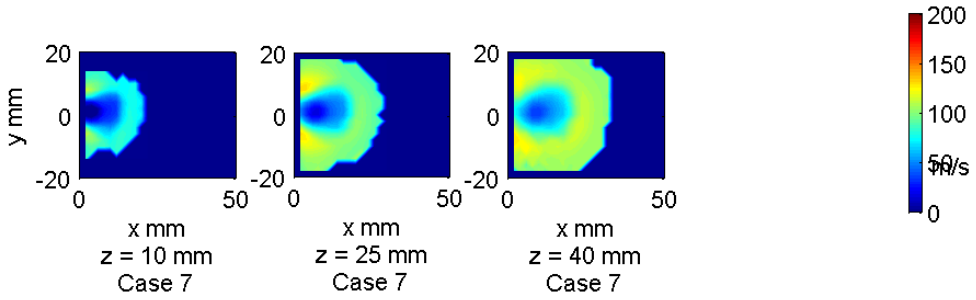

Figure B.23: ⇓ Distribution of W_{drop}; Case 7 $We_{g\,deq}$ = 704 q = 8.6

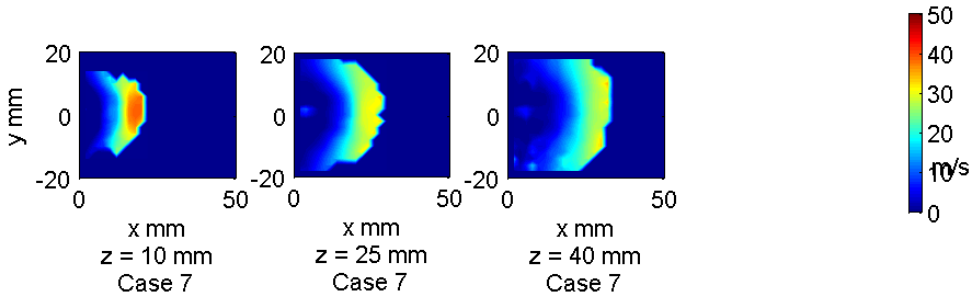

Figure B.24: ⇓ Distribution of U_{drop}; Case 7 $We_{g\,deq}$ = 704 q = 8.6

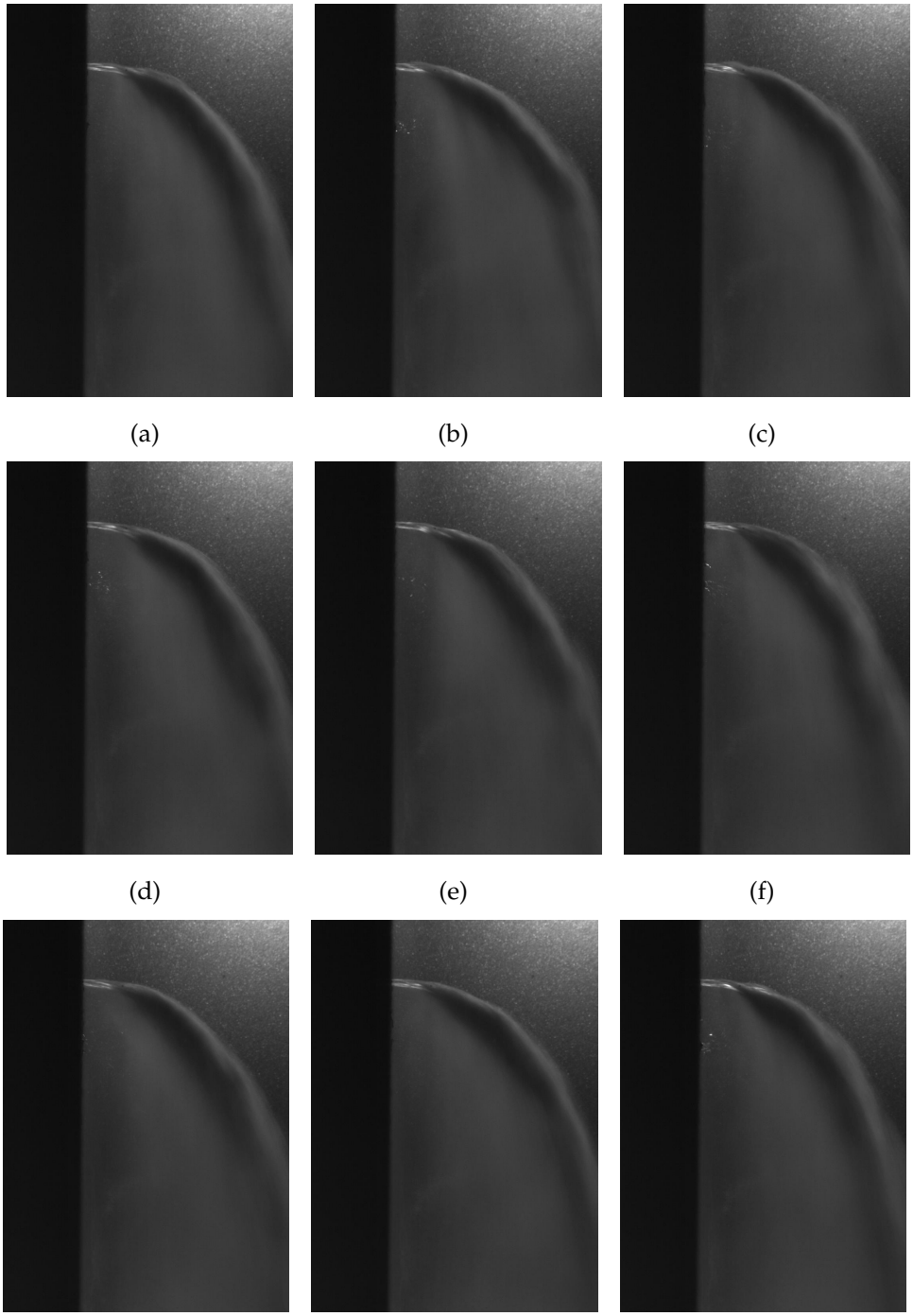

(a) (b) (c)

(d) (e) (f)

(g) (h) (i)

Figure B.25: ⇓⊖ Selection of images extracted from HSV; Case 8 $We_{g\,deq} \approx 709$ $q \approx 15.8$

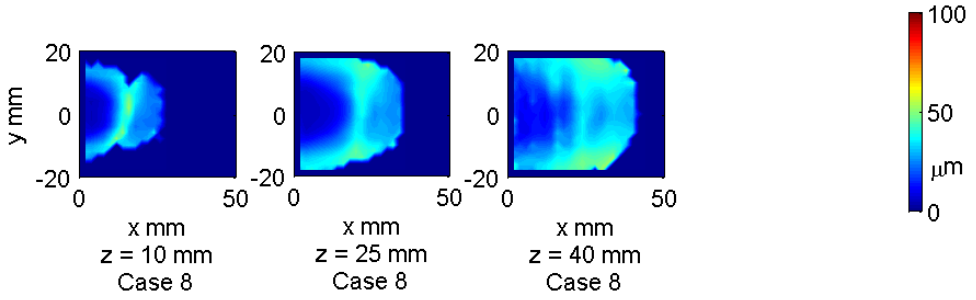

Figure B.26: ⇓ Distribution of AMD [D_{10}] ; Case 8 $We_{g\,deq}$ = 709 q = 15.8

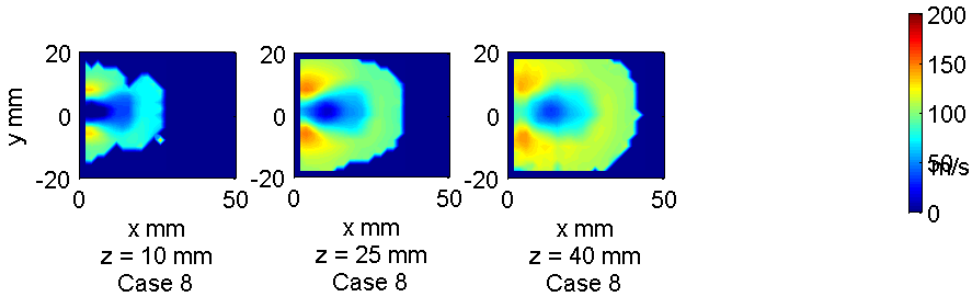

Figure B.27: ⇓ Distribution of W_{drop}; Case 8 $We_{g\,deq}$ = 709 q = 15.8

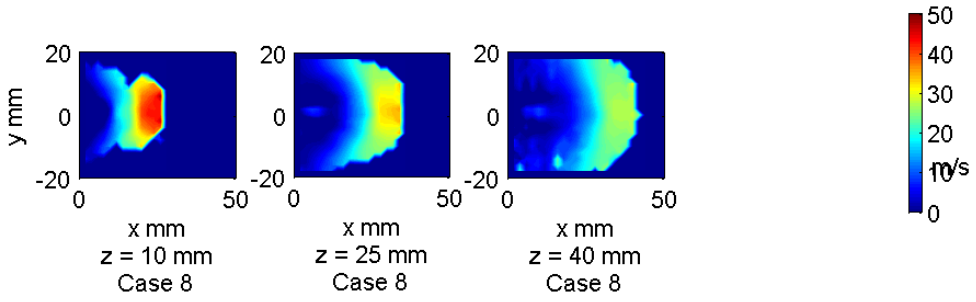

Figure B.28: ⇓ Distribution of U_{drop}; Case 8 $We_{g\,deq}$ = 709 q = 15.8

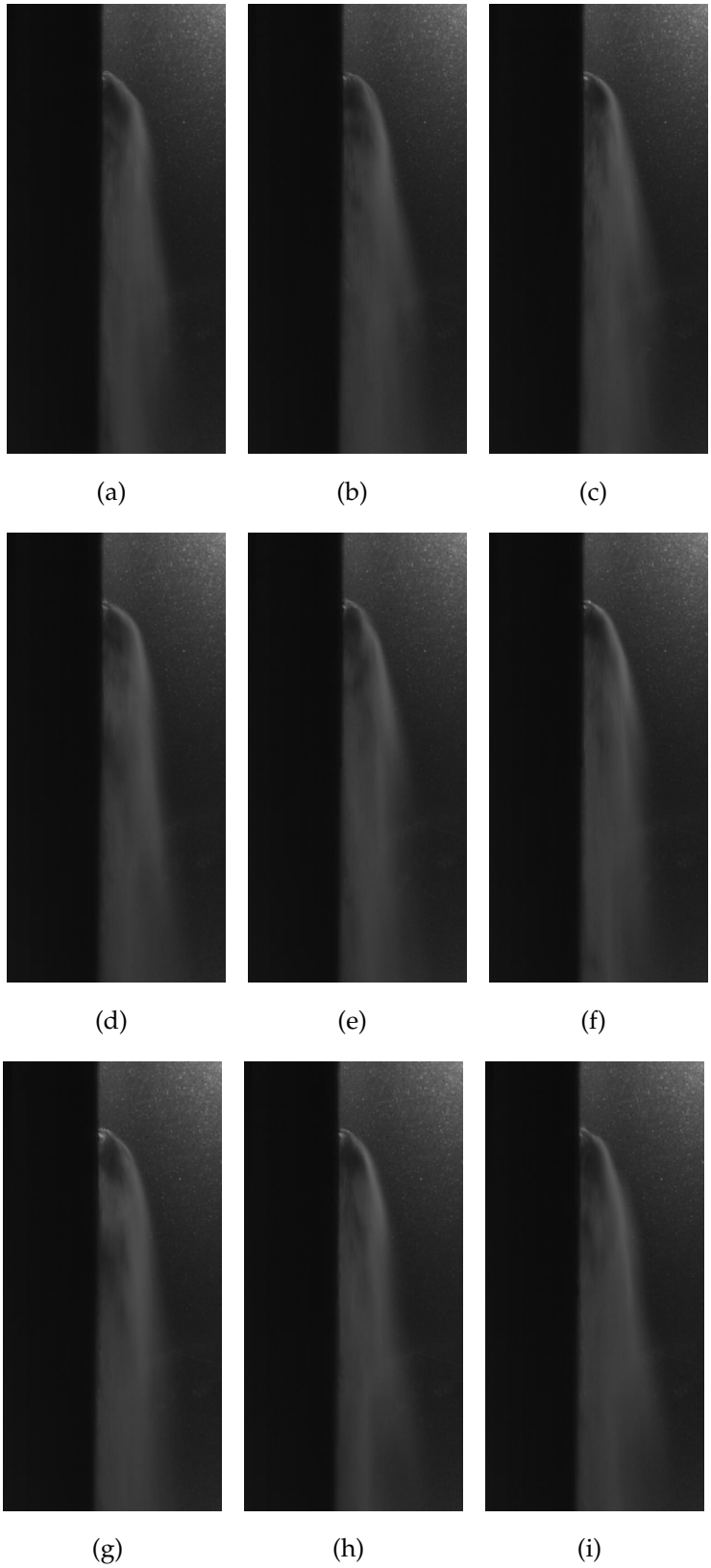

(a) (b) (c)

(d) (e) (f)

(g) (h) (i)

Figure B.29: ⇊⊖ Selection of images extracted from HSV; Case 9 $We_{g\,deq} \approx 1520$ $q \approx 0.5$

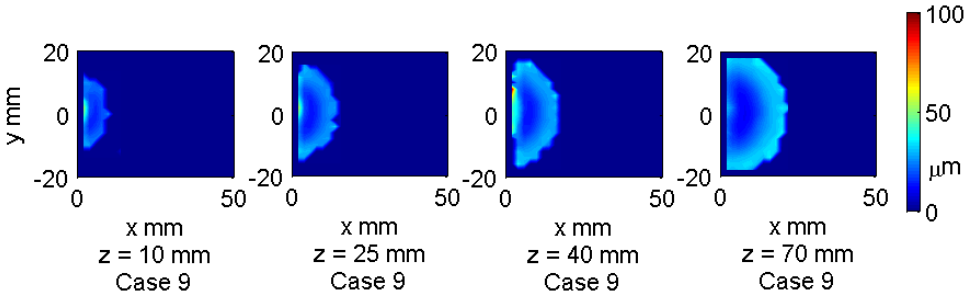

Figure B.30: ⇊ Distribution of AMD [D_{10}] ; Case 9 $We_{g\,deq} = 1520$ $q = 0.5$

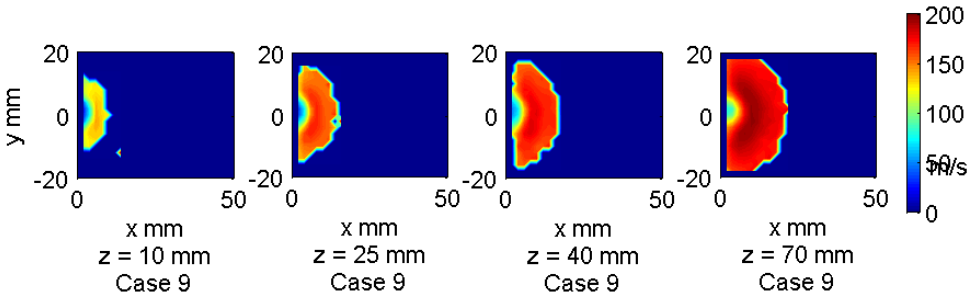

Figure B.31: ⇊ Distribution of W_{drop}; Case 9 $We_{g\,deq} = 1520$ $q = 0.5$

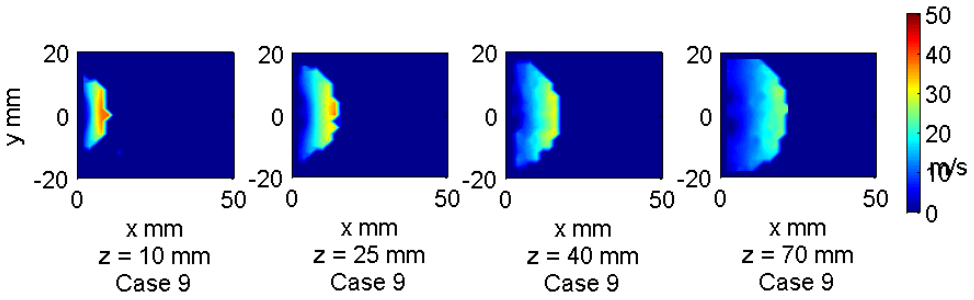

Figure B.32: ⇊ Distribution of U_{drop}; Case 9 $We_{g\,deq} = 1520$ $q = 0.5$

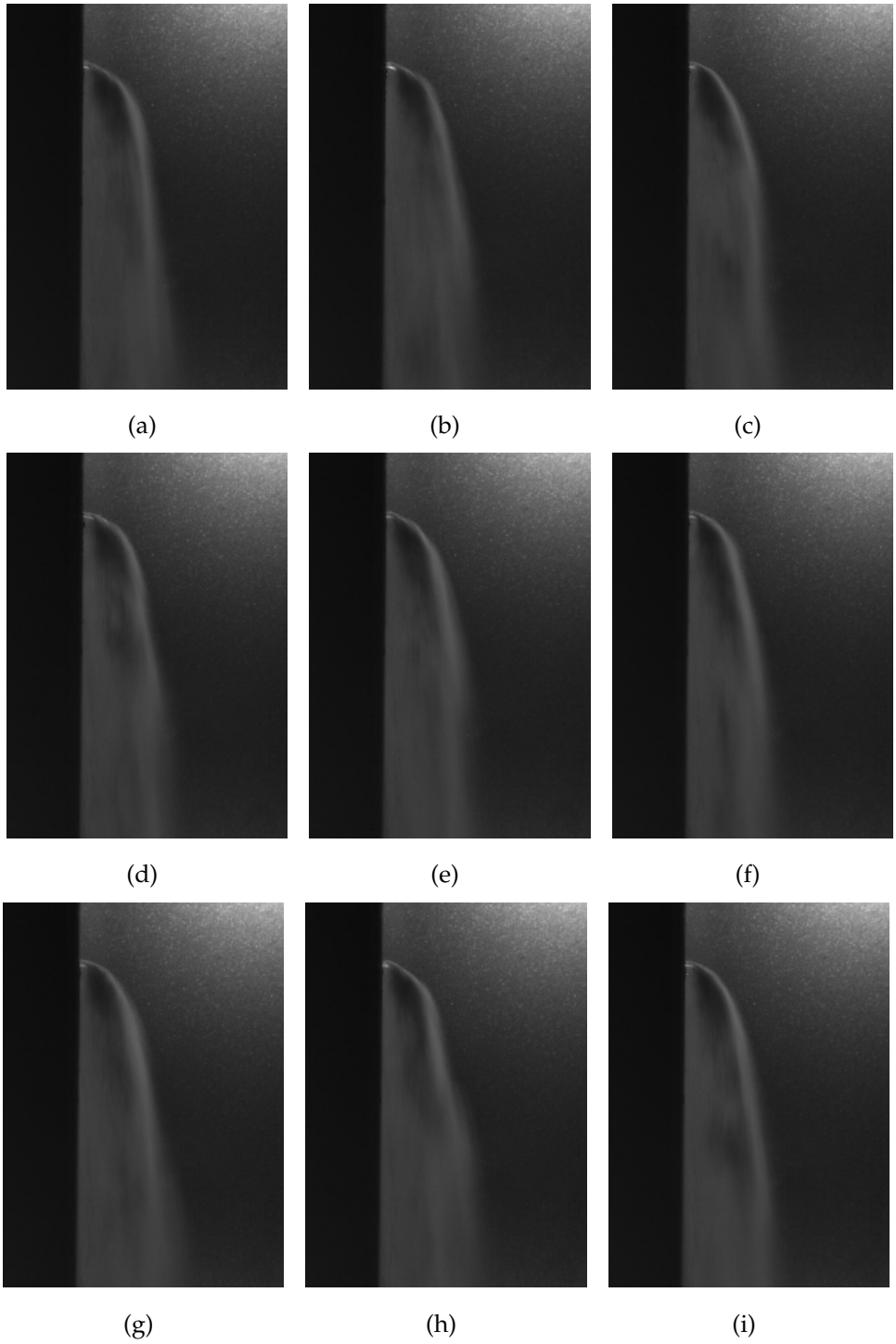

(a) (b) (c)

(d) (e) (f)

(g) (h) (i)

Figure B.33: $\overset{\Downarrow}{\ominus}$ Selection of images extracted from HSV; Case 10 $We_{g\,deq} \approx 1531$ $q \approx 1.8$

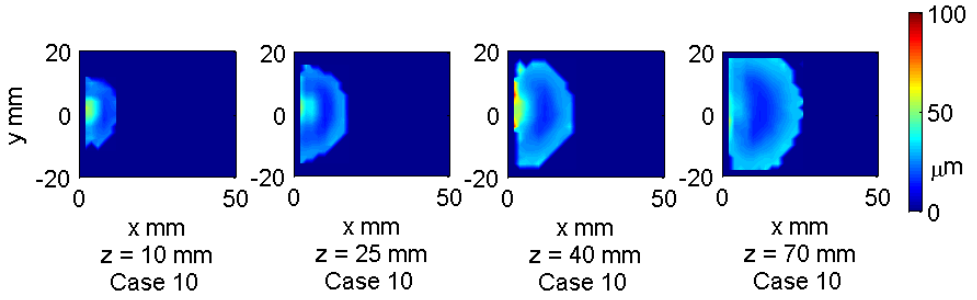

Figure B.34: ⇊ Distribution of AMD [D_{10}] ; Case 10 $We_{g\,deq}$ = 1531 q = 1.8

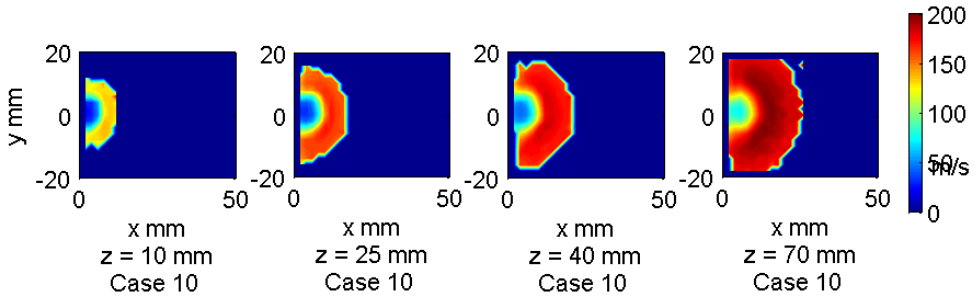

Figure B.35: ⇊ Distribution of W_{drop}; Case 10 $We_{g\,deq}$ = 1531 q = 1.8

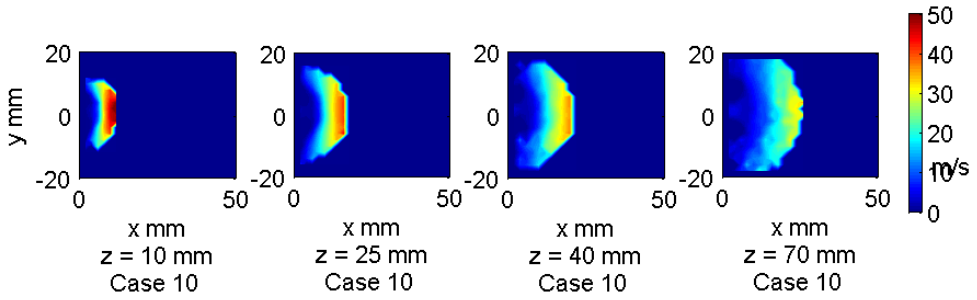

Figure B.36: ⇊ Distribution of U_{drop}; Case 10 $We_{g\,deq}$ = 1531 q = 1.8

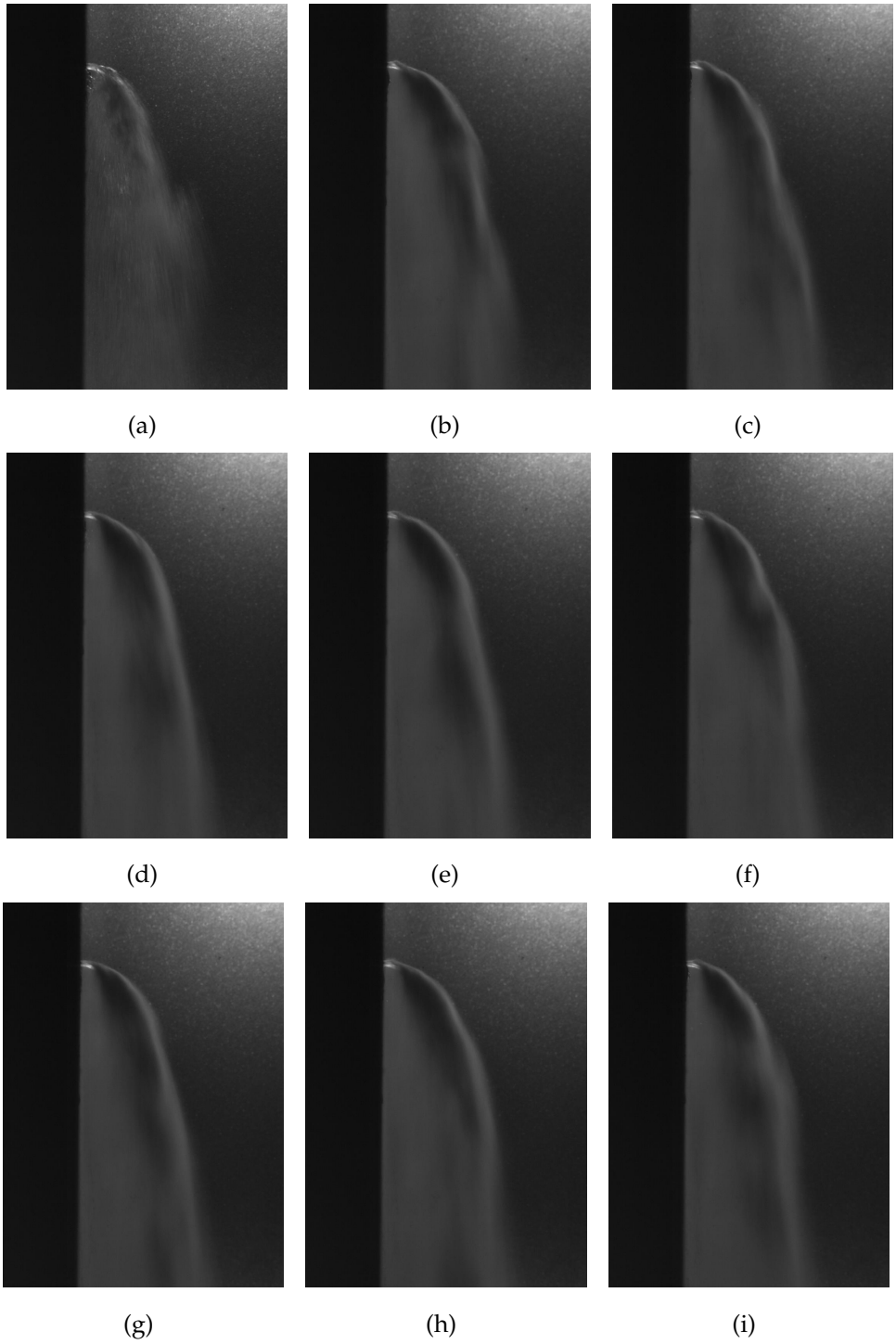

(a) (b) (c)

(d) (e) (f)

(g) (h) (i)

Figure B.37: ⇓ Selection of images extracted from HSV; Case 11 $We_{g\,deq} \approx 1444$ $q \approx 4.1$

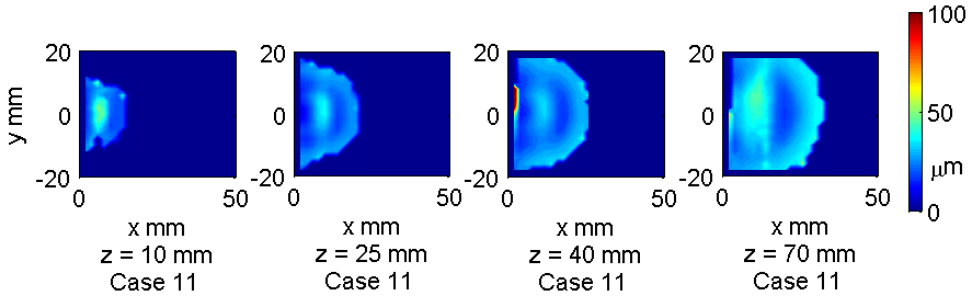

Figure B.38: ⇓ Distribution of AMD [D_{10}] ; Case 11 $We_{g\,deq} = 1444$ $q = 4.1$

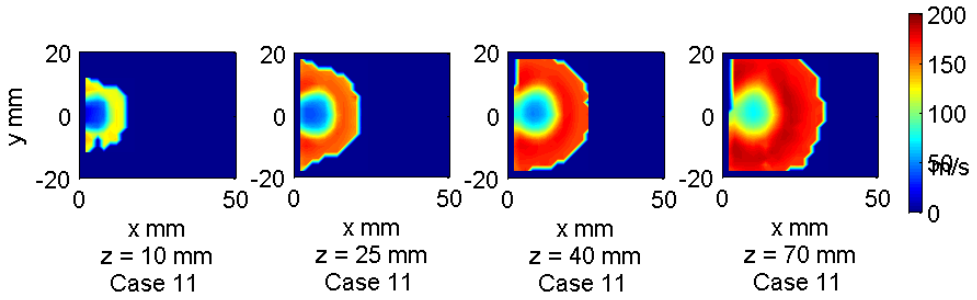

Figure B.39: ⇓ Distribution of W_{drop}; Case 11 $We_{g\,deq} = 1444$ $q = 4.1$

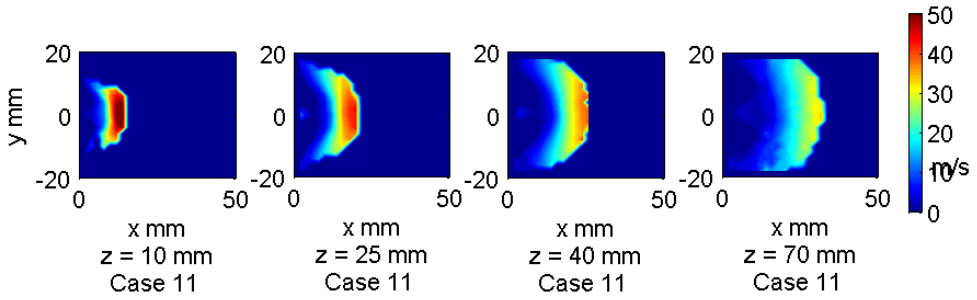

Figure B.40: ⇓ Distribution of U_{drop}; Case 11 $We_{g\,deq} = 1444$ $q = 4.1$

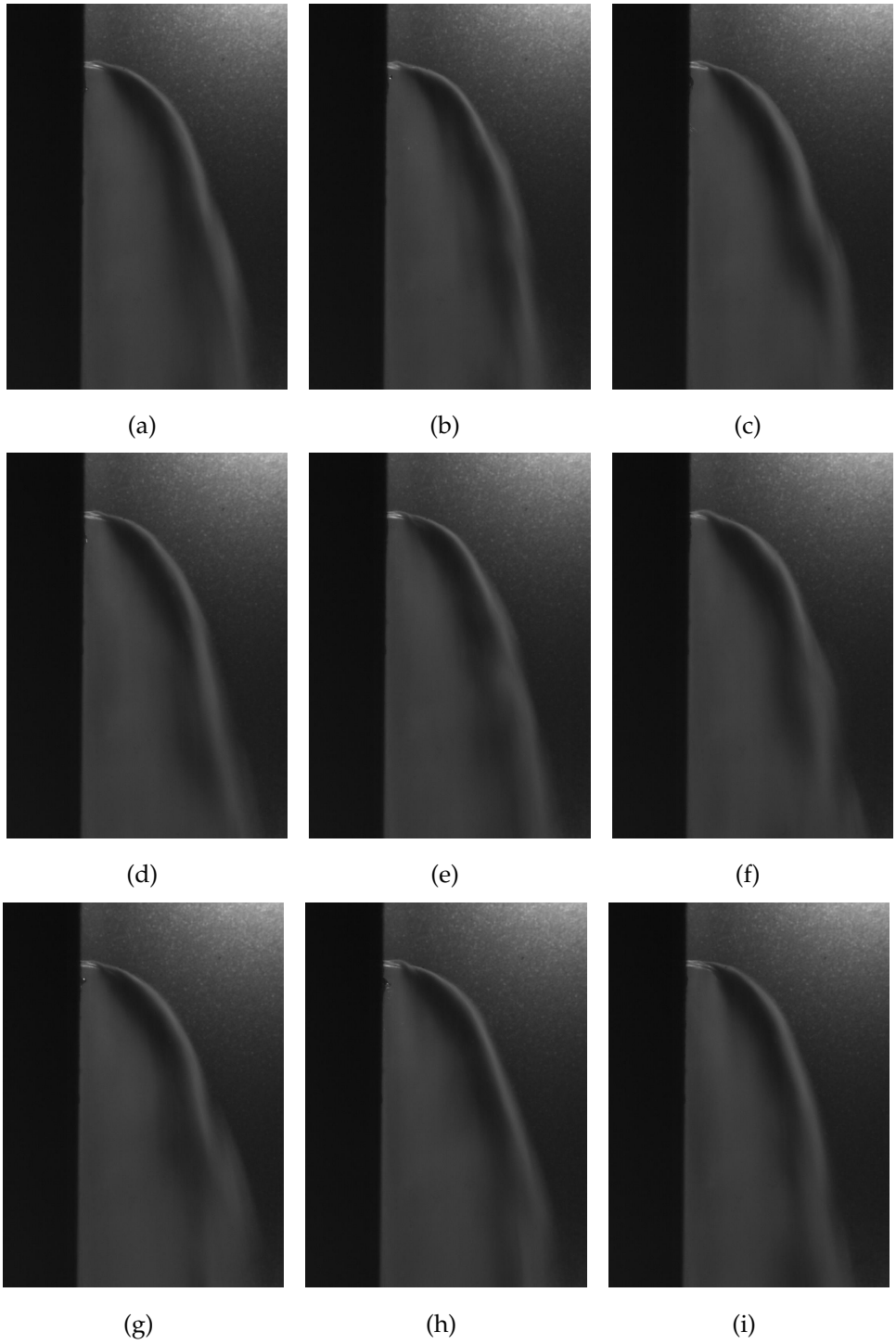

(a) (b) (c)

(d) (e) (f)

(g) (h) (i)

Figure B.41: ⇓ Selection of images extracted from HSV; Case 12 $We_{g\,deq} \approx 1263$ $q \approx 8.6$

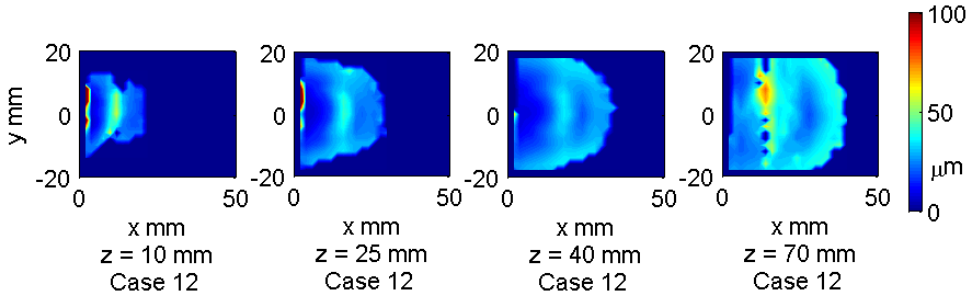

Figure B.42: ⇓ Distribution of AMD [D_{10}] ; Case 12 $We_{g\,deq}$ = 1263 q = 8.6

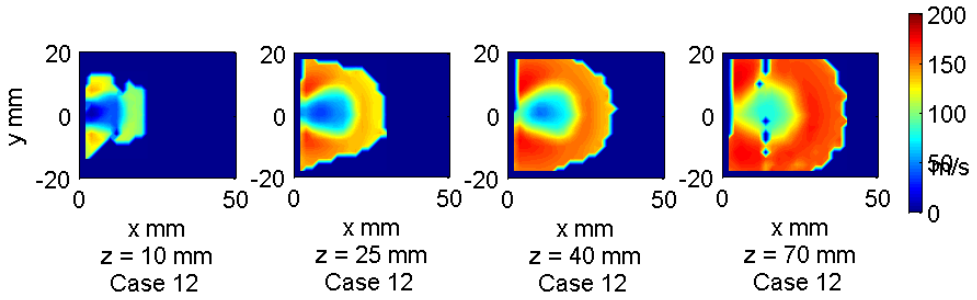

Figure B.43: ⇓ Distribution of W_{drop}; Case 12 $We_{g\,deq}$ = 1263 q = 8.6

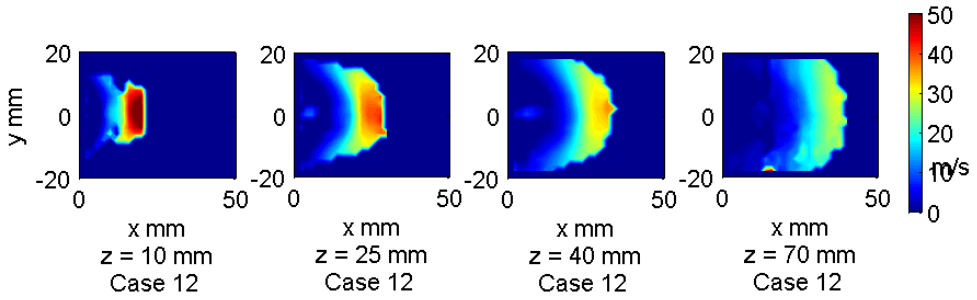

Figure B.44: ⇓ Distribution of U_{drop}; Case 12 $We_{g\,deq}$ = 1263 q = 8.6

Appendix C

Vertical Nozzle Images and Plots

	$W_{mean} \approx$ **90 m/s**	$W_{mean} \approx$ **135 m/s**	$W_{mean} \approx$ **195 m/s**
Δ**p** ≈ **0.5 bar**	Case 1: 320, (3.4)	Case 5: 699, (1.6)	Case 9: 1630, (0.6)
Δ**p** ≈ **1.5 bar**	Case 2: 331, (9.1)	Case 6: 721, (4.2)	Case 10: 1661, (1.8)
Δ**p** ≈ **3.5 bar**	Case 3: 321, (20.3)	Case 7: 710, (9.4)	Case 11: 1604, (4.2)
Δ**p** ≈ **6.5 bar**	Case 4: not possible	Case 8: not possible	Case 12: 1581, (7.5)

Table C.1: ⇊ PDPA average test conditions, $We_{g\,deq}$ (q)

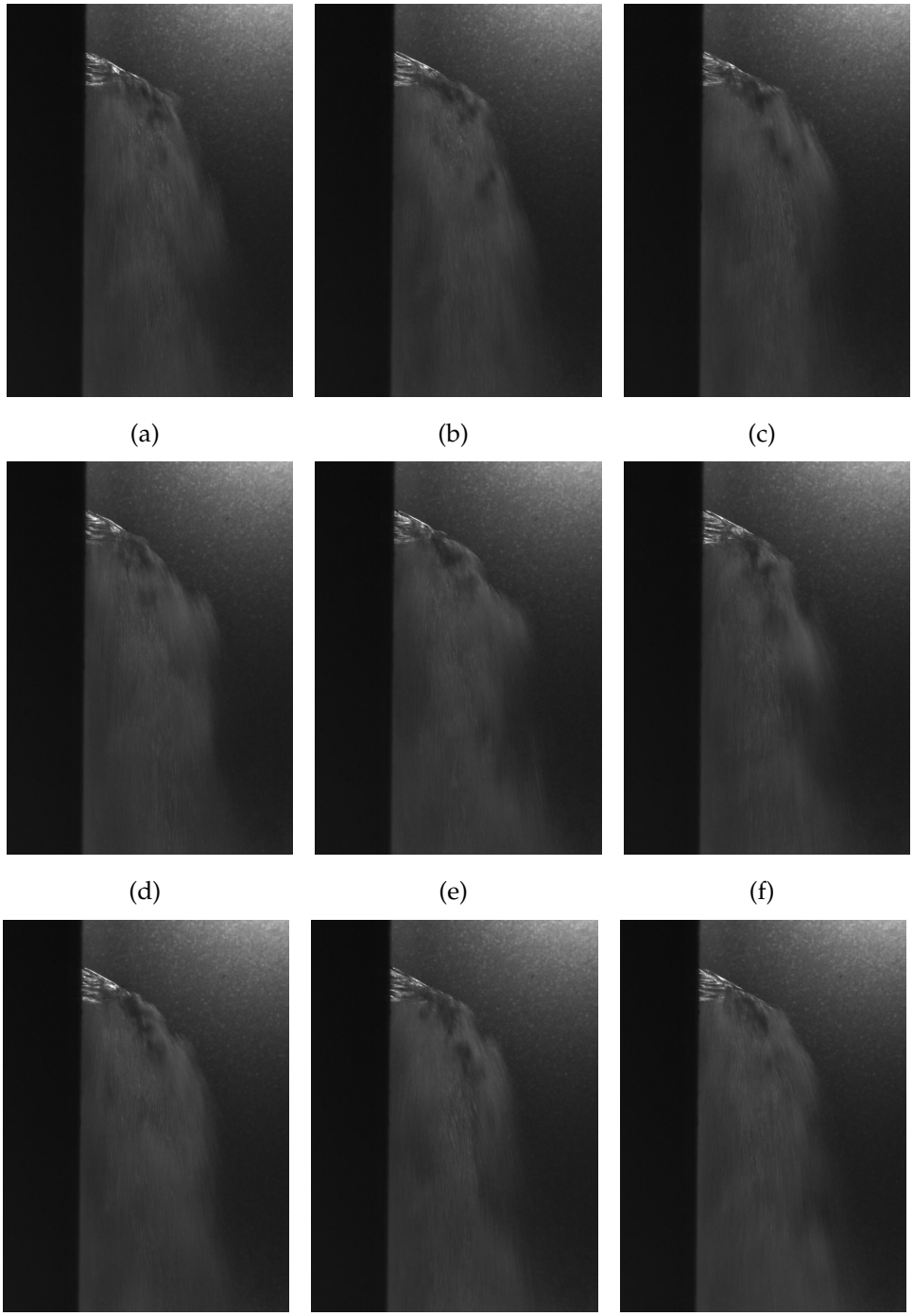

(a) (b) (c)

(d) (e) (f)

(g) (h) (i)

Figure C.1: ⇓ⓘ Selection of images extracted from HSV; Case 1 $We_{g\,deq} \approx 320$ $q \approx 3.4$

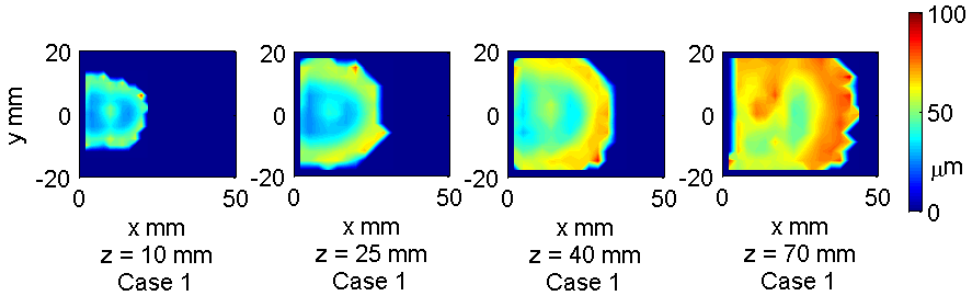

Figure C.2: ⇓ Distribution of AMD [D_{10}] ; Case 1 $We_{g\,deq} = 320$ $q = 3.4$

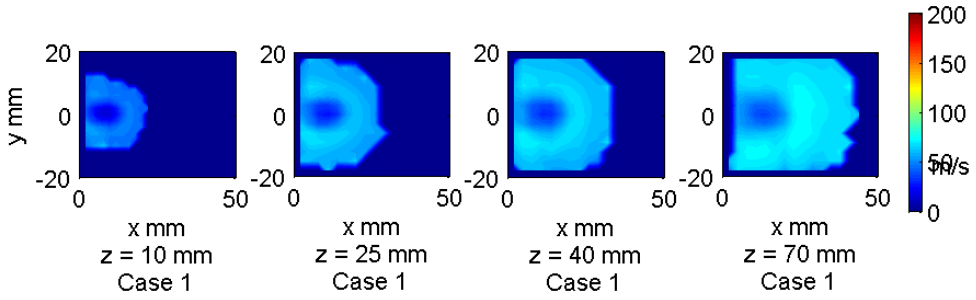

Figure C.3: ⇓ Distribution of W_{drop}; Case 1 $We_{g\,deq} = 320$ $q = 3.4$

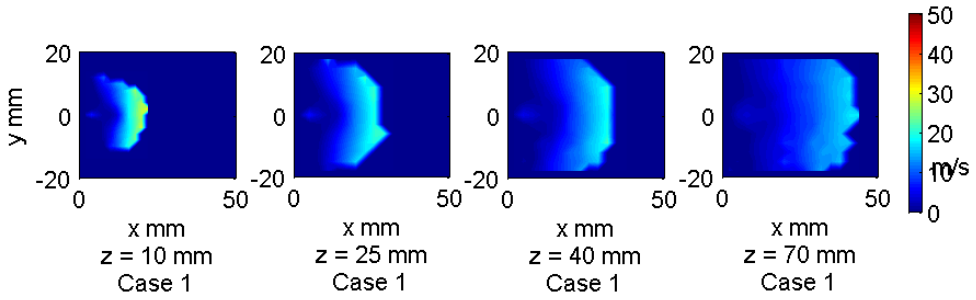

Figure C.4: ⇓ Distribution of U_{drop}; Case 1 $We_{g\,deq} = 320$ $q = 3.4$

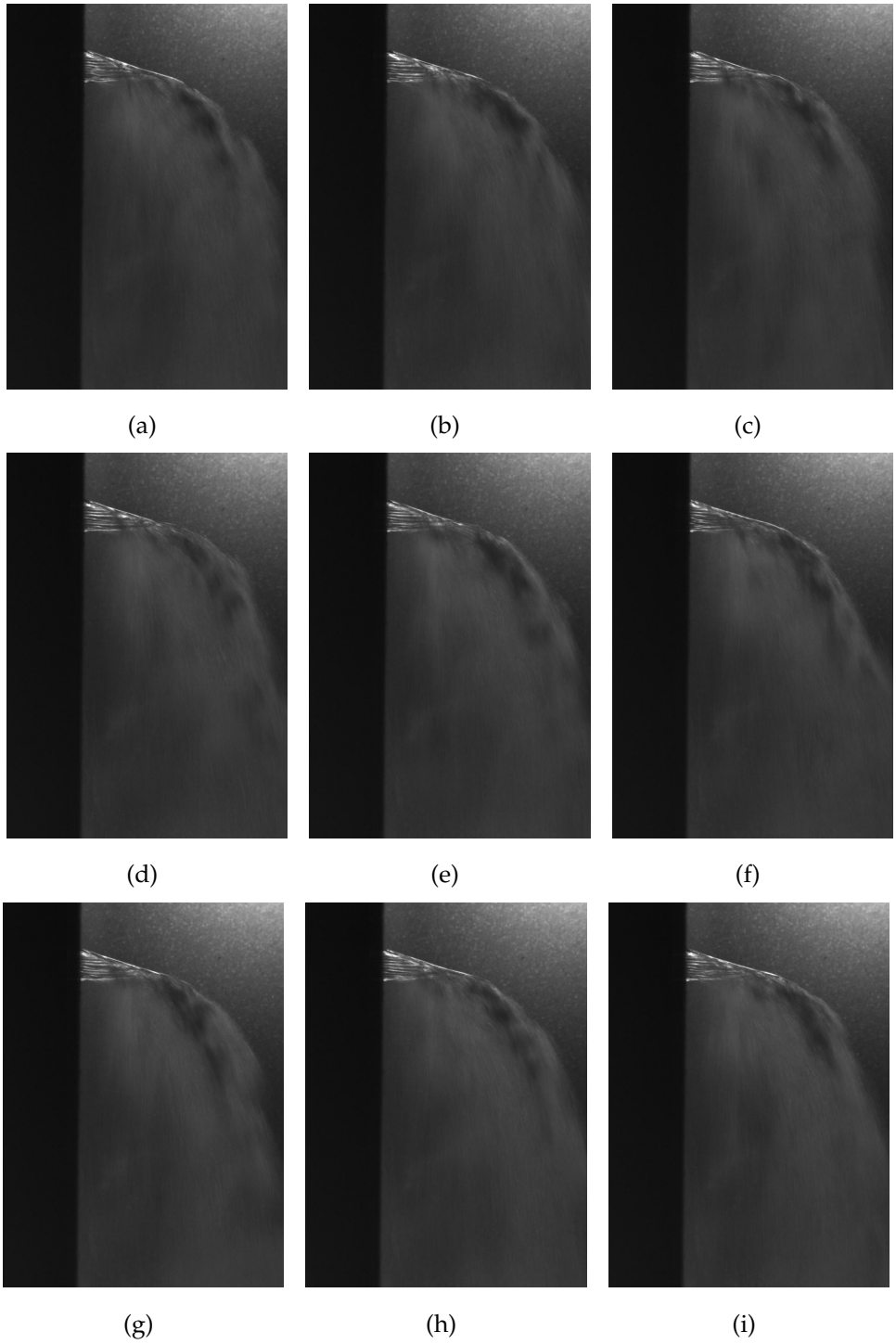

(a) (b) (c)

(d) (e) (f)

(g) (h) (i)

Figure C.5: ⇓ⓘ Selection of images extracted from HSV; Case 2 $We_{g\,deq} \approx 331$ $q \approx 9.1$

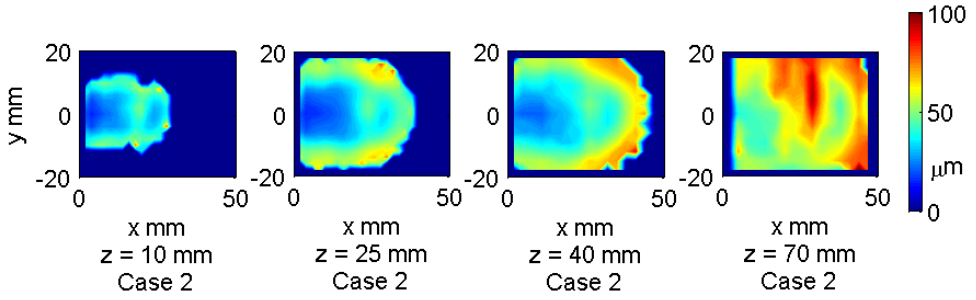

Figure C.6: ⇓ Distribution of AMD [D_{10}] ; Case 2 $We_{g\,deq} = 331$ $q = 9.1$

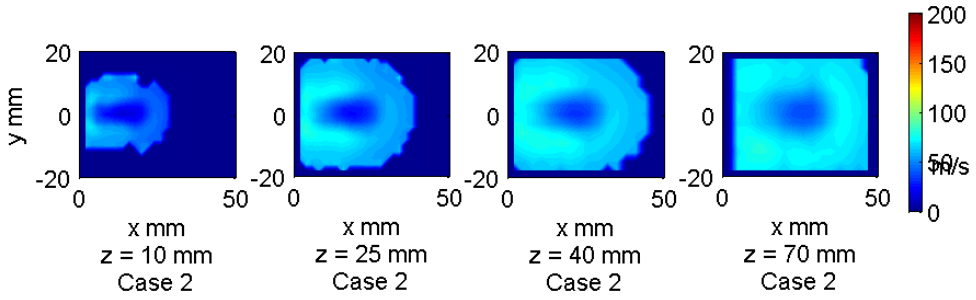

Figure C.7: ⇓ Distribution of W_{drop}; Case 2 $We_{g\,deq} = 331$ $q = 9.1$

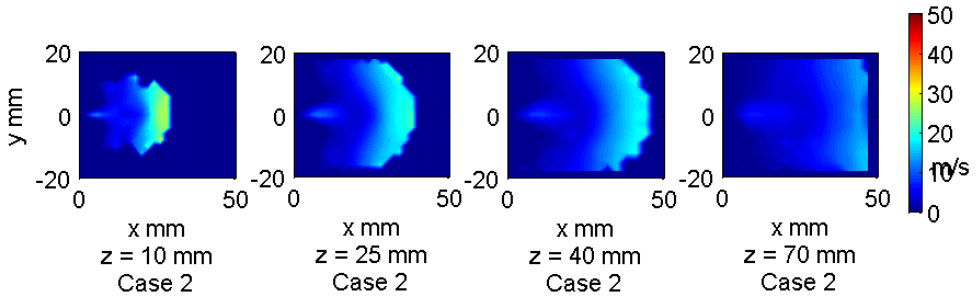

Figure C.8: ⇓ Distribution of U_{drop}; Case 2 $We_{g\,deq} = 331$ $q = 9.1$

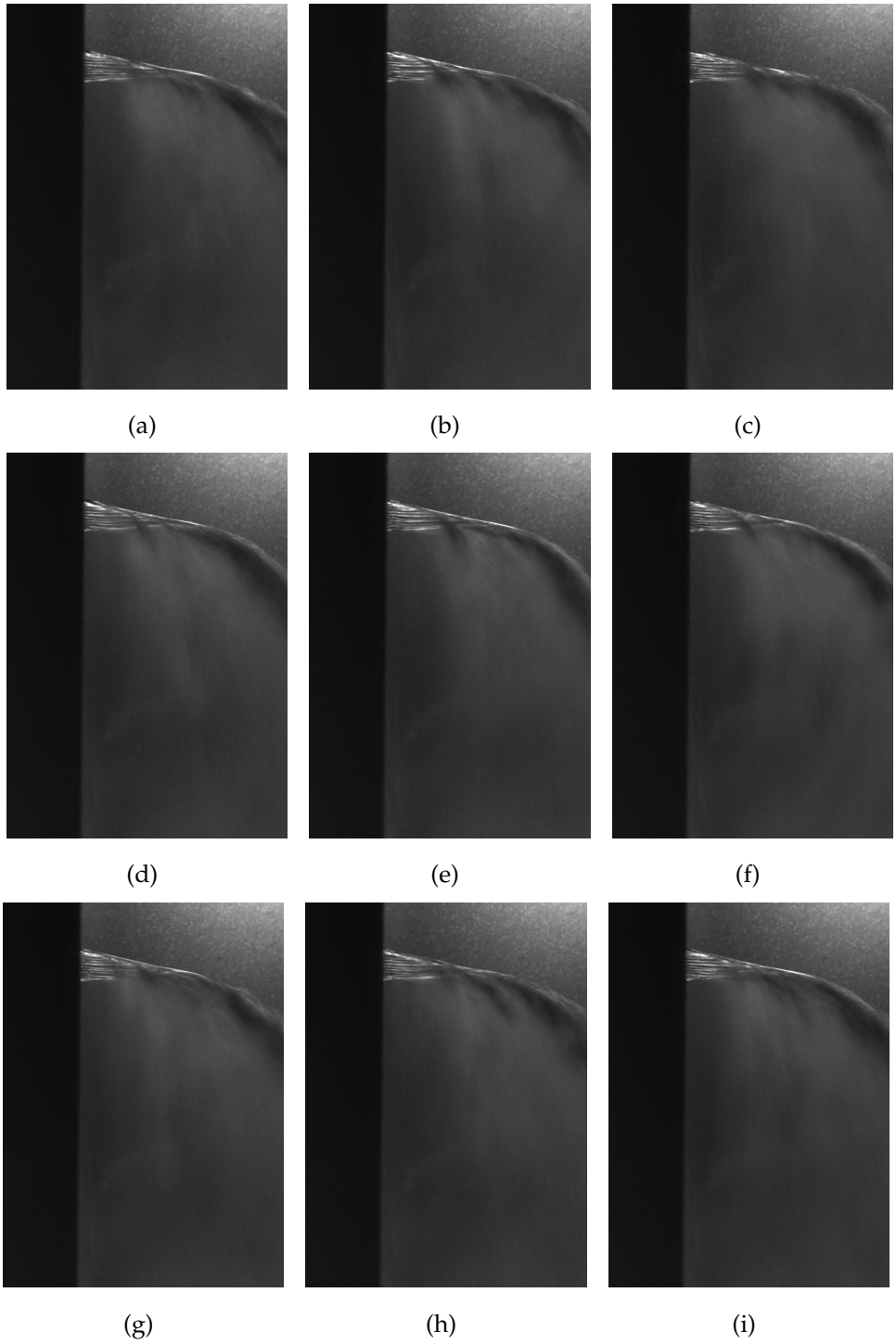

(a) (b) (c)

(d) (e) (f)

(g) (h) (i)

Figure C.9: ⇓ Selection of images extracted from HSV; Case 3 $We_{g\,deq} \approx 321$ $q \approx 20.3$

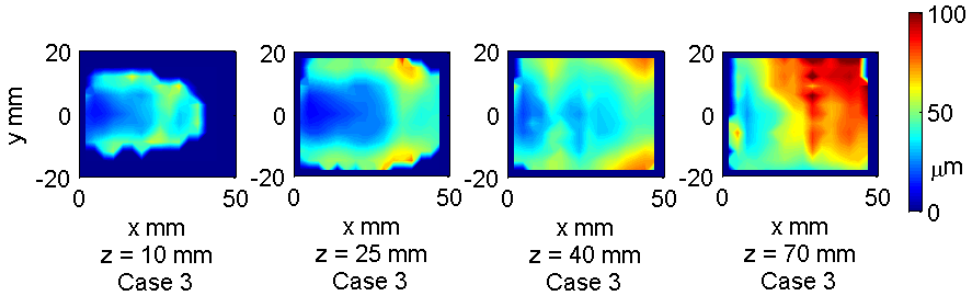

Figure C.10: ⇓ Distribution of AMD [D_{10}] ; Case 3 $We_{g\,deq} = 321$ $q = 20.3$

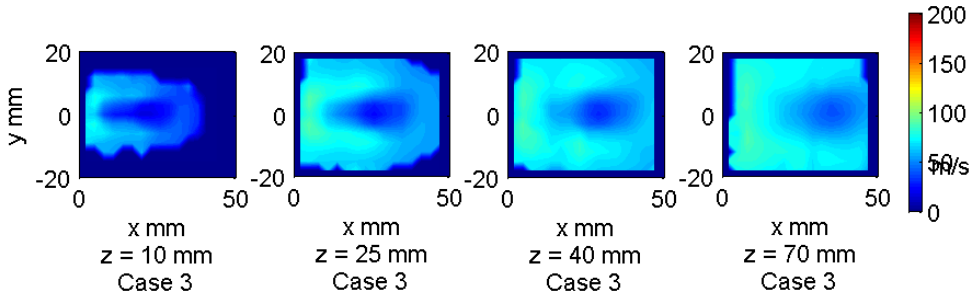

Figure C.11: ⇓ Distribution of W_{drop}; Case 3 $We_{g\,deq} = 321$ $q = 20.3$

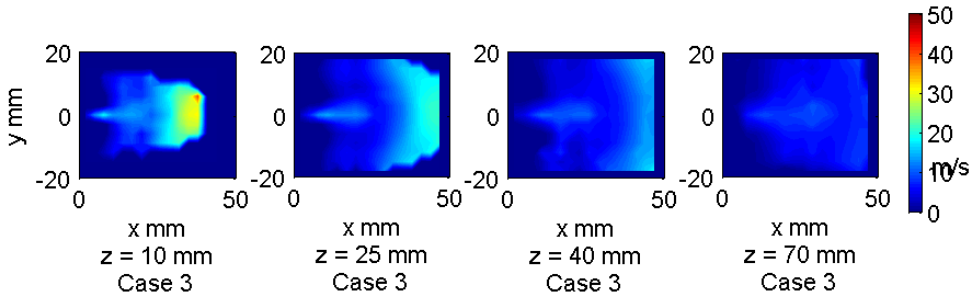

Figure C.12: ⇓ Distribution of U_{drop}; Case 3 $We_{g\,deq} = 321$ $q = 20.3$

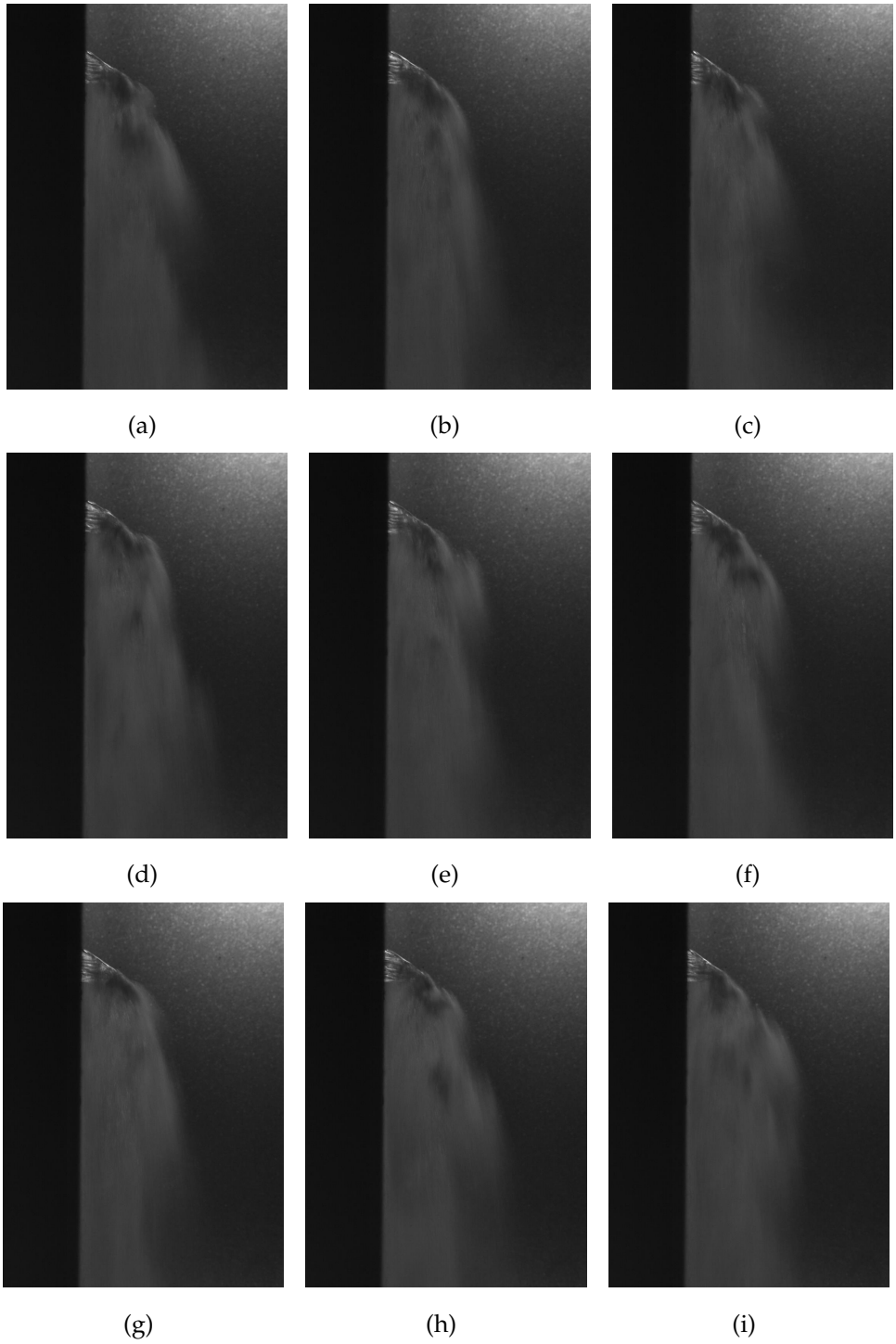

(a) (b) (c)

(d) (e) (f)

(g) (h) (i)

Figure C.13: ⇓ Selection of images extracted from HSV; Case 5 $We_{g\,deq} \approx 699$ $q \approx 1.6$

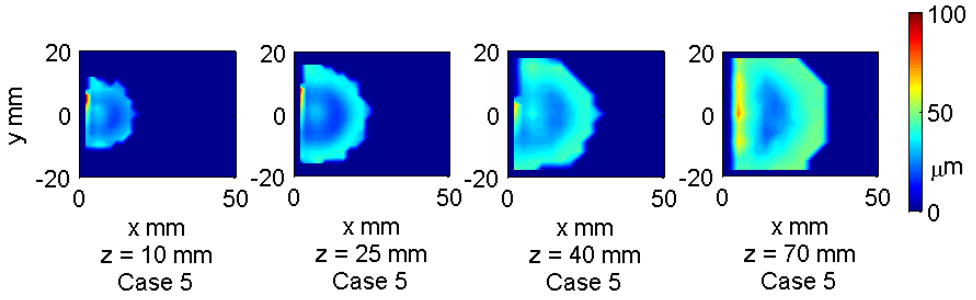

Figure C.14: ⇓ Distribution of AMD [D_{10}] ; Case 5 $We_{g\,deq} = 699$ $q = 1.6$

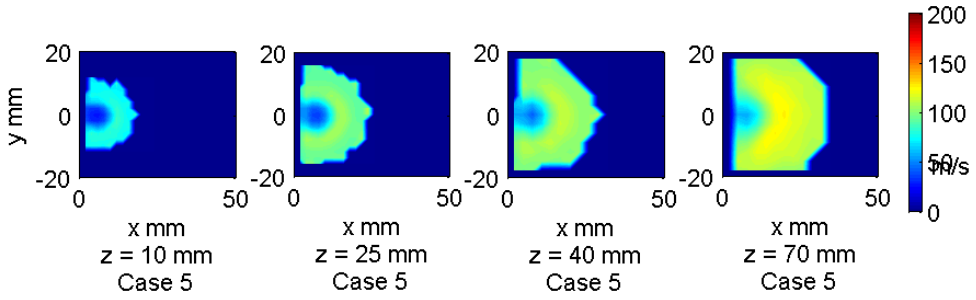

Figure C.15: ⇓ Distribution of W_{drop}; Case 5 $We_{g\,deq} = 699$ $q = 1.6$

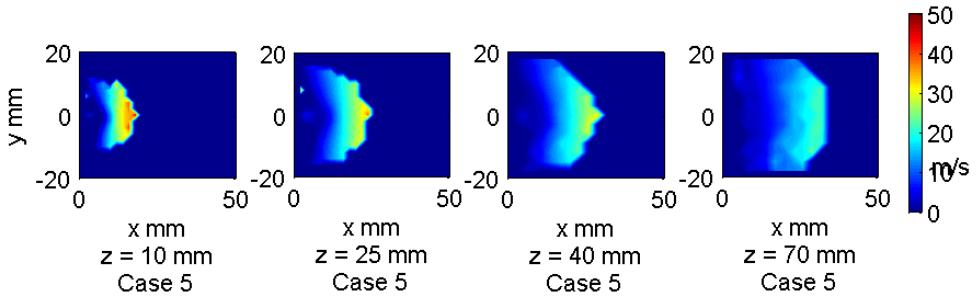

Figure C.16: ⇓ Distribution of U_{drop}; Case 5 $We_{g\,deq} = 699$ $q = 1.6$

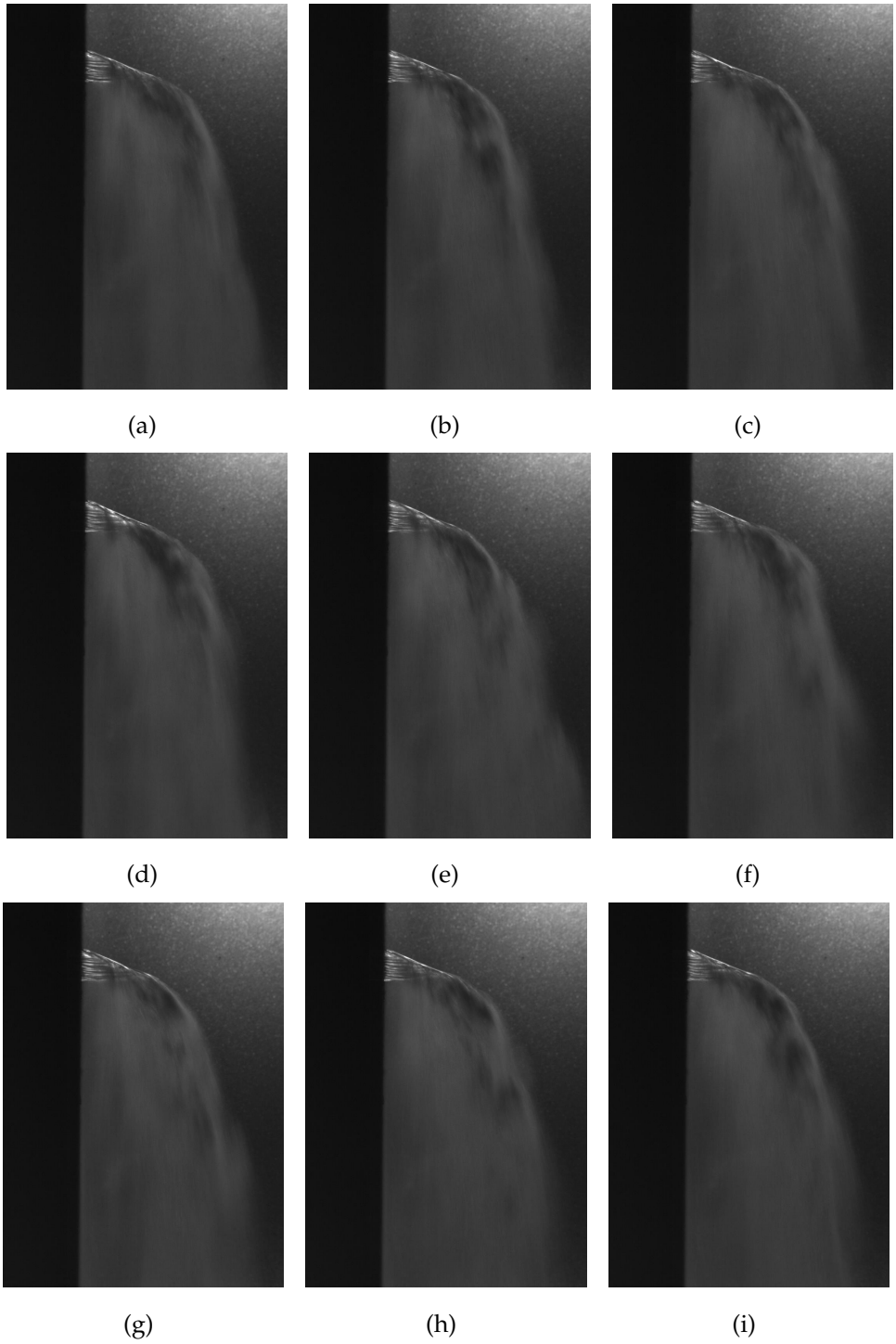

(a) (b) (c)

(d) (e) (f)

(g) (h) (i)

Figure C.17: $\Downarrow$ Selection of images extracted from HSV; Case 6 $We_{g\,deq} \approx 721$ $q \approx 4.2$

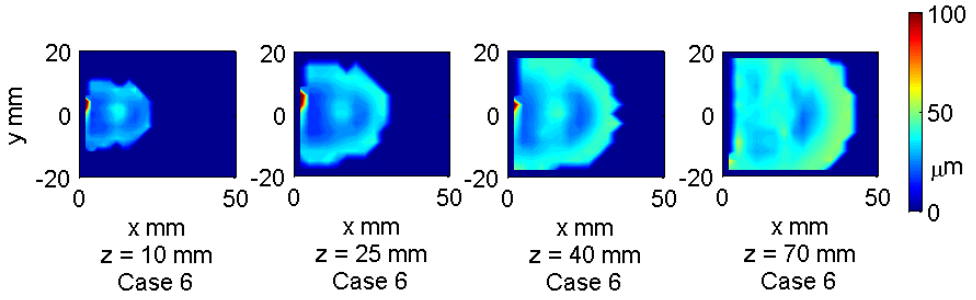

Figure C.18: ⇓ Distribution of AMD [D_{10}] ; Case 6 $We_{g\,deq} = 721$ $q = 4.2$

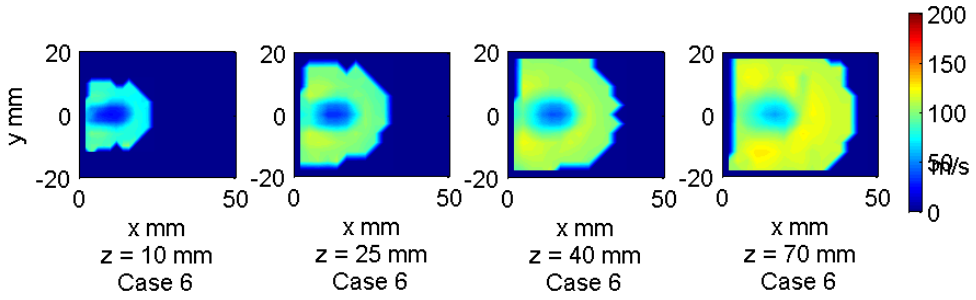

Figure C.19: ⇓ Distribution of W_{drop}; Case 6 $We_{g\,deq} = 721$ $q = 4.2$

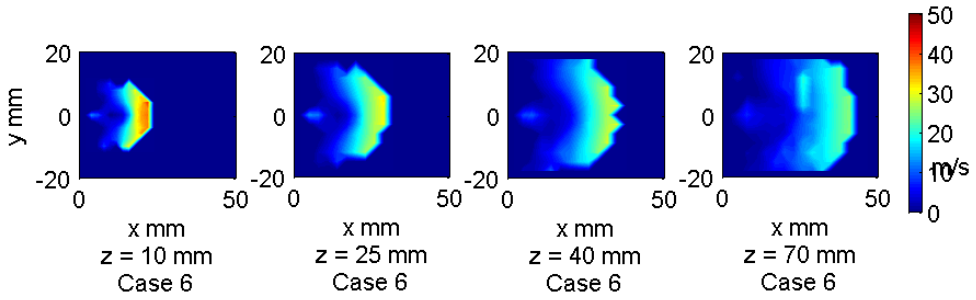

Figure C.20: ⇓ Distribution of U_{drop}; Case 6 $We_{g\,deq} = 721$ $q = 4.2$

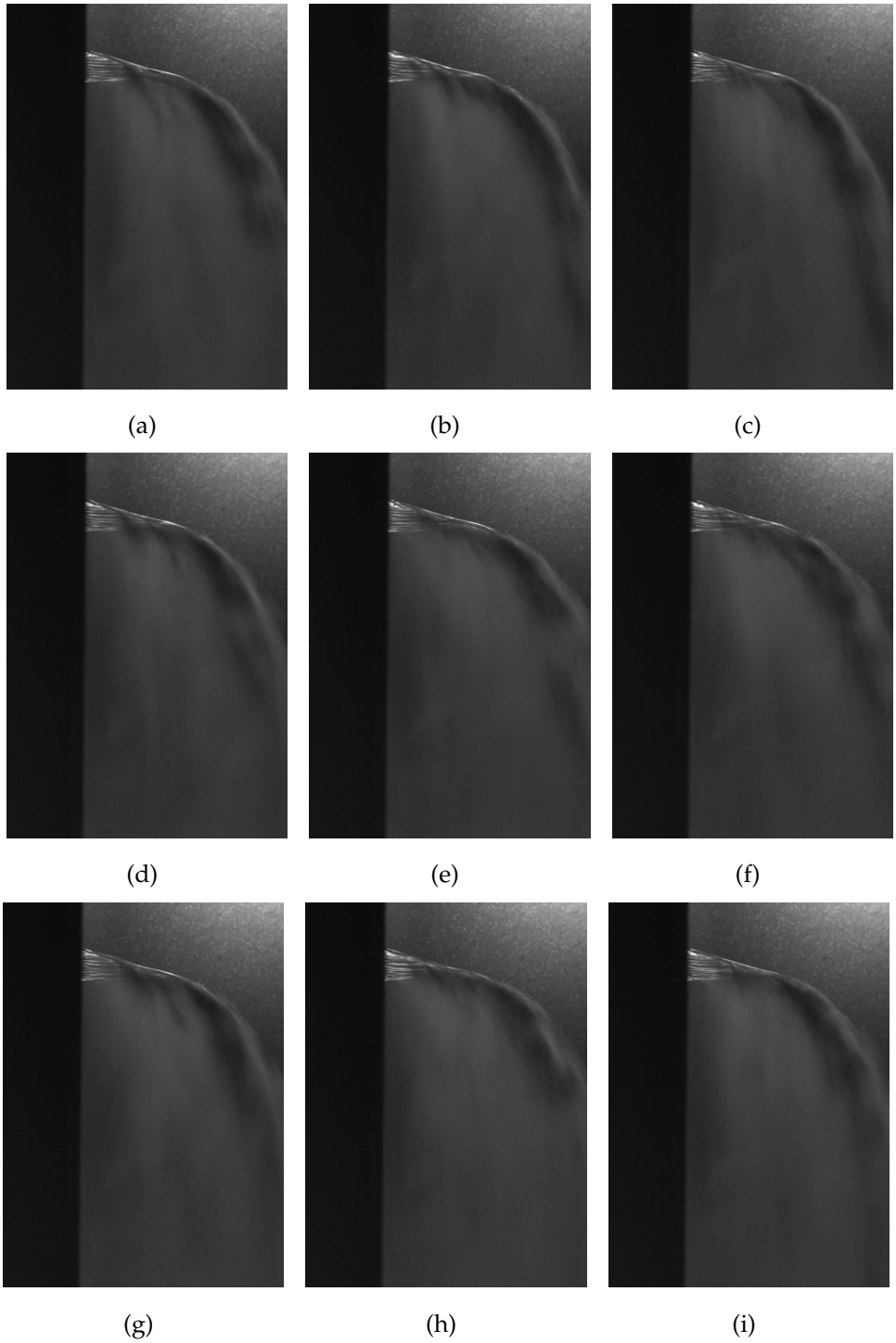

(a) (b) (c)

(d) (e) (f)

(g) (h) (i)

Figure C.21: ⇓ Selection of images extracted from HSV; Case 7 $We_{g\,deq} \approx 710$ $q \approx 9.4$

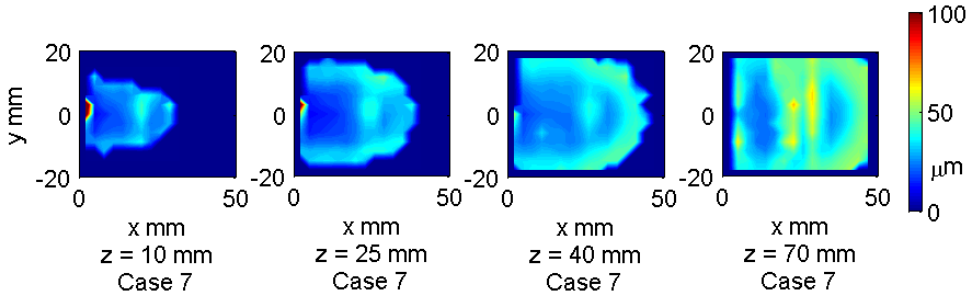

Figure C.22: ⇓ Distribution of AMD [D_{10}] ; Case 7 $We_{g\,deq} = 710$ $q = 9.4$

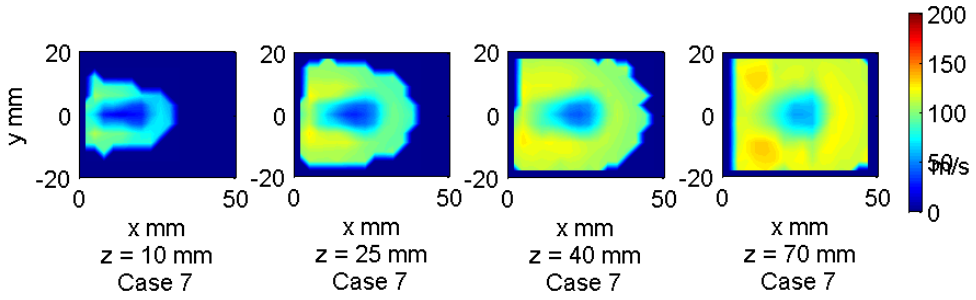

Figure C.23: ⇓ Distribution of W_{drop}; Case 7 $We_{g\,deq} = 710$ $q = 9.4$

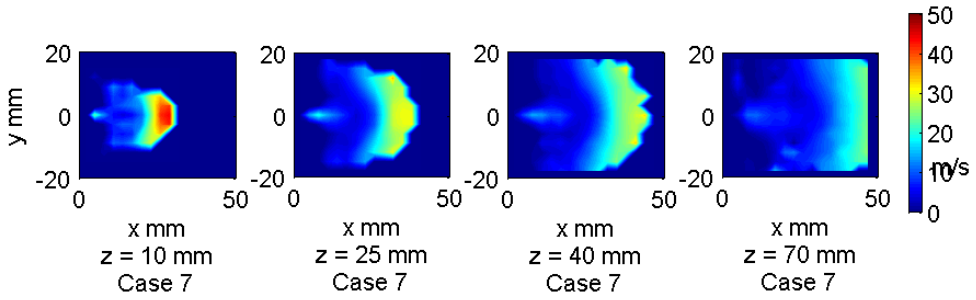

Figure C.24: ⇓ Distribution of U_{drop}; Case 7 $We_{g\,deq} = 710$ $q = 9.4$

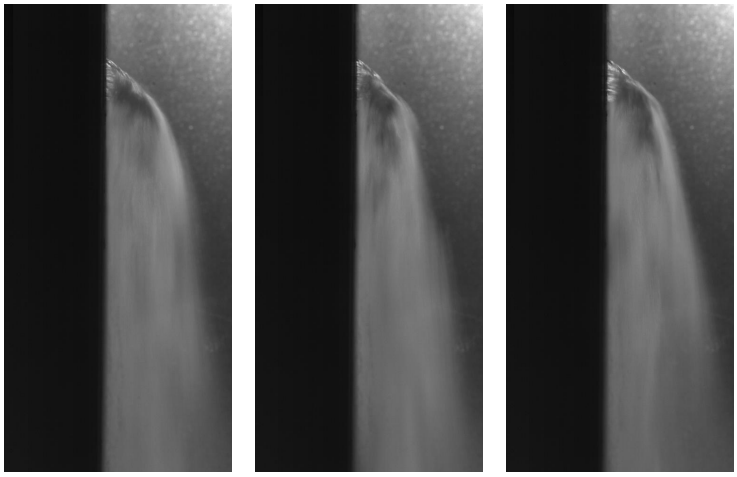

(a) (b) (c)

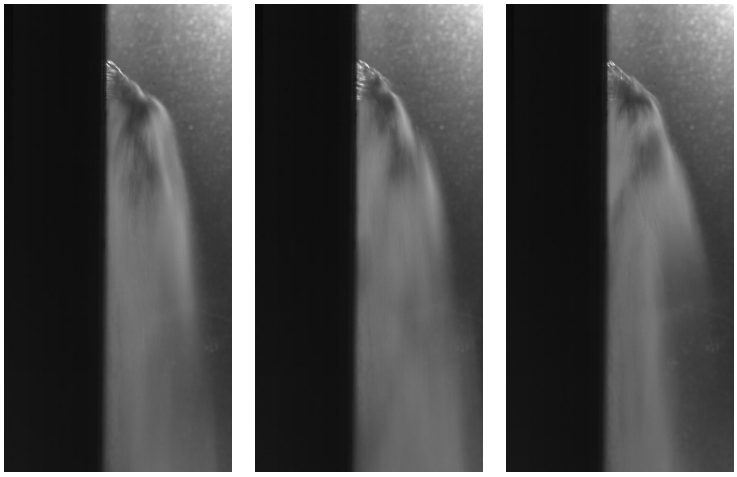

(d) (e) (f)

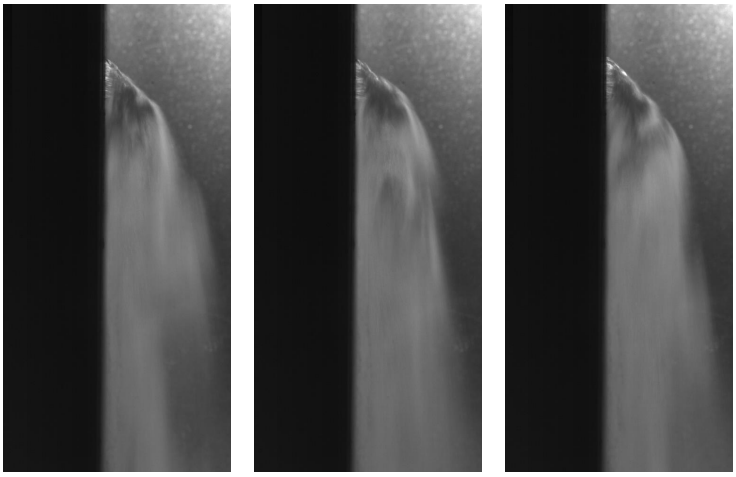

(g) (h) (i)

Figure C.25: ⇊ⓘ Selection of images extracted from HSV; Case 9 $We_{g\,deq} \approx 1630$ $q \approx 0.6$

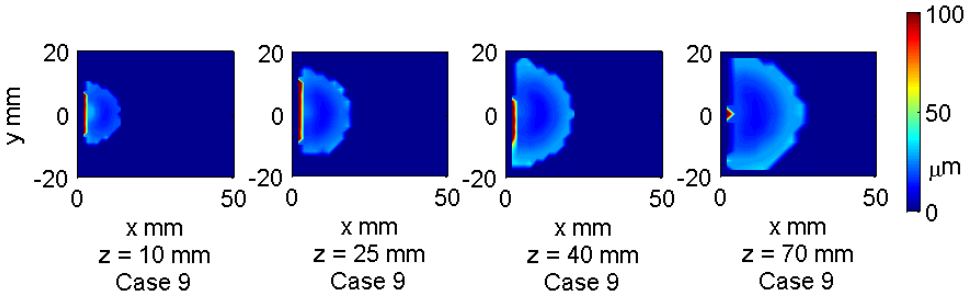

Figure C.26: ⇓ Distribution of AMD [D_{10}] ; Case 9 $We_{g\,deq} = 1630$ $q = 0.6$

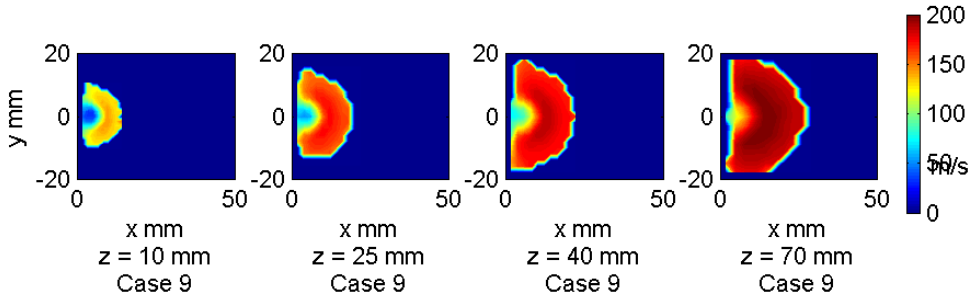

Figure C.27: ⇓ Distribution of W_{drop}; Case 9 $We_{g\,deq} = 1630$ $q = 0.6$

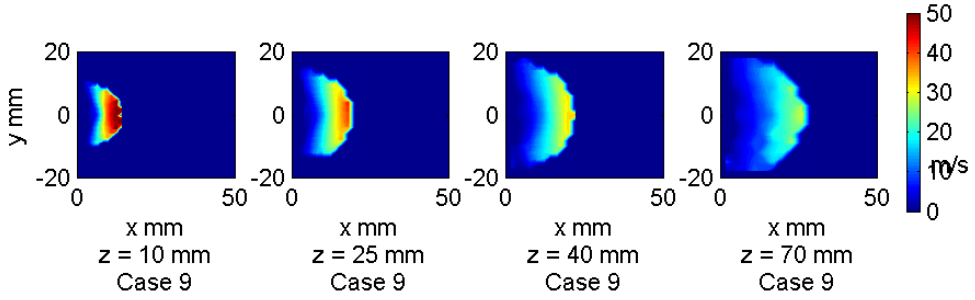

Figure C.28: ⇓ Distribution of U_{drop}; Case 9 $We_{g\,deq} = 1630$ $q = 0.6$

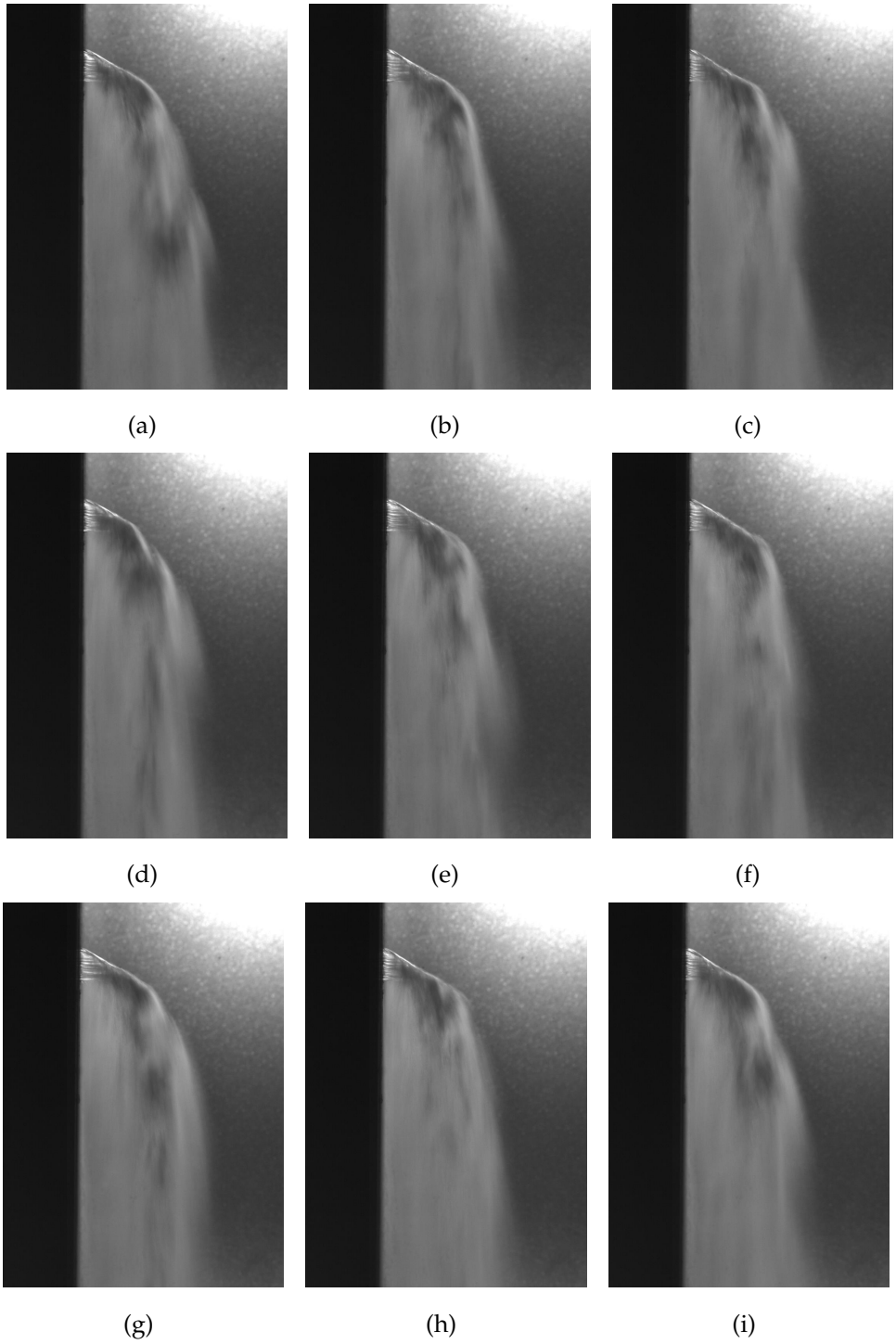

(a) (b) (c)

(d) (e) (f)

(g) (h) (i)

Figure C.29: ⇓ Selection of images extracted from HSV; Case 10 $We_{g\,deq} \approx 1661$ $q \approx 1.8$

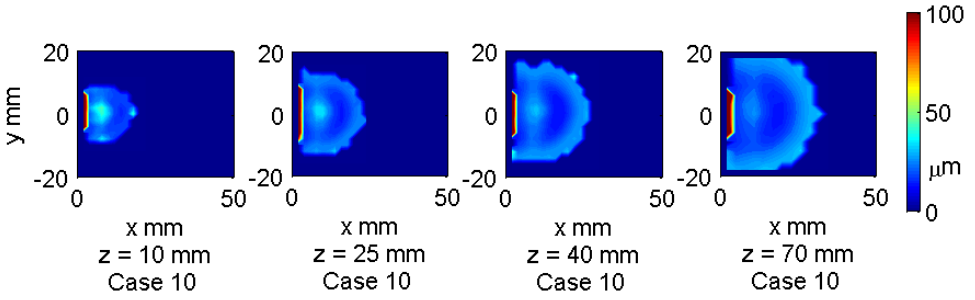

Figure C.30: ⇓ Distribution of AMD [D_{10}] ; Case 10 $We_{g\,deq}$ = 1661 q = 1.8

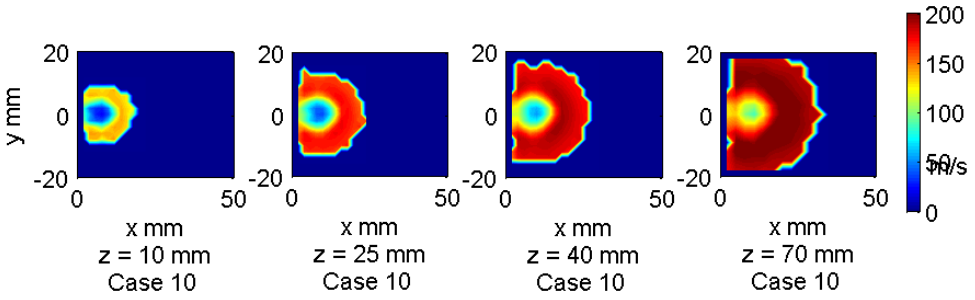

Figure C.31: ⇓ Distribution of W_{drop}; Case 10 $We_{g\,deq}$ = 1661 q = 1.8

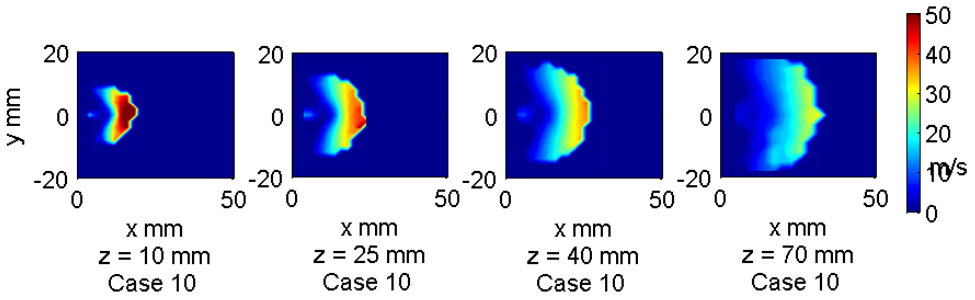

Figure C.32: ⇓ Distribution of U_{drop}; Case 10 $We_{g\,deq}$ = 1661 q = 1.8

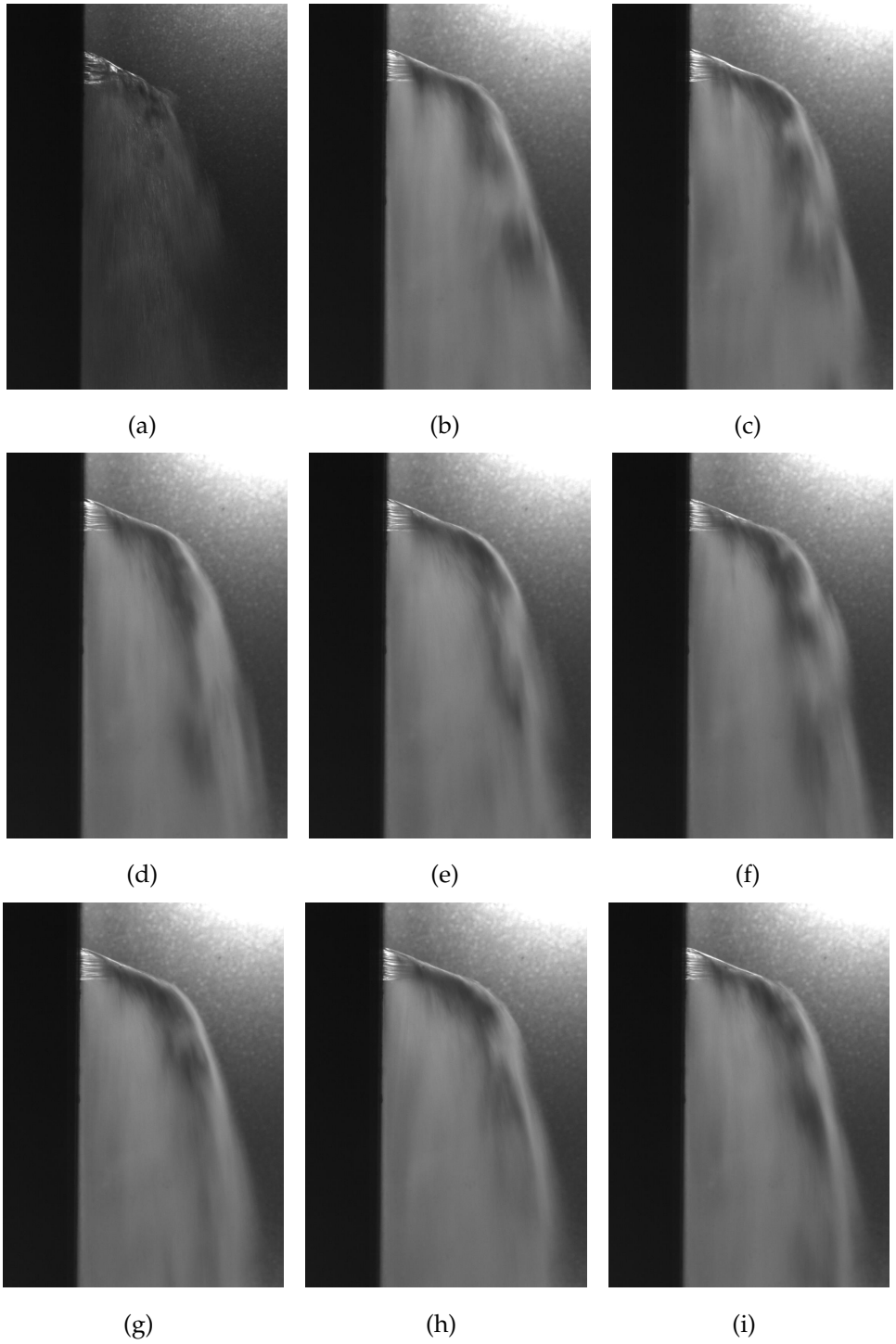

(a) (b) (c)

(d) (e) (f)

(g) (h) (i)

Figure C.33: ⇓ Selection of images extracted from HSV; Case 11 $We_{g\,deq} \approx 1604$ $q \approx 4.2$

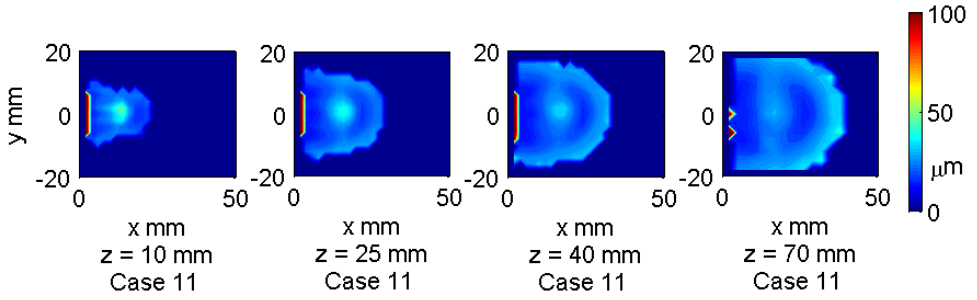

Figure C.34: ⇓ Distribution of AMD [D_{10}] ; Case 11 $We_{g\,deq} = 1604$ $q = 4.2$

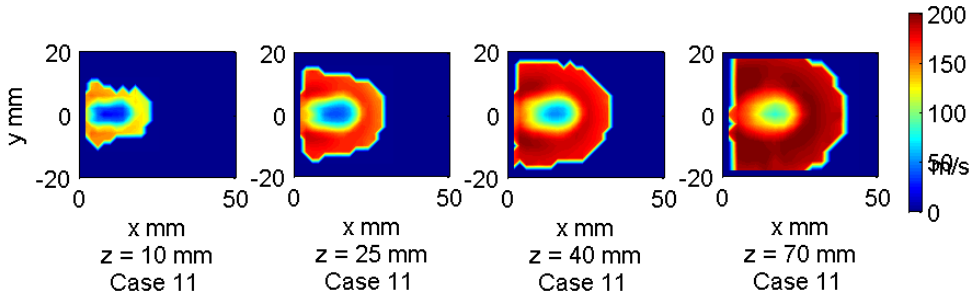

Figure C.35: ⇓ Distribution of W_{drop}; Case 11 $We_{g\,deq} = 1604$ $q = 4.2$

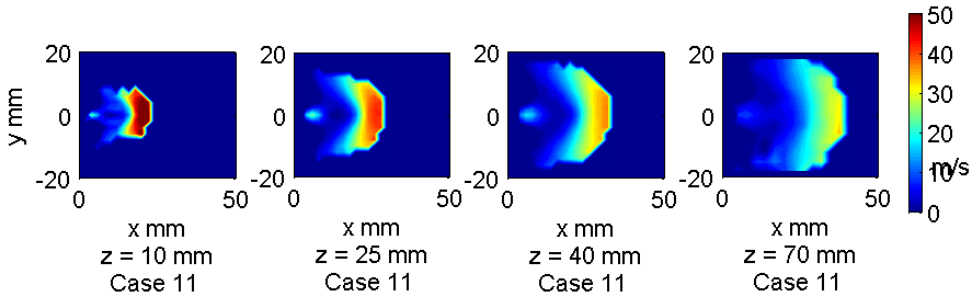

Figure C.36: ⇓ Distribution of U_{drop}; Case 11 $We_{g\,deq} = 1604$ $q = 4.2$

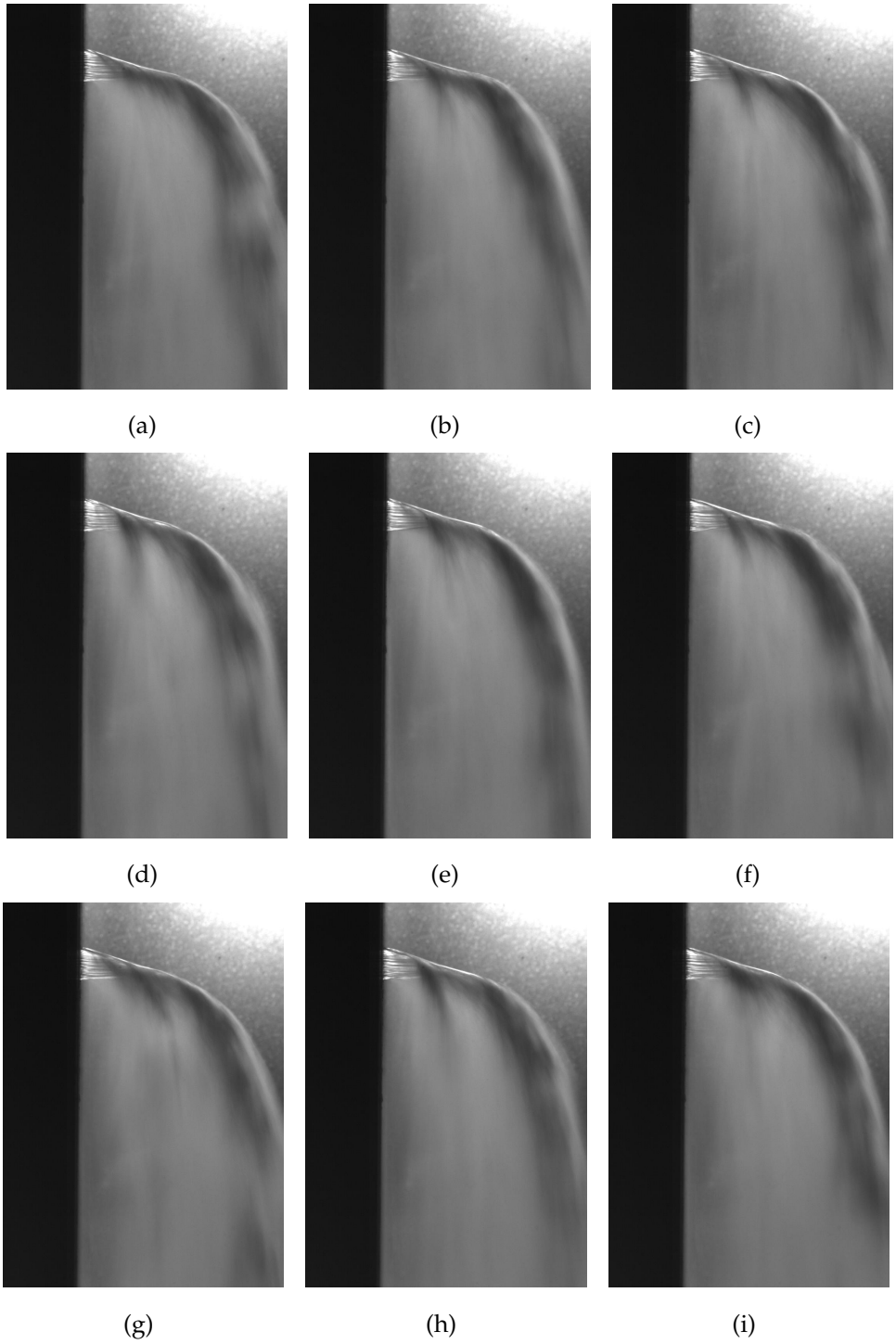

(a) (b) (c)

(d) (e) (f)

(g) (h) (i)

Figure C.37: ⇓ Selection of images extracted from HSV; Case 12 $We_{g\,deq} \approx 1581$ $q \approx 7.5$

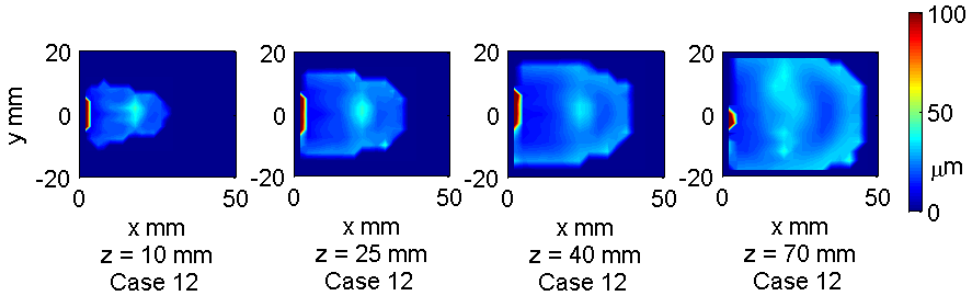

Figure C.38: ⇓ Distribution of AMD [D_{10}] ; Case 12 $We_{g\,deq} = 1581$ $q = 7.5$

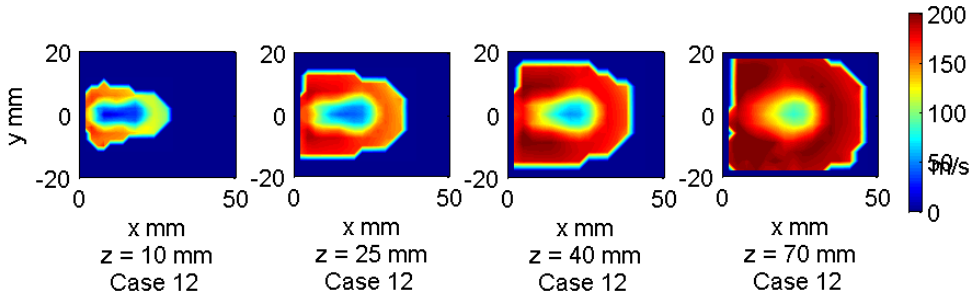

Figure C.39: ⇓ Distribution of W_{drop}; Case 12 $We_{g\,deq} = 1581$ $q = 7.5$

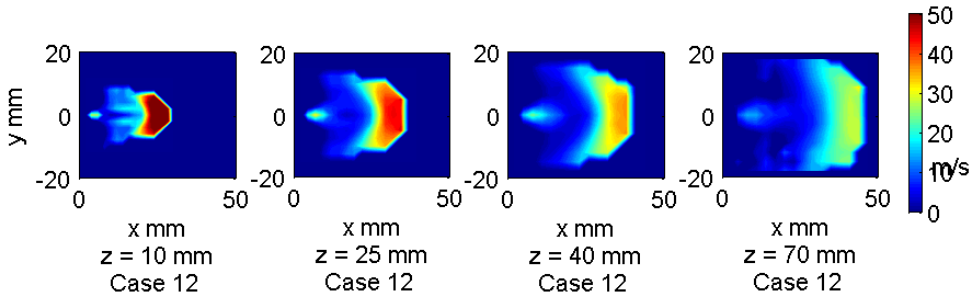

Figure C.40: ⇓ Distribution of U_{drop}; Case 12 $We_{g\,deq} = 1581$ $q = 7.5$